Blast Wave Clearing Effects on Finite-Sized Targets Subjected to Explosive Loads

Samuel E. Rigby

This thesis is submitted for partial consideration towards the degree of Doctor of Philosophy in

THE DEPARTMENT OF CIVIL AND STRUCTURAL ENGINEERING
AT THE UNIVERSITY OF SHEFFIELD

27$^{\text{th}}$ August, 2014

dedicated to Megan. . .
you are my sunshine

Abstract

A high explosive detonation is characterised by the rapid release of energy as a mass of explosive material is converted into a high pressure, high temperature gas. As this gas expands it displaces the surrounding air, causing a high pressure shock wave to travel through the air away from the explosive at supersonic speed. This shock wave can potentially cause significant damage as it impacts a structure – it is the challenge of the engineer to ensure that our infrastructure is robust enough to be able to withstand such extreme loading.

The first aspect of blast engineering is to be able to predict and quantify the spatial and temporal variation of the load acting on the target to a sufficient level of accuracy. Whilst experimental trials and higher order numerical schemes offer useful insights, the time and expense associated with such methods renders them unusable for the early stages of design. Accordingly, semi-empirical blast predictions are more often favoured.

These semi-empirical predictions assume that the target forms a reflecting surface that is effectively infinite in dimensions perpendicular to the direction of travel of the blast wave. For finite-sized targets, however, the presence of target edges is known to significantly alter the pressure acting on the loaded face in a process known as blast wave clearing – diffraction of the blast wave around the target which causes a relief wave to sweep in from the edges of the reflecting surface.

Current methods for predicting blast wave clearing fail to capture the physical process, and as such are inadequate at providing valid blast pressure predictions. Approximating the relief wave as an acoustic pulse allows for accurate predictions which are based on physically valid principles. Accurate prediction of cleared blast pressure loads has enabled the effect of blast wave clearing to be identified and quantified.

Secondly, the target response to this load must be predicted. The single-degree-of-freedom (SDOF) method approximates the distributed properties of the real life system into single point equivalent values. This procedure is well established for the target properties, and by transforming the spatial variation of cleared blast pressure in a similar manner (by conserving energy between real life and equivalent systems), clearing blast pressure loads can be modelled in SDOF analyses. The marked effect of clearing on structural response has been clearly demonstrated in this thesis.

The combined improvements to both load prediction and response modelling has allowed a full parametric study to be conducted on finite-sized targets subjected to blast loads. Neglecting clearing can be largely over-conservative for small targets, and for targets with plastic resistance significantly less than the applied transient blast force. It has been observed, however, that neglecting clearing can sometimes be non-conservative through a combination of target rebound, plasticity and early negative pressures caused by the clearing waves.

Findings in the PhD thesis should be used to highlight the complex nature of blast-target interaction, particularly when blast wave clearing is concerned, and should dispel the myth that a design will be safe if clearing is neglected. Results presented in the study can also be used by practising engineers to determine the likely effect that blast wave clearing will have on any configuration of explosive mass, stand-off, target size and dynamic properties, and the numerical models developed within have the potential for widespread use in existing commercial software.

Acknowledgements

Firstly, I would like to thank my PhD supervisors, Dr. Andy Tyas and Dr. Terry Bennett, without whom this thesis would not have been possible. I have learnt so much from you two in my short research career so far, and I hope to learn even more in the years to come. Andy, your insights into the technical aspects of the thesis have been invaluable and have helped me get the best out of myself. Terry, it has been fantastic to have a supervisor who you know will always be there to help out, but who isn't afraid to be tough when necessary! I would also like to thank: Dr. Sam Clarke for stepping in at the last minute and agreeing to supervise me at the point where the reward to work ratio was at its minimum; Steve Fay and Dr. Jim Warren from Blastech for giving me the opportunity to undertake experimental work; and Al, Roy, Mik and Danny for helping me on site. I feel privileged to have been given access to such a good testing facility – I hope my thesis does enough to show the quality of experimental work produced by Blastech.

I would also like to thank everyone in the Department of Civil and Structural Engineering, particularly those who have worked in D120a (and D120) during my time here. It is incredible how much a friendly atmosphere can encourage you to work better – I know I would have enjoyed my time here a lot less if it weren't for you guys. Thank you for showing an interest in what I'm doing, and for sharing your research with me. Prof. Harm Askes and Prof. Matthew Gilbert of the CMD group also deserve thanks. Being part of such a great research group has always motivated me to achieve the best I can – to keep up the sterling reputation of the CMD group and the University of Sheffield.

Mum and Dad, thank you for always being there for me. The support I've had from you throughout my life has always made me want to be the best I can possibly be. You two are the reason why I wanted to do a PhD, and your advice has always been well placed, reasoned and motivating. Dad, you still owe me a purple jacket! James, Jon and Steve, thank you for being such amazing big brothers and giving me something to look up to. Being the youngest has always made me strive to achieve what you guys have. I love having brothers and parents that I can also call my best friends.

Finally, and most importantly, I would like to thank Megan. For everything.

Sam Rigby,
Wednesday 27$^{\text{th}}$ August, 2014.

Contents

List of Figures

xiv

List of Tables

Nomenclature

a	-	arbitrary scalar,
		clearing coefficient (Rickman & Murrell 2007),
		sonic velocity in the reflected region
a_0	-	sonic velocity in air (at ambient conditions)
A	-	clearing coefficient (Taylor 1972),
		coefficient in JWL equation of state,
		panel area
A_e	-	element area
b	-	clearing coefficient (Rickman & Murrell 2007),
		waveform parameter (decay of exponential pressure time curve)
B	-	clearing coefficient (Taylor 1972),
		coefficient in JWL equation of state
c	-	damping coefficient
$C_{0,1}$	-	artificial bulk viscosity coefficients
$C_{1:6}$	-	coefficients in linear polynomial equation of state
C_D	-	drag coefficient
C_f	-	clearing factor (i/i_{so})
C_r	-	reflection coefficient
C_r^-	-	negative phase reflection coefficient
d	-	thickness
D	-	detonation velocity
E	-	energy,
		Young's Modulus
E_0	-	detonation energy per unit volume
f	-	natural frequency
F	-	force
F_e	-	equivalent force
$F_{e,max}$	-	peak equivalent force
$F_{e,min}$	-	peak negative phase equivalent force
F_{equiv}	-	energy equivalent uniform force
$F_{(1,2)}$	-	burn fraction

G	-	target front height or half-width (largest value)
h	-	target height
H	-	scaled target height
i	-	impulse
i_r	-	reflected positive phase specific impulse
i_r^-	-	reflected negative phase specific impulse
i_{so}	-	incident positive phase specific impulse
i_{so}^-	-	incident negative phase specific impulse
I	-	impulse ratio,
		second moment of area
k	-	stiffness
k_e	-	equivalent stiffness
K	-	scale factor
K_L	-	load factor
K_M	-	mass factor
K_S	-	spatial load factor
l_e	-	element length
$l_{e,max}$	-	maximum element length
L	-	span
m	-	mass
m_e	-	equivalent mass
M_m	-	moment capacity at mid-span
M_s	-	moment capacity at supports
O	-	over-expansion ratio
p	-	pressure
p_0	-	ambient air pressure
p_{avg}	-	average pressure
p_{eos}	-	pressure from equation of state
p_{equiv}	-	energy equivalent uniform pressure
p_r	-	reflected overpressure
$p_{r,max}$	-	peak reflected overpressure
$p_{r,min}$	-	peak reflected underpressure
p_{so}	-	incident overpressure
$p_{so,max}$	-	peak incident overpressure
$p_{so,min}$	-	peak incident underpressure
p_{stag}	-	stagnation pressure
PCJ	-	Chapman-Jouguet pressure
q	-	artificial bulk viscosity term
q_s	-	dynamic pressure
R	-	range from charge centre (stand-off),
		ratio of S/G

$R_{1,2}$	-	coefficients in JWL equation of state
R_u	-	elastic resistance
$\mathrm{d}s/\mathrm{d}t$	-	strain rate in the direction of acceleration
s^L	-	slope of ϕ from adjacent element (left)
$s^n_{j+1/2}$	-	slope of ϕ from adjacent elements
s^R	-	slope of ϕ from adjacent element (right)
S	-	target front height or half-width (smallest value)
$S^n_{j+1/2}$	-	approximation of slope of ϕ at element centroid
t	-	time
t_a	-	time of arrival of blast wave
t_c	-	clearing time
t_d	-	positive phase duration
t_d^-	-	negative phase duration
$t_{d,lin}$	-	positive phase duration (linear approximation)
$t_{d,lin}^-$	-	negative phase duration (linear approximation)
t_L	-	lighting time
T	-	natural period
u_s	-	particle velocity
v	-	material velocity
V	-	volume
V_{CJ}	-	Chapman-Jouguet relative volume
w	-	mesh velocity
W	-	explosive mass
x	-	length along beam,
		shortest distance from a point on a target to the nearest free edge
z	-	displacement
z_E	-	elastic limit
z_{max}	-	peak displacement
$z_{max,clear}$	-	peak displacement under cleared load
$z_{max,inf}$	-	peak displacement under non-cleared load
$z_{max,lin}$	-	peak displacement under linear load (triangular decay)
$\dot{z}$	-	velocity
$\ddot{z}$	-	acceleration
Z	-	scaled distance ($R/W^{1/3}$)
α	-	waveform parameter (Teich & Gebbeken 2010)
γ	-	specific heat ratio
δ	-	Hudson's time scale
$\dot{\epsilon}_{kk}$	-	trace of the strain rate tensor
η	-	Hudson's length scale
θ	-	angle of incidence
μ	-	$\rho/\rho_0 - 1$

ν	-	Poisson's ratio
ρ	-	density
ρ_0	-	ambient air density
ρ_s	-	shock density
σ	-	advection distance
σ_{ij}	-	stress tensor
τ	-	number of expansion wave crossings (Taylor 1972), shear stress
ϕ	-	arbitrary distribution of variables, normalised deflected shape
ω	-	coefficient in JWL equation of state, angular frequency

Chapter 1

Introduction

This PhD thesis will work towards developing a better understanding of the mechanism and the effects of diffraction of a blast wave around the edges of a finite-sized target.

This chapter will serve to provide an outline of the structure of the thesis, as well as describing the motivation behind the current research.

1.1 Background and Motivation

Over recent years, the use of high explosives for malicious attacks has become more common; often with the explosive being used to target critical building components with the specific intention of causing structural collapse. In the majority of high-casualty terrorist attacks – recent examples are shown in Table 1.1, after Dusenberry (2010) – the main cause of death is not from the direct effects of the blast itself, but from flying rubble, glass, or building collapse. When a truck laden with around 3,000 kg of high explosives was detonated outside the Alfred P. Murrah Building in Oklahoma City, USA, on the 19th of April 1995, the entire front face of the building collapsed, claiming 168 lives. In a similar attack on the US Embassy in Nairobi, on the 7th of August 1998, approximately 212 people were killed; most of the casualties were caused by the collapse of the nearby Ufundi building.

Furthermore, it has been suggested that the majority of non-fatal injuries from terrorist attacks are caused by either lacerations from airborne glass fragments or by damage to hearing from failed glass panels (Norville et al. 1999). The need for civilian infrastructure, therefore, to be able to resist the intense loading produced from a high explosive detonation is imperative to ensure the safety of the building's occupants.

Blast loads typically exceed the forces and actions that a building will be designed to resist during normal operation by several orders of magnitude. Existing methods to quantify and design against these loads are beyond the scope of traditional civil engineering. When this is coupled with a perceived increase in the frequency and severity of malicious high

Date	Target	Approx. size of explosive	Deaths	Injuries	Details
18th April, 1983	US Embassy, Lebanon, Beirut	910 kg	63	120	Truck bomb attack on US Embassy, seen as the beginning of modern terrorist attacks on the US. Resulted in the collapse of the entire central façade.
23rd October, 1983	US Marine HQ, Lebanon, Beirut	5,440 kg	241	75	Reportedly the largest truck bomb in history, completely levelled the cinderblock building.
19th April, 1995	Alfred P. Murrah Building, Oklahoma City, USA	3,000 kg	168	680	324 buildings were damaged by the blast, with the entire front face of the target building collapsing. The most destructive terrorist attack in the US before 9/11.
25th June, 1996	Khobar Towers, Khobar, Saudi Arabia	2,300 kg	19	372	Truck bomb detonated outside an eight-storey building housing US Air Force personnel. Six nearby high rise buildings were heavily damaged and windows were broken in buildings up to a mile away.
7th August, 1998	US Embassies, Nairobi, Kenya & Dar es Salaam, Tanzania	3,000 kg	223	4,500+	Two truck bombs exploded at the US Embassies in two East African capital cities. Most casualties in Nairobi were caused by the collapsing Ufundi building nearby. The majority of injuries came from glass lacerations.
12th May, 2003	Riyadh compound, Riyadh, Saudi Arabia	unknown	36	160	Seven car bombs detonated simultaneously. Caused considerable damage to nearby buildings.
8th October, 2004	Hilton Hotel, Taba, Egypt	2 x 200 kg	31	171	Truck bomb detonated in the hotel lobby causing 10 floors of the hotel to collapse.
22nd July, 2011	Office of the Prime Minister, Olso, Norway	unknown	8	209	Car bomb parked outside government buildings in Olso, Norway. Caused considerable damage to target building and nearby structures – majority of injuries caused by flying debris.

Table 1.1: Examples of recent high-casualty terrorist attacks on buildings using high explosives, adapted from Dusenberry (2010)

explosive attacks against buildings, the need for accessible and accurate design methods becomes obvious.

This thesis presents research which will contribute to the existing knowledge of quantifying front-face blast loading and target response of finite-sized structures subjected to the effects of a high explosive detonation. The research findings will, when appropriate, be expressed in a form which will be of practical use to civilian engineers.

1.2 Scope and Objectives of the Thesis

When designing to resist blast loads, the engineer is faced with two principal challenges: firstly, the pressures associated with the blast wave and how it interacts with the target must be quantified; secondly, the response of the target should be calculated and subsequent damage predicted with some degree of confidence.

Whilst experimental work can offer valuable insights into the typical behaviour and characteristics of blast events, it is often very expensive and time consuming. Higher order numerical schemes can be used to model 'real-life' events, but can often require considerable computational resources. These numerical schemes, such as finite element analysis, have particular strengths when used to aid the understanding of fundamental physical principles and are typically used in this manner – for research rather than design purposes.

Often the exact location, composition and size of explosive will not be known and instead it is pertinent to know, or be able to quickly determine, the likely effects of a wide range of blast events. Because of this, the majority of the work in this thesis is concerned with semi-empirical predictions of blast pressure and approximate methods for evaluating target response. Higher order schemes are also used in this thesis, primarily to explore situations where the approximations may not be valid, or to compare against and validate the simpler methods.

This thesis, therefore, has two main aims, related to the two engineering challenges introduced above:

1. To investigate the form of the blast pressure acting on a finite target, and to investigate the mechanism of diffraction around the target edge.

2. To gain a better understanding of the influence of blast wave diffraction and clearing on the dynamic response of finite targets subjected to blast loads.

1.3   Thesis Outline

The remainder of the thesis is organised into the following chapters:

Chapter 2 – Literature Review and Theoretical Background

This chapter provides background information for explosive blast loading and blast wave clearing. Current literature relating to the evaluation of blast loads on infinite and finite sized targets is reviewed, as well as the influence of different loading assumptions on target response.

Chapter 3 – Air Blast Loading Using LS-DYNA

This chapter is concerned with the modelling of explosive events using finite element software. The effects of different modelling techniques such as mesh refinement and re-mapping are studied and blast pressure predictions for incident pressure and reflected pressure on semi-infinite and finite targets are validated against experimental results.

Chapter 4 – A Study of Diffraction Loading and Clearing for Small Targets

The well-validated model for simulating blast events from Chapter 3 is used to conduct a study on the form of the blast load for small targets. Approximate methods for predicting the blast pressure are compared against the numerical results and conclusions on the mechanism of blast wave clearing are drawn.

Chapter 5 – Modelling Structural Response to Blast Loads

This chapter details a series of experimental trials that were undertaken to validate computational methods for evaluating target response to blast loads. Three techniques for modelling dynamic target deflection are compared against these numerical results, with a discussion on the relative strengths and suitability of each method.

Chapter 6 – The Influence of Clearing on Dynamic Response

The response of finite targets subjected to cleared blast loads is evaluated for a range of parameters in an attempt to both understand and quantify the influence of blast wave clearing, and also to develop and provide detailed guidance on the likely response and damage a given target will sustain for a given cleared blast load.

Chapter 7 – Summary and Conclusions

This chapter summarises the current research and makes suggestions for future work.

1.4 Published Work

The work detailed in this thesis has been published in the following peer-reviewed journal papers and is repeated herein with permission from Trans Tech Publications, Elsevier, the Institution of Civil Engineers (ICE) Publishing and Multi-Science Publishing:

- Tyas, A., Bennett, T., Warren, J. A., Fay, S.D. & Rigby, S. E. (2011), 'Clearing of blast waves on finite-sized targets – an overlooked approach', *Applied Mechanics and Materials* **82**, 669-674.

- Rigby, S. E., Tyas, A. & Bennett, T. (2012), 'Single-degree-of-freedom response of finite targets subjected to blast loading – the influence of clearing', *Engineering Structures* **45**, 396-404.

- Rigby, S. E., Tyas, A., Bennett, T., Warren, J. & Fay, S. (2013), 'Clearing effects on plates subjected to blast loads', *Engineering and Computational Mechanics* **166**(3), 140-148.

- Rigby, S. E., Tyas, A. & Bennett, T. (2014), 'Elastic-plastic response of plates subjected to cleared blast loads', *International Journal of Impact Engineering* **66**, 37-47.

- Rigby, S. E., Tyas, A., Bennett, T., Clarke, S. D. & Fay, S. D. (2014), 'The negative phase of the blast load', *International Journal of Protective Structures* **5**(1), 1-20.

- Rigby, S. E., Tyas, A., Bennett, T., Fay, S. D., Clarke, S. D. & Warren, J. A. (2014), 'A Numerical Investigation of Blast Loading and Clearing on Small Targets', *International Journal of Protective Structures* **5**(3), 253-274.

Chapter 2

Literature Review and Theoretical Background

2.1 Introduction

This chapter provides background information for explosive blast loading and blast wave clearing, as well as reviewing current literature pertinent to the subjects covered in this thesis. The predominant focus of this chapter is the evaluation of blast loads on effectively infinite and finite reflecting surfaces using semi-empirical methods, with a particular focus on current methods for predicting blast wave clearing. The influence of different loading assumptions on structural response will be reviewed, however the detailed theory and application of finite element and single-degree-of-freedom analyses will be provided in later chapters. This chapter highlights the gaps in the current knowledge base that this thesis will aim to address.

2.2 Explosive Blast Loading

2.2.1 Blast Waves in Free Air

When a mass of explosive material detonates it is converted into an extremely dense, high pressure gas. This reacting medium rapidly expands and displaces the surrounding air away from the source of the explosion at supersonic speed (faster than the speed of sound in the undisturbed air). The nature of air as a compressible fluid causes the pressure disturbance to form a shock front, a near discontinuous increase in pressure and density travelling outwards from the centre of the explosion (Baker 1973).

At a fixed distance from the explosive, the blast wave is characterised by an abrupt increase from ambient air pressure, p_0, to peak overpressure, $p_{so,max}$, followed by a temporal decay back down to ambient pressure, the duration of which is known as the positive

phase duration, t_d. The subscript 'so' indicates incident pressure values, i.e. the pressure measured by a transducer that offers no resistance to flow behind the shock front, or by a shock wave propagating parallel, or 'side-on', to a reflecting surface. The term 'overpressure' refers to the pressure increase above normal atmospheric conditions caused by the blast wave.

Following the positive phase comes a period of negative (below atmospheric) pressure caused by over expansion of the air following the shock front, known as the negative phase, which has peak amplitude $p_{so,min}$ and duration t_d^-. After the negative phase, ambient pressure is restored. An ideal blast wave is shown in Figure 2.1. The impulse, i, is defined as the integral of the pressure with respect to time, i.e. the area under the pressure-time curve.

2.2.2 Blast Wave Reflection

When an incident blast wave strikes a rigid target, conservation of mass, momentum and energy at the interface cause the pressure, density and temperature of the blast wave to be increased above the incident values. The overpressure at the rigid surface is termed the reflected pressure, the values of which are given the subscript 'r' (see Figure 2.1).
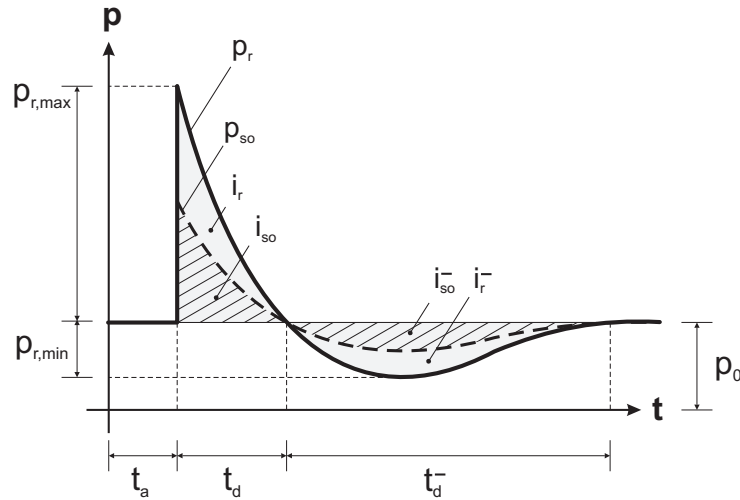
Figure 2.1: Idealised pressure-time profile for a blast wave

The Rankine-Hugoniot 'jump' conditions describe the relationship between the states of compressed air either side of a travelling shock front (Anderson 2001). Balancing mass and energy across the shock front enables the density, ρ_s, and particle velocity immediately behind the shock front, u_s, to be given as

$$\rho_s = \rho_0 \frac{(\gamma + 1)p_{so} + 2\gamma p_0}{(\gamma - 1)p_{so} + 2\gamma p_0} \tag{2.1}$$

$$u_s = p_{so}a_0\sqrt{\frac{2}{\gamma\rho_0\left[(\gamma+1)p_{so}+2\gamma p_0\right]}} \tag{2.2}$$

where ρ_0, p_0 and a_0 are density, pressure and sound speed of the ambient undisturbed air, and γ is the specific heat ratio (1.4 for air). For normal reflection, the reflected pressure, p_r, can be expressed in terms of the incident pressure, p_{so}, and dynamic pressure, q_s, as

$$p_r = 2p_{so} + (\gamma+1)q_s \tag{2.3}$$

where the first term relates to reflection of the incident pressure in the acoustic regime and the second term represents the pressure increase associated with bringing the compressed fluid to rest at the reflecting surface, with

$$q_s = \frac{1}{2}\rho_s u_s{}^2. \tag{2.4}$$

Substituting Equations 2.1, 2.2 and 2.4 into Equation 2.3 yields

$$p_r = 2p_{so}\frac{7p_0 + 4p_{so}}{7p_0 + p_{so}}. \tag{2.5}$$

The reflection coefficient, C_r, is defined as the ratio of the reflected pressure to the incident pressure, $C_r = p_r/p_{so}$. In the case of weak shocks (where the overpressure is small in relation to atmospheric pressure, i.e. $p_0 \gg p_{so}$), the reflected pressure is dominated by the acoustic term in Equation 2.3 and $C_r \approx 2.0$. For strong shocks ($p_{so} \gg p_0$), the reflection is dominated by the dynamic term, however the upper limit of $C_r = 8.0$ from Equation 2.5 is based on the assumption that the air still behaves as an ideal gas at extremely high pressures and temperatures. If real gas effects such as dissociation and ionization of the air molecules are taken into account, the reflection coefficient can be as high as 20 (US Army Materiel Command 1974).

2.2.3 Scaling Laws

Hopkinson-Cranz (or 'cube-root') scaling, proposed independently by Hopkinson (1915) and Cranz (1926), states that similarity exists between the blast waves produced at identical scaled distances from two explosive charges of similar geometry but different sizes (Figure 2.2). That is, the blast pressure profile at a distance of R from an explosive mass W will be similar to the blast pressure at a distance of KR from a mass of K^3W. This introduces the concept of *scaled distance*, Z, where the scaled distance, in units of $m/kg^{1/3}$, is given as

$$Z = \frac{R}{W^{1/3}}. \tag{2.6}$$
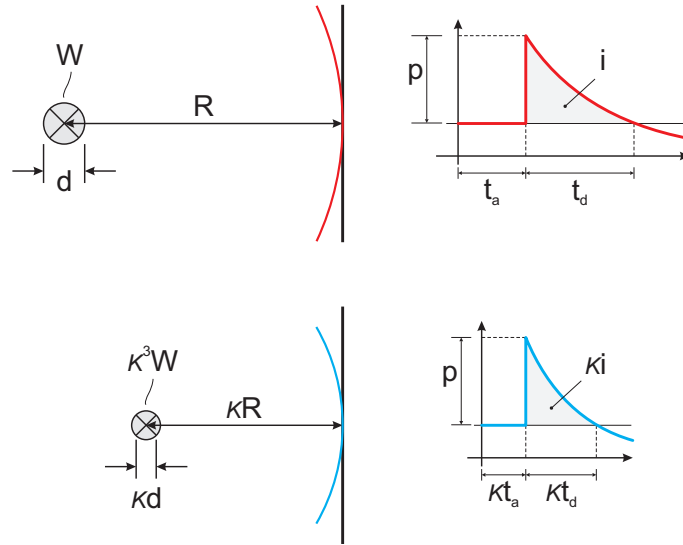
Figure 2.2: Hopkinson-Cranz blast wave scaling (Baker 1973)

In Hopkinson-Cranz scaling, all pressures are identical between scaled and actual values, and all times are scaled by the same value as the length scale factor, K, or the cube-root of the charge mass (Kinney & Graham 1985), hence the expressions in Equation 2.7 hold

$$
\begin{aligned}
p_{actual} &= p_{scaled} \\
t_{actual} &= t_{scaled}W^{1/3} \\
\text{and } i_{actual} &= i_{scaled}W^{1/3}.
\end{aligned}
\tag{2.7}
$$

2.2.4 Positive Phase Parameters

The first step when assessing the performance of a structure under explosive loading is to quantify the load that the target will be subjected to. Early analytical predictions of blast wave parameters, perhaps some of the most notable being the work by Taylor (1950), Brode (1955), and Granström (1956), are based on a number of assumptions[i] and are not directly applicable for use in design and research of structures subjected to explosive loads. Experimental tests are expensive and require careful control, and are typically used to validate numerical models which themselves require a considerable level of expertise and computational resource.

Consequently, the semi-empirical 'look-up' method of Kingery & Bulmash (1984) (hereby abbreviated as KB) is usually favoured, as it offers a quick and simple means for determining the blast pressure load.[ii]

This method utilises curves fit to a compilation of data based partly on computer analyses and partly on measurements from a number of medium to large-scale experimental blast

---

[i]e.g. point source, instantaneous release of energy and negligible atmospheric pressure compared to peak overpressure

[ii]In this thesis, ConWep and KB are used interchangeably to denote the semi-empirical predictive method.

trials, and enables the pressure, impulse, arrival time and duration to be determined for values of Z between 0.067 and 39.67 m/kg$^{1/3}$. Close-in blast parameters are largely derived from computer analyses because of the associated difficulty with measuring the extremely high pressures near to the blast source (Esparza 1986). The explosive is characterised into two main types; either a spherical free air burst (a suspended charge detonated at a height such that the entire duration of the shock wave has passed before the arrival of any waves reflected from the ground surface), or a hemispherical surface burst (a hemisphere of explosive detonated on a flat, rigid reflecting surface). The high-order polynomial curve fits are fairly cumbersome and are not usually presented in the literature, instead the blast parameters are typically presented as a set of curves, repeated here in Figure 2.3. These blast parameters form the basis of design guidance such as the US Department of Defence (2008) Design Manual UFC-3-340-02, *Structures to Resist the Effects of Accidental Explosions*, and the computer code ConWep (Hyde 1991).

Authors such as Baker (1973), Kinney & Graham (1985) and Swisdak (1994), among others, provide simplified relationships for calculating blast wave parameters; a detailed discussion of the various methods can be found in review papers by Remennikov (2003) and Ngo et al. (2007). Bogosian et al. (2002) compared simplified predictive methods with available test data and found that the KB method predicted positive phase parameters to the highest level of agreement with the experimental data.

The positive phase of the blast can be simplified as a triangular pulse,

$$p_r(t) = p_{r,max} \left(1 - \frac{t}{t_{d,lin}} \right) \tag{2.8}$$

where the linear positive phase duration, $t_{d,lin}$, can be chosen to preserve duration ($t_{d,lin} = t_d$) or to preserve impulse ($t_{d,lin} = 2i_r/p_{r,max}$). The positive phase, however, is more commonly described by an exponential decay in the form of the 'modified Friedlander equation' (Friedlander 1946),

$$p_r(t) = p_{r,max} \left(1 - \frac{t}{t_d} \right) e^{-b\frac{t}{t_d}} \tag{2.9}$$

where b, known as the waveform parameter, controls the decay of the pressure-time curve. The KB method presents a relationship for this parameter, however from inspection of Figure 2.3 it is clear that $p_{r,max}/p_{so,max} \neq i_r/i_{so}$ for all values of Z, i.e. the decay of the pressure-time curve that best reproduces the experimentally measured traces is not the same for incident and reflected pressures. Whilst this is not physically admissible, it is worth remembering the semi-empirical method only offers a fit to data with no real physical basis, rather than a solution to a set of governing equations. Regardless, this issue can be overcome by integrating Equation 2.9 to find an expression for the waveform parameter in terms of impulse and pressure, i.e.
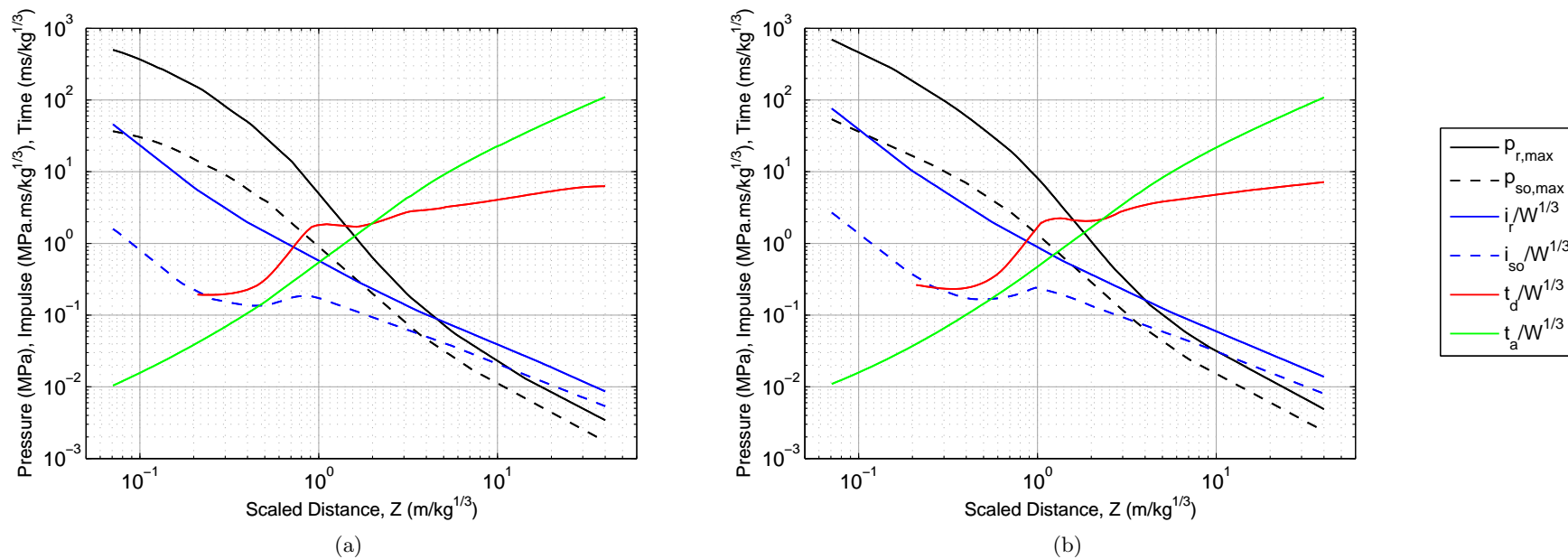
Figure 2.3: Incident and reflected positive phase blast wave parameters after UFC-3-340-02 (US Department of Defence 2008). (a) spherical charges of TNT in free air, (b) hemispherical charges of TNT on the surface

$$i_r = \int\limits_{0}^{t_d} p_{r,max} \left(1 - \frac{t}{t_d}\right) e^{-bt/t_d} \ \mathrm{d}t = \frac{p_{r,max}t_d}{b^2}\left(b - 1 + e^{-b}\right) \qquad (2.10)$$

which can be solved separately to find b for incident and reflected pressures. Figure 2.4 shows the waveform parameter given by the KB relationship, as well as exponential expressions given by Larcher (2007)[iii] and Teich & Gebbeken (2010)[iv]. The values of b, from separate solutions of Equation 2.10 to preserve incident and reflected impulse respectively are also shown. Whilst the KB values of b may be appropriate as a 'first-guess', it is recommended that the waveform parameter is determined from iteration of Equation 2.10 when defining the blast overpressure (Hyde 1991).
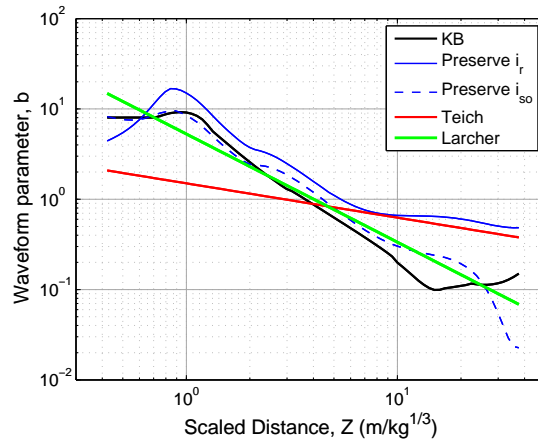
Figure 2.4: Comparison of waveform parameter, b

To illustrate the veracity of semi-empirical positive phase predictions, a number of blast trials were conducted at the University of Sheffield Blast & Impact Laboratory, Buxton, UK. 0.25 kg PE4 hemispherical explosive charges were detonated 4 m, 6 m, 8 m and 10 m away from a semi-infinite, rigid target (a 500 mm thick reinforced concrete bunker wall, 4.5 m high). The charges were detonated on a 50 mm thick steel plate, placed on a level, flat concrete ground slab, enabling the detonation to be considered as a hemispherical surface burst. A Kulite HKM 7 bar pressure gauge was placed 375 mm from the base of the target, and pressure was recorded using a 16-Bit Digital Oscilloscope at a sample rate of 100 kHz synchronised with the detonation. The blast wave could be considered as planar and angle of incidence effects could be neglected (see Section 2.2.6).

Figure 2.5 shows experimental positive phase pressure time histories and ConWep predictions where the waveform parameter was found by integrating the Friedlander equation. It can be seen that the Friedlander equation matches the form of the measured pressure-time history remarkably well and the positive phase predictions can be seen to be in excellent qualitative agreement with the experimental results. The recorded traces show a small

---

[iii]$b = 5.278Z^{-1.1975}$

[iv]$b = 1.5Z^{-0.38}$

amount of sensor ringing at the shock front and a secondary shock wave can be seen to arrive some time after the primary shock (for example, at 10.3 ms after detonation for the 4 m trace in Figure 2.5).

Immediately after detonation, a compressive shock travels through the explosive material. When this compressive wave reaches the contact interface between explosive and air, part of the shock is transferred as a compressive shock wave into the air and part of it reflects as a tensile wave, travelling back through the explosive. Once this wave reaches the end of the explosive, it is reflected again as a compressive wave and travels back through the material, transmitting a second compressive shock as it reaches the explosive/air interface. Secondary and even tertiary shocks are a known feature of experimental pressure recordings (US Army Materiel Command 1974), however they are often ignored as the pressure and impulse of these shocks are a small fraction of the primary shock.
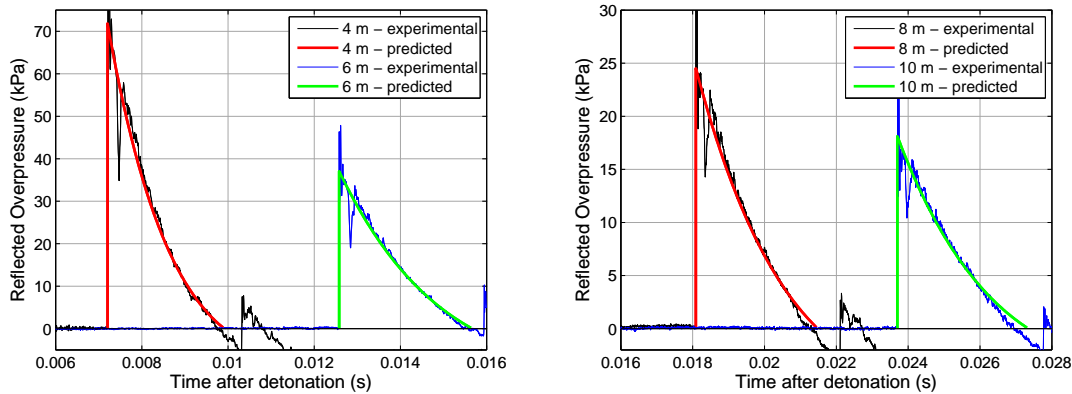
Figure 2.5: Experimental and predicted pressure time histories for a 0.25 kg PE4 (0.3 kg TNT) charge detonated on a rigid surface at ranges of 4 m, 6 m, 8 m and 10 m from a semi-infinite target ($Z = 6.0$, 9.0, 12.0 and 14.9 m/kg$^{1/3}$)

Table 2.1 shows the experimental and predicted positive phase reflected pressures and impulses. Whilst the sensor ringing mentioned above clearly prevents the peak reflected pressure from being directly measured, the effect has been demonstrated to effectively cancel out over the whole record (Smith et al. 1999) and therefore the measured trace can be temporally integrated to give the experimental specific impulse. Peak reflected pressures are given as the peak value from a least squares fit of the Friedlander equation to the pressure readings by extrapolating backwards to the arrival time.[v]

With a difference of no more than 6% between experiment and predicted peak pressures and impulses, it can be said with confidence that the ConWep predictions can be accurately used to model the positive phase load arising from a high explosive detonation.

---

[v]There is no formal method for defining the interval over which the curve should be fit to. Here, the sensor ringing was judged to have ceased at around 0.4 ms after arrival for all tests and the curve was fit between this time and the end of the experimental positive phase.

Stand-off (m)	Peak Reflected Pressure (kPa)			Peak Reflected Impulse (kPa.ms)		
	Experiment	Predicted	Ratio	Experiment	Predicted	Ratio
4	76.8	71.8	0.94	68.8	69.1	1.00
6	39.2	37.1	0.95	44.8	44.6	1.00
8	26.1	24.5	0.94	32.6	32.9	1.01
10	18.3	18.1	0.99	24.9	26.0	1.04

Table 2.1: Experimental and predicted positive phase reflected impulse and ratio of numerical/experimental

2.2.5 Negative Phase Parameters

Negative phase parameters are also available in the literature (US Department of Defence 2008, Cormie et al. 2009). However, as Bogosian et al. noted in their review, *'The precise provenance of these curves is unknown at the present time'* (Bogosian et al. 2002, page 3). They suggested that this uncertainty is due in part to the fact that *'not all* (experimental data records) *were of sufficient duration and/or quality as to be able to extract negative as well as positive values, and while some had dubious peak pressure readings, others became suspect at later time and therefore could not produce reliable impulses'* (Bogosian et al. 2002, page 9). This is perhaps inevitable in the large scale experimental tests that formed the basis of the data analysed in that work.

The original source of the negative phase parameters presented in UFC-3-340-02 is unclear, although a thorough review of the available literature indicates that it may have been from analytical work conducted in the 1950s by Granström (1956). Negative phase parameters are shown in Figure 2.6 for spherical free air bursts and hemispherical surface bursts.

For small scaled distances, the peak underpressure and negative phase impulse are very small relative to the positive phase. This is often cited as reason enough to neglect the negative phase, however it is clear from the parameter charts in Figures 2.3 and 2.6 that this observation is only true for small values of Z, and that the negative phase impulse approaches that of the positive phase for larger scaled distances, eventually exceeding the positive phase impulse when $Z > 8$. In free-field blast experiments, the rising fireball creates a lower pressure near the ground surface which draws in the surrounding air. This has the effect of further lowering the air density, which has already been over-expanded after the shock wave has passed, and hence results in larger negative phase impulses at larger stand-off distances (Needham 2010).

The influence of the negative phase has become a topic of interest over recent years, in particular the effect of the negative phase on light cladding and glazing panels (Krauthammer & Altenberg 2000, Dharani & Wei 2004, Gantes & Pnevmatikos 2004, Wei & Dharani 2006, Hooper et al. 2012, Larcher et al. 2012). If a panel is undamaged by the positive phase of the blast load, a combination of negative phase pressure and elastic rebound may cause the structure to fail towards the direction of the blast source. It has been
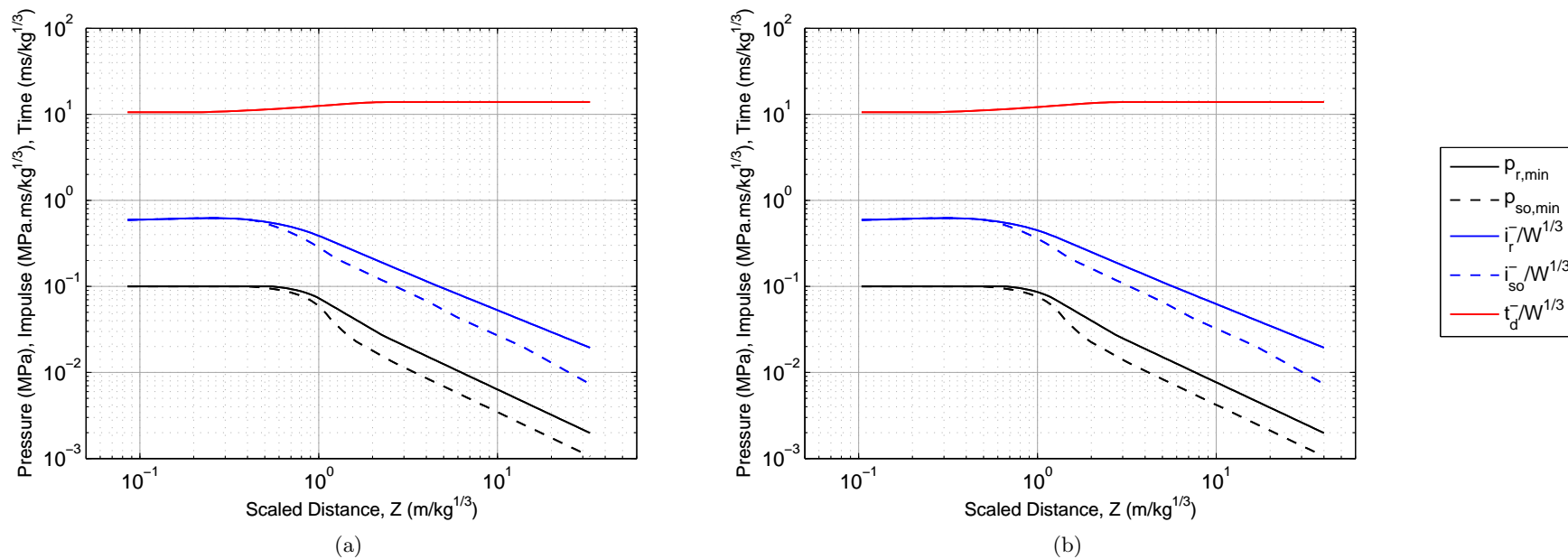
Figure 2.6: Incident and reflected negative phase blast wave parameters after UFC-3-340-02 (US Department of Defence 2008). (a) spherical charges of TNT in free air, (b) hemispherical charges of TNT on the surface

estimated that the majority of non-fatal injuries from explosions are caused by airborne glass fragments (Norville et al. 1999, Wei & Dharani 2006). In the Oslo bombing on the 22nd of July 2011, window damage was recorded out to approximately 400 m from the centre of the explosive (Christensen & Hjort 2012). It can be said, therefore, that proper understanding of the effect of the negative phase is crucial to limit the potential casualties caused by a high explosive blast and the negative phase should not be neglected in design.

Linear Approximation

Krauthammer & Altenberg (2000) studied the probability of failure of brittle glass panels. The blast load was simplified as a piecewise, bilinear expression (Equation 2.11), with the positive phase represented by a linear decay as described in Section 2.2.4 and the negative phase modelled with a rise time equal to 1/4 of the negative phase duration. As per the positive phase, the linear negative phase duration, $t_{d,lin}^-$, can be specified to preserve negative phase impulse, i.e. $t_{d,lin}^- = 2i_r^-/p_{r,min}$. The negative phase begins at t_d, rather than $t_{d,lin}$, giving a period of zero pressure between the linear positive and negative phase. This approach is recommended in UFC-3-340-02 (US Department of Defence 2008).

$$p_r(t) = \begin{cases} p_{r,max}\left(1 - \dfrac{t}{t_{d,lin}}\right), & t \leq t_{d,lin} \\[2mm] 0, & t_{d,lin} < t \leq t_d \\[2mm] -p_{r,min}\left(\dfrac{t - t_d}{0.25t_{d,lin}^-}\right), & t_d < t \leq t_d + 0.25t_{d,lin}^- \\[2mm] -p_{r,min}\left(1 - \dfrac{t - (t_d + 0.25t_{d,lin}^-)}{0.75t_{d,lin}^-}\right), & t_d + 0.25t_{d,lin}^- < t \leq t_d + t_{d,lin}^- \end{cases} \tag{2.11}$$

Extended Friedlander

Another common method of modelling the negative phase is to simply extend the Friedlander equation (2.9) to $t = \infty$, rather than truncating the expression at t_d. This is the approach adopted by Dharani & Wei (2004), Gantes & Pnevmatikos (2004), Wei & Dharani (2006), and the *LOAD_BLAST subroutine in LS-DYNA (Randers-Pehrson & Bannister 1997). As introduced previously, given the ConWep positive phase parameters for pressure, duration and impulse, the waveform parameter can be determined by integrating the Friedlander expression over the positive phase (as in Equation 2.10) which can be solved iteratively to determine the value of b to give the correct positive phase impulse at that particular scaled distance.

As the negative phase is also constructed from this expression, it is clear that the form of this negative phase is entirely dependent on the positive phase parameters only. As such there are no variables to control negative phase pressure and impulse and the values given

by this approximation may not match the semi-empirical predictions.

Integrating the negative phase of the Friedlander equation gives the negative phase impulse as

$$i_r^- = \int_{t_d}^{\infty} p_{r,max} \left(1 - \frac{t}{t_d} \right) e^{-bt/t_d} \, \mathrm{d}t = \frac{p_{r,max} t_d}{b^2} e^{-b}. \tag{2.12}$$

At $Z = 10$, for example, ConWep gives peak pressure $p_{r,max} = 31.54$ kPa, reflected impulse, $i_r/W^{1/3} = 59.33$ kPa.ms/kg$^{1/3}$ and positive phase duration $t_d/W^{1/3} = 4.788$ ms/kg$^{1/3}$. Iterating Equation 2.10 gives the waveform parameter, $b = 0.771$. When these parameters are used as input in Equation 2.12, the negative phase impulse is given as $i_r^-/W^{1/3} = 118$ kPa.ms/kg$^{1/3}$, whereas the parameter relationship in the literature, shown in Figure 2.6(b), gives the negative phase impulse as $i_r^-/W^{1/3} = 62$ kPa.ms/kg$^{1/3}$.

Extended Friedlander with Teich C_r^-

In order to better control the form of the negative phase, Teich & Gebbeken (2010) introduce the negative phase reflection coefficient, C_r^-, which is a function of the scaled distance,

$$C_r^- = \frac{1.9Z - 0.45}{Z} \quad \text{for } Z > 0.5 \tag{2.13}$$

and also offer a scaled distance relationship for an improved waveform parameter

$$\alpha = 1.5Z^{-0.38} \quad \text{for } 0.1 < Z < 30, \tag{2.14}$$

which enables the value of extended Friedlander peak underpressure to be better matched to the published semi-empirical value at that particular scaled distance (e.g. the relationships shown in Figure 2.6). This gives the piecewise positive and negative phase expression[vi] as

$$p_r(t) = \begin{cases} p_{r,max} \left(1 - \dfrac{t}{t_d} \right) e^{-\alpha \frac{t}{t_d}}, & t \leq t_d \\[3mm] C_r^- p_{so,max} \left(1 - \dfrac{t}{t_d} \right) e^{-\alpha \frac{t}{t_d}}, & t > t_d \end{cases} \tag{2.15}$$

Although the introduction of the negative phase reflection coefficient allows the peak negative phase pressure to be controlled, the new waveform parameter, α, is again given to match the *positive phase* impulse of the Friedlander expression to semi-empirical predictions, i.e. there remains no variable to control the negative phase impulse.

[vi]In Teich and Gebbeken's formulation, $p_{r,max}$ is replaced by $C_r p_{so,max}$, however for consistency with the positive phase expressions in this thesis the former notation is adopted

The Teich extended Friedlander gives the negative phase impulse as

$$i_r^- = \int_{t_d}^{\infty} C_r^- p_{so,max} \left(1 - \frac{t}{t_d}\right) e^{-\alpha t/t_d} \, \mathrm{d}t = \frac{C_r^- p_{so,max} t_d}{\alpha^2} e^{-\alpha}. \qquad (2.16)$$

Again, for $Z = 10$, the ConWep peak incident pressure, $p_{so,max} = 14.81$ kPa and the reflection coefficient and waveform parameter, $C_r^- = 1.855$ and $\alpha = 0.625$ from Equations 2.13 and 2.14 respectively, give the Teich extended Friedlander negative phase impulse as $i_r^-/W^{1/3} = 180$ kPa.ms/kg$^{1/3}$, which is far greater than the semi-empirical prediction. Furthermore, in both 'extended Friedlander' approaches, the blast pressure will have a finite pressure value for *all* values of t, hence the duration of the load, and also the impulse, cannot always be accurately captured with an extended Friedlander expression.

Cubic Negative Phase

Alternatively, the blast load can be constructed as a piecewise pressure-time function using the Friedlander positive phase (Friedlander 1946) and a cubic expression for the negative phase, shown in Equation 2.17. This negative phase expression is given by Granström (1956) and is recommended by the NavFac Design Manual 2.08, *Blast Resistant Structures* (Naval Facilities Engineering Command 1986), and the US Army Blast Effects Design Spreadsheet, SBEDS (US Army Corps of Engineers 2005).

$$p_r(t) = \begin{cases} p_{r,max} \left(1 - \dfrac{t}{t_d}\right) e^{-b\frac{t}{t_d}}, & t \le t_d \\[2ex] -p_{r,min} \left(\dfrac{6.75(t - t_d)}{t_d^-}\right) \left(1 - \dfrac{(t - t_d)}{t_d^-}\right)^2, & t_d < t \le t_d + t_d^- \end{cases} \qquad (2.17)$$

With this expression, the negative phase duration is corrected such that the integral of the cubic expression gives the same impulse as that given by the semi-empirical parameter prediction, i.e. $t_d^- = 16 i_r^-/9 p_{r,min}$.

Experimental Validation

Figure 2.7 shows negative phase approximations for $Z = 4$ and $Z = 16$ m/kg$^{1/3}$ normalised against the peak reflected pressure and positive phase duration. It is clear that the choice of negative phase approximation has a significant impact on the form of the blast pressure-time history. The lack of agreement between the different negative phase expressions highlights the need for a well validated negative phase model.

Figure 2.8 shows the negative phase pressure-time histories of the experimental trials introduced in Section 2.2.4. Table 2.2 gives a summary of the experimental and predicted negative phase reflected impulses from these tests.

(a) $Z = 4$

(b) $Z = 16$
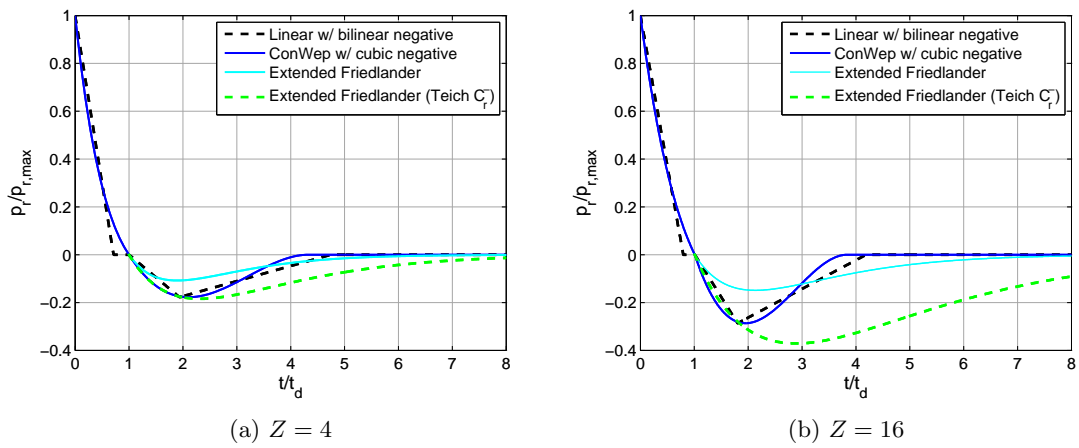
Figure 2.7: Normalised positive and negative phase approximations for $Z = 4$ and $Z = 16$ m/kg$^{1/3}$

(a) 4 m

(b) 6 m

(c) 8 m

(d) 10 m
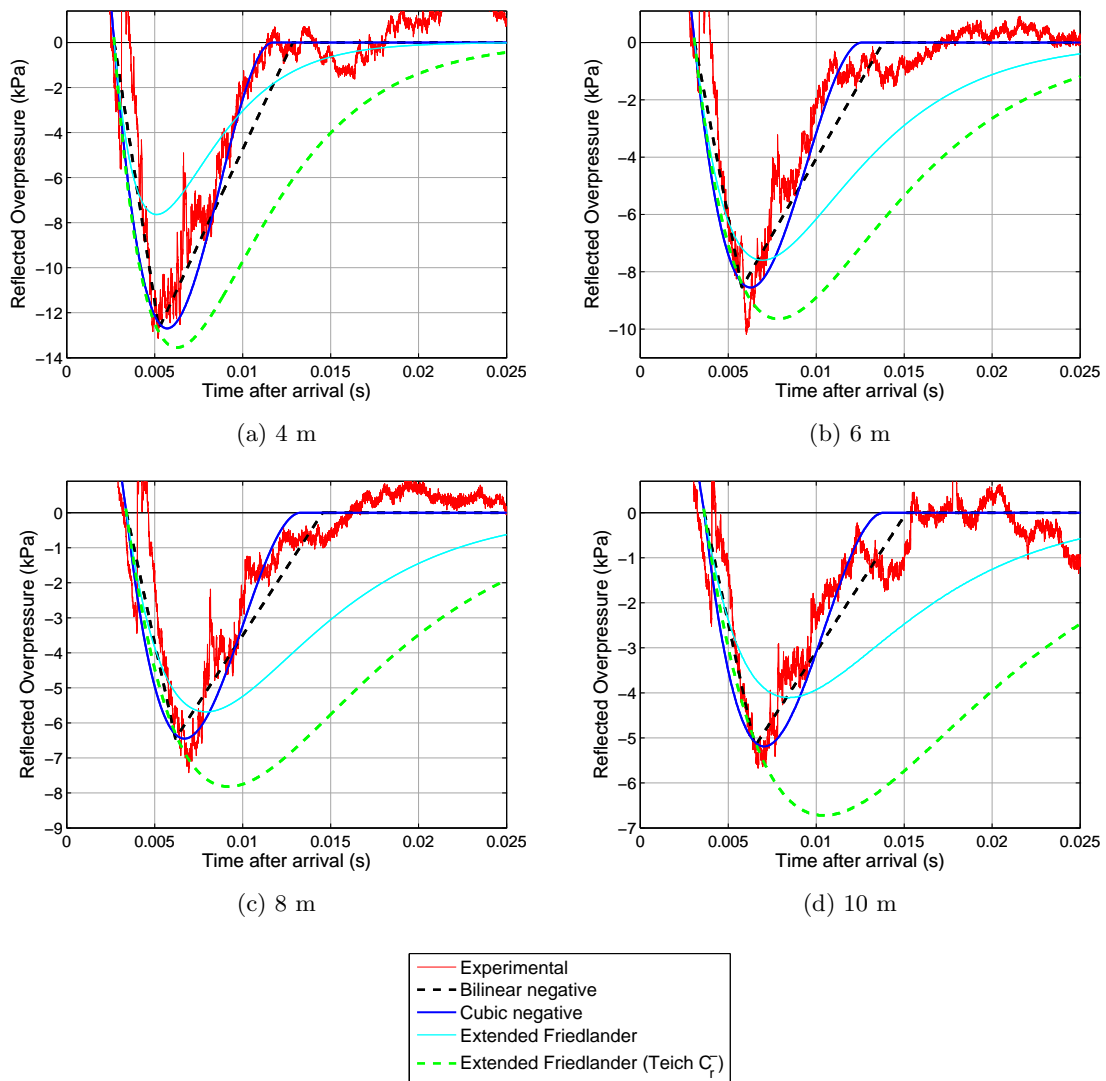
Figure 2.8: Negative phase approximations for a 0.25 kg hemispherical PE4 (0.3 kg TNT) charge

Stand-off (m)	Negative Impulse (kPa.ms)			
	Experiment	Cubic	Extended Friedlander	Extended Friedlander[*]
4	52.8	64.5	50.0	126.9
6	39.9	45.8	79.4	119.3
8	31.1	36.0	70.1	118.5
10	27.7	29.8	53.6	120.7

[*] with Teich & Gebbeken (2010) negative phase reflection coefficient, C_r^-

Table 2.2: Experimental and predicted negative phase reflected impulse

Apart from the second shock – which arrives at the beginning of the negative phase on the experimental traces – the cubic negative phase matches the experimental traces remarkably well, both in terms of peak negative pressure and general form of the negative phase. The cubic expression can model the negative phase impulse to within 10–25% of the experimental values, despite the fact that the second shock is neglected in the simplified semi-empirical prediction. The linear negative phase expression and cubic expressions are impulse-corrected such that their impulses are equal to the semi-empirical predictions for that scaled distance. It is clear, however, that the cubic expression offers a better qualitative match (Figure 2.8) as well as quantitative. Both extended Friedlander and Teich extended Friedlander approaches demonstrate considerably less good agreement, with the former over-predicting the negative phase impulse by up to 95% and latter by up to 340%.

To further illustrate the difference in impulses given by the negative phase approximations, Figure 2.9 shows the relationship between normalised net impulse ($[i_r + i_r^-]/i_r$) and scaled distance, Z. Here it can be seen that the extended Friedlander expression using the Teich reflection coefficient gives a negative phase impulse of over an order of magnitude greater than the positive phase impulse for $Z > 30$ m/kg$^{1/3}$.
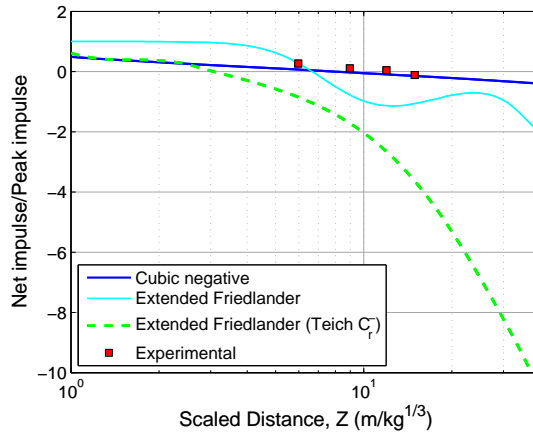
Figure 2.9: Normalised net impulse ($[i_r + i_r^-]/i_r$) with scaled distance for different negative phase approximations

It is acknowledged that the negative phase requires more stringent validation as well as a larger experimental database than those provided in this thesis. However, at this stage it is clear that the empirical predictions appear to be a good indication of the loading parameters (for both negative and positive phases), and that the cubic expression not only allows for better quantitative control of the negative phase to match these parameters, but also appears to follow the general form of the negative phase to a good level of qualitative agreement. As such, in this thesis the reflected blast pressure-time history is modelled using the piecewise expression comprising Friedlander positive phase and Granström cubic negative phase as shown in Equation 2.17.

2.2.6   Non-Ideal Blast Waves

The KB semi-empirical predictions can be used to determine the reflected pressure-time history acting at a single point some distance from a blast source. The reflected pressure predictions are based on an ideal blast wave, with the following assumptions:

- The blast wave arrives planar and impinges normally on a rigid target

- The blast wave is unimpeded between the blast source and target

- No reflections arrive from surrounding surfaces throughout the entire duration of the shock wave

- The point of interest is part of a reflecting surface that is large enough in directions normal to the direction of travel of the blast wave such that edge effects can be ignored (see Section 2.3).

There are several approaches available in the literature for considering non-ideal blast waves. Whilst reflections and obstructions from nearby targets cannot be considered in ConWep, other codes such as BLAST-X (Britt & Lumsden 1994) operate a ray-tracking approach to account for this. If the blast wave does not impinge normally on a target, or if the blast wave is not planar across the whole target, then angle of incidence effects must be taken into account. The inbuilt ConWep subroutine called Loads on Structures (LOS) calculates the pressure distribution on a rectangular target, where the pressure acting at any point on the target is a function of the reflected pressure and incident pressure at that point, and the angle of incidence of the blast wave, θ,

$$p(t, \theta) = p_r(t) \cos^2 \theta + p_{so}(t) \left(1 + \cos^2 \theta - 2 \cos \theta\right). \tag{2.18}$$

Reflection of the negative phase is less well understood, with SBEDS (US Army Corps of Engineers 2005) recommending the use of the full reflected underpressure for $0° \leq \theta \leq 45°$ and the incident underpressure for $\theta > 45°$.

If the reflecting surface is not perfectly rigid, then fluid-structure interaction (FSI) effects may occur. As an upper bound, when a blast wave impinges on a target of effectively infinite mass or stiffness there is no pressure reduction through FSI and the full reflected impulse is transmitted. As a lower bound, a blast wave impinging on a plate travelling at exactly the same velocity as the shock front will transmit the incident impulse only. Kambouchev et al. (2006, 2007) analysed the interaction of blast waves with, and the impulses imparted to, free standing plates of varying mass, and it was found that the displacements required to exploit impulse reduction through FSI may be impractical. Subramaniam et al. (2009) and Teich & Gebbeken (2012) analysed the interaction of a blast wave coupled with a structural model. In both articles, the reduction in displacement of the target through FSI was only realised for very low mass or very low stiffness systems such as large span, lightweight cable-net façades. FSI effects are likely to make very little difference to the cases studied in this thesis and are therefore neglected when using semi-empirical pressure predictions.

The main topic of interest for this thesis is the final category of non-ideal blast waves, i.e. when edge effects of the target cannot be ignored. Such a problem requires a thorough review and is the subject of the following section.

2.3   Blast Wave Clearing

2.3.1   The Physical Process of Clearing

The Kingery and Bulmash semi-empirical load predictions assume that the target is part of a reflecting surface that is effectively infinite in dimensions perpendicular to the direction of travel of the blast wave. If this is not the case, then blast wave clearing will occur.

Clearing begins the moment a blast wave reaches the free edge of a reflecting surface with finite lateral dimensions. At this free edge, whilst the reflected shock front begins to reflect away from the target surface, the incident shock front continues unimpeded past the edge of the target, causing diffraction around the free edge. At the same time a pressure imbalance between the lower pressure incident wave and higher pressure reflected wave initiates flow between the higher and lower pressure regions as the pressure begins to equalise. The diffraction generates a low pressure rarefaction wave, which is driven by the flow conditions and travels along the loaded face, beginning at the boundaries and propagating in towards the centre of the target (see Figure 2.10). As it passes over a point of interest, the rarefaction wave reduces the pressure acting on the loaded face and hence reduces the total positive phase impulse imparted to the target.

The problem of blast wave clearing is complex and analytical solutions for blast wave diffraction normal to the direction of blast wave travel are rare in the literature. In a study of weak shock diffraction, Hunter & Keller (1984) assume that flow conditions behind the shock front are constant, which is only applicable for situations where the target is con-

siderably smaller than the length of the blast wave. As such, these analytical predictions are unable to describe the processes that occur for larger targets. Empirical predictions therefore form the basis of literature guidance for predicting blast wave clearing.
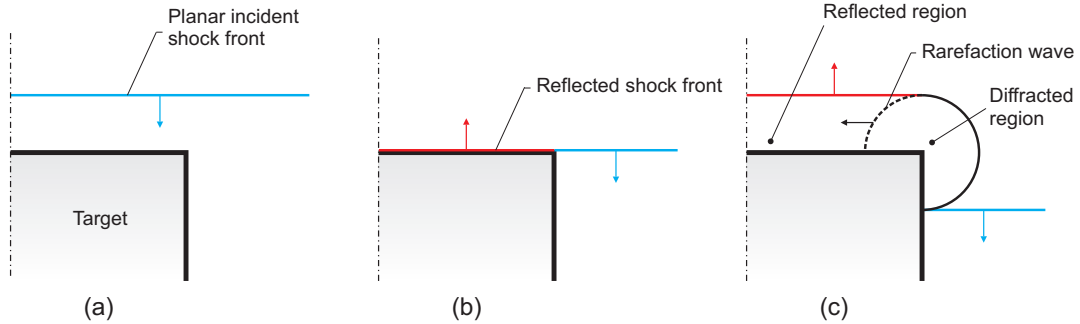
Figure 2.10: Diffraction of a blast wave around a finite target causing the propagation of a rarefaction clearing wave

2.3.2   Empirical Clearing Predictions

The earliest observations of blast wave clearing appear to have been drawn from large scale nuclear bomb trials undertaken in the 1950s. Murtha (1955) and Morris (1959) report the findings from blast-pressure measurements taken from pressure transducers embedded within a $6 \times 6 \times 12$ ft structure situated 2200 ft from the source ('ground-zero') of a nuclear blast.[vii] With such a small reflecting surface in relation to the length of the blast wave, any clearing effects will occur very quickly in relation to the positive phase duration, and will be relatively uniform across the entire reflecting surface.

Accordingly, the early empirical clearing corrections – first introduced by Norris et al. (1959) and repeated in similar methodologies throughout the literature – only attempt to correct the entire impulse acting on the target, and not the temporal or spatial distribution of cleared pressures. These empirical methods assume that clearing relief acts uniformly over the whole loaded face, beginning immediately at the time of arrival of the blast wave. The cleared blast pressure decays linearly from the peak reflected pressure to the stagnation pressure over a characteristic clearing time, t_c, as in Figure 2.11.

The stagnation pressure is given as the sum of the incident and drag pressure,

$$p_{stag}(t) = p_{so}(t) + C_D q_s(t) \tag{2.19}$$

where C_D is the drag coefficient, which is given as 1.0 for front wall loading (US Department of Defence 2008)[viii], and q_s is the dynamic pressure defined in Equation 2.4.

[vii]$1.8 \times 1.8 \times 3.6$ m situated 670 m from the source

[viii]The drag coefficient depends on the shape and orientation of the target. For cubic structures loaded face on, a drag coefficient of 1.0 is considered adequate. For roof and side-wall loading, the drag coefficient varies between -0.4 for low pressures (<170 kPa) and -0.2 for high pressures (>340 kPa).
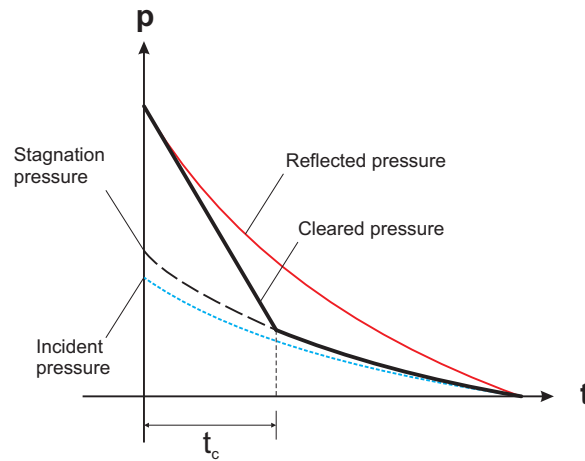
Figure 2.11: Clearing corrections from UFC-3-340-02 (US Department of Defence 2008)

The clearing time is given by Kinney & Graham (1985) as

$$t_c = \frac{3S}{a} \tag{2.20}$$

where S is height or half structure width, whichever is smallest, and a is the sonic velocity in the reflected region. This is often known as the 2D case because only clearing along the smallest target dimension, S, is considered (Ethridge 1977, Lottero 1981).

The methodology in UFC-3-340-02 (US Department of Defence 2008) gives the clearing time as

$$t_c = \frac{4S}{(1+R)a} \tag{2.21}$$

where R is the ratio of S/G and G is height or half structure width, whichever is largest. This expression represents the 3D case because clearing is considered along both the height and width of the target.[ix]

These empirical predictions, although they give slightly different methods for calculating the clearing time, are based on the assumption that the cleared blast pressure is reduced by an infinite series of interacting expansion waves, each with diminishing strength (Taylor 1972). The net effect of this is, after a *given number of expansion wave crossings*, the cleared blast pressure has effectively reached the stagnation value and subsequent expansion wave crossings can be neglected. It can be seen for the 2D case (Equation 2.20) that for a target with infinite height and a half-width of S, the time taken for an expansion wave to reach the centre of the target is S/a. For this case, clearing is assumed to be completed at $3S/a$, i.e. after the clearing wave has interacted at the centre, edge, and again the centre of the target. For the same target, the UFC-3-340-02 (US Department

---

[ix]The factors of 3 and 4, which appear in Equations 2.20 and 2.21 respectively, will be explained below.

of Defence 2008) predictions give a clearing time equivalent to 4 wave interactions. As explained previously, the decay from reflected pressure to stagnation pressure is assumed to be linear throughout the duration of the rarefaction wave crossings.

Taylor (1972) introduced an alternative method based on observations from shock tube tests on small sized structures. In his experiments, Taylor found that the average pressure acting on the front surface of 2D and 3D targets would be 'nearly coincident' if the time scale was given as the number of rarefaction wave crossings. Tests were conducted on 2D structures and 3D structures with half width equal to height, $S = G$.[x]

The average cleared blast pressure was given as

$$\frac{p}{p_r} = \left(1 - \frac{p_{stag}}{p_r}\right) e^{-A\tau^B} + \frac{p_{stag}}{p_r} \tag{2.22}$$

where $\tau = ta_0(1 + R)/S$ represents the number of rarefaction wave crossings and A and B are empirical coefficients used to fit the curve to the data (Taylor 1972, Ethridge 1977). The selection of A and B requires prior knowledge of the blast pressure, and hence the Taylor clearing expression has limited application for *predicting* the cleared pressure acting on a target.

It can be seen in Equation 2.22 that the blast pressure approaches the stagnation pressure as a limit as the number of wave crossings, τ, tends to infinity. The magnitude of pressure relief also decreases with an increasing number of wave crossings – both of these features are more in keeping with the theory of which the above methods are based on.

It is important to note at this stage that these observations are based on experiments where the length of the blast wave was very large in comparison to the size of the target, i.e. the time taken for an expansion wave to traverse the surface of the target and hence the time taken for the cleared load to reach stagnation value (known as the diffraction phase) was very short in relation to the positive phase of the blast load.

Table 2.3 gives an indication of the different types of loading for different target sizes. 'Pure drag' indicates targets where the clearing time is effectively zero and the loading is almost entirely the stagnation pressure for the entire positive phase, whereas 'mainly drag' indicates targets whose clearing time is small and experience some diffraction during the positive phase. Early empirical clearing predictions are based on targets of this size and below. 'Mainly diffraction' indicates targets where the clearing time is comparable to or larger than the positive phase, and 'mainly reflected' denotes targets with large dimensions such that the clearing wave does not reach parts of the target during the positive phase. Full incident and full reflected pressure represent the limits of no target and an infinite sized target respectively.

---

[x]For the 2D case, $G = \infty$ and $R = 0$, for the 3D case, $G = S$ and $R = 1$, hence τ for the 3D case is exactly twice that for the 2D case.

Target size:	0		$\longrightarrow$			∞
Loading type:	Incident	Pure drag	Mainly drag	Mainly diffraction	Mainly reflected	Reflected

Table 2.3: Types of cleared blast loading with different target sizes

2.3.3 Improved Clearing Predictions

The methods of correcting the blast load to account for clearing detailed above inherently assume that the target is sufficiently small such that the cleared pressure acts relatively uniformly across the target surface. For non-nuclear explosives, the length of the blast wave is more comparable to the target dimensions and the observations of the early empirical clearing corrections may not be valid.

The lack of agreement in the literature on how to calculate the clearing time is enough to cast doubt on the validity of these methods. Furthermore, if the calculated clearing time is greater than the positive phase duration then blast wave clearing is assumed to *not take place at all*, which is not true for finite sized targets of the 'mainly drag' and 'mainly reflected' loading types. Also, the assumption that the reflected pressure begins to decay immediately after the arrival of the shock wave is true for the *total* load acting on the face of the target, however it cannot be valid for the pressure at a point on the target located away from a free edge, since there will be a transient time for the clearing wave to arrive. The spatial variation of cleared pressures therefore cannot be determined using the methods outlined previously.

It has also been shown both experimentally (Smith et al. 1999, Rose et al. 2006, Rickman & Murrell 2007, Tyas et al. 2011a,b) and numerically (Rose & Smith 2000, Ballantyne et al. 2010) that the cleared pressure can 'overshoot' the stagnation pressure and lead to early negative pressures acting on the target. This, again, cannot be accounted for in the traditional clearing predictive methods. Such shortfalls have led to the development of improved methodologies for predicting blast pressure relief on a loaded surface.

In an attempt to provide an improved empirical based method for predicting blast wave clearing, Smith et al. (1999) conducted a series of small scaled experiments on finite-sized targets, measuring the pressure at various locations on the loaded face. Whilst the process of clearing was shown in the experiments, considerable experimental spread prevented such an empirical method from being drawn up. This led the authors to consider a numerical based semi-empirical method, using the Computational Fluid Dynamics (CFD) code Air3D (Rose 2002). In the extension of the original study, Rose & Smith (2000) ran a series of numerical simulations of blast waves interacting with rigid, finite sized targets. The targets were chosen to have a width to height aspect ratio of 2:1 to ensure that any rectangular surface with equal reflecting area but different aspect ratio will clear more quickly and therefore the results presented will be conservative. Scaled distances of 0.5, 1.0, 2.0, 4.0, 8.0 and 16.0 m/kg$^{1/3}$, and scaled target heights, H, of 0.1, 0.2, 0.4 and 0.8

$m/kg^{1/3}$ were analysed, giving a total of 24 stand-off and target size combinations. The pressure was monitored at 5 locations along the vertical centreline of the structure and the specific impulse was averaged between the 5 values.

Scaled distance	Clearing factor, $C_f = i/i_{so}$			
$(m/kg^{1/3})$	$H = 0.1$ $(m/kg^{1/3})$	$H = 0.2$ $(m/kg^{1/3})$	$H = 0.4$ $(m/kg^{1/3})$	$H = 0.8$ $(m/kg^{1/3})$
0.5	12.271	12.673	9.642	5.384
1.0	3.222	3.825	3.837	3.173
2.0	1.969	2.400	2.865	2.990
4.0	1.161	1.296	1.681	1.995
8.0	1.026	1.060	1.251	1.573
16.0	1.025	1.023	1.079	1.396

Table 2.4: Cleared/side-on impulse ratios (Rose & Smith 2000)

The analyses were repeated with the reflecting structure omitted so that the results could be presented in terms of a *clearing factor* – the ratio of the cleared impulse to the incident impulse, $C_f = i/i_{so}$.[xi] These clearing factors are summarised in Table 2.4.

Whilst this method is straightforward and based on a physically valid process for evaluating blast wave clearing, it still gives no means for determining the spatial and temporal characteristics of the cleared pressure acting on the target.

Ballantyne et al. (2010) extended this methodology and used the Air3D code to simulate the interaction of blast waves with structural columns of varying flange width. For all practical sizes of bare column (assumed rigid), the impulse was found to be almost identical to the incident impulse, suggesting that the target clears sufficiently early such that diffraction effects can be neglected and incident values used in the design of structural columns subjected to blast loads.

Rickman & Murrell (2007) conducted a series of small scale experiments using 72.6 g hemispheres of C4 (92 g TNT equivalent) and measured the cleared pressure-time histories at 5 locations on the reflecting surface of a rigid target. Two target sizes were used for the test series, corresponding to scaled target heights of 1.00 and 1.63 $m/kg^{1/3}$, with the explosives located at scaled distances ranging from 0.323–9.11 $m/kg^{1/3}$.

From the experimental pressure-time recordings, it was observed that the ConWep predictions '*agreed remarkably well with the measurements made on the small-scale experiments, until onset of the relief wave*' (Rickman & Murrell 2007, page 200). Using this rationale, the authors subtracted the full reflected pressure from the measured pressure at the arrival of the clearing wave to isolate the relief function, so that when applied in reverse, the superposition of the relief wave and reflected pressure would yield the cleared pressure at

---

[xi]The incident impulse was given as the value of impulse at the bottom-centre of the target, rather than the average of the 5 gauge locations. This way, the clearing factor can simply be applied to the incident impulse given by ConWep.

that point. The relief function is presented in the form

$$\ln(p) = a + be^{-t} \tag{2.23}$$

where a and b are clearing coefficients which are presented as functions of stand-off. Whilst the authors make it clear that the pressure predictions can be applied for any charge weight (simply by scaling the time), it is not clear how the relief function varies with distance from the free edge. Nevertheless, the methodology of superposition of the reflected pressure and relief wave, as well as the experimental observations, go some way towards explaining the physical process of blast wave clearing.

2.3.4 The Hudson Predictive Method

Hudson (1955) presented the spatial and temporal distribution of a clearing relief wave caused by the impingement of a planar blast wave on a rigid target, approximating the rarefaction wave as an acoustic pulse. This method is based on the assumptions that the shock is weak (i.e. although the clearing wave travels through shocked air, it is acceptable to assume that it propagates at the ambient sonic velocity), the blast wave is planar (i.e. the lateral dimensions of the target are small in comparison to the stand-off, R) and the depth of the target is sufficiently large to ensure that no clearing waves arrive from the back face during the duration of loading. Given these assumptions, the acoustic approximation can be used to determine the pressure acting at any point on the target face, giving full spatial and temporal distribution of the cleared blast pressure.

Hudson (1955) presents the contours of relief pressure (normalised against the peak incident overpressure) in terms of non-dimensional length and time parameters. Figure 2.12 shows the temporal and spatial distribution of the clearing relief wave, where Hudson's non dimensional length scale, η, is given as

$$\eta = \frac{x}{a_0 t_d} \tag{2.24}$$

where x is the distance from the point of interest to the nearest free edge, a_0 is the sonic sound speed in air (assumed to be 340 m/s) and t_d is the positive phase duration. Hudson's time scale, δ, is given as

$$\delta = \frac{t}{t_d} - \eta \tag{2.25}$$

where t is time.

Figure 2.13 shows the relief functions for select values of η. The clearing wave can be seen to become more rounded, lower in magnitude and longer in duration as it propagates over the target face. For any point on a target, $0 < \eta \leq 1$, the time-varying pressure
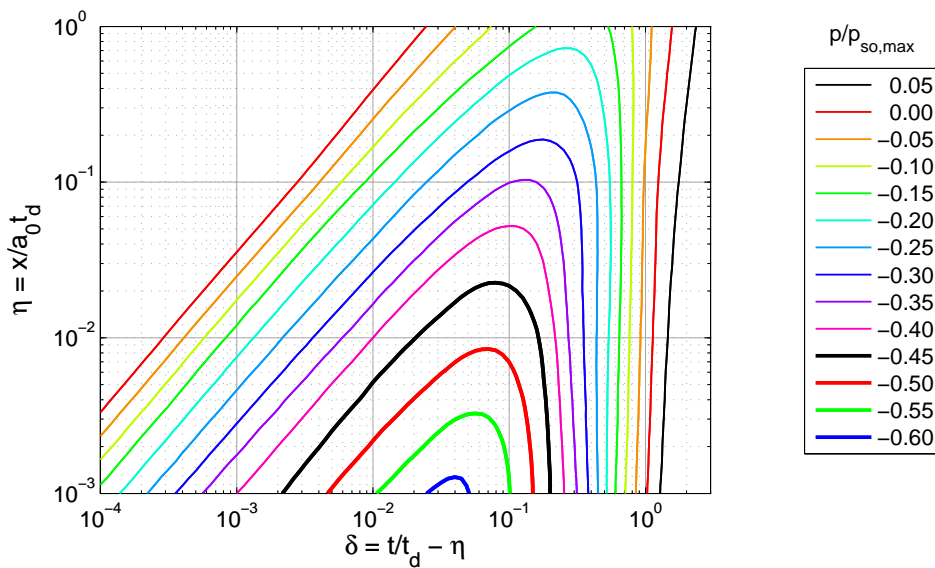
Figure 2.12: Spatial and temporal properties of the rarefaction relief wave (Hudson 1955)

associated with the clearing wave can be evaluated, dimensionalised and superimposed with the reflected pressure acting on the target to determine the cleared pressure at that point.[xii]

Tyas et al. (2011a,b) conducted a series of experiments to validate the Hudson predictive method. Whilst the results are not repeated here in full, Figure 2.14 gives an indication of the level of agreement achieved. In this example, the gauge location was 337.5 mm away from the vertical edge of the target and 355 mm away from the horizontal edges. The positive phase duration was 2.7 ms, giving a blast length of 0.92 m and vertical and horizontal η values of 0.37 and 0.39 respectively. The Hudson method permits the superposition of multiple clearing waves, which can be seen to arrive at roughly the same time, 8.2 ms, in Figure 2.14.

The Hudson method provides a simple yet physically robust means for determining the pressure acting on a target whose reflecting surface cannot be assumed to be infinite. The non-dimensional formulation of the Hudson method, as well as the ease with which it can be combined with ConWep semi-empirical predictions mean the method is suitable for parametric study, and is used to model cleared blast pressures in the parametric study of this thesis (Chapter 6).

[xii]$\eta = 0$ indicates a point on the free edge where clearing relief will begin immediately upon the arrival of the blast wave. $\eta > 1$ indicates a point that will experience the full reflected pressure for the entire duration of the positive phase
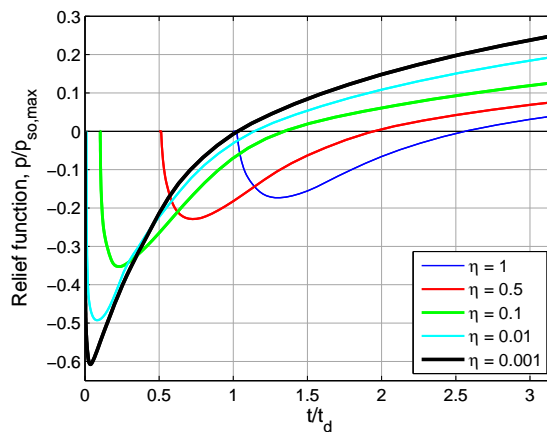
Figure 2.13: Hudson clearing functions.
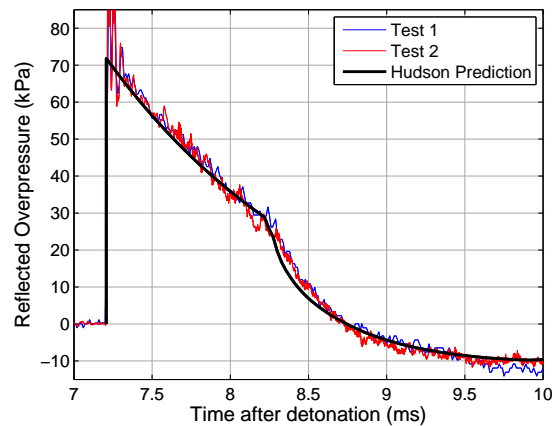
Figure 2.14: Validation of the Hudson predictive method, adapted from the results in Tyas et al. (2011a,b)

2.4 Structural Response to Blast Loads

So far, this chapter has focussed on estimating blast loads and how structural properties and geometry may influence the loading it is subjected to. For the remainder of this chapter, the reverse situation will be considered.

The topic of structural response to blast loads is very broad and covers a wide range of parameters and areas of interest. It is not the purpose of this section to review all the current and past research in this field, instead it is intended that this review will bring the reader up to speed with the relevant areas of research, and will highlight subject areas where knowledge is still lacking, or where commonly made assumptions do not hold true. It is not the purpose of this chapter to provide information on how finite element and single-degree-of-freedom methods calculate structural response; such information will be presented when it is relevant to the current research in later chapters.

2.4.1   Current Best Practice

For an engineer tasked with predicting the response characteristics of a structure subjected to a blast load, there are 3 main options available; simplified numerical analysis, detailed numerical analysis or experimental tests.

The single-degree-of-freedom (SDOF) design charts found in *Introduction to Structural Dynamics* (Biggs 1964), which are also available in design guidance (US Department of Defence 2008, Cormie et al. 2009), allow the peak dynamic displacement to be simply 'read-off', given knowledge of the peak pressure and duration of the load, and the target material properties (mass, stiffness, yield strength) and span. Such a simple method clearly has mass appeal[xiii], however these charts are based on the assumption of a linearly decaying load, an assumption that, as demonstrated by the simple validation in section 2.2.4, does not accurately represent real life blast pressures.

Li & Meng (2002) analysed an SDOF model under different pulse shapes and observed an important contribution of load shape when the structure is loaded dynamically. Gantes & Pnevmatikos (2004) reproduced the design charts of Biggs (1964) but with an exponentially decaying load extended into the negative phase. As shown by the validation in Section 2.2.5, an 'extended Friedlander' is not appropriate for modelling the negative phase of the blast load, which limits the applicability of the results. The linear load is modelled with $t_{d,lin} = t_d$, meaning the positive phase impulse of the exponential load decreases relative to the triangular load with increasing decay coefficient, b. As such, the observations of the linear load being 'significantly over-conservative' does not distinguish between the effects of the reduced positive phase impulse or the inclusion of the negative phase. Whilst Krauthammer & Altenberg (2000), Dharani & Wei (2004) and Wei & Dharani (2006) have found situations where the negative phase can cause stresses up to double those caused by the positive phase, the findings are only intended to demonstrate the importance of the negative phase.

In order to provide more robust and extensive design guidance, Teich & Gebbeken (2010) quantified the influence of the negative phase by comparing SDOF models analysed with and without the negative phase. One of the key findings of the research was that, at large scaled distances ($Z > 40$), the displacement caused by the negative phase was up to an order of magnitude greater than that caused by the positive phase alone. As discussed in Section 2.2.5, however, the negative phase approximations from this study are considerably larger than experimentally measured values, so more complete validation is required before any reliable conclusions can be drawn.

The SDOF method assumes the application of a uniform pressure load. If blast wave clearing is considered, the load is not uniform spatially, nor is the distribution of spatial pressure constant with time. In the case of near field explosions, where the distribution

---

[xiii]According to *Google Scholar*: at the time of writing this thesis 'An Introduction to Structural Dynamics' has been cited over 1,200 times. 265 of these citing articles have been published since 2010

of pressure and impulse varies spatially but not temporally, the problem becomes simpler. Cormie & Arkinstall (2012) introduces a new method for analysing SDOF systems subjected to non-uniform loads by calculating a deflected shape at the start of the analysis based on the initial loading distribution. This is shown to be in agreement with more sophisticated multiple degree analyses. Tyas & Pope (2003, 2004) extend the work of Jones (1971) on predicting residual plastic deformation of thin plates by including an allowance to model non-uniform loading. Whilst the methods detailed above are valid in their own right, they require further modification before they are applicable for the problem of blast wave clearing.

Numerical analysis offers a powerful tool for modelling structural response to blast loads, however it is apparent from the literature that there is still considerable vagueness involved when dealing with blast load modelling. A recent review paper by Rajendran & Lee (2009) provides references for over 90 articles relating to the area of analysis of blast loaded plates. Of the studies where the plate is modelled using finite elements, the loading is prescribed in a number of different ways, such as:

- Modelling the explosion process and blast wave propagation through air using finite elements (Børvik et al. 2009, Chafi et al. 2009, Safari et al. 2011, Zakrisson et al. 2011, Tabatabaei et al. 2013).[xiv]

- Applying the pressure-time history using the semi-empirical pressure predictions (Børvik et al. 2009, Spranghers et al. 2012, 2013, Borenstein & Benaroya 2013).

- Using experimental measurements of structural response and numerical simulations to obtain the load via the 'inverse approach' (Xu et al. 2010).

- Measuring the load experimentally and using this as input for the numerical model (Jacinto et al. 2001, Danesi et al. 2002).

2.4.2 The Influence of Clearing

Clearly there is no best approach for modelling the response of targets subjected to blast loads. Also, it is apparent from the literature survey that there has been very little attempt to quantify the influence of blast wave clearing on the dynamic response of structures. This is due to a combination of a) a lack of understanding of the physical process of blast wave clearing, b) the assumption that ignoring blast wave clearing is conservative, and c) no access to the correct computational tools to analyse the effect of clearing. In the experimental work of Dennis et al. (2002), Nassr et al. (2012) and Spranghers et al. (2012, 2013) the targets were purposefully embedded in a larger reflecting surface to reduce the effect of blast wave clearing. In practice, the engineer is not given the convenience of simply being able to ignore clearing or factor it out.

[xiv]Modelling of blast waves using finite elements is the subject of Chapter 3

For structures whose dimensions are comparable to the length of the blast wave, the time taken for the clearing wave to propagate across the target face is comparable to the duration of loading. For these structures, the Hudson predictions can accurately predict the form of the relief wave (Tyas et al. 2011a,b) and the loading is known as diffraction-type (Table 2.3). For structures whose dimensions are far smaller than the length of the blast wave (such as the targets in the nuclear trials of the 1950s from where the original clearing predictions originate), the transit time of the clearing wave and hence the time taken for pressures to equalise in the reflected and diffracted region is relatively short compared to the duration of loading. For these scenarios, the loading is known as drag-type (Table 2.3). In a numerical study on tall buildings subjected to cleared loads, Rose et al. (2004) highlighted another scenario: buildings whose height is sufficiently large compared to their width such that the full reflected pressure no longer develops along the height of the building. This case is only of practical importance for targets with scaled height larger than the scaled distance, $H > Z$, due to the longer path length and the non-normal impingement of the blast wave at higher points on the building. In this study, normal blast wave clearing, i.e. $H < Z$, will be considered.

Section 2.3 discussed current experimental and numerical methods for predicting blast wave clearing on a rigid target. Only two cases were found in the literature where clearing was investigated with regards to deformable targets. Van Netten & Dewey (1997) conducted a series of experimental tests on cantilevers subjected to explosive loads. In these tests the width of the loaded face was 30 mm, with the blast length ($a_0 t_d$) estimated to be around 5 m. The numerical model was loaded with the drag pressure only (Equation 2.4) and was found to be in excellent agreement with the experimental results. Shi et al. (2007) performed a series of numerical analyses on structural columns subjected to blast loads and suggested a semi-empirical method for determining the pressure and impulse imparted to columns of various sizes. The dynamic response of the column was studied only as a means for quantifying the effect of column-blast wave interaction on impulse (which, it was concluded, had very little effect, even if the column stiffness was varied over two orders of magnitude), and not for quantifying the likely displacement the column would experience as a result of the blast.

It can be concluded that there remains no published work detailing the influence of clearing on the response of flexible targets.

2.5 Summary

This chapter has focussed on the formation of blast waves and the interaction of blast waves with structures, as well as detailing semi-empirical methods for predicting positive and negative phase parameters. Experimental pressure-time histories are used to demonstrate the accuracy of the semi-empirical blast prediction method – the positive phase matches the experimental measurements closely, however the negative phase is less well validated

and as such there are several methods found in the literature which do not give satisfactory results.

Blast wave clearing has been discussed, and current methods for predicting the effect of clearing are introduced, including the Hudson method, which forms the basis of the numerical predictions of blast wave clearing in this thesis.

Existing research on the analysis of structures subjected to blast loads has been reviewed, with a particular focus on different attempts at quantifying the blast load. Whilst studies of blast wave clearing exist in the current literature, none detail or quantify the influence of clearing on dynamic response.

Chapter 3

Air Blast Loading Using LS-DYNA

3.1 Introduction

Non-linear finite element (FE) software, such as LS-DYNA (Hallquist 2006), can be used to model explosive detonation and subsequent shock wave propagation through the surrounding media. Differential equations governing the conservation of mass, momentum and energy are satisfied at each step in time by spatially discretising a continuous domain into finite elements. Interpolation 'shape' functions are used to construct approximations to variables such as displacements and stresses, which are solved at individual nodal points rather than throughout the whole continuum. Numerical analyses are a powerful tool as they allow a vast array of physical parameters to be modelled explicitly without the need for approximation.

Whilst it is well known that FE software can be used to model structural deformation, this chapter is only focused on the modelling of air blast. It is the purpose of this chapter to validate LS-DYNA against a series of well controlled experiments and semi-empirical pressure predictions to demonstrate the accuracy with which LS-DYNA can simulate explosive events. The effects of different modelling techniques, such as mesh refinement and re-mapping will also be studied.

3.2 The ALE Method

A finite element model can be defined by a Lagrangian framework, where the numerical mesh is fixed to the material and deforms with the continuum it is representing, i.e. there is no transport of material through elements. It can also be defined in an Eulerian framework where the mesh is fixed in space and the material flows through the mesh, i.e. there is no mesh distortion.

Typically, fluid flow problems are solved using an Eulerian framework, however material mixing and the need to accurately track material interfaces can become problematic and computationally expensive. Also, a greater number of elements are generally required for Eulerian analyses (Hallquist 2006). Lagrangian formulations can solve multi-material problems significantly more robustly due to the fact that the grid is attached to the material itself. This has setbacks, however, as large deformations can lead to severe mesh distortion, entanglement and instabilities.

3.2.1 Governing Equations and Advection Method

The Arbitrary Lagrangian Eulerian (ALE) method is a formulation for solving the governing equations for a material flowing through a mesh that moves with an arbitrary velocity relative to the material. The governing equations for conservation of mass, momentum and energy for compressible flow of a moving control volume are given by Souli et al. (2000) as

$$
\begin{aligned}
\frac{\partial \rho}{\partial t} &= -\rho \frac{\partial v}{\partial x} - w \frac{\partial \rho}{\partial x} \\
\rho \frac{\partial v}{\partial t} &= \sigma_{ij} + \rho b - \rho w \frac{\partial v}{\partial x} \\
\rho \frac{\partial E}{\partial t} &= \sigma_{ij} v + \rho b v - \rho w \frac{\partial E}{\partial x}
\end{aligned}
\tag{3.1}
$$

where v is the velocity of the material and w is the relative velocity between the material and mesh, ρ and E are the density and specific energy of the fluid, and σ_{ij} is the stress tensor, defined as $\sigma_{ij} = -p + \tau$, where p is pressure and τ is shear stress.

The above is known as Arbitrary Lagrangian Eulerian because it describes an arbitrary case which is neither a fully Lagrangian nor a fully Eulerian situation. It can be seen that if $w = v$, the Eulerian equations are recovered from Equation 3.1. If there is no relative motion between the material and mesh, i.e. $w = 0$, the Lagrangian equations are recovered from Equation 3.1. In LS-DYNA, the ALE method is solved in two steps in a process known as an operator split. First, Equation 3.1 is solved with $w = 0$ and a Lagrangian cycle is performed. After this, the deformed mesh is transported back to its original (un-deformed) position as mass, energy and momentum are transported across element boundaries in an Eulerian process, known as the advection phase. The Eulerian advection stage is purely computational as all the time-dependent physics are solved in the Lagrangian stage. This process is shown schematically in Figure 3.1.

The ALE method is attractive for simulating blast events because excessive mesh deformations associated with Lagrangian formulations are avoided due to the advection 're-mapping' process. The ALE method is also more capable of handling multi-material formulations and tracking material interfaces than Eulerian formulations (Souli et al. 2000). The solution method for the advection stage in LS-DYNA can be accessed through the
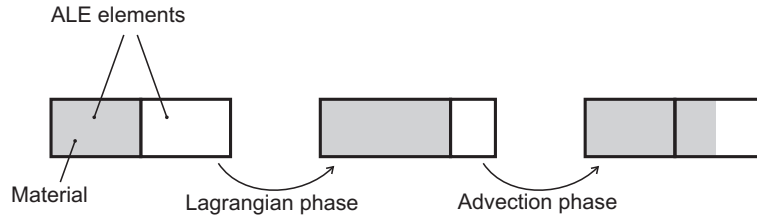
Figure 3.1: Lagrangian and Advection phases in an ALE analysis

*CONTROL_ALE card. Hallquist (2006) recommends using Van Leer (1977) advection with Half-Index shift for high explosive problems.

The Van Leer MUSCL (monotone upwind scheme for conservation laws) algorithm, when applied to the linear convection of an arbitrary distribution of variables

$$\frac{\partial \phi}{\partial x} = a(x)\frac{\partial \phi}{\partial t} \tag{3.2}$$

is monotonic and conservative, meaning that no new maxima or minima are created, and that variables are conserved during advection, i.e.

$$\int_V \phi_{new} \ \mathrm{d}V = \int_V \phi_{old} \ \mathrm{d}V. \tag{3.3}$$
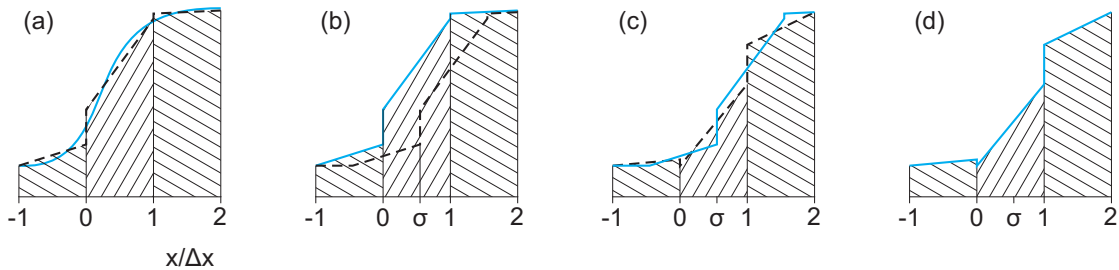
Figure 3.2: Advection of variables using the Van Leer (1977) MUSCL scheme

With reference to Figure 3.2, the Van Leer advection algorithm is implemented in the following way:

(a) Approximating the initial value distribution (solid line) by a piecewise linear function (broken line). Conservation is guaranteed by expanding the linear function about the element centroid ($x = j + 1/2$), such that

$$\phi_{j+1/2}^n(x) = S_{j+1/2}^n(x - x_{j+1/2}^n) + \phi_{j+1/2}^n \tag{3.4}$$

where x is the volume coordinate and $S_{j+1/2}^n$ is an approximation of the slope (Hallquist 2006).

(b) The approximate initial distribution (solid) is advected over a distance of $\sigma\Delta x$ (broken line). For the ALE method in LS-DYNA, this distance is equal to the Lagrangian displacement that has occurred between advection cycles.[i]

(c) The new linear distribution is defined (broken line), as per Equation 3.4 with monotonicity constraints as defined in Equations 3.5–3.8.

(d) The advection stage is complete and the value distribution is taken as the initial values for the next step.

To ensure monotonicity, the value of the *slope* at the element centroid, $S^n_{j+1/2}$, is constructed such that the values of the variable at the element centroid, $\phi^n_{j+1/2}$, and the values of the variable at adjacent element centroids, $\phi^n_{j-1/2}$ and $\phi^n_{j+3/2}$, are not exceeded.

$$S^n_{j+1/2} = \frac{1}{2}\left(\text{sgn}(s^L) + \text{sgn}(s^R)\right) \times \min\left(|s^L|, |s^n_{j+1/2}|, |s^R|\right) \tag{3.5}$$

$$s^L = \frac{\phi^n_{j+1/2} - \phi^n_{j-1/2}}{\frac{1}{2}(x_{j+1/2} - x_j)} \tag{3.6}$$

$$s^R = \frac{\phi^n_{j+3/2} - \phi^n_{j+1/2}}{\frac{1}{2}(x_{j+1} - x_{j+1/2})} \tag{3.7}$$

$$s^n_{j+1/2} = \frac{\phi^n_{j+3/2} - \phi^n_{j-1/2}}{x_{j+3/2} - x_{j-1/2}} \tag{3.8}$$

This is illustrated in Figure 3.3 for different distributions of ϕ.
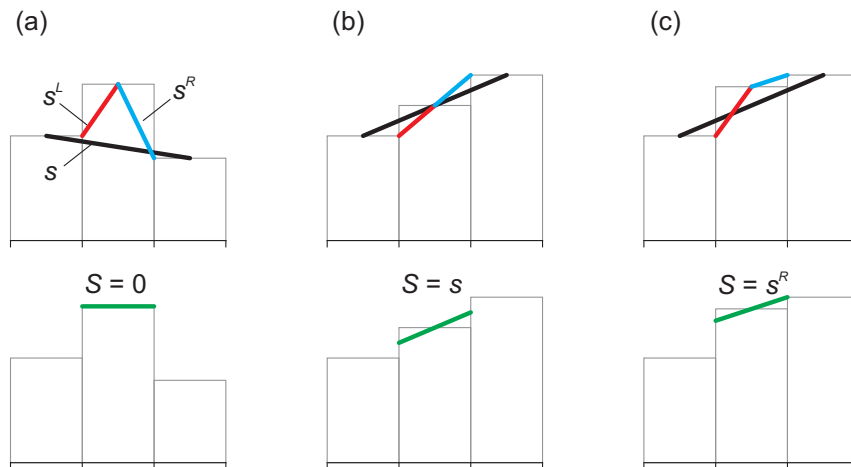
Figure 3.3: Monotonicity limits of the slope, S, for different distributions of variables, ϕ. (a) $\text{sgn}(s^L) \neq \text{sgn}(s^R) \Rightarrow S = 0$. (b) $\min(|s^L|, |s|, |s^R|) = |s| \Rightarrow S = s$. (c) $\min(|s^L|, |s|, |s^R|) = |s^R| \Rightarrow S = s^R$, adapted from Kaurin & Varslot (2010)

[i]In most circumstances, the advection cycle is performed after 1 Lagrangian phase, although this can be set higher using the variable NADV in the *CONTROL_ALE card.

The Van Leer advection method is second order accurate and less dissipative than first order schemes, and is generally more robust when large pressure gradients are expected (Hallquist 2006).

3.2.2   Material Models and Equations of State

LS-DYNA requires the definition of *parts* within the numerical model. Each part represents an individual component such as the explosive, the air, the target etc., and each part must have a material model assigned to it in order to link stress to deformation and internal energy within each element. In the case of explosive modelling (modelling of fluids) an Equation of State (EOS) must be defined for each fluid part, which expresses a relationship between the pressure, p, specific volume, V and specific energy, E.

In this thesis, the air is modelled as an ideal gas using the MAT_NULL and EOS_LINEAR_POLYNOMIAL material model and equation of state respectively. The linear polynomial equation of state is given as

$$p = C_0 + C_1\mu + C_2\mu^2 + C_3\mu^3 + (C_4 + C_5\mu + C_6\mu^2)E \qquad (3.9)$$

where $C_0, C_1, C_2, C_3, C_4, C_5, C_6$ are constants, $\mu = \rho/\rho_0 - 1$ and ρ and ρ_0 are the current and initial densities of air. For ideal gasses, $C_0 = C_1 = C_2 = C_3 = C_6 = 0$ and $C_4 = C_5 = \gamma - 1$ and the equation reduces to the ideal gas equation of state

$$p = (\gamma - 1)E\rho/\rho_0 \qquad (3.10)$$

where E is the specific internal energy and γ is the ratio of specific heats, defined as the ratio of the heat capacity at constant temperature to the heat capacity at constant volume. For air, $\gamma = 1.4$. A specific internal energy of $E = 253.4$ kPa gives an atmospheric pressure of 101.36 kPa.

If the detonation process is modelled explicitly, then a material model and EOS must be specified for the explosive. In LS-DYNA, MAT_HIGH_EXPLOSIVE_BURN is typically used, which requires the density, ρ, detonation velocity, D, and Chapman-Jouguet pressure, PCJ, of the explosive to be defined. The EOS used for high explosives is the Jones-Wilkins-Lee (JWL) empirical formula (Lee et al. 1968), EOS_JWL, which describes the pressure, volume, energy relation of the explosive as

$$p = A\left(1 - \frac{\omega}{R_1 V}\right)e^{-R_1 V} + B\left(1 - \frac{\omega}{R_2 V}\right)e^{-R_2 V} + \frac{\omega E}{V} \qquad (3.11)$$

where A, B, R_1, R_2 and ω are constants, V is the volume and E is the internal energy. The parameters for air, TNT and C4 are shown in Table 3.1, with the JWL parameters for TNT and C4 given in Dobratz & Crawford (1985).

Air	MAT_NULL							
	ρ_0							
	1.225							
	EOS_LINEAR_POLYNOMIAL							
	C_0	C_1	C_2	C_3	C_4	C_5	C_6	E_0
	0.0	0.0	0.0	0.0	0.4	0.4	0.0	253.4E3
TNT	MAT_HIGH_EXPLOSIVE_BURN							
	ρ_0	D	PCJ					
	1630	6930	2.10E9					
	EOS_JWL							
	A	B	R_1	R_2	ω	E_0		
	371.20E9	3.231E9	4.15	0.95	0.30	7.0E9		
C4	MAT_HIGH_EXPLOSIVE_BURN							
	ρ_0	D	PCJ					
	1601	8193	2.80E10					
	EOS_JWL							
	A	B	R_1	R_2	ω	E_0		
	609.77E9	12.95E9	4.50	1.40	0.25	9.0E9		

Table 3.1: Material model and Equation of State parameters for air, TNT and C4 (SI units). Parameters for TNT and C4 are given in Dobratz & Crawford (1985)

3.2.3 Relevant Keywords and Advancements in LS-DYNA

LS-DYNA accesses various algorithms through the use of *keywords* in the input file. A number of capabilities have been added in recent years which have improved the ability of LS-DYNA to simulate explosive events. Those keywords relevant to the numerical study in this thesis are introduced here.

- *ALE_MULTI-MATERIAL_GROUP enables each element to contain more than one different material (Luo et al. 2004, Alia & Souli 2006), which is essential for modelling the interaction between the explosive products and air. Up to 10 multi-material groups can be defined.

- *ALE_REFINE can be used to refine ALE elements in areas of high pressure or volume fraction (Aquelet 2012). This technique could be used to produce an adaptive region of fine mesh that moves with the shock front, however Alia & Souli (2006) suggest that mixing of small and large elements in the same model should be avoided as much as possible because such models tend to reduce simulation accuracy.

- *BOUNDARY_NON_REFLECTING prescribes the boundary condition at a free surface. This allows material to flow out of the model without reflections from the boundary contaminating results.

- *CONTROL_ALE allows global parameters for ALE analyses to be set, such as the

number of cycles between advections (NADV), the advection method (METH), various smoothing controls, and allows a reference pressure to be added to the free surfaces of the ALE domain (PREF).

- *DATABASE_TRACER will save the history of either a material point (TRACK=0) or spatial point (TRACK=1). This keyword can be used to give pressure-time histories at a fixed coordinate in the mesh, which will give the blast overpressure when ambient pressure is subtracted.

- *INITIAL_ALE_MAPPING initialises the analysis with data from the previous run, after Aquelet & Souli (2008). This allows the analyst to change mesh size or model size during the simulation, and is particularly useful for changing from 2D to 3D (thus saving a great deal of computational expense), when the propagation of the blast wave can still be performed in axi-symmetry. Lapoujade et al. (2010) found that energy was conserved when re-mapping to meshes up to 20 times coarser than the original.

- *INITIAL_DETONATION is required to define the location of high explosive detonation. The lighting time of an element, t_L is given as the distance from the centre of the element to the detonation point divided by the detonation velocity, D. The burn fraction, F, which controls the release of chemical energy, is defined (in 2 dimensions) as

$$F = \max(F_1, F_2)$$

where

$$F_1 = \begin{cases} 0 & t \le t_L \\ \dfrac{2\,(t - t_L)\,Dl_{e,max}}{3A_e} & t > t_L \end{cases} \tag{3.12}$$

$$F_2 = \frac{1 - V}{1 - V_{CJ}}$$

where $l_{e,max}$ is the maximum element length, A_e is the element area, V is relative volume and V_{CJ} is the Chapman-Jouguet relative volume. F_1 corresponds to the programmed burn of the explosive, and F_2 is known as the 'beta burn', i.e. detonation caused by volumetric compression. The pressure within the detonating element is given as the product of the burn fraction and JWL EOS pressure, i.e.

$$p = Fp_{eos}(V, E). \tag{3.13}$$

If F exceeds 1 it is reset to 1 and is held constant thereafter. It typically takes several time steps for F to reach 1, hence the burn front is usually spread over several elements (Hallquist 2006).

- *INITIAL_VOLUME_FRACTION_GEOMETRY allows a volume within a user-defined geometry to be filled with ALE multi-material groups. For blast applications, this means that the high explosive can be represented without the need to explicitly model it (with different elements) in the mesh.

- *LOAD_BLAST_ENHANCED applies ConWep LOS pressure predictions (Equation 2.18) to surfaces within the model given a charge mass and stand-off. This has been coupled with ALE ambient elements (Slavik 2009), negating the need to model the initial detonation and subsequent blast wave propagation as it only considers the blast wave once it is within the vicinity of the structure. This has particular application for far field loading, however the ambient element layer used as input must be far enough from the target structure such that reflections from this boundary do not contaminate results (Schwer 2010).

3.2.4   Bulk Viscosity

In order to reduce any high frequency numerical oscillations that typically follow the shock front, an artificial bulk viscosity term, q, is added to the pressure term (Hirsch 1988). The shock discontinuity is smeared into a rapidly varying but continuous transition region over the length of a few elements. Artificial bulk viscosity increases the stability of the analysis, as well as reducing numerical dispersion, but may cause excessive smearing of the shock front, reducing the amplitude of peak overpressure.

The bulk viscosity term, q, is given by Hallquist (2006) as

$$
\begin{aligned}
q &= C_0 \rho l_e{}^2 \left(\frac{\mathrm{d}s}{\mathrm{d}t} \right)^2 - C_1 \rho l_e a \left(\frac{\mathrm{d}s}{\mathrm{d}t} \right) && \text{if} \quad \dot{\epsilon}_{kk} < 0 \\
q &= 0 && \text{if} \quad \frac{\mathrm{d}s}{\mathrm{d}t} \geq 0
\end{aligned}
\tag{3.14}
$$

where l is the thickness of the element, $\dfrac{\mathrm{d}s}{\mathrm{d}t}$ is the strain rate in the direction of the acceleration, ρ and a are the density and sound speed respectively, $\dot{\epsilon}_{kk}$ is the trace of the strain rate tensor and C_0 and C_1 are dimensionless constants which default to 1.5 and 0.06 respectively. Values of C_0 and C_1 are user defined and can be accessed via the *CONTROL_BULK_VISCOSITY keyword in LS-DYNA.

3.3   Blast Wave Propagation in Free Air

3.3.1   Preliminary Mesh Study

A preliminary mesh study was undertaken to investigate two techniques for representing a hemispherical surface explosive, as shown in Figure 3.4;

(a) A radial mesh, with the explosive modelled as a separate part. The mesh was generated in a purpose written MatLab script with element size increasing with increasing distance from the explosive, i.e. a constant aspect ratio was kept for air elements. This allows for a spherically uniform shock propagation.

(b) A Cartesian grid with uniform element size. The explosive was represented using the keyword *INITIAL_VOLUME_FRACTION_GEOMETRY with CONTYP = 6 (spherical container requiring the radius and coordinates of the origin of the sphere as input values). This method does not require individual meshing of the explosive – a different charge mass can be specified by changing the parameter R0.

(a)   (b)
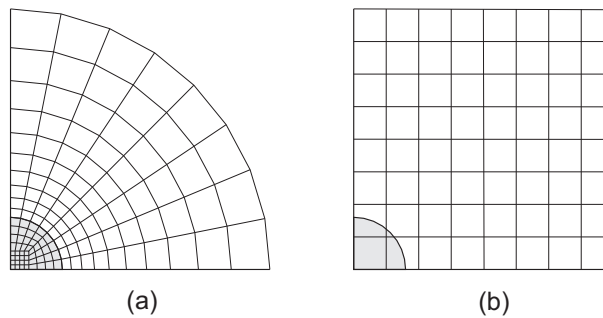
Figure 3.4: Representation of (a) radial mesh and (b) Cartesian grid mesh used in the preliminary mesh study

The preliminary analyses simulated a hemispherical TNT charge with 0.05 m radius propagating through free air, using 2D axi-symmetric elements with material properties for air and TNT outlined in Table 3.1. Bulk viscosity parameters of 3.0 and 0.12 were selected for C_0 and C_1 based on the findings of an initial bulk viscosity study. These values are double the default values for LS-DYNA, and were selected so to minimise the energy lost through numerical dispersion at larger scaled distances.

The ground surface was modelled with nodal displacements constrained against vertical translation. For the radial mesh, contact between the explosive and air was achieved using shared nodes along the boundary, as this is both reliable and economic (Wang 2001, Alia & Souli 2006). The radial mesh contained 100,000 air elements and 11,700 explosive elements and the grid mesh contained 250,000 elements in total over a 1 m air domain.

One disadvantage of the advection methods implemented in LS-DYNA is that the values of ϕ in the transport volumes are calculated using the one-dimensional expressions (Equation 3.4). This means that there is no coupling between an element and adjacent elements that share only vertices with the element (elements that do not share edges in 2D and faces in 3D), which introduces a second order advection error. Crucially, this second order error is only significant when material is transported diagonally along the mesh (Hallquist 2006).

Figure 3.5 shows the overpressure-time histories for both mesh techniques at a distance of 0.7 m from the centre of the explosive. It is clear from Figure 3.5 that the radial mesh
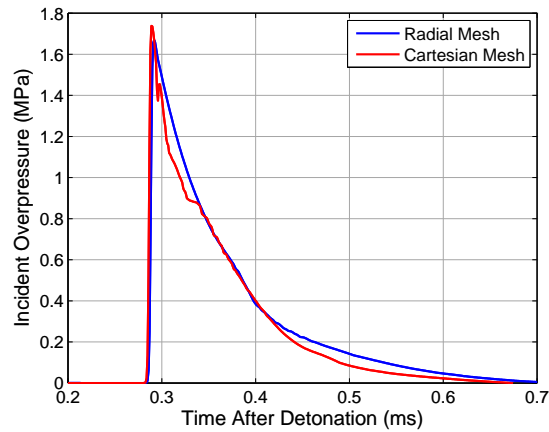
Figure 3.5: Overpressure-time histories for 0.8535 kg TNT spherical air burst at 0.7 m for radial and Cartesian (grid) mesh

is significantly less dispersive than the grid mesh. With the radial mesh, the spherical expansion of the shock wave is aligned with the elements, whereas the material transport through the grid mesh occurs along the diagonals of elements, introducing the second order advection error. The radial mesh is also more efficient, as smaller elements are only located where necessary, which can give a higher mesh resolution for a given run time compared to the grid mesh, or can give a shorter run time for a given minimum element (or time-step) size.

Explicitly modelling the explosive should be preferred over *initial_volume_fraction for curved charges. The necessity to accurately model the explosive/air interface is demonstrated in Figure 3.6, which shows pressure contours in the air domain 0.15 ms after detonation (by which time the blast wave has travelled ∼0.5 m) for both meshes.

(a)   (b)
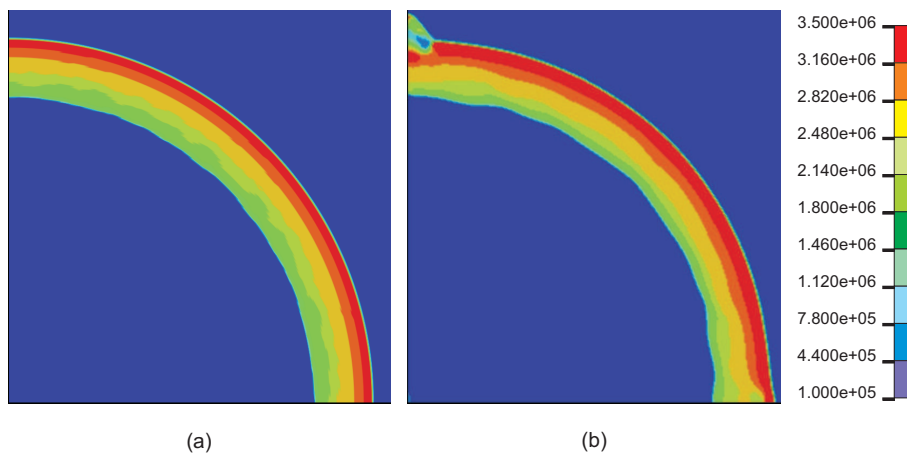
Figure 3.6: Contours of pressure (units in Pa) at $t = 0.15$ ms after detonation for (a) radial mesh and (b) grid mesh. The blast wave has travelled ∼0.5m from the source of the explosive

The explosive can only be represented by square elements in the grid mesh, and any elements along the interface have material distributed across the whole element based on the volume fraction in that cell. This results in a non-spherical energy release, as can be seen by the increased pressure in the upper left and bottom right corner of Figure 3.6(b). The non-spherical expansion of the blast wave when using *INITIAL_VOLUME_FRACTION can also be seen.

In light of the points raised above, the initial stages of explosive modelling for the remainder of this thesis are conducted using the radial mesh technique.

3.3.2 Mesh Sensitivity

The radial mesh enables the number of elements along the radius and circumference of the 2D axi-symmetric domain to be specified separately. It was found that increasing the number of circumferential elements independent of the number of elements along the radius of the domain had little effect on the fidelity of the simulations. Therefore, a fixed aspect ratio of 0.2 (short side length in the radial direction and large side length in the circumferential direction) was chosen for the air elements, which is greater than the minimum value of 0.1 suggested by Hallquist (2006) for stability purposes, and will be no less accurate than a mesh comprising more circumferential elements or a shorter circumferential element length. The mesh sensitivity study is thus focussed on the number of elements along the radial length of the domain (i.e. in the direction of the blast wave propagation), the results of which are presented here.
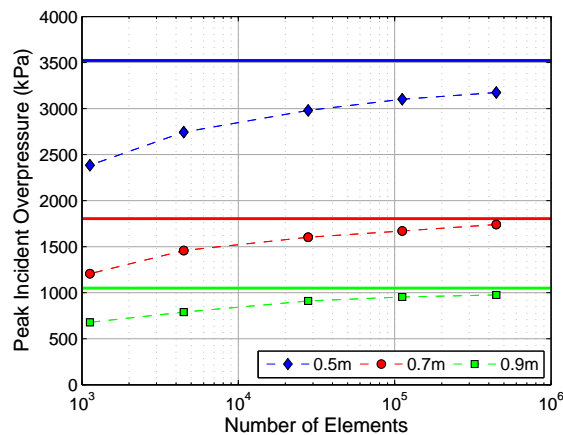
Figure 3.7: Peak incident overpressure for different mesh densities at three gauge locations. Solid lines indicate values given by ConWep (Hyde 1991)

A mesh sensitivity analysis was conducted for mesh densities ranging from 1,125 axi-symmetric elements[ii] to 446,800 axi-symmetric elements[iii]. Figure 3.7 shows the peak incident overpressure for the different mesh densities at three gauge locations – 0.5, 0.7

[ii]10 elements along the circumference and 100 elements along the radius of the air domain
[iii]200 elements along the circumference and 2000 elements along the radius of the air domain

and 0.9 m from the centre of the explosive (0.8535 kg TNT with a radius of 50 mm). The solid lines indicate values of peak incident pressure given by ConWep (Hyde 1991). The ability of the numerical model to capture the sharp discontinuity of the shock front is heavily dependent on the density of the mesh in the direction of travel of the blast wave.

The results generally tend towards the semi-empirical predictions for peak incident over-pressure with increasing mesh density. It is worth noting, however, that the shorter stand-off case does not appear to be converging as well. The reliability of the KB predictions in the near-field – which are predominantly based on early numerical computations – are generally recognised as being unreliable and have already been questioned by Esparza (1986) and more recently by Cormie et al. (2013). This lack of convergence therefore can be put down to a limitation of the KB method for near-field events, rather than a limitation of the computer model.

Figures 3.8, 3.9 and 3.10 show pressure-time and impulse-time histories for the numerical analyses at 0.5, 0.7 and 0.9 m, for a fine mesh (comprising 446,800 elements), a medium mesh (27,975 elements[iv]) and a coarse mesh (1,125 elements), all with an aspect ratio of ~0.2 for air elements. The influence of mesh density on resolution of the shock front can clearly be seen, with the discontinuity being smeared over ~25 μs for the coarsest mesh but being accurately represented by the finer meshes. Mesh density has less of an effect on the incident impulse, suggesting that similar amounts of energy are released from the explosive regardless of the mesh, and that little energy is lost during blast wave propagation. Alia & Souli (2006) suggest that no less than 16 elements are required along the radius of the explosive to accurately model the detonation process. For the coarsest mesh, 15 elements were used along the radius of the charge and similar amounts of energy were released when compared to the finer meshes, suggesting that this observation is valid.

Overall, there is a good level of agreement between the semi-empirical and numerical results for peak pressure and arrival time. The numerical model consistently under-predicts the incident impulse, however the preservation of peak pressure suggests that this is not due to cumulative energy losses in the numerical model. In a review of simplified predictive methods, Bogosian et al. (2002) found that ConWep predictions for incident impulse were on average 15% higher than experimental test results. In the experimental work of Tabatabaei et al. (2013), it was found that ConWep incident impulses were up to 40% higher than the measured free-field impulses, suggesting there is an inherent over-conservatism in ConWep incident impulse predictions.

[iv]50 elements along the circumference and 500 elements along the radius of the air domain
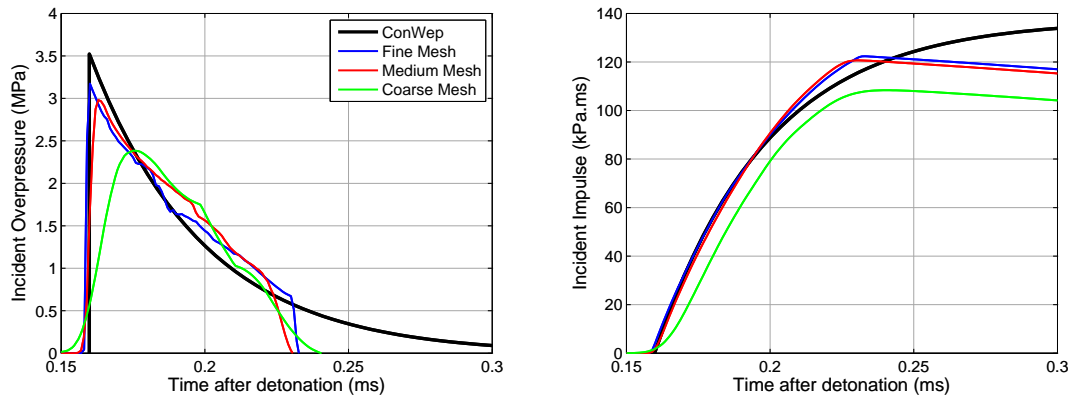
Figure 3.8: Incident pressure-time and impulse-time histories at 0.5 m from the explosive centre (0.8535 kg TNT) for fine (446,800 elements), medium (27,975 elements) and coarse (1,125 elements) radial meshes
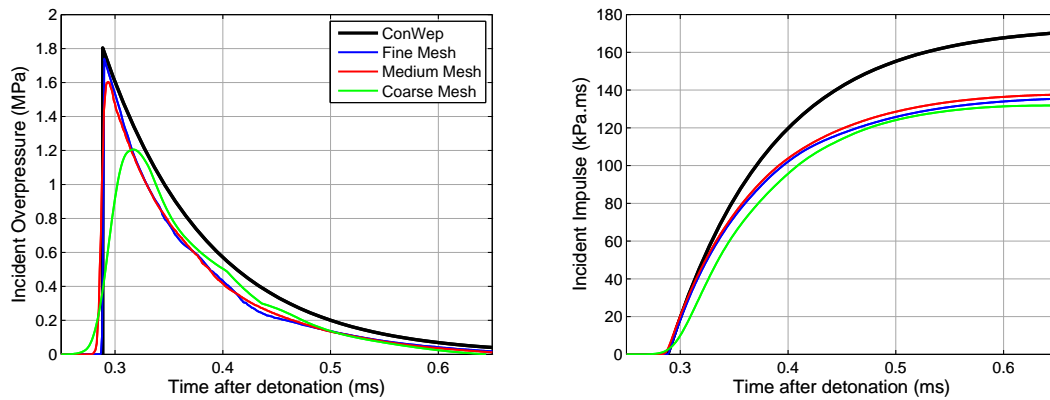
Figure 3.9: Incident pressure-time and impulse-time histories at 0.7 m from the explosive centre for fine, medium and coarse radial meshes
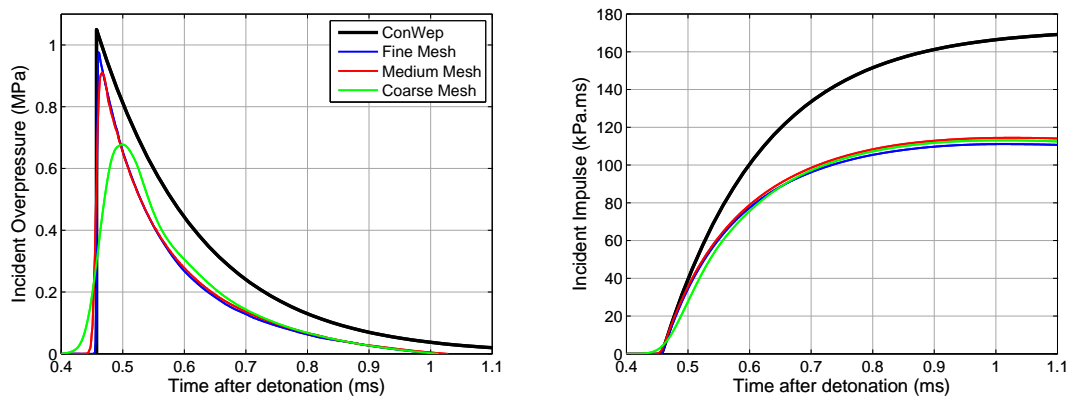
Figure 3.10: Incident pressure-time and impulse-time histories at 0.9 m from the explosive centre for fine, medium and coarse radial meshes

3.4 Reflected Pressure on a Semi-Infinite Surface

In this section, the experimental trials introduced in Section 2.2.4 are used to validate numerical simulations of 250 g hemispherical PE4 (nominally similar to C4) charges detonated 4, 6, 8 and 10 m away from a semi-infinite, rigid target. Empirical predictions were evaluated from ConWep using an assumed TNT equivalence of 1.2 after Tyas et al. (2011a,b).

The detonation process and blast wave propagation was simulated using an axi-symmetric radial mesh, similar to that used in the initial mesh study, with a charge radius of 42.09 mm. One simulation was run with the blast wave propagating through free air, and separate map files were written at $t = 7.1$, 12.5, 18.0 and 23.8 ms after detonation, corresponding to travel distances of (slightly less than) 4, 6, 8 and 10 m. The map files, which contained information of the incident wave, were re-mapped onto a regular grid mesh (still in axi-symmetry) to allow the planar structure to be modelled using only nodal constraints, i.e. nodes along the boundary simulating the air/structure interface were constrained against horizontal translations. The rigid ground surface was again modelled using vertical translational constraints. Performing the first stage of the analysis using the radial mesh and re-mapping onto a regular grid just before the blast wave strikes the target ensures that the blast wave is still spherically symmetrical whilst greatly simplifying the modelling of the reflecting surface.

*initial_ale_mapping allows the user to specify the offset of the mapping data in relation to the mesh. For these analyses, the same grid mesh used for all four analyses with a different offset distance specified for each stand-off tested. The explosive was modelled as C4, with JWL parameters taken from Dobratz & Crawford (1985), shown in Table 3.1.

Figures 3.11, 3.12, 3.13 and 3.14 show the pressure-time and impulse-time histories for the experiments and numerical simulations. Empirical predictions are given by ConWep positive phase and cubic negative phase as detailed in the previous chapter.
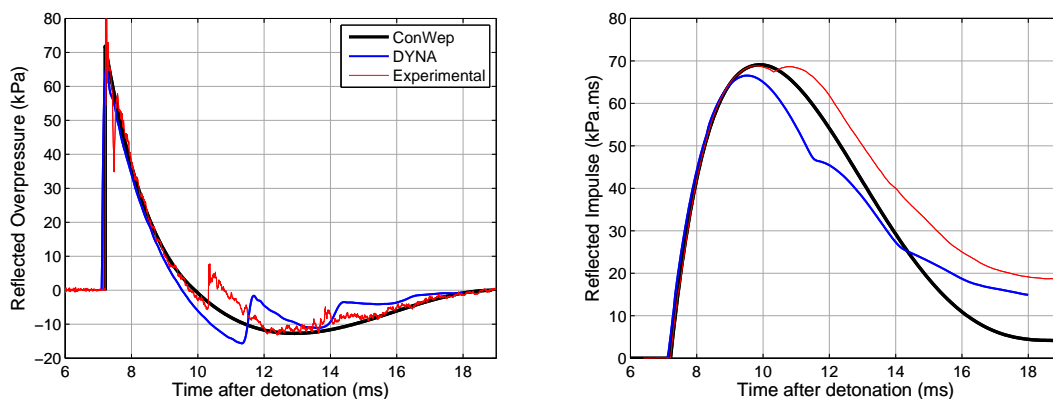
Figure 3.11: Reflected pressure-time and impulse-time histories for a semi-infinite rigid wall located 4 m away from a 250 g hemispherical PE4 charge
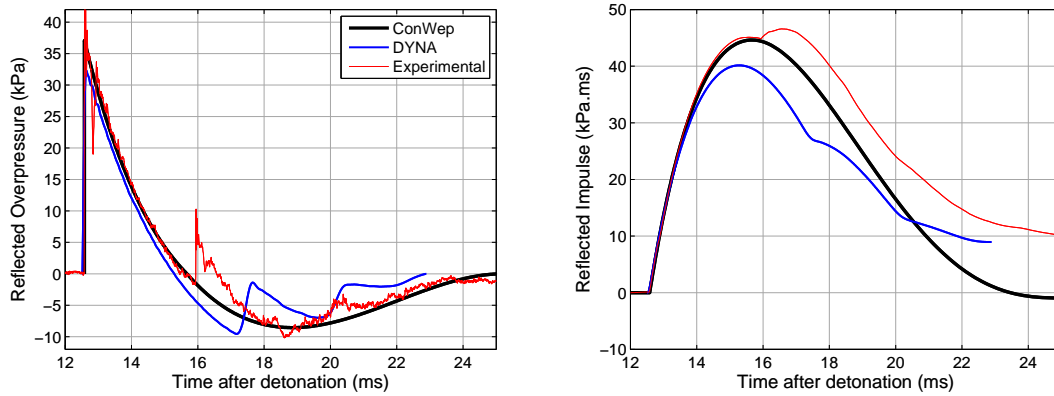
Figure 3.12: Reflected pressure-time and impulse-time histories for a semi-infinite rigid wall located 6 m away from a 250 g hemispherical PE4 charge
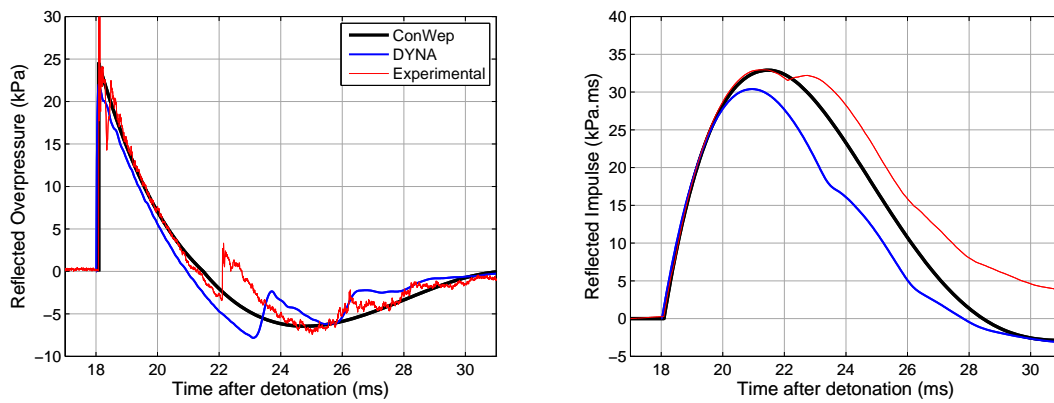
Figure 3.13: Reflected pressure-time and impulse-time histories for a semi-infinite rigid wall located 8 m away from a 250 g hemispherical PE4 charge
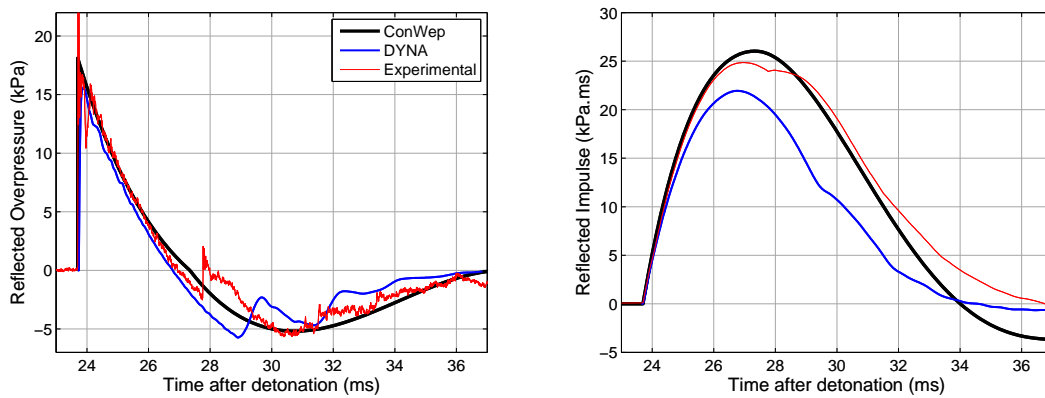
Figure 3.14: Reflected pressure-time and impulse-time histories for a semi-infinite rigid wall located 10 m away from a 250 g hemispherical PE4 charge

Overall, the numerical model is in very good agreement with both the semi-empirical predictions and the experimental results for the positive phase of loading. This suggests that the conservation of mass, momentum and energy associated with shock wave reflection at the boundary between air and structure is sufficiently modelled. There is a small amount of numerical dispersion following the shock front, which becomes more apparent with increased stand-off. This could be remedied by increasing the artificial bulk viscosity, however such an increase will decrease the sharpness of the shock front without benefiting the stability of the solution.

Table 3.2 shows experimental and numerical values of peak reflected pressure and the ratio of numerical to experimental peak pressures. As in Section 2.2.4, the peak experimental pressure is given by a curve fit to the recorded data (post sensor ringing) which is then extrapolated backwards to the arrival time. The numerical model is able to predict the peak pressure to within 14% of the experimental results.

Stand-off (m)	Peak Pressure (kPa)		
	Exp	DYNA	Ratio
4	76.8	67.7	0.88
6	39.2	33.9	0.86
8	26.1	24.5	0.94
10	18.3	16.7	0.91

Table 3.2: Peak experimental and numerical reflected pressure for a 0.25 kg hemispherical PE4 charge (0.3 kg TNT) and ratio of numerical/experimental

In general, the duration of the positive phase is shorter than observed in the experimental results, which leads to slightly reduced values of peak impulse in the numerical simulations. The form of the negative phase is well represented by the semi-empirical predictions, which generally tend to follow the experimental measurements. There is a slight difference between the form of experimental and numerical negative phases, as well as a slight difference in the peak value of underpressure, however it can be seen in Table 3.3 that the peak impulses and total (net) impulses are generally in agreement between experiment and simulation. It is not useful to present ratios of numerical and experimental net impulse due to the proximity of the results to zero.

Stand-off (m)	Peak Reflected Impulse (kPa.ms)			Net Reflected Impulse (kPa.ms)	
	Exp	DYNA	Ratio	Exp	DYNA
4	68.8	66.7	0.97	18.4	17.5
6	44.8	40.0	0.89	6.6	7.1
8	32.6	29.7	0.91	1.9	−1.6
10	24.9	21.9	0.88	−2.8	−0.6

Table 3.3: Peak and net experimental and numerical reflected impulse for a 0.25 kg hemispherical PE4 charge (0.3 kg TNT) and ratio of numerical/experimental peak impulse

The physical process of the 'second shock' (outlined in Section 2.2.4) is captured in the numerical model, however the arrival time is over-predicted in all numerical simulations. The formation of the second shock is dependent on several variables, including the detonation velocity, and the density (and hence wavespeed) in the explosive products. The magnitude of this second shock is typically less than 10% of the main shock and, although it does affect the impulse transmitted through the shock, it is not of primary concern; the numerical model is still able to calculate the net impulse imparted to the target to within 3.5 kPa.ms (Table 3.3). Peak pressures, peak impulses and net impulses associated with the experimental and numerical results are summarised in Figure 3.15, along with semi-empirical predictions for reference. As the second shock arrives during the negative phase, it acts to reduce the negative impulse and increase the net impulse acting on the target. Because the semi-empirical method has no means to account for the second shock, these predictions for net impulse appear to offer a lower bound estimate.
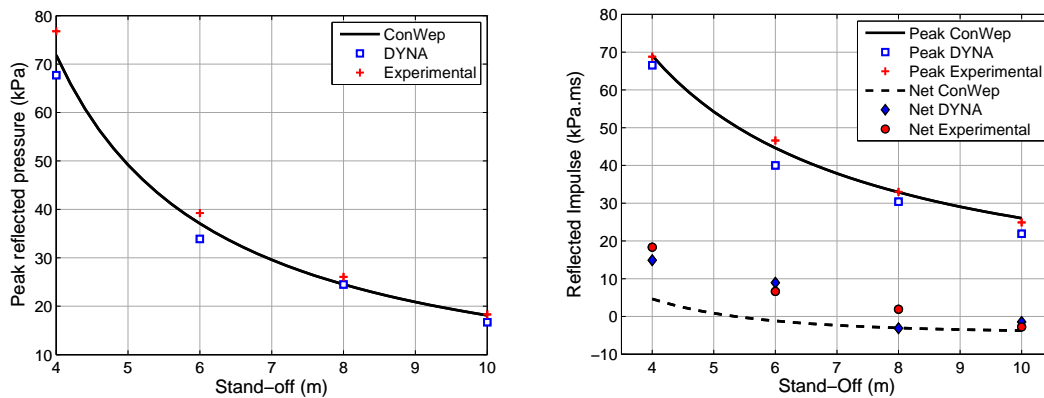
Figure 3.15: Peak pressure, peak impulse and net impulse for the experimental results and numerical simulations compared to semi-empirical predictions

3.4.1   A Brief Note on TNT Equivalence

So far, a TNT equivalence of 1.2 has been used for C4. Ackland et al. (2012) questioned the use of a single equivalence factor and suggested a factor that varies with scaled distance. The energy equivalence is an intrinsic function of the chemical composition of the explosive, and therefore the notion of a factor that varies with distance from the explosion has no physical basis.

The reflected pressure simulations were repeated with 300 g of TNT (44.5 mm radius), assuming a TNT equivalence of 1.2 for C4/PE4. It can be seen from Figure 3.16 that there is no discernible difference between the positive phases of the two pressure readings – the only difference comes with the arrival of the second shock which, as discussed previously, makes little quantitative difference to the blast pressure load. Similar results were obtained for 6, 8 and 10 m but are not shown for brevity. It can be concluded that, for the range of scaled distances of interest, a *single* equivalence value of 1.2 for C4 is applicable when using semi-empirical TNT predictions.
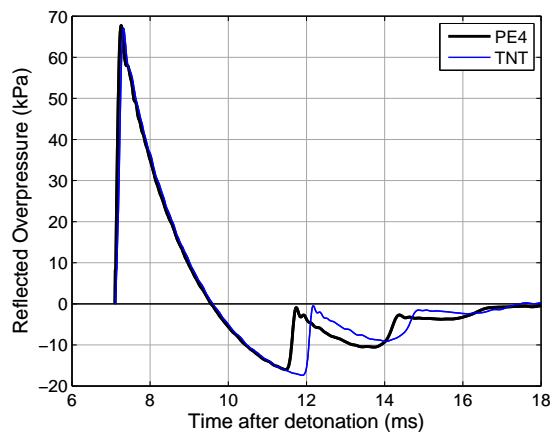
Figure 3.16: Numerical reflected pressure-time histories for a 250 g hemispherical C4/PE4 charge and 300 g hemispherical TNT charge at 4 m stand-off (assuming a TNT equivalence of 1.2)

3.4.2   Expansion Waves From the Domain Edges

The *boundary_non_reflecting keyword purports to allow for infinite domains to be represented in the numerical model. From the numerical analyses conducted thus far, however, it appears that this method is inadequate at preventing expansion waves from propagating in from the edges of the domain.

As the pressure wave reaches the non-reflecting boundary, there is an imbalance between the incident pressure wave *within* the domain and the ambient pressure applied to the *edge* of the domain. This imbalance, in the same mechanism as blast wave clearing, is equalised with the initialisation of an expansion wave as the higher pressure incident air flows out of the domain. The reference pressure is constant along the entire edge of the domain, hence there is no means for the pressure to truly equalise, and a large amount of
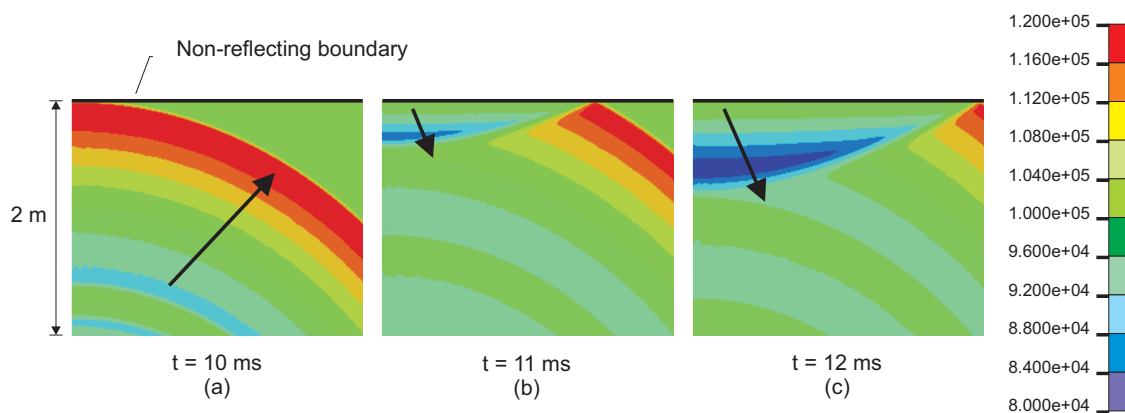
Figure 3.17: Contours of pressure (units in Pa) from numerical analysis. (a) Incident blast wave reaching the boundary and (b) and (c) propagation of the expansion wave into the air domain

material is lost from the domain. This behaviour can be seen in Figure 3.17, which shows the top corner of the domain used in the 4 m analysis. It can be seen that the expansion wave has travelled ∼0.7 m in 2 ms, indicating a wavespeed of 340 m/s.

Once this expansion wave reaches the area of interest, it can contaminate the results. Therefore, when modelling an infinite domain, it is recommended that the boundary is placed far enough from the area of interest such that no expansion waves arrive throughout the duration of the analysis (Schwer 2010).

3.5 Reflected Pressure on a Finite Surface

The experimental results from Tyas et al. (2011a,b), introduced in Section 2.3.4, are used in this section to validate the ability of LS-DYNA to simulate the pressure acting on a finite target subjected to a cleared blast load. A rigid finite target, with dimensions shown in Figure 3.18, was subjected to 250 g C4 charges again at 4, 6, 8 and 10 m, with the presence of target edges able to influence the late-time pressure development on the face of the target. In this test series, two experiments were conducted at each stand-off.
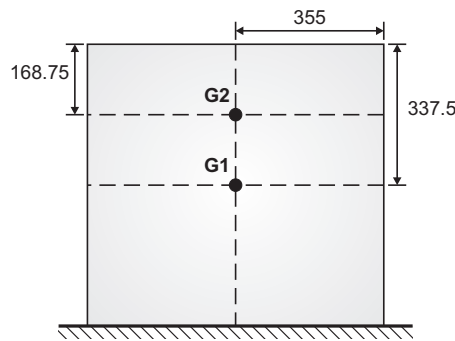
Figure 3.18: Gauge locations in the finite target (dimensions in mm)

The mapping files written from the analyses in Section 3.4 were re-mapped onto a 3D domain of solid ALE elements to simulate the interaction between a propagating blast wave and a finite sized target, namely to simulate the effect of blast wave clearing around the target edges. When re-mapping from 2D to 3D, it is important to be aware of two conflicting issues:

- **Domain Size** – in order to fully capture the pressure-time history from the 2D analysis, the 3D mesh must be large enough to contain a sufficient 'length' of the blast wave (Aquelet & Souli 2008). For the 10 m simulation, the positive phase duration is ∼3.6 ms. Assuming a wave speed of 340 m/s gives a positive phase wavelength of 1.2 m, i.e. the ALE domain must be at least this length in front of the target to capture the whole of the positive phase. If the entire negative phase is to be re-mapped, domain lengths of ∼5 m are required. It is also important to have the domain large enough to ensure that expansion waves from the edge of the domain

do not reach the monitoring points during the analysis and contaminate results (see Section 3.4.2 and Schwer (2010)).

- **Element Size** – As shown in the preliminary mesh study, ALE analyses are sensitive to element size, particularly when considering the resolution of the shock front. The elements in the ALE domain should therefore be as small as possible.

A compromise is required in order to generate models of reasonable size and analysis time. Also, it is often not possible to achieve similar mesh densities between 2D and 3D analyses owing to the increased number of elements in the additional plane and hence increased memory requirements of 3D models. In this validation, it was important to validate the mechanism of clearing and the reduction of positive phase pressure, so a domain length of 1 m was chosen for the air in front, above, and adjacent to the extreme edges of the target to permit analysis durations of ∼3 ms. A domain length of 0.5 m was modelled behind the target to give a 1 m distance from the edge of the target to the boundary and back, again ensuring no expansion waves would arrive before ∼3 ms.

The domain was discretised using elements of side length ∼17.5 mm, with an aspect ratio of 1, giving 578,816 elements in total. As with the 2D case, the rigid target was modelled with nodal constraints rather than fluid-structure interaction. Half-symmetry was used, with appropriate boundary conditions along the vertical boundary. The rigid ground was again modelled with vertical translational constraints as nodal boundary conditions.

Figures 3.19–3.22 show the numerical and experimental pressure time histories for both gauge locations. The smoothing of the shock front can be seen for all cases, which is the result of mapping from a fine mesh to a coarser mesh, as can be justified by the fact that such smoothing was not observed in the 2D analyses conducted in Section 3.4 (where the mapping was performed between meshes of similar densities). Nevertheless, the agreement between numerical and experimental results is very good, and the numerical model is able to capture the physics of blast wave clearing to a sufficient level of accuracy.
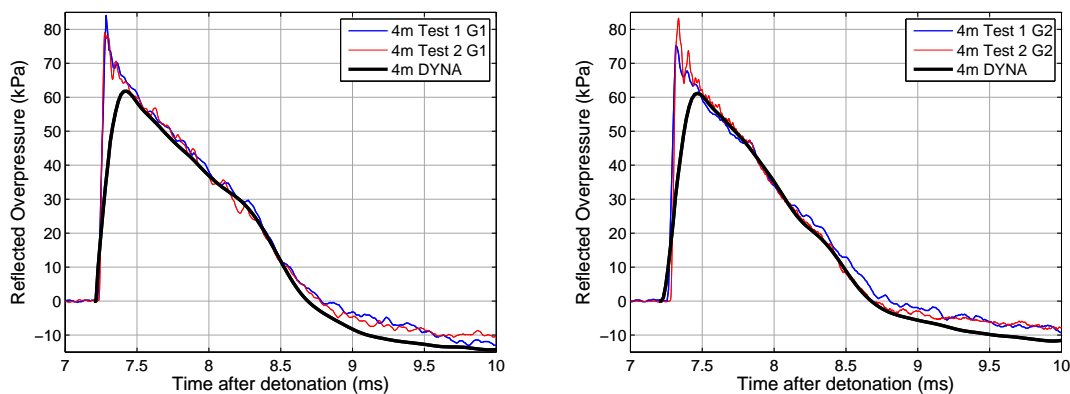
Figure 3.19: Experimental and numerical pressure-time histories for two gauge locations on a finite target located 4 m away from a 250 g hemispherical PE4 charge. Gauge locations and target dimensions are shown in Figure 3.18
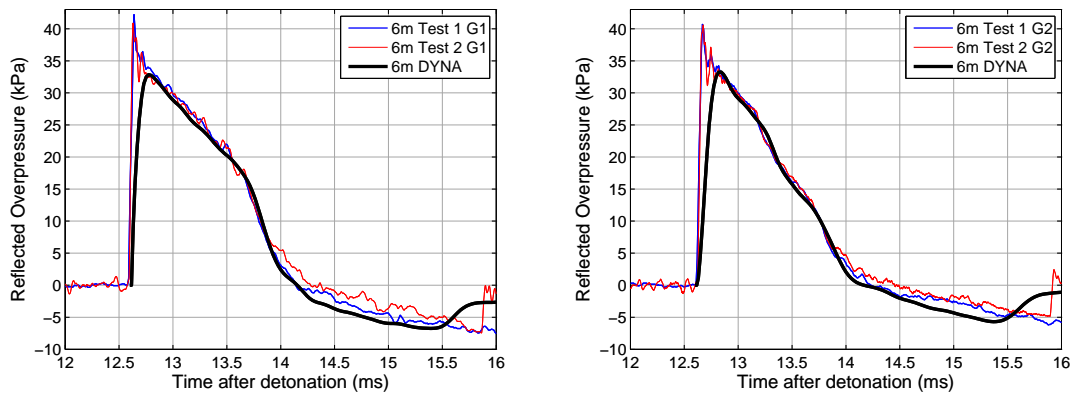
Figure 3.20: Experimental and numerical pressure-time histories for two gauge locations on a finite target located 6 m away from a 250 g hemispherical PE4 charge
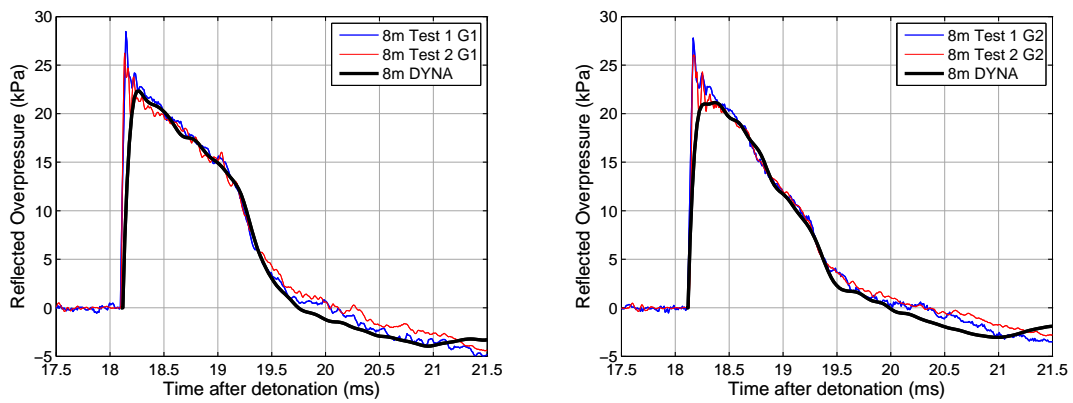
Figure 3.21: Experimental and numerical pressure-time histories for two gauge locations on a finite target located 8 m away from a 250 g hemispherical PE4 charge
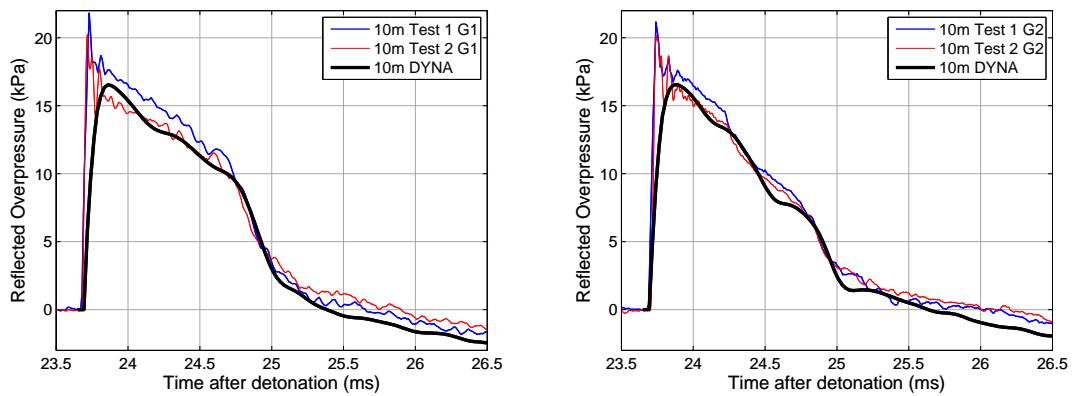
Figure 3.22: Experimental and numerical pressure-time histories for two gauge locations on a finite target located 10 m away from a 250 g hemispherical PE4 charge

The mechanism for blast wave clearing can be considered as a shock wave in reverse; it begins as a sharp pressure discontinuity between reflected and incident pressure at the target edge and becomes more rounded as the wave travels along the target face because the higher pressures at the head of the wave travel quicker than the trailing lower pressures. By the time the clearing wave reaches the gauge locations, the relief pressures are smooth enough to be represented by the coarse mesh; it is likely that further mesh refinement would yield a sharper initial rise to peak pressure but have little effect on the clearing pressures thereafter.

Table 3.4 shows the peak impulse at each gauge location for the experiments and numerical simulations. The experimental values are taken as the average between the two tests. Overall, the numerical impulse is within 12.5% of the experimental results, with a general trend towards increasing difference with increasing stand-off, which is likely due to the numerical dispersion seen in the 2D cases. Table 3.4 is also summarised in Figure 3.23, which shows full ConWep reflected pressures as an indication of the level of impulse reduction attributed to blast wave clearing.

Stand-off (m)	Peak Reflected Impulse (kPa.ms)					
	Gauge 1			Gauge 2		
	Exp[*]	DYNA	Ratio	Exp[*]	DYNA	Ratio
4	56.5	52.0	0.92	50.8	46.9	0.92
6	32.6	30.2	0.93	29.3	27.3	0.93
8	22.8	20.9	0.92	20.9	19.2	0.92
10	17.4	15.2	0.87	16.2	14.2	0.88

[*] averaged result

Table 3.4: Peak reflected impulse comparison for numerical and experimental trials in both gauge locations
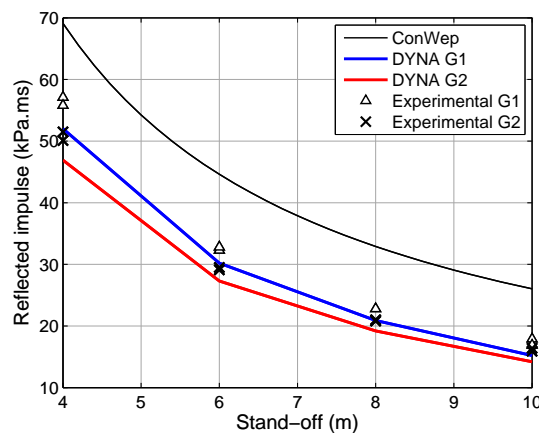
Figure 3.23: Numerical and experimental peak impulse at both gauge locations for all stand-offs

3.6   Summary

LS-DYNA has been used to simulate high explosive detonations for incident and reflected blast wave parameters, in both near and far field applications.

In the initial mesh study, a mesh with elements radiating out from the centre of the charge was compared with a grid mesh with regular element size throughout. The explosive in the radial mesh was modelled explicitly and in the grid mesh it was represented using the *INITIAL_VOLUME_FRACTION keyword. It was found that blast wave propagation was better simulated with the radial mesh because the elements are generally orientated to the direction of travel of the pressure wave, which reduces the second order advection errors and results in less numerical dispersion (see Figure 3.5). Representation of the explosive as an explicit part is also favourable as construction of the interface between explosive and air is not mesh sensitive as it is with the grid mesh. For the blast wave propagation through free air, peak pressure values were approaching ConWep values, however incident impulses were slightly lower.

The *INITIAL_ALE_MAPPING ability in LS-DYNA allowed the radial mesh to be re-mapped onto a Cartesian grid when interaction with a structure was required. Experimental pressure-time histories were used to validate LS-DYNA results for airblast loading on a semi-infinite target and it was found that peak pressures and peak impulses were in very good agreement between experimental, numerical and semi-empirical values (typically within 10-15%). Net impulse was also in acceptable agreement, however the form of the negative phase and arrival of the second shock was slightly different between experiments and numerical simulations.

Blast loading on a finite target was also evaluated, with the experiments detailed in Tyas et al. (2011a,b) being replicated in LS-DYNA. Despite smoothing of the shock front due to re-mapping from a fine mesh to a coarser mesh, the experimental and numerical results were in good agreement, with a difference in peak impulse of no more than 14%. In order to better capture the shock front, the mesh could be refined locally around the target using the ALE_REFINE keyword, however Alia & Souli (2006) recommend keeping element size as uniform as possible because mixing of small and large elements tends to decrease simulation accuracy.

It can be concluded that LS-DYNA is suitable for simulating high explosive detonations and subsequent blast wave propagation, as well as being able to accurately model phenomena such as shock wave reflection and blast wave clearing.

Chapter 4

A Study of Diffraction Loading and Clearing for Small Targets

4.1 Introduction

The loading experienced by a point on a finite target remote from a free edge can be characterised by three distinct phases:

1. The full reflected pressure will be experienced until the clearing wave arrives.

2. The blast pressure will be relieved as the expansion waves reach and propagate over the point of interest in what is termed the diffraction phase

3. The drag phase occurs, where the diffraction process has ceased, the pressures have equalised across the front face of the target, and the target is subjected to quasi-steady drag loading (Ethridge 1977).

As introduced in Section 2.3.2, the current understanding of blast wave clearing suggests that the diffraction phase consists of a series of expansion waves travelling back and forth across the target face. Once an expansion wave reaches the opposite edge of the target, it will diffract around that target edge, sending a lower magnitude wave inwards along the target face in the opposite direction. As noted by Hudson (1955, page 26) *'we should expect oscillations of rather large amplitude... these oscillations are caused by the movement of the rarefaction and compression waves around the target'*.

This behaviour is perhaps best illustrated in a shock front distance-time diagram, as per Figure 4.1, which shows a schematic of the clearing wave oscillations across the front of a finite-sized target. The main plot of Figure 4.1 shows the location of the shock front along the vertical front face of the target, and the sub plots show shock front progression at the times t_i, t_{ii} and t_{iii} as indicated in the main figure. It can be seen that once the initial diffraction wave reaches the base of the target (between t_i and t_{ii}) it is reflected

61

upwards. Once this wave reaches the top edge of the target, it too initiates a diffraction wave (between t_{ii} and t_{iii}) which itself travels along the front of the target, reflects off the base and diffracts again upon reaching the vertical extent of the target. This process is repeated in an infinite series, each wave having decreasing magnitude. Given a large enough number of expansion wave crossings, the blast pressure will oscillate about, and eventually approach, the stagnation pressure as a limit.
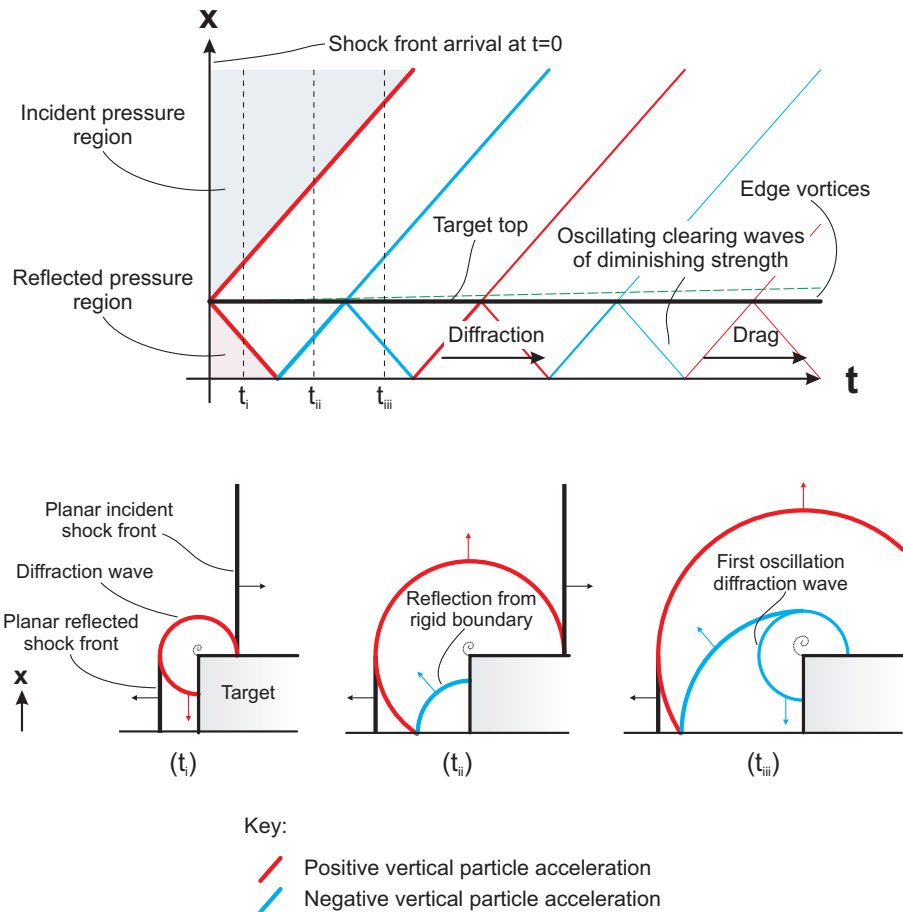
Figure 4.1: Schematic shock front distance-time diagram for a series of clearing waves travelling across the target face. Subplots show shock front progression at the times indicated

Figure 4.1 uses the following sign convention: positive vertical particle accelerations are coloured red, whilst negative (downward) vertical particle accelerations are shown in blue. At this stage, it is important to distinguish between *particle* motion and *wave* motion: in the main plot, which shows the shock front location, the colour indicates the particle motion whereas the gradient of the line indicates the wave velocity. It can be seen in Figure 4.1(t_{ii}) that the reflected diffraction wave is accelerating the particles downwards whilst the wave front is propagating upwards.[i] Expansion waves occur when the particle acceleration is in the opposite direction to the wave propagation, and compression waves occur when the respective motions are in the same direction.

---

[i]In the subplots of Figure 4.1, arrows on the shock fronts indicate direction of wave propagation

Clearly, for small targets, the time taken for a clearing wave to traverse the target face will be very small in relation to the positive phase duration. The oscillations, therefore, should dissipate quickly enough such that their form can effectively be ignored (or may not even be captured in the experimental set up), and only the average behaviour taken into account. The early nuclear bomb trials involved an arrangement of small targets and large blast waves (Murtha 1955, Morris 1959, Norris et al. 1959), hence the pressure would have equalised so quickly so that the actual mechanism of *how* it equalised could effectively be ignored on account of it being less important than the global effect of pressure equalisation.

The validation work undertaken in the previous chapter, and the experimental work of Rickman & Murrell (2007) and Tyas et al. (2011a,b), has been concerned with larger targets and smaller blast waves (arising from high explosives rather than large nuclear weapons). In these trials, the duration of the diffraction phase was similar to or often greater than the positive phase, and typically only one clearing wave crossing was seen. It has been shown for these arrangements that the Hudson method can accurately model the clearing effect.

There remains a gap in the knowledge in terms of the form of the blast pressure load for targets whose dimensions are small enough such that the diffraction phase is resolved during the load application, yet large enough such that this behaviour constitutes a greater portion of the total loading duration. In his discussion of drag loading for small targets, Hudson (1955, page 10) observed that *'as an approximation, we may write from our experience that the pulse associated with a wave having traveled* (sic) *more than the length of the originating edge is negligible'*, i.e. only one traverse of the expansion wave was seen to affect the recorded blast pressure. This suggests that blast wave clearing is not properly understood for smaller target dimensions and that the series of expansion wave interactions may be a misinterpretation of diffraction loading on small targets.

It is known that the reflected pressure is approached as a limit as the target size tends to infinity, and that the incident pressure is approached as the target size tends towards zero.[ii] The transition to the upper limit can easily be explained by the fact that the distance that the clearing wave can travel along the target decreases relative to the target size as the dimensions of the target increase, i.e. the effect of clearing diminishes as the target size increases. No proper explanation exists as to how the blast load reaches the incident pressure in terms of the known mechanism of clearing.

This chapter focusses on using numerical analysis to study blast wave clearing and diffraction loading of smaller targets in an attempt to better understand how the cleared pressure approaches the incident pressure as the target reaches infinitesimal size. This chapter will also serve to offer guidance, based on physical principles, of the regions where blast wave clearing can be neglected, purely on the basis of the form of the load. Regions where blast wave clearing can be neglected based on its influence on finite-target dynamic response is analysed and discussed in the following chapters.

[ii]See Table 2.3 in Section 2.3.2

4.2   Numerical Study

4.2.1   Preliminary Modelling Considerations

Modelling the blast events explicitly using finite elements has several advantages over attempting to develop an analytical solution, namely:

- The assumptions required to develop analytical solutions often render the method suitable only for very few applications. For example, in the analytical study of Hunter & Keller (1984) on the diffraction of blast waves normal to the direction of travel, a solution is derived for a weak shock wave with constant conditions behind the shock front. This has several limitations: firstly, the solution is only true for one passing of the diffracted wave, i.e. once the wave reaches the opposite edge of the target, or interacts with the wave travelling in from the opposite edge, the method is no longer valid; secondly, the solutions cannot be applied to a strong shock or a shock wave with temporally varying pressure behind the shock front.

- Modelling the explosive and subsequent blast wave propagation allows for a *realistic* blast load to be represented in the model. Analysing the propagation of this blast wave over a target will give results that are *directly* applicable to guidance on blast resistant design, as they directly relate to real life situations. If a scenario is modelled using finite elements, and the model is well validated, then the results can be directly translated to our understanding of real-life blast events. Cube-root scaling of blast events widens the range of which the results may apply. Furthermore, the model can be used to study clearing behaviour for blast waves of varying strength and temporal decay.

Justification for 2D Analysis

For structures whose size is effectively infinite in one dimension only (the 2D case, as introduced in Section 2.3.2), blast wave clearing will occur only perpendicular to this dimension. For targets with two finite dimensions, it has been shown that the clearing effect can be separated into two principal dimensions (Tyas et al. 2011a). Therefore, it is only relevant to consider the clearing effect in one dimension in order to investigate the form of the blast load for small targets and target sizes approaching zero.[iii]

As shown in the mesh sensitivity analysis of the previous chapter, ALE analyses are particularly sensitive to mesh size and element orientation with respect to the direction of travel of the blast wave. The relatively little computational expense of 2D analyses facilitates the use of a fine mesh and can give results that can more accurately capture the

---

[iii]As demonstrated by Hudson (1955), the size of the target in the direction of travel of the blast wave has negligible effect on the blast load on the front face of the target, and is therefore assumed to be infinite to facilitate the use of the Hudson predictive method.

behaviour seen in real life. Accordingly, the numerical analyses discussed in this chapter were performed on 2D axi-symmetric finite element models with a radially symmetric mesh, which were re-mapped onto a rectangular grid immediately prior to reflection of the blast wave. The target was, again, assumed to be rigid and modelled using nodal point constraints.

Relevant Parameters

There are a number of parameters which influence the level of clearing relief a target will experience. These include pressure, impulse, decay of the blast pressure, stand-off, and target dimensions and shape. In order to facilitate a more focussed numerical study, this section details how the problem of clearing on small targets can be reduced to two main parameters.

Firstly, if the mass of explosive is set at 1 kg, scaling durations and impulses becomes trivial because the *scaled* and *actual* time scales are identical (see Section 2.2.3). Varying the stand-off distance, therefore, allows parameters such as pressure, impulse and temporal decay of the blast wave to be altered. Secondly, the level of blast wave clearing is directly related to the size of the target. For a given scaled distance, there exist many combinations of charge mass and target height that will give the same value of Hudson's dimensionless length scale, η (repeated as Equation 4.1 below for clarity).

$$\eta = \frac{x}{a_0 t_d}. \tag{4.1}$$

Cube root scaling ensures that the length (x) and time (t_d) parameters are always scaled by the same factor, K – as in the example shown in Figure 4.2 for two similar arrangements whose charge mass differs by the factor K^3 – and hence the Hudson clearing length in Equation 4.1 is independent of scaling parameters. For the two arrangements shown in Figure 4.2, therefore, both targets will give the same value of η at any similar point on the target and hence will experience identical time-scaled loads.

By varying the scaled target height, H, or specifically the ratio of the scaled distance to the scaled target height, Z/H, the effect of clearing on different target sizes can be studied, knowing that the results apply for any situation that has the same ratio at that particular scaled distance. The problem has now been condensed into two parameters, Z and Z/H.

4.2.2 Weak Shock Study

The problem was first considered for weak shock conditions, where the blast and diffraction waves can be considered as acoustic rather than shock waves. The situation shown in Figure 4.3 was modelled, with a 1 kg charge detonated 8 m away from rigid, finite-sized targets. Scaled target sizes of $H = Z/8$, $Z/16$, $Z/32$, $Z/64$, $Z/128$ and $Z/256$ and $Z/512$,
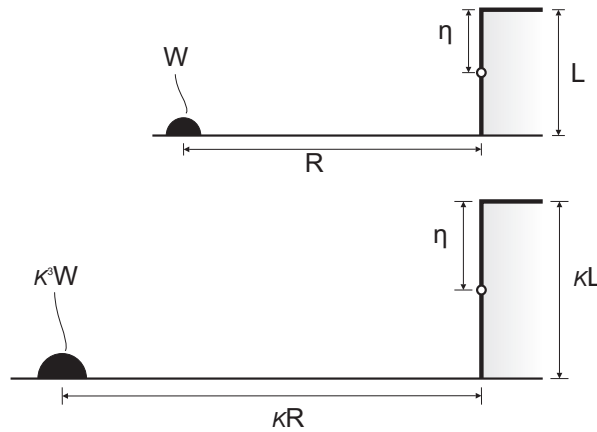
Figure 4.2: Scaled target dimensions giving the same value of η at the mid-point of the target

corresponding to actual heights of 1000 mm to 15.625 mm, were analysed to study the mechanism of blast wave clearing for smaller targets and to indicate the transition between diffraction and drag-type loading.
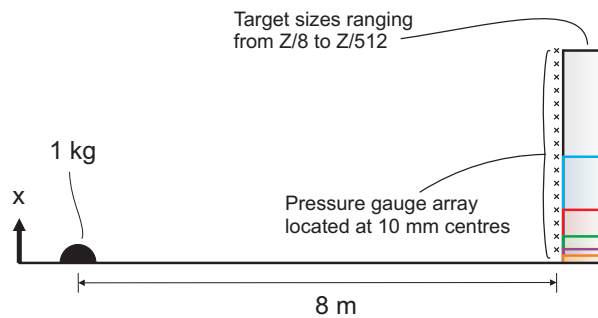
Figure 4.3: Arrangement of the FE models considered in the numerical study for weak shock conditions

The model was also run with free-field conditions and with an infinite sized target so that the cleared readings could be compared against the incident and fully reflected cases. The *DATABASE_TRACER keyword was used to save fixed point values (TRACK=1) at 10 mm spacing from $x = 0$ (ground level) up to $x = 1$ m for all analyses.

Pressure-Time History

Figure 4.4 shows numerical pressure-time histories at the base of the targets ($x = 0$), as well as numerical reflected and incident pressures for reference. Results for $Z/H = 512$ are not shown here but will be discussed in later sections. For a 1 kg hemispherical surface burst at 8 m stand-off, ConWep gives semi-empirical peak reflected and incident pressures and positive phase duration as 44.11 kPa, 20.34 kPa and 4.454 ms respectively, which are in good agreement with the numerical values.

(a) Z/H = 8

(b) Z/H = 16

(c) Z/H = 32

(d) Z/H = 64

(e) Z/H = 128

(f) Z/H = 256
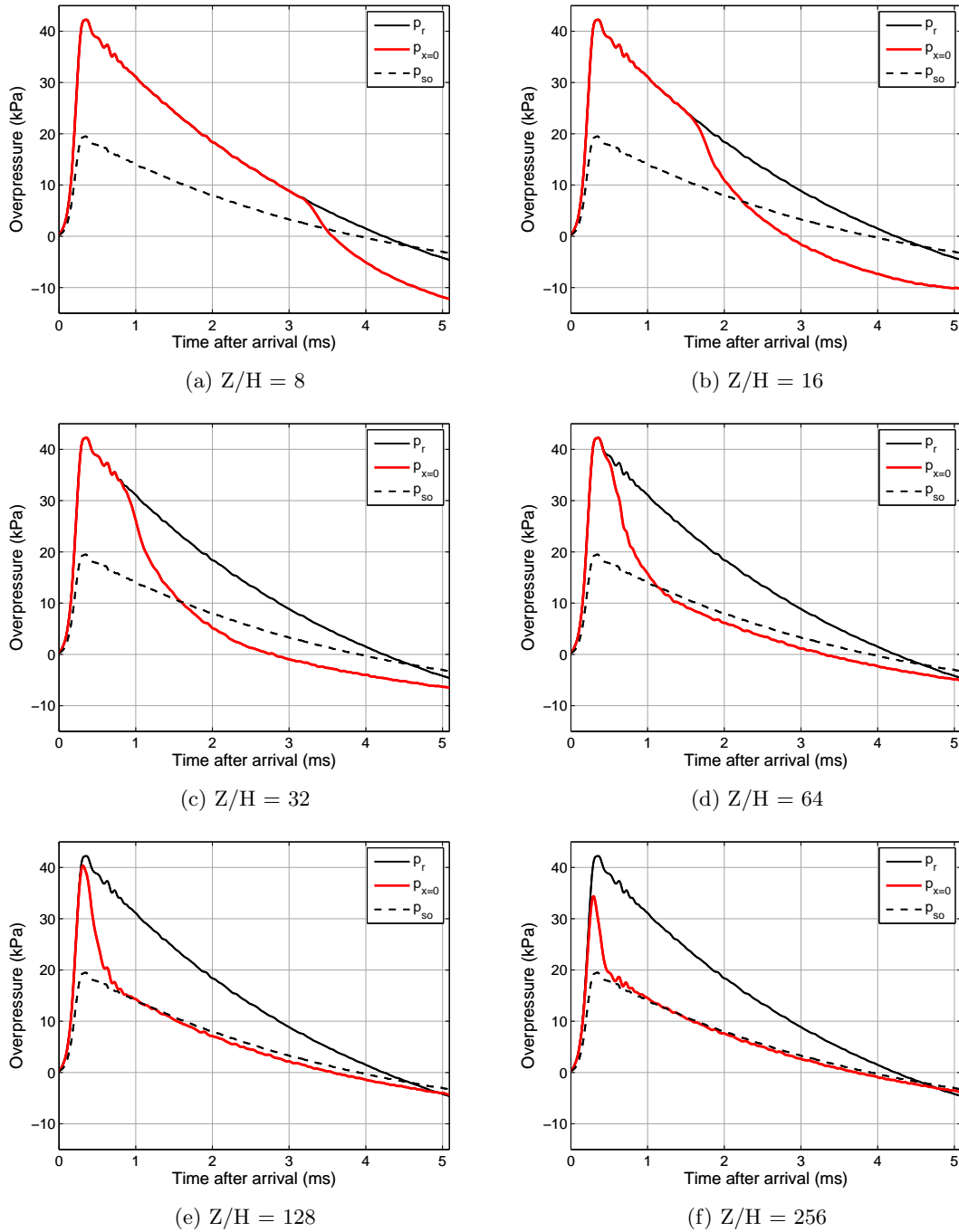
Figure 4.4: Pressure-time histories at the base of the finite targets ($x = 0$)

The effect of blast wave clearing is apparent from the pressure-time traces, which exhibit a sharp drop off in pressure following the arrival of the rarefaction relief wave. What is apparent, despite what the current theory suggests, is that there appears to be no trace of any subsequent oscillations of the cleared pressure caused by additional diffraction waves. Take Figure 4.4(c) as an example. With a target height of 250 mm, the arrival time of the clearing wave (assuming a shock front velocity of 340 m/s) to reach the gauge location from the top of the target is 0.74 ms after arrival of the blast wave. As stated before, this is clearly seen in the numerical model. Assuming the shock front velocity remains unchanged, one would expect to see a positive oscillation (pressure increase) at 2.21 ms, and a subsequent negative oscillation (pressure decrease) at 3.68 ms after the arrival of the blast wave.[iv] It is acknowledged that the clearing wave should be expected to lose energy as it propagates, and that the diffracted signal will be lower in magnitude than the original wave, however some oscillations should still be expected to be seen *based on the current theory*, particularly for the smaller targets where the energy losses from propagating the small distances across the target face will be negligible. This absence of subsequent oscillations after the primary pulse, despite being in disagreement with the accepted theory on blast wave clearing, is in agreement with the experimental observations of Hudson (1955).

Figure 4.5 shows pressure-time fringe plots for the gauges aligned vertically along the front face of the target (see the model arrangement in Figure 4.3), with the target height indicated by the solid horizontal line. The pressure is shown as cleared pressure minus incident pressure to allow the form of the clearing waves to be isolated.

When the blast wave reaches the top edge of the target, an expansion wave can be seen to travel along the target away from the edge (down), whilst a compression wave can be seen to travel through the air immediately above the target (up), both waves orthogonal to the direction of travel of the blast wave itself. Following reflection from the rigid boundary, the expansion wave changes direction and propagates back along the face towards the target edge, and beyond into the free air. Following the passing of this expansion wave, the pressure acting on the target face falls below, and remains below the incident pressure. It can be seen for all cases that the pressure acting on the entire target face falls below the incident pressure once the reflected expansion wave has passed across the point of interest.

The air remains over-expanded for the remainder of the loading duration, rather than experiencing oscillations. This suggests that the blast pressure does not approach the stagnation pressure but instead reaches and maintains a pressure somewhat below this value. It appears as though the over-expansion of the air is a function of target size, and that the larger the target, the more the clearing wave causes the air in front of the target to over-expand. This is divergent from the current theory and deserves further consideration.

[iv]These times correspond to odd multiples of the transition time of the clearing wave, i.e. the time taken to travel from the top of the target to the bottom for the first wave, this time plus the time taken to travel from the bottom of the target to the top and back again for the first positive oscillation, etc.
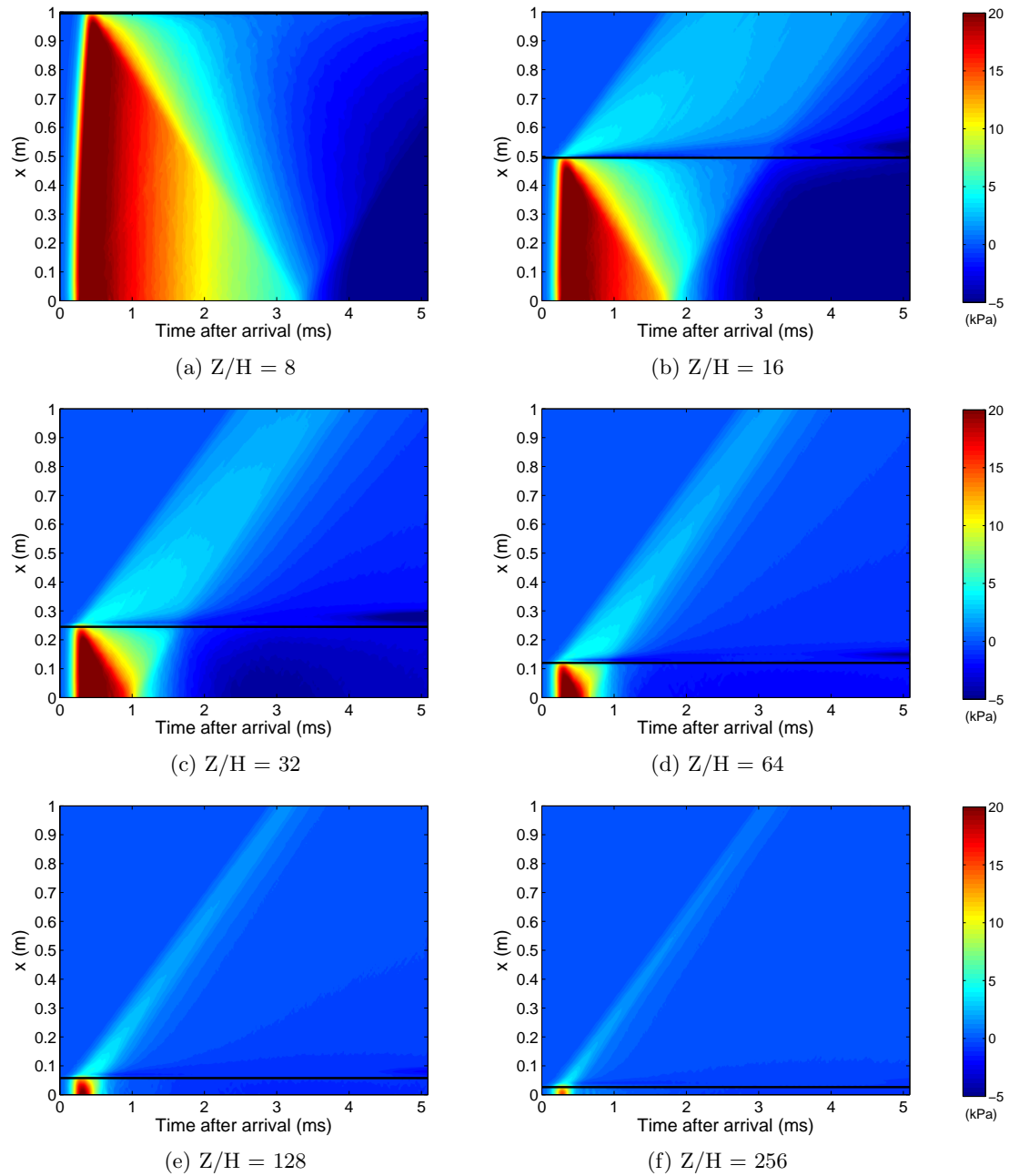
Figure 4.5: Fringe plots of cleared pressure minus incident pressure versus time for gauge locations aligned vertically along the front face of the target (arrangement shown in Figure 4.3). Target top edge (x-location) is indicated by the solid horizontal line

Particle Acceleration-Time History

The Rankine-Hugoniot 'jump' conditions for conservation of momentum either side of
a moving shock front state that the increase in pressure is equal to the product of the
ambient density, shock velocity and particle velocity (Anderson 2001). The change in
air density can be considered negligible compared to the changes in pressure and particle
velocity, hence it can be said with justification that the pressure of the moving shock is
effectively proportional to the particle velocity. Differentiating this relation with respect
to time indicates that the rate of change of pressure is effectively proportional to the
particle acceleration. Acceleration-time plots, therefore, are analogous to the slope of the
pressure-time plots and can be used to construct the shock front distance-time diagrams
as per Figure 4.1.

Figure 4.6 shows numerical vertical particle acceleration-time fringe plots for the finite-
sized targets, again for the gauges located vertically along the target face and again with
the free field values subtracted for better presentation of the effects of clearing. The
gradient of any shock front is dependent on the size of the mesh as much as it is on the
physics of the problem, hence the magnitude of the acceleration should be considered less
important than the actual sign, or direction, of acceleration. This figure follows the sign
convention introduced earlier in the chapter, with red being vertical accelerations and blue
being vertical decelerations.

The shock front emanating from the top edge of the target can be seen very clearly, as
can the reflection (and sign reversal) off the rigid boundary. Again there appears to be
no diffraction wave oscillation after the initial clearing wave has passed the edge of the
target.

Accelerations caused by numerical oscillations following the reflected shock front can be
seen emanating from the bottom-centre of the target at $t = 0$. This is a non-physical
feature which is present in all of the numerical results and should not be interpreted as
physical behaviour of the reflected or clearing shock fronts. The region of vortices can be
seen at the top edge of the target.

4.2.3 The Mechanism of Clearing for Weak Shock Conditions

Based on evidence from the numerical analyses, the mechanism of blast wave clearing for
smaller targets can be interpreted as follows:

- At the moment a shock wave reaches the edge of a finite target, the wave diffracts
  around the edge of the reflecting surface, causing a clearing wave to travel inwards
  along the target face. The wave travels *away* from the target edge but accelerates
  the particles *towards* the edge, hence acting as an expansion wave and reducing the
  pressure acting on the target.

(a) Z/H = 8

(b) Z/H = 16

(c) Z/H = 32

(d) Z/H = 64

(e) Z/H = 128

(f) Z/H = 256
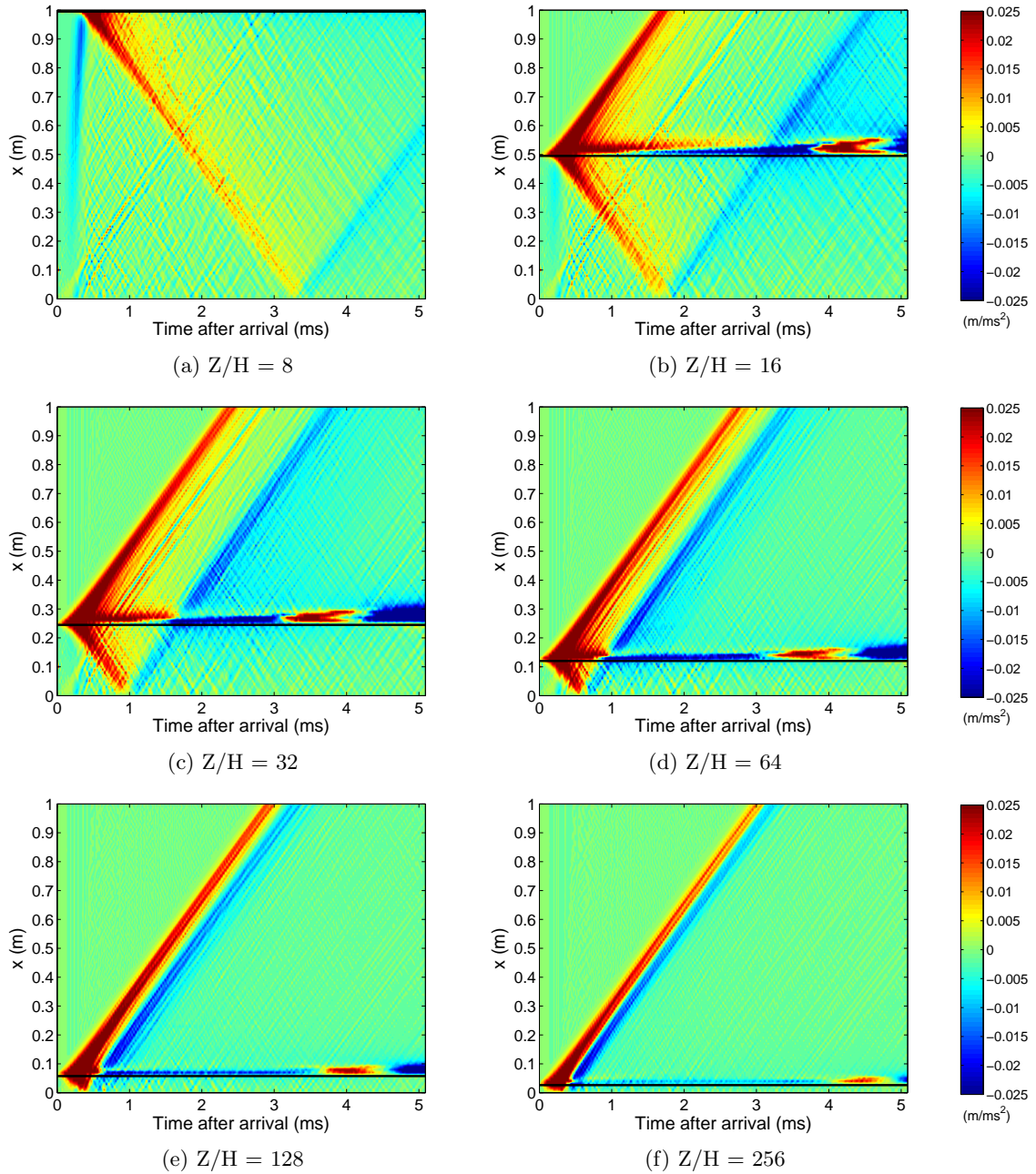
Figure 4.6: Fringe plots of cleared particle acceleration minus incident particle acceleration versus time for gauge locations aligned vertically along the front face of the target (arrangement shown in Figure 4.3). Target top edge (x-location) is indicated by the solid horizontal line

- If the target is situated on a rigid ground surface, the wave then reflects off the surface and propagates back towards the origin of the clearing wave, i.e. the top edge of the target.[v] Reflection causes both the shock front velocity and the particle acceleration to reverse.

- This reflected clearing wave continues to propagate beyond the target into the free air above, decreasing in magnitude as it expands both vertically and horizontally. No diffraction waves are sent back along the target.

- A region of over-expanded air is present in front of the target, which expands outwards. The air behind this expanding shock front is in local equilibrium.

A target of zero height will be subjected to the incident pressure, however a target of *any finite height* will be subjected to the mechanism described above. There is no physical way for the blast loading to simply switch from one mechanism to the other, therefore it must be explained how this transition occurs. This, and the fact that no subsequent diffraction waves are initialised once the reflected clearing wave reaches the target edge, can be explained using the following conceptual model, shown in Figure 4.7.
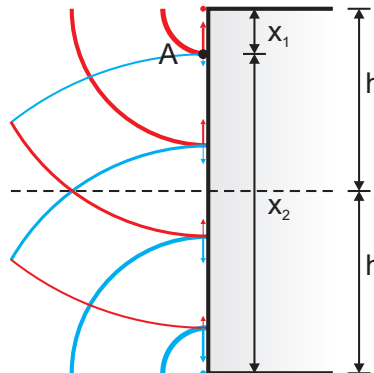
Figure 4.7: Conceptual model of clearing for small targets. Arrows show direction of particle movement rather than wave propagation

Considering the top edge of the target of height h to be the point source of a clearing pressure pulse; the reflected clearing wave can be represented as the mirror of this primary pulse, originating from a point source located at the exact same distance from, and on the opposite side of, the rigid reflecting surface. In this way, the interaction of the two waves is physically and conceptually identical to blast wave clearing arising from free air bursts acting on a target of height $2h$. Figure 4.7 shows the temporal progression of the primary (red) and secondary (blue) pressure pulses.

Now consider a point A, located at some distance, x_1, from the origin of the primary clearing wave. The pressure reduction, or more specifically the vertical velocity imparted

[v]If the target is subjected to a free air burst and is located some distance from the ground, the problem can be expressed as a hemispherical surface burst with a rigid ground surface by introducing a symmetry plane along the centre of the target in the direction of travel of the blast wave

to the air at that point, will be proportional to the distance that the primary clearing wave has travelled, x_1. As the pressure pulse expands outwards, the magnitude of clearing relief rapidly decreases, such that when the secondary (reflected) clearing wave arrives, the 'corrective' velocity applied to that point (acting in the opposite direction to the primary pulse) will *always* be less than the velocity imparted by the primary wave. The air at point A will therefore have a residual velocity acting towards the source of the primary clearing wave.

At the limit as h tends towards zero, x_1 tends towards x_2. For a theoretical target of zero height, the velocity imparted to point A from the secondary clearing wave will be exactly equal in magnitude and in the opposite direction of the velocity imparted by the primary wave, and, importantly, will occur at *exactly the same time*. As the distance from the free edge is zero across the whole target, the time taken for the clearing wave to arrive at any point will also be zero, hence the target will clear from the reflected pressure to the incident pressure *immediately* upon arrival of the blast wave. Clearly, this situation is only theoretical and for any real-sized target the reflected pressure and clearing duration will act out over a finite, non-zero time, however the explanation adequately describes how the mechanism of blast wave clearing resolves for target sizes approaching zero.

As the target size increases, the *actual* difference between x_1 and x_2 increases. The decrease in strength of the clearing wave is not linear with an increase in distance (Hudson 1955). Hence, as the target gets larger, the difference in net velocity imparted to any point on the target increases, as does the duration that this velocity acts before being reduced by the secondary clearing wave. The air immediately in front of the target is over-expanded by the clearing waves imparting a net residual velocity towards the target edge. With increasing target sizes this net velocity is greater – the larger the target, the more the air is over-expanded. This explains the 'overshoot' pressure seen in experimental (Smith et al. 1999, Rose et al. 2006, Rickman & Murrell 2007, Tyas et al. 2011a,b) and numerical results (Rose & Smith (2000), Ballantyne et al. (2010) and Figures 4.4 and 4.5).

A revised shock-front distance-time diagram is shown in Figure 4.8. As the target size approaches zero, the primary and secondary clearing waves tend towards perfect destructive interference. This results in the over-expanded region, and hence the pressure imparted to the target, tending towards the incident pressure.
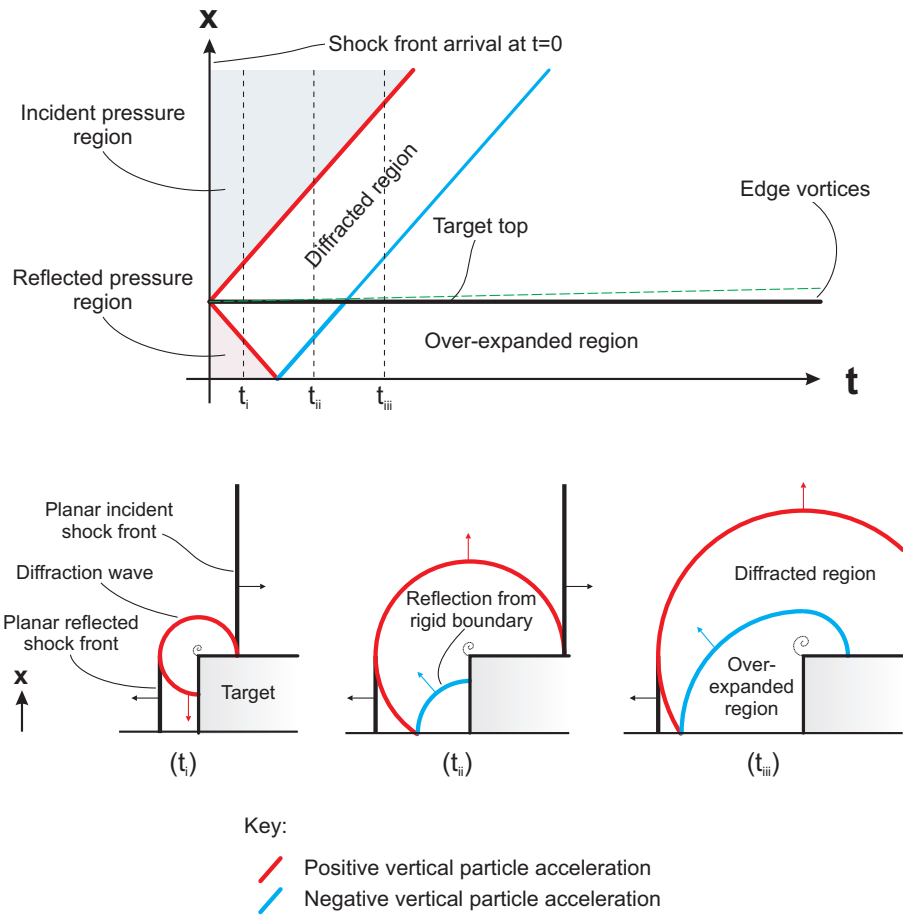
Figure 4.8: Schematic shock front distance-time diagram for a primary and secondary (reflected) clearing wave travelling across the target face and over-expanding the air in front of the target. Subplots show shock front progression at the times indicated

4.3   The Limits of Blast Wave Clearing

4.3.1   Clearing Factor and Over-Expansion Ratio

The clearing factor, C_f, expresses the ratio of the average impulse acting on the target face to the incident impulse,

$$C_f = \frac{i}{i_{so}}. \tag{4.2}$$

It has been shown both numerically (Rose & Smith 2000) and experimentally (Tyas et al. 2011a) that at large scaled distances and/or small scaled target dimensions, clearing occurs 'completely' and the average specific impulse on the target face tends towards the incident value. Figure 4.9 shows the cumulative specific impulse-time plots from the numerical analyses, where the impulse is given as an average of the specific impulse acting on the

face of the 2D target recorded from the gauge array depicted in Figure 4.3. The peak numerical incident impulse is also shown.
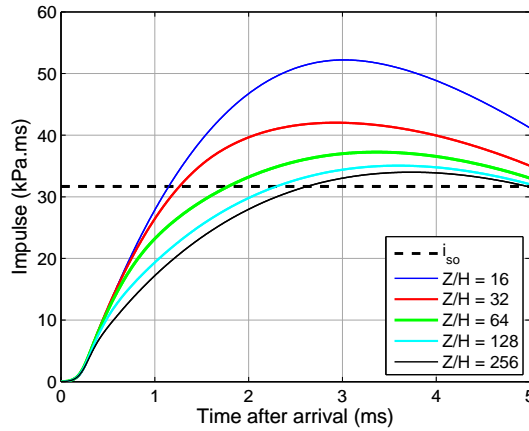
Figure 4.9: Impulse-time histories for numerical tests

Table 4.1 shows the clearing factors for the numerical analyses, compared to the 3D numerical results of Rose & Smith (2000), which have been logarithmically interpolated from the values given in Table 2.4 for the scaled target sizes used in this study. 3D results for target sizes less than $Z/80$ are not available for this scaled distance.

Although the 2D clearing factors are higher than those for the 3D case, as would be expected, and they approach unity more gradually than the 3D case, they still give a good indication of the behaviour of clearing.[vi] The 2D results can be used as a conservative case when evaluating the influence of clearing on small target sizes.

Case	Clearing factor, $C_f = i/i_{so}$						
	Z/H						
	512	256	128	64	32	16	8
2D	1.030	1.073	1.106	1.176	1.326	1.648	1.946
3D (Rose & Smith 2000)	-	-	-	1.037	1.118	1.347	-

Table 4.1: Clearing factors for the 2D numerical results compared to the 3D numerical results of Rose & Smith (2000)

Taking the ratio of the two impulses to evaluate the clearing factor offers useful guidance into the global effect of clearing. It is possible, however, that by using this factor alone one may be overlooking the actual mechanism of clearing. Consider the situation where the additional reflected impulse associated with the blast pressure *prior* to clearing is exactly cancelled out by the below-incident impulse associated with over-expansion *after* clearing. In this case, if only the impulse is considered one might conclude that clearing has occurred

---

[vi]In the 2D case, diffraction is only permitted around the top edge of the target, with reflection off the bottom edge. In the 3D case, diffraction around the vertical edges and reflection at the vertical centreline of the target is also permitted

completely, as the cleared impulse would match the incident impulse exactly. In reality, however, clearing has a very definite impact on the form of the blast pressure load and should not be ignored.

Figure 4.10 shows normalised incident pressure minus average cleared pressure versus time plots for the numerical analyses; values greater than 1 show that the air in front of the target has been over-expanded. It can be seen that pressure is relieved immediately once the clearing waves arrive, and the peak over-expansion is quickly reached before the system gradually begins to return towards equilibrium. Again, the magnitude of over-expansion is clearly related to the size of the target and can also be used as a measure of the influence of clearing.
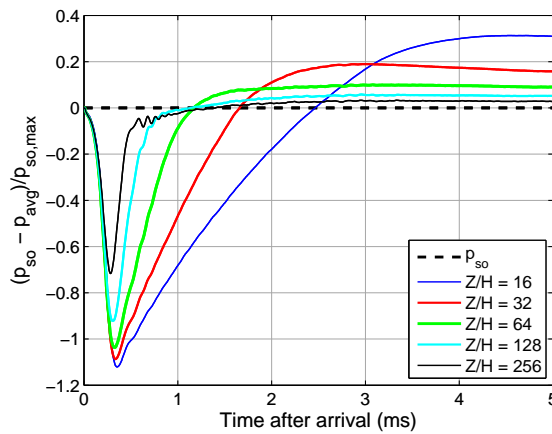
Figure 4.10: Normalised incident minus average cleared pressure-time histories for numerical tests

The over-expansion ratio, O, can be given as the peak difference between the cleared and incident pressure. If this is normalised against the peak incident pressure, adding 1 to the expression ensures that the factor tends towards 1 (from above) with decreasing target size, in the same way that the clearing factor, C_f, does.

$$O = \max \left(\frac{p_{so} - p_{avg}}{p_{so,max}} \right) + 1. \tag{4.3}$$

Table 4.2 shows the over-expansion ratio at different target sizes from the numerical analyses. The largest target size, $H = Z/8$, was omitted because the difference between the average cleared pressure and incident pressure did not reach maximum during the positive phase.

	Z/H					
	512	256	128	64	32	16
Over-expansion ratio, O	1.020	1.033	1.058	1.100	1.190	1.316

Table 4.2: Over-expansion ratios from the numerical analyses at different target sizes

We now have two factors which, broadly speaking, give an indication of the relative magnitude of both the effect (impulse) and the mechanism (over-expansion) of clearing. As both values tend towards unity with decreasing target size, and both approach this asymptote from greater than 1, the two factors can be combined to determine when the cleared blast pressure has converged with the incident pressure. This is done by defining the *convergence ratio* as the root mean square of the clearing factor, C_f, and the over-expansion ratio, O,

$$\text{Convergence ratio} = \sqrt{\frac{C_f{}^2 + O^2}{2}}. \tag{4.4}$$

4.3.2   Scaled Distance and Target Size Limits

At smaller scaled distances the duration of the blast decreases and the rate of decay of the blast pressure increases. The diffraction wave will act less like a supported wave (where pressure conditions change slowly or remain constant for the air that the diffracted wave propagates into) and more like an unsupported wave. Also, regular reflection for stronger shocks causes greater amplification in the reflected pressure, hence whilst the magnitude of the pressure differential driving the clearing wave increases, so does the magnitude of the reflected impulse it needs to relieve and the relative time available to do so decreases.

As discussed previously, the two main factors contributing to the form of blast wave clearing are scaled target size and scaled distance. The numerical analyses were repeated for $Z = 1$, 2, 4 and 16, again for scaled target sizes ranging from $Z/8$ to $Z/512$. The convergence ratios for these analyses, as well as for $Z = 8$ m/kg$^{1/3}$ – determined from Equations 4.2, 4.3 and 4.4 – are shown in Figure 4.11.
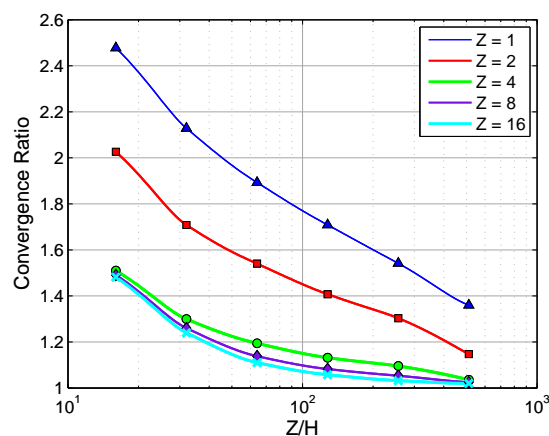
Figure 4.11: Clearing convergence ratio (root mean square of clearing factor, C_f, and over-expansion ratio, O, from Equations 4.2 and 4.3 respectively) for the 2D cases at different scaled distances and scaled target size

It is clear for $Z > 4$ m/kg$^{1/3}$, and particularly for $Z > 8$ m/kg$^{1/3}$, that the cleared behaviour at larger scaled distances is nearly coincident. The waveform parameter of the Friedlander equation, b, which describes the rate of decay of the pressure-time curve, remains constant at around 0.7 for $7 < Z < 20$ and only slightly decreases to around 0.5 for $Z >> 20$ (Figure 2.4). Slight variations in the decay of the pressure-time curve, as well as the fact that for larger scaled distances the reflection coefficient is almost exactly equal to 2.0, suggests that the behaviour of blast wave clearing is effectively the same when considering 'far-field' blast events.

For far-field conditions, the convergence ratio is less than 1.1 for $Z/H \geq 100$, for which it is reasonable to say that clearing has occurred fully and the blast pressure can be approximated as the incident pressure. For near-field conditions, however, no such convergence is achieved and clearing can be said to occur, and to have significant magnitude so as to not be neglected, for any reasonable target size. For example, at $Z = 2$ m/kg$^{1/3}$, the blast pressure has not converged even for $H = Z/512$ m/kg$^{1/3}$. This suggests that a 39 mm target located 20 m away from a 1000 kg TNT burst will still experience some pressure and impulse greater than the incident value.

It can be concluded that, whilst the mechanism for clearing can be ignored for smaller targets at larger scaled distances, it should still be considered for smaller targets at small scaled distances.

4.3.3   Hudson Clearing Predictions for Small Targets

Tyas et al. (2011a,b) experimentally validated the Hudson (1955) method for predicting the cleared pressure acting on targets subjected to diffraction-type loading, where the time taken for the clearing wave to propagate across the target face was comparable to the duration of loading. From the numerical study conducted in this chapter, it has been shown that the mechanism of clearing does not feature multiple rarefaction wave crossings but rather a single rarefaction wave originating from the free edge, propagating across the target face and into the incident air beyond the opposite edge of the target. It stands to reason, therefore, that the Hudson predictive method will still be able to predict the cleared pressure acting on small targets as there are no subsequent diffraction waves to consider aside from the original pulses.

Figure 4.12 shows the reflected, incident and cleared blast pressure at the base of the target ($x = 0$) from the numerical analyses (as in Figure 4.4). Also included are the Hudson (1955) cleared blast pressures and superposition of the cleared pulse with the reflected pressure to give the pressure predictions at the base of the target. The Hudson predictions were constructed using the contours of cleared blast pressure and normalised spatial and temporal parameters as described in Section 2.3.4.

(a) Z/H = 8

(b) Z/H = 16

(c) Z/H = 32

(d) Z/H = 64

(e) Z/H = 128

(f) Z/H = 256
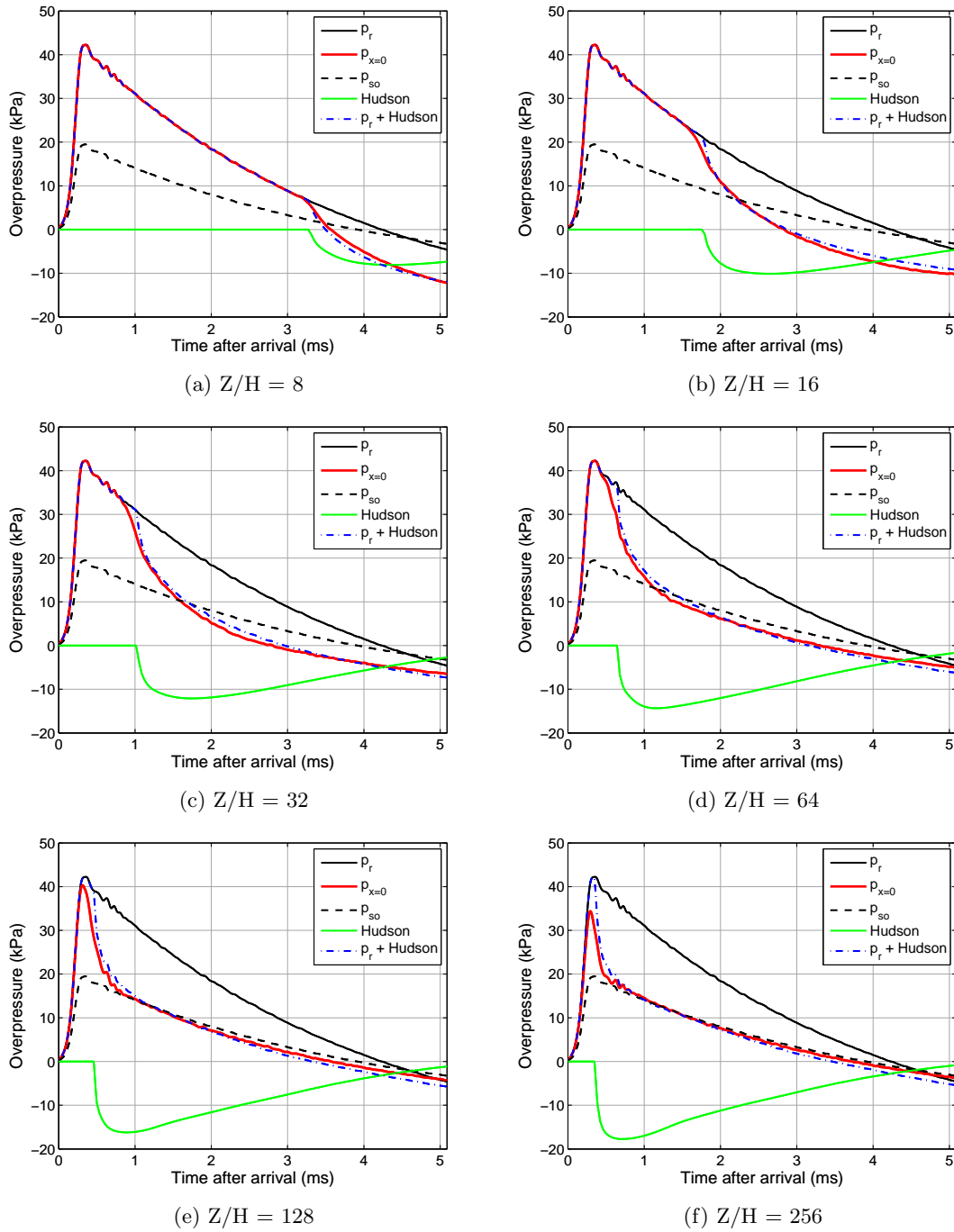
Figure 4.12: Pressure-time histories at the base of the finite targets ($x = 0$) with Hudson (1955) clearing corrections

The superposition of the numerical reflected pressure and the Hudson clearing corrections are in excellent agreement with the numerical cleared pressures for all the target sizes studied. This strongly suggests that given knowledge of the free-field and reflected blast load, and geometry of the target, the cleared blast pressure can be accurately predicted using the Hudson method.

Interestingly, the empirical clearing predictions of Kinney & Graham (1985), appear to be in better agreement for smaller target sizes. The clearing time, t_c, is given as $3H/a_0$, which, for $Z/H = 64$ shown in Figure 4.12(d), gives $t_c = 1.1$ ms. According to this method, the cleared blast pressure should have reached drag pressure between 1.1 ms and 1.4 ms after arrival of the blast wave, depending on whether the true arrival time is taken as 0.0 ms, or when the pressure is at its peak value at 0.3 ms (accounting for numerical rounding of the shock front). From Figure 4.12(d), the numerical cleared blast pressure reaches the incident pressure at approximately 1.2 ms. The fact that the early empirical clearing predictions appear to be accurate for smaller targets is indicative of the fact that the experimental arrangements, and hence the developed methods, were only suitable for observing and recording the behaviour of blast wave clearing for scenarios where the loading quickly approached the incident pressure relative to the positive phase duration. Such methods have been demonstrated to be unsuitable for situations where the diffraction phase constitutes a larger portion of the positive phase, whereas the Hudson clearing predictions have been shown to be valid for both drag-type and diffraction-type loading.

4.4   Summary

In this chapter, the mechanism of blast wave clearing has been studied in an attempt to better understand the process by which the pressure on the front face of rigid target subjected to a blast load approaches the incident pressure.

The current theory on the mechanism of blast wave clearing suggests that the load acting on the target face is made up of an infinite series of crossing diffraction waves, each wave having decreasing magnitude, causing the blast pressure to oscillate about and, for small targets, rapidly approach the incident pressure. This is explained in terms of a shock front distance-time plot.

Hudson (1955) did not observe this behaviour in a series of full scale blast tests, yet the theory and subsequent predictions of blast wave clearing based on this theory are still widely accepted and prevalent in literature guidance (US Army Materiel Command 1974, US Department of Defence 2008, Cormie et al. 2009). To see if these observations could be repeated, a series of numerical analyses were conducted using LS-DYNA, where the detonation, blast wave propagation and interaction with a parallelepiped structure were modelled using 2D axi-symmetric ALE elements. Pressure was recorded along the vertical centreline of a series of rigid targets of decreasing size, with a view to observing how

clearing affected the blast load for smaller target sizes.

It was observed that rather than a series of crossing rarefaction waves, the cleared blast pressure features only one rarefaction wave from the free edge, which travels along the target face, crosses with the clearing wave travelling from the opposite edge (for free air bursts), or reflects off the rigid ground surface (for surface bursts), and propagates past the target edge into the incident region beyond the extents of the target. This causes a region of over-expanded air (relative to the incident blast conditions) to exist in front of the target, with larger targets resulting in a greater over-expansion.

The ratio of over-expansion to the incident pressure was combined with the ratio of cleared to reflected impulse to describe how the features of clearing change with both scaled distance and scaled target size. It was seen that for far-field conditions – judged to be applicable for scaled distances greater than 4 m/kg$^{1/3}$ – the cleared conditions converged with the incident conditions at around $Z/H = 100$, meaning that clearing can effectively be ignored for targets smaller than this and the blast load can be represented by the incident pressure. This value was computed as a result of the 2D analyses where clearing was allowed over the top edge of the target only and the surface was assumed to be infinite in the horizontal dimension. For 3D targets, i.e. targets with non-infinite lateral dimensions, the behaviour is likely to converge with the incident pressure more rapidly with decreasing target size, hence $Z/H = 100$ can be seen as a conservative estimate for the smallest target size at which the clearing effect cannot be ignored. It was also shown that no such convergence is achieved for near-field conditions, i.e $Z < 4$ m/kg$^{1/3}$, and that the blast pressure must properly be quantified as it cannot be simplified to either the reflected or incident pressure for any realistic target size.

Finally, it was shown that the Hudson method can accurately capture the features of blast wave clearing for small target sizes, based on the fact that the load is comprised of only one clearing wave propagation across the target face from each free edge.

Chapter 5

Modelling Structural Response to Blast Loads

5.1   Introduction

Once the engineer has quantified the blast load a target will be subjected to, the next step is to predict the likely damage the target will sustain from such a blast in order to assess whether the design is adequate or not.

There are several numerical methods for determining structural response to blast loads, in decreasing levels of complexity, that are studied in this chapter:

- Coupled ALE-Lagrangian analysis – The structure is modelled using Lagrangian finite elements and the surrounding air domain is modelled using ALE elements. The detonation process and subsequent blast wave propagation is modelled using finite elements in order to get a full description of the spatial distribution of blast pressure and the load is transferred to the target via fluid-structure interaction. Results of this type are labelled 'ALE'.

- Uncoupled Lagrangian finite element analysis – The structure is modelled using Lagrangian finite elements and the loading is simplified by applying the semi-empirical pressure-time history as nodal-point load curves. Results of this type are labelled 'DYNA'.

- Uncoupled single-degree-of-freedom analysis – The structure is simplified as a single point equivalent and the loading is further simplified as a single force-time history. Results of this type are labelled 'SDOF'.

Whilst it appears that the higher resolution schemes may offer the most accurate representations of the target response, lower resolution schemes may provide equally accurate results without the associated computational expense.

This chapter details a series of experimental trials that were undertaken to validate computational methods for evaluating target response to blast loads. Numerical simulations relating to the three techniques above are also detailed in this chapter, as is the derivation of an improvement to the SDOF procedure to take non-uniform loading into account.

5.2   Experimental Work

5.2.1   Experimental Setup

In order to quantify the response of flexible structural targets to cleared and non-cleared blast loading, a series of small-scale experimental trials was conducted on test plates situated in:

- An effectively infinite reflected surface, where the plate will experience the full 'non-cleared' pressure load

- A finite reflecting surface, where blast wave clearing will influence the late-time pressure acting on the target and the plate will experience a 'cleared' pressure load with reduced impulse.

Measuring the displacement of the test plates allows the influence of clearing to be isolated and quantified, with experimental data available for validation of the various numerical modelling approaches detailed above.

Hemispherical PE4 charges were placed 6 m away from a reinforced concrete bunker wall which contained a steel plate lined porthole (320 × 305 mm clear dimensions) into which the non-cleared test plate was located. The minimum distance from the test plate to a free edge of the bunker wall was at least 4 m. The positive phase durations of the hemispherical charges used were all less than 3 ms – a clearing wave travelling at 340 m/s from the nearest free edge would take >11.5 ms to reach the target before it could begin to affect the loading on the target, hence the reflecting surface can be assumed to be effectively infinite in lateral extent and semi-empirical predictions for reflected pressure can be used.

Orthogonal to the bunker wall, 6 m away from the centre of the explosive, a second ('cleared') test plate was located within a finite reflecting surface, comprising a rigid block with dimensions such that the target would experience cleared loading. The depth of the target block was >2 m, ensuring no clearing waves would arrive from the back of the target. The experimental set up, shown in Figure 5.1, enabled the dynamic deflection of plates subjected to cleared and non-cleared blast loads to be measured, providing two sets of data for validation.

The test plates were 0.835 mm thick mild steel. Non-cleared test plates were located in a 305 mm wide, 320 mm high porthole that had been cut in the bunker wall, 305 mm above
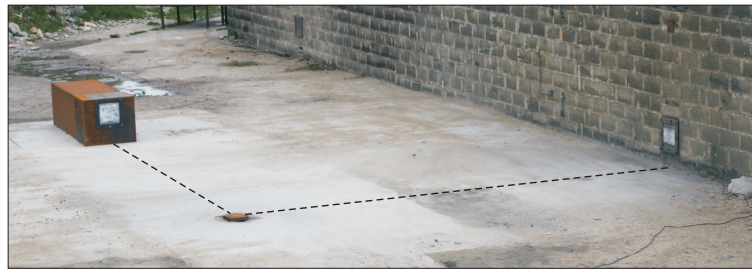
(a)
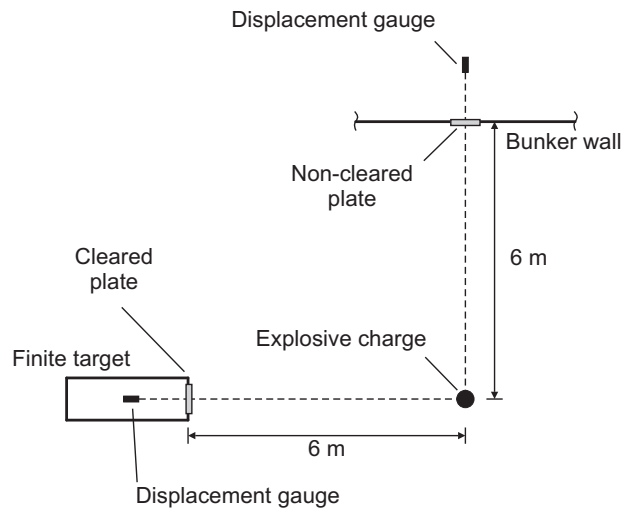
(b)

Figure 5.1: (a) General arrangement of the test arena and (b) Schematic of the test setup

ground level. The target block was a 600 mm square by 1.8 m long reinforced concrete block clad in 15 mm thick steel plate to provide a flat regular surface. An additional steel frame, fabricated from 15 mm steel plate, was attached to the front, providing housing for the laser displacement gauge. A porthole was cut in the front of the steel frame, with the same dimensions as the porthole in the bunker wall, at the same height above the ground surface. The test plate in the finite surface was located along the vertical centreline of the front face of the target block, with 238.5 mm either side to the edges of the reflecting surface, and 65 mm to the top edge. Dimensions of the finite target (in mm) are shown in Figure 5.2.

A clamping plate was attached to the front of both finite and infinite targets using 8 × M10 bolts, and was used to constrain rotation at the supports, whilst the bolt holes in the test plates were oversized, allowing free horizontal translation. Additionally, molybdenum grease was liberally applied to the faces (of both the porthole frame and clamping plate) that were in contact with the target plate in order to minimise the in-plane frictional resistance at the supports. The plates were one-way spanning (horizontally spanning the 305 mm) and were slightly undersized in the vertical dimension to allow the top and
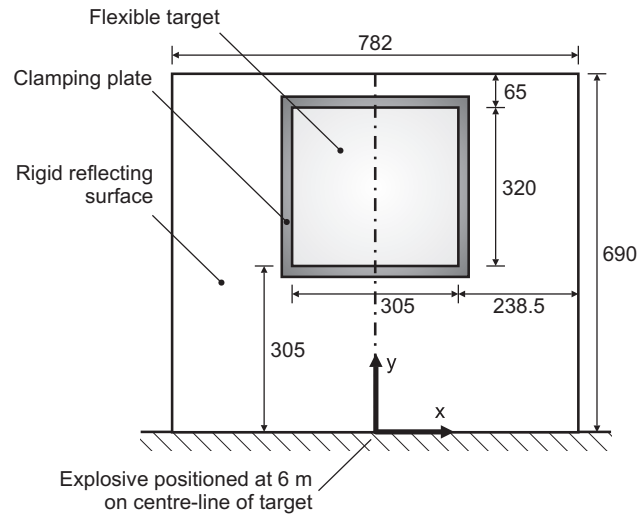
Figure 5.2: Dimensions of the finite reflecting surface (dimensions in mm)

bottom edges to translate freely without striking the porthole frame.

Deflection was measured by M7 laser distance sensors (bandwidth of 10 kHz and resolution accuracy of ± 0.6 mm) manufactured by MEL Microelektronik GMBH.

The laser gauge in the finite target was located in the steel housing and was attached to a bracket fixed directly to the rigid concrete block, insulating the unit against ground shock. The power and signal cables were fed through a hole punched in the concrete ground slab, maintaining the smooth reflecting surface of the steel-clad concrete block for the incident wave to propagate over. The laser gauge measuring the displacement of the non-cleared target was located within the control room of the bunker and was mounted on a heavy steel beam, serving to isolate the laser gauge from any potential vibrations caused by the blast. Displacement data were recorded using a TiePie Handyscope 4 digital oscilloscope, recording samples at 312.5 kHz and 14 bit resolution. Recording was triggered by the failure of a break-wire wrapped around the detonator, to synchronise the records with the time of detonation. The hemispherical charges were detonated using electronically activated L2A1 detonators. The laser gauges were aligned with the centre of the targets to give displacement readings at mid-span.

The experimental trials were conducted with hemispherical PE4 charges ranging from 50-175 g, with the stand-off set at 6 m throughout. Five charge masses were tested, with one repeat test per charge mass. In each test, the displacements of the cleared and non-cleared plates were measured, giving a total of 20 test results. A summary of the test plan is shown in Table 5.1.

Test	Charge mass (g PE4)	Stand-off (m)	Scaled distance[*] $(m/kg^{1/3})$
1, 2	50	6	15.3
3, 4	75	6	13.4
5, 6	108	6	11.9
7, 8	140	6	10.9
9, 10	175	6	10.1

* Using a TNT equivalence of 1.2 for PE4 (see Section 3.4.1)

Table 5.1: Charge masses and stand-offs used in experimental trials

5.2.2   Experimental Results

The experimental results are shown in Figure 5.3 and are summarised in Table 5.2. The displacement data were smoothed using a 10-point moving average algorithm (over a period of 32 μs) to eliminate signal noise and were time-shifted such that the initial motion of the plates coincided with the arrival times predicted by ConWep. In all cases this was never more than ± 50 μs. The experimental results will be discussed further with reference to the numerical results in subsequent sections.

Test	Charge mass (g PE4)	Peak displacement (mm)	
		Cleared	Non-Cleared
1	50	5.39	8.23
2	50	5.18	8.14
3	75	7.33	10.27
4	75	7.20	10.25
5	108	9.13	13.83
6	108	9.53	13.72
7	140	11.29	16.79
8	140	11.97	16.85
9	175	12.88	19.40
10	175	12.61	19.51

Table 5.2: Peak experimental displacements

(a) 50g PE4

(b) 75g PE4

(c) 108 g PE4

(d) 140 g PE4

(e) 175 g PE4
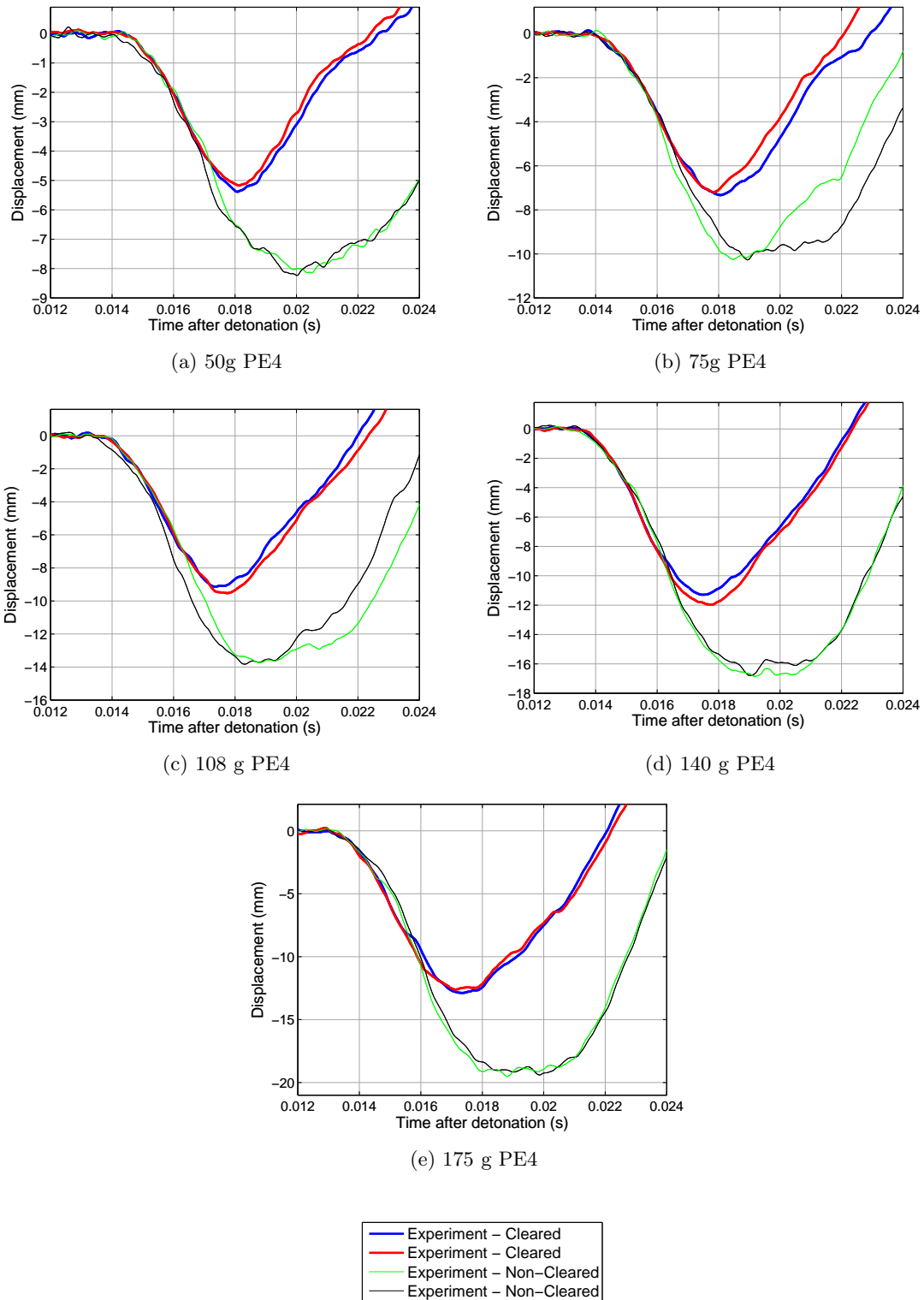
Figure 5.3: Experimental displacement-time histories for cleared and non-cleared plates

5.3   Coupled ALE-Lagrangian Finite Element Analysis

5.3.1   Preliminary Plate Mesh Study

The influence of mesh density in the air domain was detailed in Section 3.3.2, with the results showing that air-blast calculations are very sensitive to mesh size. This section details a preliminary study undertaken on a Lagrangian plate to examine the influence of mesh size on the ability to model the deformation of a target subjected to a blast load. In this example, a 1 m square steel plate with thickness 10 mm and elastic material properties ($E = 210$ GPa, $\rho = 7850$ kg/m^3 and $\nu = 0.3$) was subjected to a spatially uniform, linearly decaying load with a peak pressure of 10 kPa and a duration of 10 ms.

The plate was analysed under two support conditions: fully clamped on all four edges and simply supported on the vertical edges only, effectively giving upper and lower bound displacements for the plate. Mesh densities ranged from 16×16 elements to 512×512 elements. Figure 5.4 shows the peak displacement of the plates against mesh size, as well as indicating a suitable convergence value (0.1% of the displacement of the finest mesh). It can be seen that convergence is attained at around 900 elements for the clamped plate and 3000 elements for the simply supported plate, suggesting a mesh size of 64×64 elements is adequate.
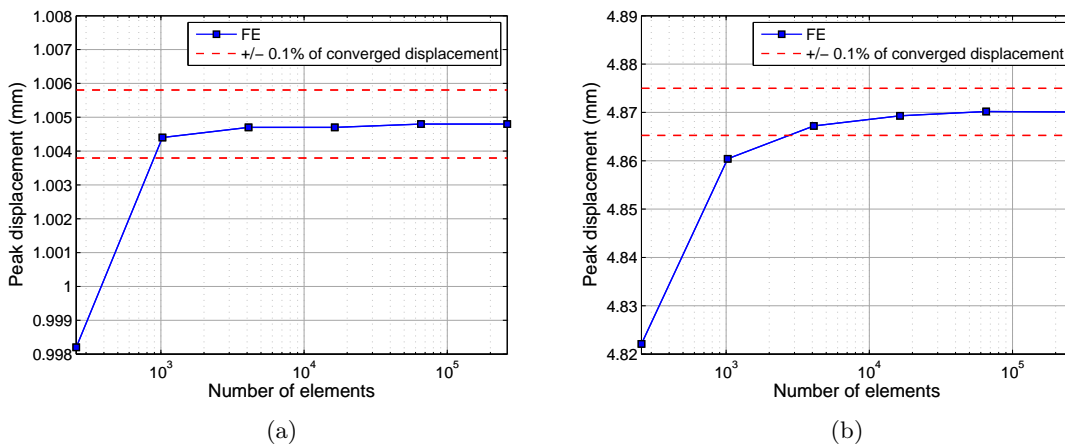
Figure 5.4: Mesh convergence for Lagrangian plate under uniform, linear decaying load for (a) clamped and (b) simply supported boundary conditions

5.3.2   Model Setup

Following the same procedure outlined in the previous chapter, the initial detonation and subsequent blast wave propagation was modelled using 2D axi-symmetric ALE multi-material elements. The chosen mesh density was 50 circumferential elements and 500 elements along the radius of the 6m domain, giving an aspect ratio of 0.2 for the air elements, giving a reasonable compromise between numerical stability, analysis time and fidelity of results (see Section 3.3.2).

The analysis was terminated when the shock wave had travelled 6 m, and a mapping file was written using the *INITIAL_ALE_MAPPING keyword. The analysis time was chosen to be typically 0.2-0.3 ms less than the arrival time given by ConWep, to account for smearing of the shock front into adjacent elements and early shock wave arrival. The duration times, as well as the radii used in the axi-symmetric ALE analyses are shown in Table 5.3. The explosive and air were modelled using the *EOS_JWL and *EOS_LINEAR_POLYNOMIAL equations of state respectively and *MAT_HIGH_EXPLOSIVE_BURN and *MAT_NULL material properties respectively. The PE4 and air parameters are given in Table 3.1.

Charge mass (g PE4)	Radius (mm)	ConWep t_a (ms)	Duration (ms)
50	24.61	14.23	14.00
75	28.18	13.85	13.60
108	31.82	13.48	13.30
140	34.69	13.19	12.90
175	37.37	12.94	12.70

Table 5.3: Charge mass, radius, and duration for the 2D axi-symmetric analyses

Based on the experimental results in Figure 5.3, a duration of 10 ms was chosen for all 3D analyses (i.e. 10 ms after the time at which the blast wave was re-mapped onto the 3D domain). Assuming a wavespeed of 340 m/s and a loading duration of 10 ms, a 3.4 m domain in front of the target is required to ensure that sufficient information is mapped from the 2D to the 3D case. Sufficient length behind, above and adjacent to the target is also required to ensure that no expansion waves arrive from the boundary throughout the duration of the analysis. A domain size of 1.7 m from the edge of the reflecting surface in these directions gives enough distance to ensure that the time taken for the blast wave to reach of the edge of the domain plus the time taken for the subsequent expansion wave to reach the target from the domain edge exceeds the analysis duration.

Half-symmetry was utilised by constraining all nodes along the vertical boundary against horizontal displacement. The ground surface was also modelled using a rigid boundary. The target plate was modelled using shell elements and the air domain was modelled using solid brick elements and was represented by two parts, air 'in front' of the target (air in contact with the front of the shell) and air 'behind' the target (air in contact with the back of the shell). This enabled better modelling of the contact between the plate and air (see Section 5.3.3). Contact between the two air parts was achieved using shared nodes, which is essential to track the boundary between the two air parts and the target plate. All other nodes along the boundary of the two air parts, aside from those occupying the same space as the target, were constrained against displacement to model the rigid reflecting surface. The air domain was discretised into 20 mm cube elements and the target was discretised into 6 mm square elements, giving no less than 4 coupling points for each ALE element, which is greater than 2–3 per element as suggested by Hallquist (2006).

Figure 5.5 shows the 3D domain used in the analyses, as well as labelling the rigid boundaries (all other boundaries were modelled as non-reflecting). The same mesh was used for all 3D analyses by offsetting the mapping data by 6 m, using the X0 control in the *INITIAL_ALE_MAPPING keyword and setting the origin as the bottom corner of the reflecting surface. The plates were modelled as fully clamped, elastic ($E = 210$ GPa, $\rho = 7850$ kg/m^3 and $\nu = 0.3$) one-way spanning beams (spanning the horizontal dimension) with rotational restraint and translational restraint in the x plane at the supports, and a shell thickness of 0.835 mm.
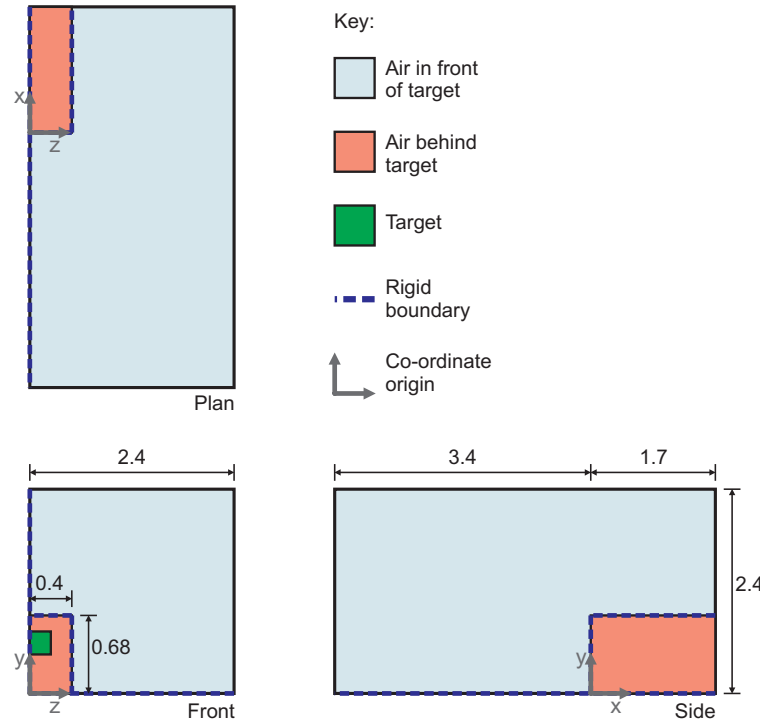
Figure 5.5: Parts, co-ordinate origin and dimensions (m) of the 3D domain

5.3.3 Fluid-Structure Coupling

Fluid-Structure penalty coupling was achieved using the *CONSTRAINED_LAGRANGE_IN_SOLID keyword. In penalty coupling the contact interface is tracked and nodal penalty forces are applied if a fluid particle penetrates a Lagrangian element within the time-step (Zakrisson et al. 2011). These 'recall' penalty forces are sufficient to prevent penetration from occurring, and are applied to both master and slave node sets in opposite directions to ensure equilibrium (Chafi et al. 2009).[i] Penalty coupling prevents flow through the Lagrangian structure and ensures energy is conserved (as opposed to constraint-coupling, whereby momentum is conserved but not energy).

---

[i]In LS-DYNA, contact occurs when a Lagrangian structure spatially overlaps an ALE mesh; the structure is assigned as the slave set and the air/explosives assigned as the master set (Hallquist 2006).

The applied penalty force is in the form of a linear elastic spring resistance. The main advantages of penalty based methods include:

- No new degrees of freedom are introduced into the system

- Symmetric treatment of contact is permitted

- Very little numerical noise is introduced, avoiding severe hourglassing for under-integrated elements

- Straightforward implementation

- Arbitrary intersection of master and slave surfaces is permitted, unlike constraint based contact which cannot operate for two or more master surfaces (Sauvé & Morandin 2004).

The scaling of the estimated penalty stiffness is based on the geometry and material properties of the elements associated with the master surface. This adaptive method ensures that the time-step size remains relatively unchanged by the contact algorithm (Sauvé & Morandin 2004).

In the analyses conducted as part of this numerical study, separate contact was defined for the Lagrangian structure interacting with the air part 'in front' and the air part 'behind' the target, as indicated in Figure 5.5. This was done to ensure that the correct effects of below atmospheric pressure were modelled; if a lower pressure acts in front of the target compared to the pressure behind the target, coupling the structure to both of these forces will ensure that the net force acts in the opposite direction of blast wave travel, effectively modelling the suction forces. Penalty contact must be aligned with the surface normal of the shell elements, therefore the NORMTYPE control was used to flip the normal of the shell when defining contact between the target and the air behind the target. The DIREC control, used to define the coupling direction, was set as '*normal only, compression and tension*' to model the effect of suction from negative pressures acting on the target. All other contact parameters were kept as the default values.

5.3.4   Results and Discussion

The numerical displacement-time histories are shown in Figure 5.6 with the cleared experimental displacements for comparison. Table 5.4 summarises the peak numerical and experimental displacements and shows the ratio of numerical to experimental peak displacements. Displacements are given from the history variables of the node located in the centre of the plate.

(a) 50g PE4

(b) 75g PE4

(c) 108 g PE4

(d) 140 g PE4

(e) 175 g PE4

Experiment – Cleared
Experiment – Cleared
ALE
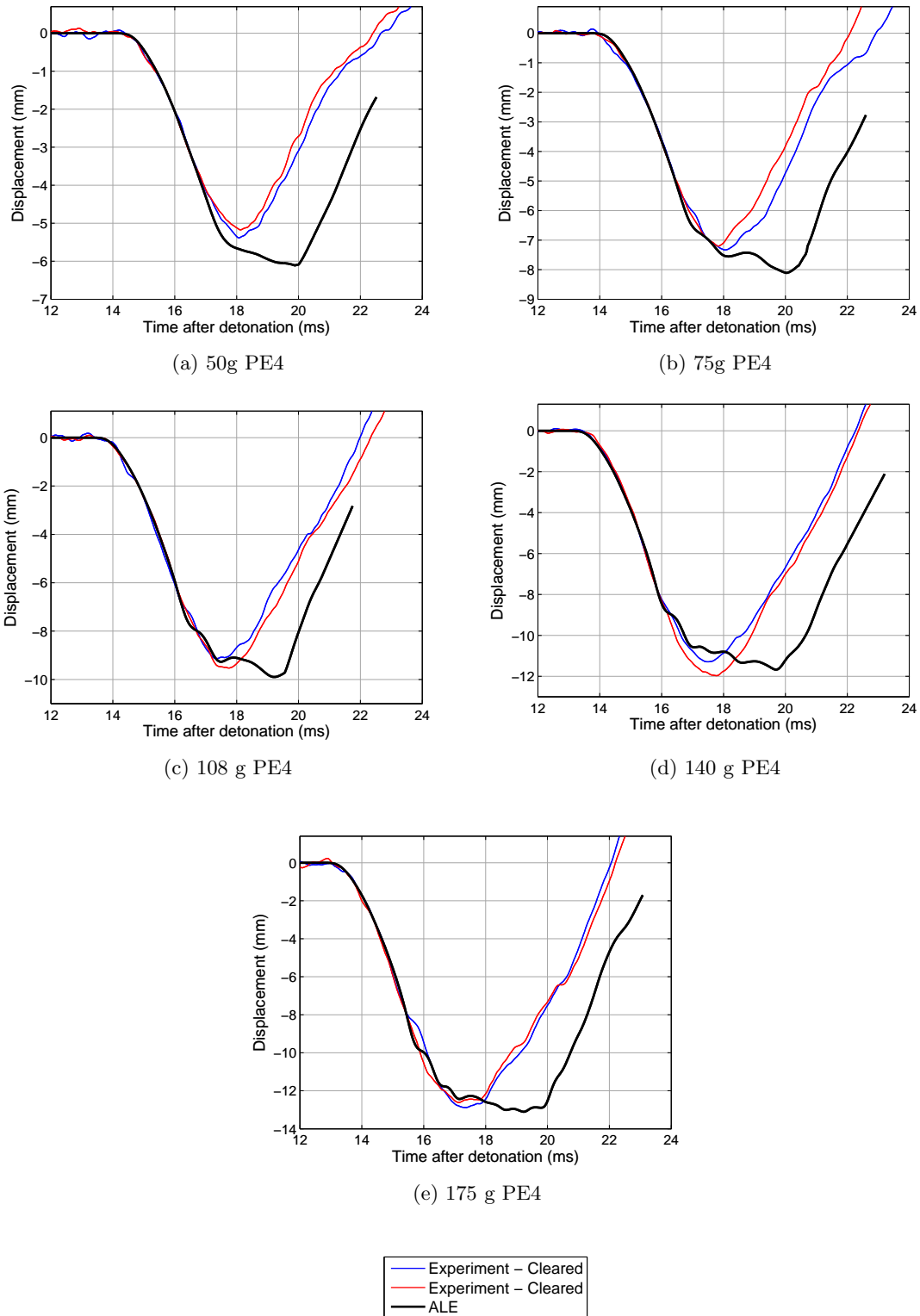
Figure 5.6: Experimental and coupled ALE-Lagrangian numerical displacement-time histories for the cleared plates

Charge mass	Peak displacement (mm)		Ratio
(g PE4)	Experimental[*]	Numerical - ALE	
50	5.29	6.11	1.15
75	7.26	8.11	1.12
108	9.33	9.90	1.06
140	11.63	11.67	1.00
175	12.75	13.10	1.03

[*] averaged result

Table 5.4: Peak experimental and coupled ALE-Lagrangian numerical displacements for the cleared plates

Qualitatively, the coupled ALE-Lagrangian displacements from Figure 5.6 match up with the experimentally recorded displacements remarkably well for the first ∼3 ms of analysis. This suggests that penalty coupling between fluid and structure is effective at modelling the interaction between blast wave and target; with the level of agreement between the early-time displacement profiles it is clear that not only is impulse conserved when remapping from 2D to 3D but also the correct level of impulse is imparted to the target through fluid-structure interaction.

The latter stages of the displacement-time history are not in as good agreement. During this stage of displacement negative clearing pressures are acting on the target, causing suction and rebound. It appears that the numerical model doesn't capture this behaviour as accurately. As evidenced by the early stage displacement, penalty coupling can correctly transfer compressive forces between the air and the target, suggesting that suction, or tensile forces, can be correctly modelled also. The discrepancy between numerical and experimental displacements can therefore be explained by the loading itself – the domain is sufficiently large such that a finer mesh will be too computationally expensive, and therefore the coarser elements used in the analyses may result in improper representation of the clearing expansion wave. As was seen in Section 3.3.2, impulse is dependent on mesh resolution. In this numerical model, the clearing wave has a lower impulse because of mesh effects and therefore relieves the reflected pressure to a lesser degree than in the experiments, hence delaying the rebound displacement.

This effect, however, has only a relatively small impact on the peak displacement, as can be seen by the values of peak displacement in Table 5.4. The numerical model is able to evaluate the peak displacements of the target to within 15% of the experimental displacements, with a typical error of around 7%.

The models were run for 168 hours (1 week) on *iceberg*, the University of Sheffield High Performance Computing (HPC) server. While the results lie within an acceptable level of agreement, the fact that large computational resources were required in order to conduct these analyses gives reason enough to question the need for such complex methods. Accordingly, an uncoupled Lagrangian finite element analysis was conducted.

5.4 Uncoupled Lagrangian Finite Element Analysis

5.4.1 Model Setup

The blast pressure load can be applied directly to the target in a Lagrangian only structural analysis, where the development of reflected pressure on the target face is assumed to be independent of the target response, i.e. FSI effects are not taken into account. Whilst this may over-simplify the blast pressure load, the influence of FSI is only significant for low stiffness, low mass systems (Kambouchev et al. 2006, 2007, Teich & Gebbeken 2012). In situations where the stand-off is relatively large, modelling the structure only could result in savings in computational cost of several orders of magnitude (Slavik 2009). This purely Lagrangian method is particularly attractive for simple scenarios: where there is a direct line of sight between the target and source of the blast (i.e. no obstructions which may cause shadowing) and the target geometry is relatively simple (i.e. there is no focussing of the shock front). Furthermore, in the ALE-Lagrangian coupled model, the critical time-step was dictated by the shell elements, combining a small time-step with expensive ALE calculations. Reduced integration shell elements are computationally inexpensive and a finer mesh can be specified for uncoupled Lagrangian analyses in order to better model the spatial variation of clearing pressure at relatively little extra computational cost.

Based on the initial mesh study (Section 5.3.1), the plate was discretised into a grid of 64×64 shell elements with four integration points through the thickness of the shell. The same elastic material properties and boundary conditions were used as those in the ALE-Lagrangian models. To model the cleared and non-cleared plates, two load cases were defined:

- Non-cleared plates were subjected to full reflected pressure. Pressure was applied using the *LOAD_BLAST keyword.

- Cleared plates were subjected to blast pressure using superposition of semi-empirical pressure predictions and Hudson (1955) clearing corrections.

*LOAD_BLAST

The *LOAD_BLAST keyword is an LS-DYNA loading module based on the implementation of ConWep semi-empirical load predictions after Randers-Pehrson & Bannister (1997). *LOAD_BLAST requires the definition of a SEGMENT SET, to which the blast load is applied using the following expression

$$p(t,\theta) = p_r(t) \cos^2 \theta + p_{so}(t) \left(1 + \cos^2 \theta - 2 \cos \theta \right) \tag{5.1}$$

where θ is the angle between the segment normal and the line from the explosive charge to that point. *LOAD_BLAST allows the user to specify either a hemispherical surface burst or

a spherical free air burst, and requires only the input of the charge mass and co-ordinates of the centre of the explosive, and an optional 'time of detonation', which can be set as $-\min(t_a)$ so that the beginning of the analysis coincides with the arrival of the blast wave.

Although *LOAD_BLAST allows the treatment of arbitrary target geometries, it assumes that the target forms a part of an infinite reflecting surface and therefore cannot be used to model the cleared target plates.

Hudson Clearing Corrections

The plates in the finite target were analysed under cleared loading according to the Hudson (1955) clearing corrections. Following the method outlined in Section 2.3.4, the blast pressure was applied to the numerical model in the following way:

- The full reflected pressure-time history, given the charge mass and stand-off, was applied to every node. It was assumed that the shock front arrived at every node simultaneously and was assumed to be uniform in magnitude (i.e. slant distance and angle of incidence effects were ignored). With a scaled target height of 0.5 m/kg$^{1/3}$ at a scaled distance of >10.0 m/kg$^{1/3}$ this is a reasonable assumption to make – the peak pressure and time of arrival given by ConWep Loads on Structures (LOS) differ by no more than 1% across the plate.

- For each node, the distances x_1 and x_2 to the free edges enabled the Hudson clearing lengths, η_1 and η_2, to be evaluated (Equation 2.24). The corresponding pressure-time function (Figure 2.12) given by the superposition of both curves was applied to each node with identical x coordinates (33 node sets, given symmetry about the vertical axis). The co-ordinate system is shown in Figure 5.2.

- The same procedure was adopted for the clearing relief wave corresponding to the distance to the vertical free edge of the target and the reflection of the relief wave from the rigid ground surface. Both waves were applied to each node with identical y coordinates (65 node sets).

- Each node was therefore subjected to the superposition of three load curves; the reflected pressure and x and y components of clearing relief (the pressure was multiplied by the element area to give a load-time history).

A total of 99 load curves were defined for the 4225 nodes and were generated using a purpose written MatLab pre-processor. Numerical analyses were performed for all five charge masses, with separate runs for Hudson and *LOAD_BLAST loading options, totalling 10 analyses. Hudson's clearing length scale (η, Equation 2.24) changes with positive phase duration, hence the Hudson clearing functions were evaluated for each charge mass separately. Physical damping of the target plate was not included in the numerical model

as it could not be accurately quantified for the target and is likely to make little difference to the first quarter cycle of displacement (i.e. to first peak deflection).

Figure 5.7 shows the pressure predictions from a 75 g PE4 charge at 6 m. ConWep predictions for reflected pressure show the typical load that the non-cleared plate was subjected to in tests 3 and 4, and Hudson predictions for the furthest and nearest points from the free edge of the finite target give an indication of the range of pressures acting on the cleared plate. For the point in the bottom-centre of the target, $(0.000, 0.305)$, the clearing lengths associated with the x and y distances to the free edge are 0.48 and 0.49 respectively; clearing waves from the top and sides arrive approximately half way through the positive phase. For the top corners of the plate, $(0.153, 0.625)$ and $(-0.153, 0.625)$, the x and y clearing lengths are 0.08 and 0.30, and the clearing waves can be seen to arrive much earlier; the clearing wave from the top face arrives 0.2 ms after load application.
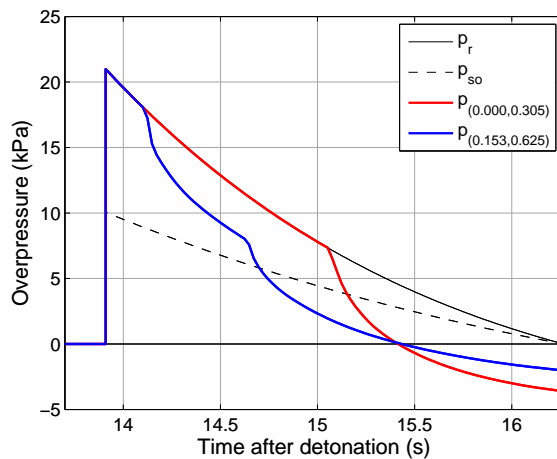
Figure 5.7: Reflected pressure (p_r), incident pressure (p_{so}) and clearing pressure acting at the furthest ($p_{(0.000, 0.305)}$) and nearest ($p_{(0.153, 0.625)}$) points from the free edge for 75 g PE4 at 6 m stand-off

Surface plots of the pressure acting across the target at t = 14.50, 14.75, 15.00 and 15.25 ms after detonation are shown in Figure 5.8, where propagation of the relief waves across the target face can clearly be seen.

5.4.2 Results and Discussion

The numerical displacement-time histories are shown in Figure 5.9 with the experimental displacements for comparison. Table 5.5 summarises the peak numerical and experimental displacements and shows the ratio of numerical to experimental peak displacements, for both cleared (Hudson) and non-cleared (*LOAD_BLAST) plates. Displacements are given from the history variables of the node located in the centre of the plate. In the numerical model, the load was applied at time $t = 0$ and the displacements were time-shifted to correspond with the arrival time given by ConWep.

(a) 14.50 ms

(b) 14.75 ms

(c) 15.00 ms

(d) 15.25 ms
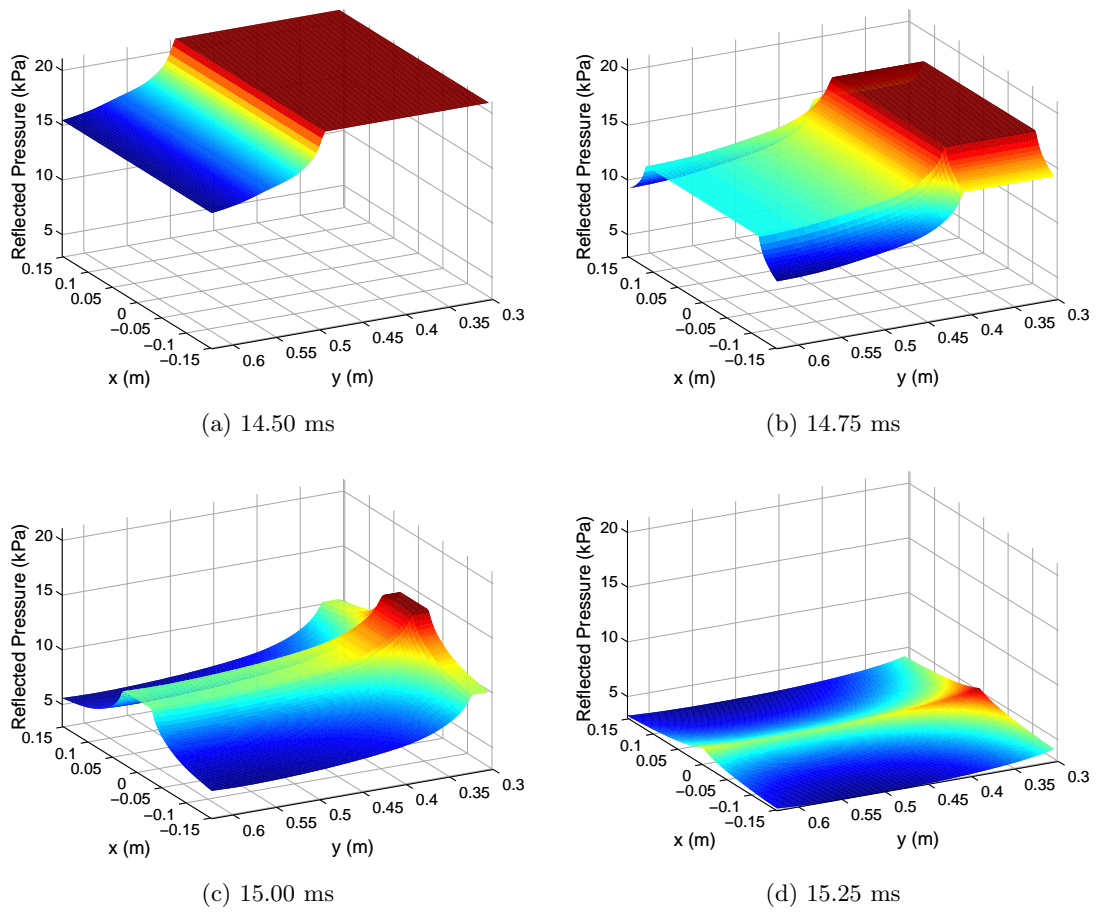
Figure 5.8: Surface plots of reflected pressure acting on the target for 75 g PE4 at 6 m stand-off. Dimensions of the finite target and reflecting surface are shown in Figure 5.2

(a) 50g PE4

(b) 75g PE4

(c) 108 g PE4

(d) 140 g PE4

(e) 175 g PE4
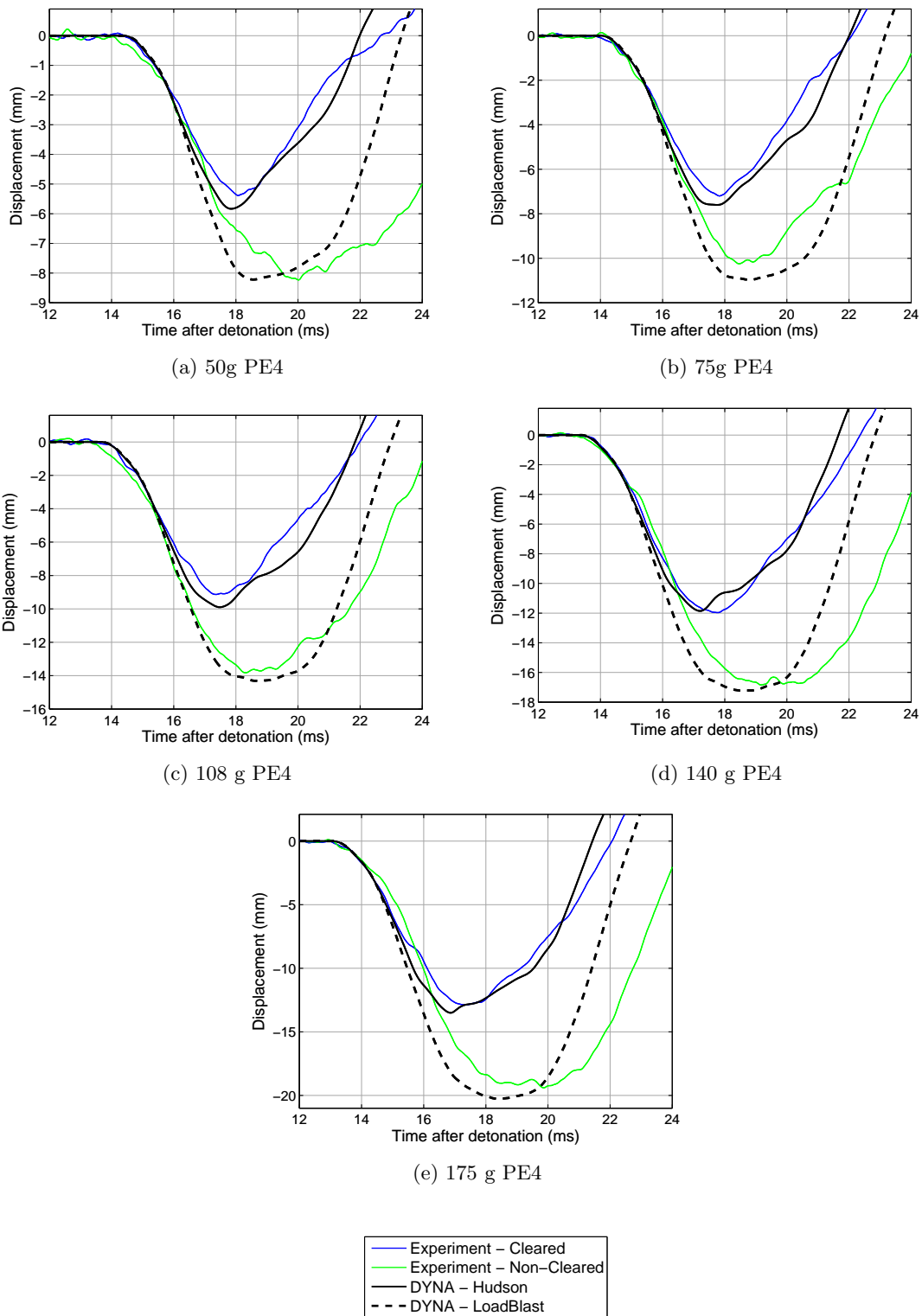
Figure 5.9: Experimental and DYNA Hudson displacement-time histories for cleared plates and experimental and DYNA *load_blast displacement-time histories for non-cleared plates

| Charge mass | Peak displacement (mm) | | | | | |
| (g PE4) | Cleared | | | Non-Cleared | | |
	Experimental[*]	DYNA Hudson	Ratio	Experimental[*]	DYNA LOAD_BLAST	Ratio
50	5.29	5.83	1.10	8.19	8.22	1.00
75	7.27	7.60	1.05	10.26	10.97	1.07
108	9.33	9.90	1.06	13.78	14.31	1.04
140	11.63	11.86	1.02	16.82	17.22	1.02
175	12.75	13.50	1.06	19.46	20.26	1.04

[*] averaged result

Table 5.5: Peak experimental and numerical displacements for cleared (Hudson) and non-cleared plates (LOAD_BLAST)

The displacement-time histories from Figure 5.9 for the cleared plates are in very good agreement for all analyses. The late-time displacement profile of the non-cleared plates shows a slight difference between numerical and experimental results. *LOAD_BLAST models the negative phase by extending the Friedlander equation past the positive phase duration, which has been shown in Section 2.2.5 to be incapable of capturing the correct form of the negative phase. This has little effect on the peak deflection of the target, as the majority of the negative phase occurs after the target has reached the maximum value.

There is little appreciable difference between the cleared and non-cleared plate deflections until the arrival of the clearing wave (between 14 and 16 ms after detonation for all analyses), justifying the assumption that the blast wave arrives planar and angle of incidence effects can be ignored. Upon arrival of the clearing wave the displacement of the cleared and non-cleared plates begin to diverge. A combination of reduced positive phase impulse and early negative pressure serves to decelerate the cleared plates and leads to the plates beginning to rebound ~2 ms earlier than the non-cleared plates. This behaviour was observed for all tests and is accurately captured by the numerical model.

It can be seen from Table 5.5 that the numerical model is able to evaluate the peak deflection to within 10% of the experimental values, with typical errors of 5% for the Hudson load model and 3% for *LOAD_BLAST, which, considering the computational time of no more than ten minutes, is a vast improvement on the ALE-Lagrangian coupled analyses.

The Hudson method can be readily implemented into commercial FE software, enabling the deflection of finite targets to be evaluated whilst retaining the simplicity and low computational cost of a Lagrangian only analysis. It is worth noting, however, that the current best practice for uncoupled Lagrangian analyses is to use the *LOAD_BLAST loading option, which is useful to gain a first approximation of the typical response characteristics and peak displacement of plates subjected to blast loads, but can lead to over-conservative estimations through neglecting clearing. Through this numerical study, the need to accurately model blast wave clearing becomes apparent. If the results from the non-cleared

numerical analyses are taken as estimations for the peak displacement of the cleared plates (i.e. if the engineer neglected clearing in the numerical model), peak displacements would be over-predicted by 48-59%.[ii] This over-conservatism can be overcome by using the Hudson clearing corrections when modelling plate deflections in an uncoupled Lagrangian analysis.

In situations where the centre of the charge is far from the reflecting surface, and the blast wave is unobstructed between the detonation point and the target, then the low computational cost and demonstrated validity of the Hudson predictive method should be preferred over more complex schemes such as ALE-Lagrangian coupled analyses.

5.5 The Single-Degree-of-Freedom Method

5.5.1 Introduction

It is not always necessary nor practical to model the target using finite elements (multiple degrees of freedom). The single-degree-of-freedom (SDOF) method, developed by Biggs (1964), provides a computationally inexpensive approach to evaluating target response to blast loads and is recommended in various design guidance including *SBEDS* (US Army Corps of Engineers 2005), UFC-3-340-02 (US Department of Defence 2008) and *Blast effects on buildings* (Cormie et al. 2009). Based on physically valid approximations, the SDOF method can be used to accurately ascertain the typical response characteristics of a structure, and offers a 'first-guess' at the likely damage a target will sustain when subjected to a blast load. Because of these reasons, the SDOF method is well established in practice (Morison 2006).

The dynamic equation of motion of a distributed system (an example of a simply supported beam with a transiently varying, spatially uniform load is shown in Figure 5.10) is

$$m\ddot{z} + c\dot{z} + kz = F(t), \tag{5.2}$$
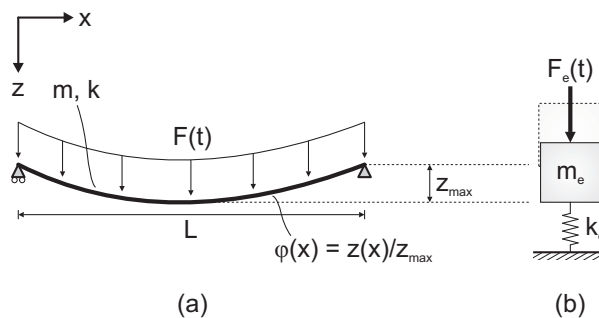
Figure 5.10: (a) Distributed and (b) equivalent SDOF systems

[ii]Taking the peak displacement under *LOAD_BLAST and dividing by the experimental peak displacements for the cleared plates

where m, c and k are the mass, damping and stiffness of the system, $\ddot{z}$, $\dot{z}$ and z are the acceleration, velocity and displacement, and $F(t)$ is the externally applied force. The equivalent SDOF method works on the basis of 'transforming' the distributed properties of the real life system into equivalent single-point properties, where the displacement of the single-degree system is defined as the displacement at the point of peak displacement in the real life system (Figure 5.10). Ignoring damping, the dynamic equation of motion of the equivalent system is

$$m_e \ddot{z} + k_e z = F_e(t), \tag{5.3}$$

where m_e, k_e and $F_e(t)$ are the equivalent mass, stiffness and force. The transformation from distributed to single-degree properties is performed by equating energy between the two systems: the equivalent mass has equal kinetic energy, the equivalent resistance has equal internal strain energy and the equivalent loading has equal work done to the distributed system. This introduces the concept of 'transformation factors', which will be explained in the following section. For any distribution of mass and loading, providing the transformation is performed correctly, the response of the SDOF system will be identical to the response of the chosen reference point of the real life system, in both magnitude and time (Morison 2006).

5.5.2 Transformation Factors and Natural Period

In order to transform the distributed properties into their single-degree equivalents; mass, stiffness and load transformation factors are required. The normalised deflected shape function, ϕ, is given as the deflected shape at any point on the structure divided by the displacement at the point of maximum deflection, i.e. $\phi(x) = z(x)/z_{max}$.

By equating the kinetic energy of the two systems, the *mass factor*, K_M, defined as the factor used to transform the distributed mass into the equivalent mass, $m_e = K_M m$, is given as

$$K_M = \frac{\int_0^L \phi(x)^2 \, \mathrm{d}x}{L} \tag{5.4}$$

where L is the span of the element. The *load factor*, K_L, defined as the factor used to transform the distributed load into the equivalent load, $F_e(t) = K_L F(t)$ is given by equating the work done of the real and distributed systems,

$$K_L = \frac{\int_0^L \phi(x) \, \mathrm{d}x}{L}. \tag{5.5}$$
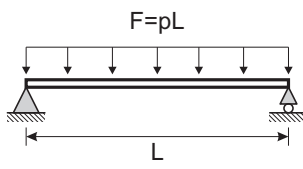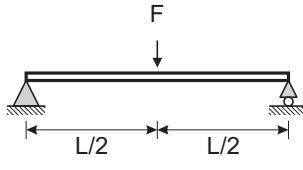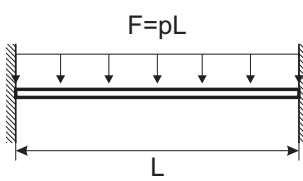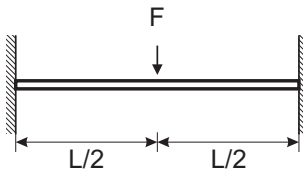
Loading diagram	Strain range	Load Factor, K_L	Mass Factor, K_M	Max. Resistance, R_u	Spring constant, k
F=pL (simply supported, distributed)	elastic	0.64	0.50	$\dfrac{8M_m}{L}$	$\dfrac{384EI}{5L^3}$
	plastic	0.50	0.33	$\dfrac{8M_m}{L}$	0
F (simply supported, point load, L/2 L/2)	elastic	1.00	0.49	$\dfrac{4M_m}{L}$	$\dfrac{48EI}{L^3}$
	plastic	1.00	0.33	$\dfrac{4M_m}{L}$	0
F=pL (fixed, distributed)	elastic	0.53	0.41	$\dfrac{12M_s}{L}$	$\dfrac{384EI}{L^3}$
	elastic/plastic	0.64	0.50	$\dfrac{8(M_s + M_m)}{L}$	$\dfrac{384EI}{5L^3}$
	plastic	0.50	0.33	$\dfrac{8(M_s + M_m)}{L}$	0
F (fixed, point load, L/2 L/2)	elastic	1.00	0.37	$\dfrac{4(M_s + M_m)}{L}$	$\dfrac{192EI}{L^3}$
	plastic	1.00	0.33	$\dfrac{4(M_s + M_m)}{L}$	0

Table 5.6: Transformation factors for beams and one-way slabs (Biggs 1964)

Equating internal strain energy between the two systems yields the same transformation factor as Equation 5.5, hence the equivalent stiffness can be given as $k_e = K_L k$. The dynamic equation of motion for the SDOF system now becomes

$$K_M m\ddot{z} + K_L kz = K_L F(t). \tag{5.6}$$

Transformation factors based on static deformation profiles are given in Table 5.6 for one-way spanning beams under different loading and support conditions. The maximum resistance, R_u, is given in terms of the moment capacity at mid-span, M_m, and moment capacity at the supports, M_s. The spring constant, k, is also shown in Table 5.6, in terms of EI, the bending stiffness of the element.

With knowledge of the equivalent mass and stiffness, the angular frequency of an SDOF system under free vibration, ω, can be given as

$$\omega = \sqrt{\frac{k_e}{m_e}} \tag{5.7}$$

which gives the natural period as

$$T = \frac{2\pi}{\omega} = 2\pi\sqrt{\frac{m_e}{k_e}}. \tag{5.8}$$

5.5.3   Closed Form Solution

Biggs (1964) presents an analytical solution for the dynamic response of an equivalent SDOF system subjected to a suddenly applied, linearly decaying triangular pulse of peak value, $F_{e,max}$, and duration, t_d, i.e.

$$F_e(t) = \begin{cases} F_{e,max}\left(1 - \dfrac{t}{t_{d,lin}}\right), & t \le t_{d,lin} \\[2mm] 0, & t > t_{d,lin} \end{cases} \tag{5.9}$$

The time-varying displacement of the system can be evaluated purely as a function of the equivalent force, stiffness and angular frequency and is computed in two stages: response during load application ($t \le t_d$) and response after load application ($t > t_d$),

$$z(t) = \begin{cases} \dfrac{F_{e,max}}{k_e}(1 - \cos\omega t) + \dfrac{F_{e,max}}{k_e t_d}\left(\dfrac{\sin\omega t}{\omega} - t\right), & t \le t_d \\[3mm] \dfrac{F_{e,max}}{k_e \omega t_d}\left[(\sin\omega t) - \sin\omega(t - t_d)\right] - \dfrac{F_{e,max}}{k_e}\cos\omega t, & t > t_d \end{cases} \tag{5.10}$$

Whilst this is a potentially very powerful tool for predicting the response of structures subjected to blast loads, the over-simplification of the blast pressure may not be valid. Closed form solutions for exponentially decaying loads are presented by Gantes & Pnevmatikos (2004), however the negative phase is represented by an extended Friedlander form, which, as discussed previously, may not be an accurate representation of the negative phase of the blast load. In order to evaluate target response for more complex forcing and resistance functions, explicit numerical analysis is required.

5.5.4   Linear Acceleration Method

The equation of motion (5.6) can be solved using the linear acceleration method (Biggs 1964) depicted in Figure 5.11. Assuming the acceleration varies linearly across the time-step, Δt, the acceleration at any time, t_j, between times t_i and $t_{i+\Delta t}$, can be given as

$$\ddot{z}_j = \ddot{z}_i + \frac{\ddot{z}_{i+\Delta t} - \ddot{z}_i}{\Delta t}(t_j - t_i). \tag{5.11}$$
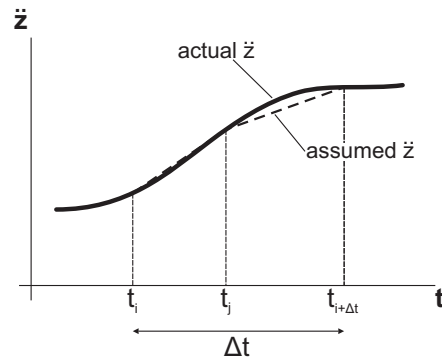
Figure 5.11: Linear acceleration method

The velocity is given as

$$\dot{z}_j = \dot{z}_i + \int_{t_i}^{t_j} \ddot{z} \, dt$$

$$\text{or} \quad \dot{z}_j = \dot{z}_i + \ddot{z}_i \left(t_j - t_i \right) + \frac{\ddot{z}_{i+\Delta t} - \ddot{z}_i}{2\Delta t} \left(t_j - t_i \right)^2 ,$$

(5.12)

which, at $t_j = t_{i+\Delta t}$ becomes

$$\dot{z}_{i+\Delta t} = \dot{z}_i + \frac{\Delta t}{2} \left(\ddot{z}_{i+\Delta t} - \ddot{z}_i \right).$$

(5.13)

The displacement at $t_{i+\Delta t}$ is given as

$$z_{i+\Delta t} = z_i + \int_{t_i}^{t_{i+\Delta t}} \dot{z} \, dt$$

$$\text{or} \quad z_{i+\Delta t} = \dot{z}_i \Delta t + \frac{(\Delta t)^2}{6} \left(2\ddot{z}_i + \ddot{z}_{i+\Delta t} \right).$$

(5.14)

In order to determine the displacement at $t_{i+\Delta t}$, the acceleration at $t_{i+\Delta t}$ must be known. The equation of motion of the SDOF system (5.3) gives the acceleration at $t_{i+\Delta t}$ as

$$\ddot{z}_{i+\Delta t} = \frac{F_e(t_{i+\Delta t})}{m_e} - \frac{k_e z_{i+\Delta t}}{m_e}$$

(5.15)

which can be substituted into Equation 5.14 to yield

$$z_{i+\Delta t} = \frac{z_i + \dot{z}_i \Delta t + \dfrac{(\Delta t)^2}{3} \ddot{z}_i + \dfrac{(\Delta t)^2}{6} \dfrac{F_e(t_{i+\Delta t})}{m_e}}{1 + \dfrac{(\Delta t)^2}{6} \dfrac{k_e}{m_e}}.$$

(5.16)

This allows the equation of motion for the SDOF system to be solved at each interval

until the solution time is reached. The linear acceleration method does not require the complete mathematical description of force and resistance functions and instead can use any arbitrary time-varying or displacement-varying function. One drawback of the linear acceleration method when compared to the closed form solution is that the accuracy is dependent on time-step size. A greater accuracy requires a greater number of calculations, but given the simplicity of the calculations at each time-step, convergence is rarely difficult to achieve.

5.5.5   Verification of an SDOF Model Under a Uniform Load

An equivalent SDOF model was run and the results compared to the finite element plate displacements obtained from the preliminary mesh study conducted in Section 5.3.1. The SDOF model was analysed under the same loading conditions (a linear load decaying from 10 kPa over a duration of 10 ms), boundary conditions (one model with the plate fully clamped on all sides, and one model with the plate simply supported on two opposite edges only), material properties and span. The SDOF properties of the two plates are shown in Table 5.7, where the transformation factors for the simply supported plate are given in Biggs (1964) (summarised in Table 5.6) and the transformation factors for the clamped plate are given in Morison (2006).

Parameter	Symbol	Unit	Value	
			Clamped	Simply Supported
Span	L	m	1	1
Thickness	d	mm	10	10
Load factor	K_L	-	0.308	0.640
Mass factor	K_M	-	0.182	0.500
Elastic stiffness coefficient	$k/(EI/L^3)$	-	808.5	76.8
Equivalent stiffness	k_e	kN/m	4357.8	860.2
Equivalent mass	m_e	kg	14.29	39.25
Natural frequency	f	Hz	87.90	23.56
Natural period	T	ms	11.38	42.44

Table 5.7: Dynamic properties of the clamped and simply supported plates used for verification of the SDOF method

Figure 5.12 shows the SDOF and FE displacements for both cases. It can be seen that the overall behaviour is well captured by the SDOF approximation, and that there is good agreement between the two models for peak displacement and natural period. The peak SDOF displacements are 1.06 mm for the clamped plate and 5.18 mm for the simply supported plate, which correspond to differences of 5% and 6% between the SDOF and FE models. It can therefore be said with confidence that the SDOF method can be used to accurately represent elastic plate deflections under uniform loading.
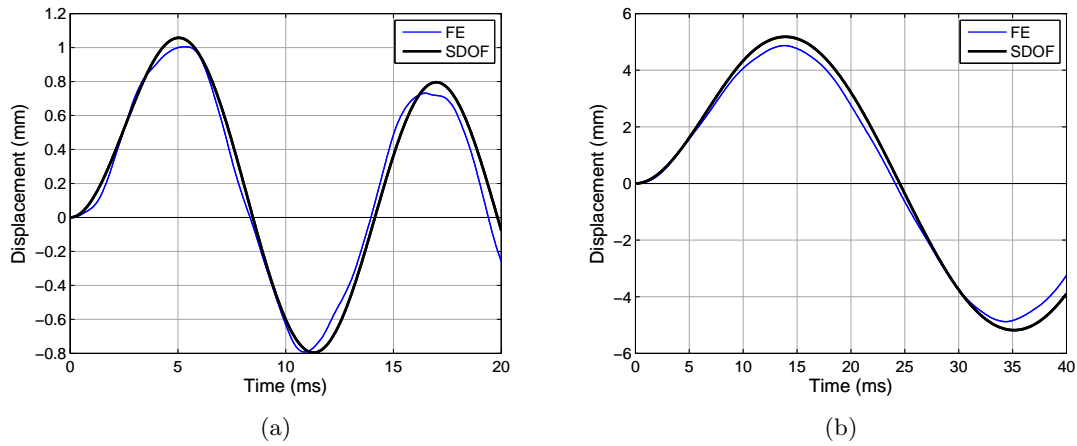
Figure 5.12: Finite element and SDOF displacements for 1m square, 10mm thick plates under a spatially uniform, linearly decaying load with a peak of 10 kPa and duration of 10 ms for (a) Clamped (b) Simply supported boundary conditions

5.5.6 SDOF Under Non-Uniform Load

This section details the derivation and verification of a spatial load factor for the inclusion of a spatially non-uniform load in an SDOF model. The spatial load factor has been developed specifically for work conducted as part of this thesis, but has a wider application as will be discussed in Chapter 7 of this thesis.

Derivation of the Spatial Load Factor

The derivation of the SDOF load transformation factor for a loaded plate assumes that the spatial variation of pressure is invariant of time. This assumption is not valid when considering the effects of blast wave clearing. In order to ensure that the spatially varying pressure, $p(x, y, t)$, acting on the face of a target can be validly represented in an SDOF model, the *energy equivalent uniform pressure* and *spatial load factor* are derived in this section.

Following the energy balance methodology of the equivalent SDOF method, the spatially varying blast pressure acting on a target can be transformed into an energy equivalent uniform pressure such that the work done at any instant is equal for both the uniform pressure, $p_{equiv}(t)$, and 'real-life' pressure, $p(x, y, t)$, i.e.

$$\int_A p(x, y, t)\phi(x, y) \ \mathrm{d}A = \int_A p_{equiv}(t)\phi(x, y) \ \mathrm{d}A, \qquad (5.17)$$

where A is the panel area and ϕ is the shape function describing the normalised deflected shape of the target.

Since the uniform pressure is independent of x and y, Equation 5.17 can be rearranged to give

$$p_{equiv}(t) = \frac{\displaystyle\int_A p(x,y,t)\phi(x,y) \, \mathrm{d}A}{\displaystyle\int_A \phi(x,y) \, \mathrm{d}A}, \tag{5.18}$$

where the two-dimensional shape function can be expressed in separable variable form, $\phi(x,y) = \phi(x)\phi(y)$ and is constant with time (Blevins 1979). This assumes that the spatial variation of pressure is not sufficiently non-uniform at any instant in time to cause deviation from the static deformed profile under a uniform load. This also implies that the non-uniformity of the load changes over short enough durations to ensure the plate does not have enough time to adopt a different deformed shape.

The SDOF equivalent force can be given as

$$F_e(t) = K_L F_{equiv}(t) \tag{5.19}$$

where K_L is the load factor and $F_{equiv}(t)$ is the energy equivalent uniform pressure multiplied by the area of the plate, $F_{equiv}(t) = A p_{equiv}(t)$.

The spatial load factor, $K_S(t)$, can be defined as a time varying load factor used to transform the *total* force acting on the plate at any instant into the *energy equivalent* force. The equivalent SDOF force now becomes

$$F_e(t) = K_L K_S(t) F(t). \tag{5.20}$$

Equations 5.19 and 5.20 can be combined to give

$$K_S(t)F(t) = F_{equiv}(t), \tag{5.21}$$

and from the definition of the energy equivalent force acting on the plate (Equation 5.18 multiplied by the target area) the time-varying spatial load factor, K_S, can be expressed as

$$K_S(t) = \frac{\displaystyle\int_A p(x,y,t)\phi(x,y) \, \mathrm{d}A}{\displaystyle\int_A p(x,y,t) \, \mathrm{d}A \int_A \phi(x,y) \, \mathrm{d}A}. \tag{5.22}$$

K_S is effectively a measure of the non-uniformity of the applied pressure and, combined with the traditional load factor, can be used to ensure that the force acting on the SDOF model is equivalent in terms of energy to the real life system for the entire duration of loading. It can be easily seen from Equation 5.22 that if the distribution of pressure, $p(x, y, t)$, is uniform (independent of x and y) at an instant in time, the spatial load factor is equal to unity for that value of t. A spatially uniform pressure therefore has $K_S = 1$ for the entire duration.

The spatial load factor is derived using the same assumptions and conditions as the traditional load factor and ensures the analysis is consistent with the SDOF method. Although the spatial load factor is used to model the effects of blast wave clearing, it could in practice be used to transform any spatially varying load into an energy equivalent uniform load.

Verification of the Spatial Load Factor

In order to demonstrate the ability of the spatial load factor to conserve energy between a non-uniform 'real life' distribution of pressure and an SDOF equivalent uniform pressure, an SDOF model with a non-uniform load was set up and compared to a finite element model.

The plate was modelled as a 1×1 m steel plate with 10 mm thickness and elastic material properties, with fully clamped boundary conditions. The plate was loaded with a linearly decaying pressure load of 10 kPa over 10 ms, with a central 0.5×0.5 m section loaded with a pressure of magnitude 20 kPa decaying over a duration of 10 ms, as shown in Figure 5.13. The FE model was modelled with the pressure load applied as nodal-point forces at the nodes.
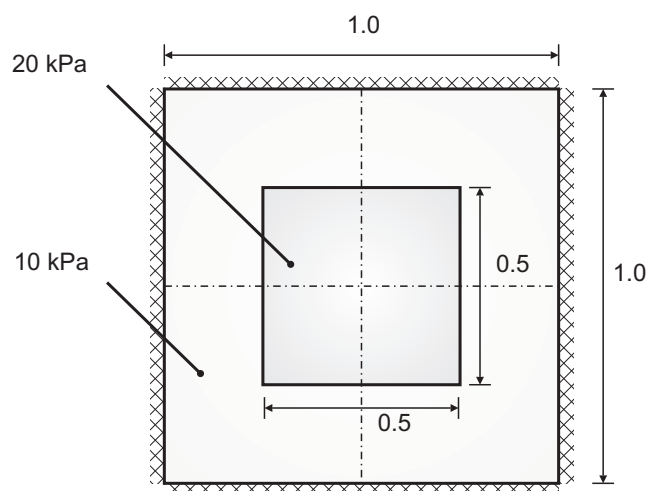
Figure 5.13: Arrangement of the plate used for verification (dimensions in m)

The corresponding SDOF model was analysed under two load cases:

- Conserving energy using the spatial load factor, K_S. From Euler-Bernoulli beam theory, ignoring in-plane membrane resistance, the deflected shape of a fixed-fixed beam under a uniform load gives the shape functions as

$$\phi(x) = \frac{16x^2(L-x)^2}{L^4}, \qquad \phi(y) = \frac{16y^2(L-y)^2}{L^4}. \qquad (5.23)$$

  Numerically solving Equation 5.22 gives $K_S(t) = 1.30$. The peak total force acting on the plate is 12.5 kN; applying the spatial load factor gives the peak energy equivalent uniform force as $F_{e,max} = 16.25$ kN.

- Assuming $K_S(t) = 1$ and modelling the SDOF under the total load only, with $F_{e,max} = 12.5$ kN.

Figure 5.14 shows the displacement-time histories of the FE plate and SDOF models, along with the respective applied force-time histories (spatial load factor shown on minor vertical axis). It can be seen that, by using the spatial load factor as a simple adjustment to balance energy between the real life and SDOF applied forces, the SDOF method is able to evaluate the response of a system to non-uniform loading.
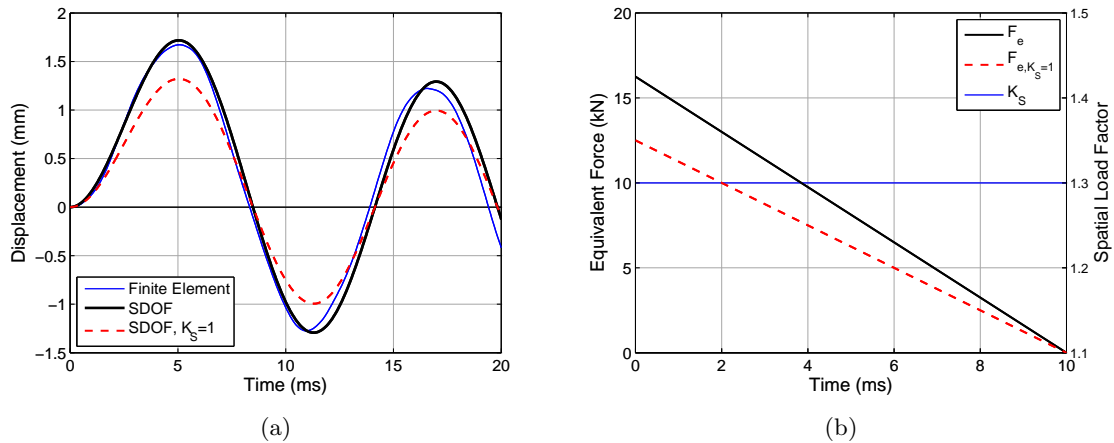
Figure 5.14: (a) Finite element and SDOF displacements and (b) Energy equivalent uniform pressure (F_e) and average pressure ($F_{e,K_S=1}$) loads applied to the SDOF model shown on major vertical axis. Temporal variation of $K_S(t)$ shown on minor vertical axis

The spatial load factor is attractive for scenarios where the spatial variation of load and thus K_S are not constant with time. For these scenarios, the temporal function of $K_S(t)$ can be evaluated at the start of the analysis and used throughout, as it is a function of the normalised deformed profile only, which is assumed to be unchanged during the analysis, rather than being a function of actual plate deformation. This approach is simple and is congruent with the inherent assumptions of the SDOF method, suggesting that wherever the SDOF method is applicable, so is the use of the spatial load factor.

5.6 SDOF Analysis

5.6.1 Model Setup

With a verified model for analysing elastic plates subjected to non-uniform loading, a series of SDOF analyses was performed to model the displacement of plates subjected to blast loads in order to validate the results against the experimental displacements detailed in Section 5.2. The dynamic SDOF properties of the plate are shown in Table 5.8.

Parameter	Symbol	Unit	Value
Span	L	m	0.305
Thickness	d	mm	0.835
Load factor	K_L	-	0.53
Mass factor	K_M	-	0.41
Elastic stiffness coefficient	$k/(EI/L^3)$	-	384
Equivalent stiffness	k_e	kN/m	23.39
Equivalent mass	m_e	kg	0.262
Natural frequency	f	Hz	47.52
Natural period	T	ms	21.04

Table 5.8: Dynamic properties of the plate used in the SDOF analysis

Clearing Predictions

Section 2.3 detailed several clearing predictive methods which have particular application for approximate design approaches such as the SDOF method. The empirical clearing predictions of Kinney & Graham (1985) and UFC-3-340-02 (US Department of Defence 2008), shown in Equations 5.24 and 5.25 respectively, are not suitable for use in this application because the expressions yield clearing times of 3.45 and 2.94 ms respectively, which are both larger than the positive phase duration for all scaled distances.

$$t_c = \frac{3S}{a} \tag{5.24}$$

$$t_c = \frac{4S}{(1+R)a} \tag{5.25}$$

where

$$
\begin{aligned}
t_c &= \text{clearing time (s)} \\
a &= \text{shock front velocity (m/s)} \\
S &= \text{min(front height, half-width) (m)} \\
G &= \text{max(front height, half-width) (m)} \\
R &= S/G
\end{aligned}
$$

In the case where the clearing time is larger than the positive phase, the literature recommends neglecting clearing and simply using the full reflected pressure. From the difference in the experimental displacements between cleared and non-cleared loading it is evident that neglecting blast wave clearing is not valid for this arrangement.

The improved methodology of Rose & Smith (2000) (Section 2.3.3) cannot be used for this application either. The scaled target heights for the SDOF analyses in this section range from 1.76 $m/kg^{1/3}$ (for the smallest charge mass) to 1.16 $m/kg^{1/3}$ (for the largest charge mass), which exceed the largest scaled target size of 0.8 $m/kg^{1/3}$ for which clearing estimations are available (Table 2.4).

The ConWep Loads on Structures (LOS) subroutine calculates the specific positive phase impulse acting on a rectangular target by discretising the target into a grid of 65 × 65 nodes and providing impulse values at each node. This subroutine claims to account for blast wave clearing by reducing the specific impulse, however the methodology behind this is unclear. With reference to Figure 5.7, the Hudson method predicts that the clearing wave will reach the furthest point (from the vertical free edges) of the target within 1.2 ms of load application. ConWep LOS impulse predictions for 75 g PE4, shown in Figure 5.15, suggest that an area of approximately 305 × 200 mm of the target will experience the full reflected impulse and remain unaffected by clearing. This indicates that the clearing wave has travelled only 190 mm during the positive phase (failing to even reach the target from the vertical edges of the reflecting surface), with a wavespeed of approximately 80 m/s. This suggests that the clearing methodology implemented in ConWep LOS may significantly under-estimate the effect of clearing and thereby over-estimate the impulse acting on a target, a point also highlighted in Tyas et al. (2011a).
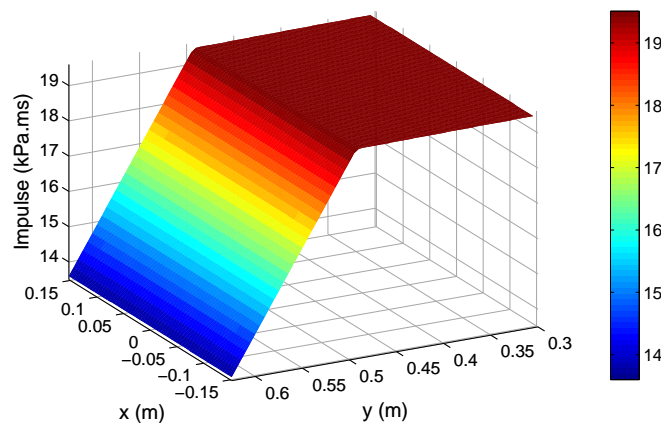
Figure 5.15: ConWep LOS specific impulse acting on the cleared target for 75 g PE4. Dimensions of the finite target and reflecting surface are shown in Figure 5.2

Load Cases Applied to the SDOF Model

The SDOF model was analysed under four load cases for each scaled distance, giving a total of 20 analyses. The load cases represent the typical ways blast pressure is modelled in the literature:

- **Cleared** – The load curves determined from the superposition of Hudson clearing corrections and full reflected pressure from Section 5.4.1 were used as inputs to solve Equation 5.22 at each time-step – giving the temporal relationship for $K_S(t)$, which was then used to give the temporal variation of the SDOF equivalent force (Equation 5.20). This process was repeated for all charge masses to give the energy equivalent uniform load acting on the plates. Figure 5.16 shows the transformation from average pressure to energy equivalent pressure using the spatial load factor for 175 g PE4, assuming the elastic deformed profile of $\phi(x)$ for a clamped beam from Equation 5.23 and $\phi(y) = 1$.
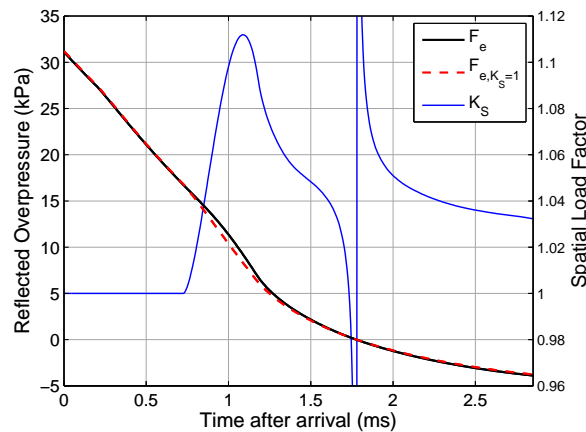
Figure 5.16: Energy equivalent uniform pressure (F_e) and average pressure $(F_{e,K_S=1})$ acting on the plate (major vertical axis) and temporal variation of spatial load factor (minor vertical axis) for 175 g PE4

It can be seen that $K_S = 1$ before any clearing waves arrive because the applied pressure is still uniform. The clearing wave from the top face arrives at $t = 0.19$ ms, however the spatial load factor remains unchanged as the plate is unsupported in the y direction and the work done between the total force and energy equivalent force is identical. As soon as the clearing waves arrive from the vertical edges of the target at $t = 0.70$ ms, $K_S > 1$. As the clearing wave travels in from the edges, the central portion of the target is still subjected to the full reflected pressure. This is acting at the point of largest deflection and doing more work, hence the scenario is similar to that in Figure 5.13 and the energy equivalent pressure is greater than the average pressure, hence $K_S > 1$. There is a discontinuity in K_S when the loading changes from positive to negative.

- **Non-Cleared** – Full reflected positive and negative phase pressure applied as a uniform load with no clearing corrections. The positive phase was modelled with the Friedlander equation and the negative phase was modelled using the cubic approximation. Blast parameters were determined from the semi-empirical predictions in UFC-3-340-02 (US Department of Defence 2008).

- **Linear** – A triangular pulse with peak reflected pressure and shortened duration to preserve positive phase impulse. The negative phase is neglected. This does not include clearing and is typically used as a first stage in design.

- **ConWep LOS** – The equivalent uniform impulse, given by ConWep LOS, applied as a bilinear triangular pulse. The applied pressure is given as

$$
p_r(t) = \begin{cases} p_{so,max}\left(1 - \dfrac{t}{t_{d,lin}}\right) + (p_{r,max} - p_{so,max})\left(1 - \dfrac{t}{t_c}\right), & t \leq t_c \\[2ex] p_{so,max}\left(1 - \dfrac{t}{t_{d,lin}}\right), & t \leq t_{d,lin} \end{cases}
\tag{5.26}
$$

where the clearing time is calculated such that the integral of Equation 5.26 is equal to the equivalent uniform impulse, i, given by ConWep LOS, i.e.

$$
t_c = \frac{2(i - i_{so})}{p_{r,max} - p_{so,max}}
\tag{5.27}
$$

This takes ConWep clearing predictions into account but ignores the negative phase.

Figure 5.17 shows all four separate pressure-time histories applied to the SDOF model for 175g PE4, truncated at the end of the positive phase of the non-cleared load. Loading parameters for all SDOF analyses are summarised in Table 5.9.
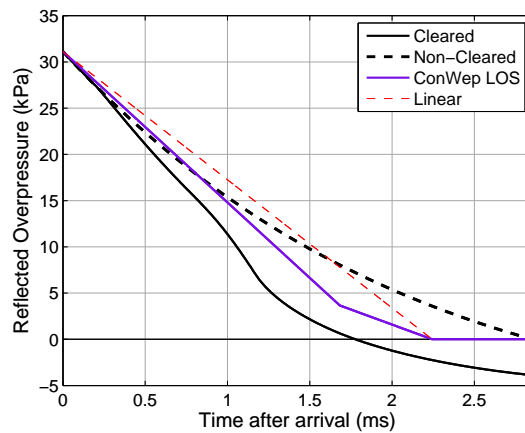
Figure 5.17: Positive phase pressure-time histories used in the SDOF analysis for 175 g charge mass

W	Loading	Parameter						
(g PE4)		t_a (ms)	$p_{r,max}$ (kPa)	$p_{r,min}$ (kPa)	t_d (ms)	t_d^- (ms)	i_r (kPa.ms)	i_r^- (kPa.ms)
50	Cleared	14.29	17.52	5.01	1.357	5.472	11.49	17.12
	Non-Cleared	14.29	17.52	5.06	2.147	5.994	14.82	17.05
	Linear	14.29	17.52	-	1.692	-	14.82	-
	ConWep LOS	14.29	17.52	-	1.692	-	14.34	-
75	Cleared	13.91	20.98	5.57	1.468	6.052	14.69	21.15
	Non-Cleared	13.91	20.98	5.77	2.356	6.736	19.55	21.87
	Linear	13.91	20.98	-	1.864	-	19.55	-
	ConWep LOS	13.91	20.98	-	1.864	-	18.66	-
108	Cleared	13.54	24.78	6.11	1.589	6.610	18.32	25.51
	Non-Cleared	13.54	24.78	6.50	2.560	7.482	25.08	27.35
	Linear	13.54	24.78	-	2.024	-	25.08	-
	ConWep LOS	13.54	24.78	-	2.024	-	23.65	-
140	Cleared	13.27	27.97	6.53	1.684	7.029	21.46	29.11
	Non-Cleared	13.27	27.97	7.07	2.714	8.062	29.96	32.08
	Linear	13.27	27.97	-	2.142	-	29.96	-
	ConWep LOS	13.27	27.97	-	2.142	-	27.87	-
175	Cleared	13.01	31.12	6.91	1.776	7.409	24.58	32.56
	Non-Cleared	13.01	31.12	7.61	2.854	8.598	34.91	36.79
	Linear	13.01	31.12	-	2.244	-	34.91	-
	ConWep LOS	13.01	31.12	-	2.244	-	32.13	-

Table 5.9: SDOF loading parameters for the numerical analyses

5.6.2   Results and Discussion

The SDOF displacement-time histories for the plates under the cleared load case are shown in Figure 5.18, along with the experimental displacement of the cleared plates for comparison. For clarity, SDOF displacements to all other load cases are omitted but will be discussed later. Table 5.10 summarises the peak displacement for the SDOF models under all load cases, as well as the peak experimental displacements for cleared and non-cleared plates. As with the previous numerical models, the load was applied at time $t = 0$ and the displacements were time-shifted to correspond with the arrival time given by ConWep.

There is a very good level of agreement between numerical and experimental displacements in Figure 5.18 for all charge masses. The peak displacement and duration of inward displacement (i.e. the natural period) is well predicted by the SDOF model under the cleared load. It is interesting to note that the early-time SDOF response slightly over-predicts the response of the plate, the effect of which is most pronounced at approximately 16 ms after detonation for all tests. There are two contributing factors to this: firstly, assuming the blast wave strikes planar to the target and subjects the entire target to the peak reflected pressure at the beginning of the analysis may slightly over-predict the initial

(a) 50g PE4

(b) 75g PE4

(c) 108 g PE4

(d) 140 g PE4

(e) 175 g PE4

Experiment – Cleared
Experiment – Cleared
SDOF
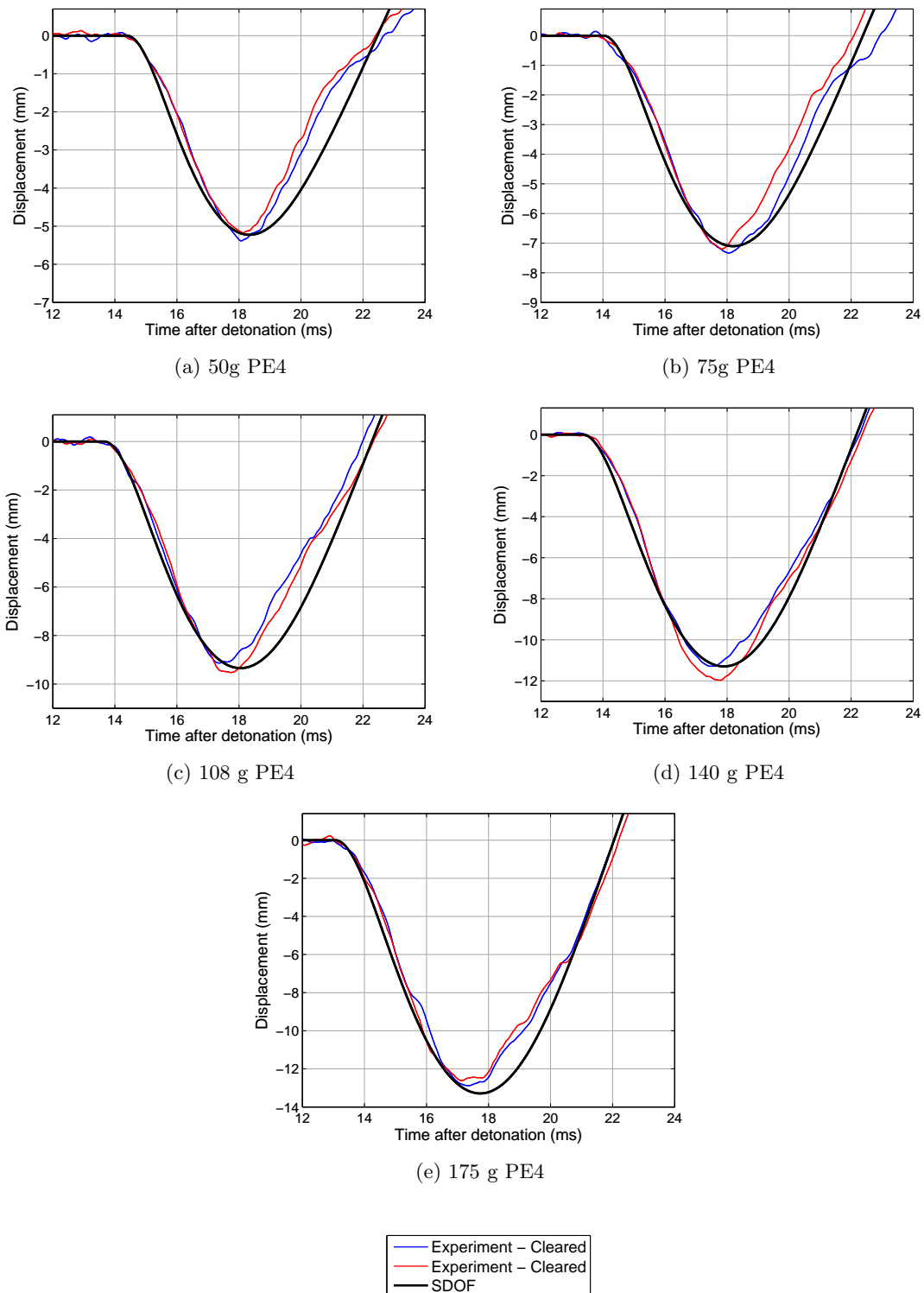
Figure 5.18: Experimental and SDOF displacement-time histories for the cleared plates

W	Peak displacement (mm)					
(g PE4)	Experimental[*]		SDOF			
	Cleared	Non-Cleared	Cleared	Non-Cleared	Linear	ConWep LOS
50	5.29	8.19	5.23	7.50	9.97	9.63
75	7.27	10.26	7.10	10.45	13.14	12.53
108	9.33	13.78	9.34	14.03	16.86	15.83
140	11.63	16.82	11.29	17.18	20.07	18.69
175	12.75	19.46	13.29	20.42	23.36	21.52

[*] averaged result

Table 5.10: Peak experimental and SDOF displacements

velocity; secondly, the assumption that the plate begins to deform in the normalised shape *immediately* after application of the load implies that the initial velocity in the centre of the target is larger than the initial velocity at the edges, which may cause an over-prediction of initial kinetic energy.

These assumptions are inherent to the SDOF method, and any work towards correcting the modelling of initial conditions would not likely yield noticeable or worthwhile improvements. The agreement between experimental and numerical peak displacement of the plates, and the times at which these occur, give confidence in both the ability of the SDOF method to model plate deformation and also of the Hudson clearing corrections to accurately model the cleared blast pressure acting on the target. The difference between peak displacement for the cleared SDOF and experimental results, with reference to Table 5.10, is less than 5% for all analyses.

The peak displacements for non-cleared experimental and SDOF analyses, also given in Table 5.10, show that if the target is part of a reflecting surface that is infinite in lateral extent, modelling the target as an equivalent SDOF system under the full (non-cleared) reflected blast pressure history can predict target response to within 2-8% of the experimental non-cleared peak displacement, which again provides evidence for the validity of the equivalent SDOF method.

Whilst the results of the non-cleared plates are in good agreement between experimental and numerical results, it is worth examining what would happen if clearing were neglected for this series of analyses. If the peak displacements for the SDOF model under the *non-cleared* load were taken as approximations of the displacement of the plates in the finite reflecting surface, the results would be over-predicted by between 42-60%.

The need to model the negative phase correctly is also highlighted by the peak displacements in Table 5.10. For the non-cleared plates, modelling the blast pressure as an impulse-preserved triangular pulse does not yield satisfactory results, over-predicting the non-cleared displacements by 19-28%. This over-prediction in peak displacement is solely due to the inability of the linear load to model the reduction in impulse caused

by the negative phase, which is a particularly important consideration for large scaled distances and impulsive target response (Teich & Gebbeken 2010). If the response under the linear load was taken as an approximation to the displacement of the cleared plates (i.e. if both the negative phase and clearing were neglected), the numerical model would over-predict the experimental displacements by as much as 88%.

It is also clear from the numerical results that the clearing predictions from ConWep LOS do not allow correct modelling of the cleared blast pressure and therefore cannot be used to accurately model the deflection of plates situated in a non-infinite reflecting surface. Not only are the results typically 61-82% greater than the experimental displacements of the cleared plates, but the reduction in peak displacement attributed to clearing is significantly lower than the experimental values – by taking the peak displacement under ConWep LOS and dividing by the peak displacement under the linear load, the supposed reduction in peak displacement attributed to blast wave clearing varies from 3-8%. The experimental results show that the effect of clearing is much more pronounced, with clearing accounting for a reduction in peak pressure of 29-35%.

The SDOF modelling in this section has shown that transforming the total force acting on the plate into an energy equivalent uniform force using the spatial load factor, K_S, allows non-uniform cleared blast pressures to be included in equivalent SDOF models.

5.7   Discussion of Modelling Approaches

This chapter has detailed three different modelling approaches: coupled ALE-Lagrangian finite element, uncoupled Lagrangian finite element and single-degree-of-freedom analyses. It is the purpose of this section to discuss the suitability of these methods for evaluating target response, and also to collate the data from the numerical analyses.

All numerical methods achieved a similar level of agreement with the experimental results, both qualitatively and quantitatively. Figures 5.19 and 5.20 summarise the peak finite element and SDOF displacements respectively from Tables 5.4, 5.5 and 5.10. From the results presented it can be said that, discounting the linear load SDOF approximations for reasons outlined previously, each method can adequately model (or approximate) the physical processes and therefore can be used with confidence as a means for modelling the response of flexible targets subjected to blast loads.

The results demonstrate that an increase in model complexity does not necessarily correlate to an increase in the quality and fidelity of the results, nor does it make the model inherently more capable of considering additional factors. If the underlying assumptions of a model are valid and based on rigorous treatment of physical principles there is nothing to suggest that more complex situations cannot be represented by simplifications. This has been evidenced by the inclusion of blast wave clearing in SDOF models as part of this study.
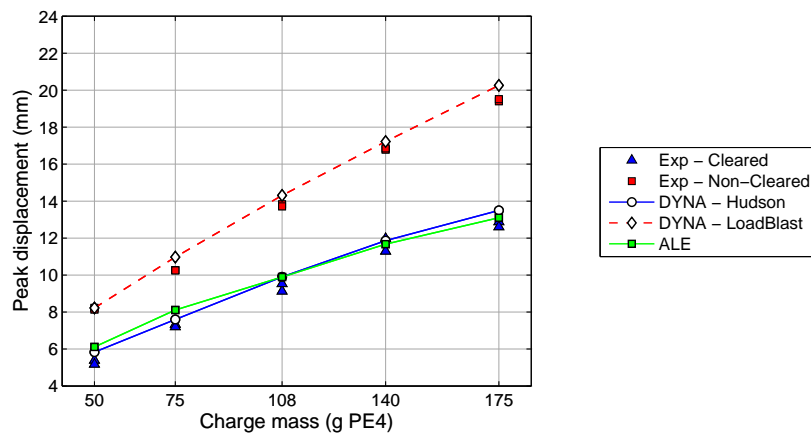
Figure 5.19: Experimental and FE peak displacements
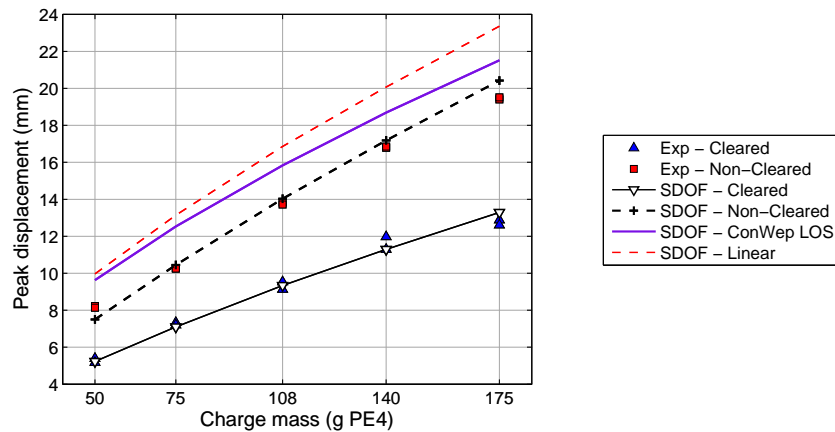
Figure 5.20: Experimental and SDOF peak displacements

With increasing model complexity there is a growing conflict between the ability of the model to accurately replicate the physical processes and the need for reasonably sized simulations that will allow the analysis to be completed within a realistic timeframe. In the case of the coupled ALE-Lagrangian analyses the requirements to accurately model the blast wave propagation through air, the process of blast wave clearing, the interaction between the blast wave and the target and the response of the target itself, all using finite elements, cannot all be satisfied and a compromise must be met in the form of a coarser mesh and shortened analysis time. These compromises adversely affect the quality of the model, leading to no improvement in the results at considerably increased computation time.

Figure 5.21 shows the ratio of peak numerical to peak experimental displacements of the cleared plates for the three different numerical approaches for all charge masses. The average difference between numerical and experimental results for the coupled analyses is 7.3%, compared to 5.8% for the uncoupled analyses and 2.1% for the SDOF analyses.
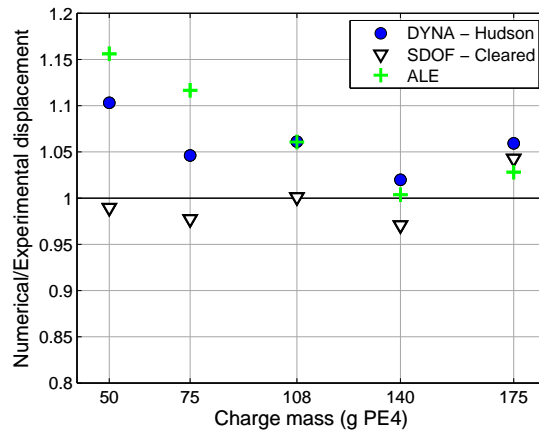
Figure 5.21: Ratio of numerical/experimental peak displacements for the cleared plates

The difference in peak response is negligible, however, when considering the running times of the analyses:

- The coupled analyses were run for 168 hours on the University of Sheffield HPC server. The time taken to simulate the blast wave propagating, in 2D axi-symmetry, through 6 m of free air was around 5 hours.

- The uncoupled analyses were typically run for 5–8 minutes (not including the time taken to generate the load curves using MatLab).

- The SDOF analyses were completed within seconds, including the time taken to generate the spatial and temporal variation of the clearing pressure and the time taken to evaluate the spatial load factor.

When analysing target response to cleared blast loads, the demonstrated validity and accuracy of approximate numerical methods should see such approaches preferred over complex numerical schemes. The dimensionless formulation of the Hudson approximation coupled with the short analysis time of the SDOF method enables a more detailed study of blast wave clearing to be undertaken, which is the subject of the following chapter.

5.8   Summary

This chapter has detailed a series of carefully controlled experimental measurements of the temporal deflection of simple elastic plates subjected to cleared and non-cleared blast loads. Deflection-time histories were recorded for steel plates located within a finite reflecting surface and a reflecting surface of effectively infinite lateral extent. A total of twenty tests were conducted, with the test plates located 6 m from hemispherical PE4 charges ranging from 50–175 g. This experimental work was conducted both to assess the accuracy of, and provide validation for, numerical modelling using different approaches.

Coupled ALE-Lagrangian analyses were conducted, where the detonation process and blast wave propagation through free air was evaluated in 2D axi-symmetry and then mapped onto a 3D air domain containing a part representing the target, which was meshed using shell elements. The blast pressure was transferred to the target using penalty coupling, with the process of blast wave clearing, and hence determination of the load, modelled using ALE elements. It was found that this method could determine the peak deflection of the finite targets to within 15% (typically within less than 8%) of the experimental displacements. The main cause for the difference between numerical and experimental results is attributed to the need for a large domain in order to model a sufficient length of the blast wave and hence increased mesh size of the model.

Following on from this, uncoupled Lagrangian analyses were conducted, where the plate was modelled using finite elements and the blast pressure was prescribed using load curves, i.e. fluid-structure interaction effects were ignored. The non-cleared plates were loaded using *load_blast, an in-built LS-DYNA loading module, whereas the cleared plates were loaded using the superposition of reflected pressure and Hudson (1955) clearing corrections.

Significant computational savings were achieved through not modelling the surrounding air, with the models running for 5–8 minutes as opposed to the 168 hour run time of the coupled models. The modelling results using simple load curves with and without the inclusion of clearing effects showed excellent correlation with the experimental deflection-time and peak deflection data, with the peak values differing by no more than 10% for both loading options. This indicates that using load curves derived from simple semi-empirical predictive methods and the application of the Hudson clearing corrections can be used with confidence in modelling, as long as the limiting assumptions of the Hudson approach are valid.

The single-degree-of-freedom method was introduced, which approximates the target as a single point equivalent and solves the dynamic equation of motion for the equivalent system. The spatial load factor, K_S, was derived as a function of the applied spatially non-uniform pressure and the normalised deflected shape of the target. This enabled a spatially non-uniform load to be correctly represented in an SDOF model (i.e. conserving energy between real life and equivalent systems) and has been verified for a simple non-uniform load case.

SDOF models were run under four load cases: cleared pressures comprising an energy equivalent superposition of reflected pressure and Hudson clearing corrections; non-cleared reflected pressures; a linearly decaying load with peak pressure and reflected impulse preserved; and a bilinear decaying load with peak pressure preserved and a reduced impulse to account for ConWep LOS clearing predictions. The linear and bilinear ConWep LOS load approximations did not yield satisfactory results, highlighting the need to model the load correctly even in the early stages of design.

Strikingly, the SDOF analyses with and without cleared loading corrections were in excel-

lent agreement with the experimental data, with peak displacements differing by no more than 8% of the experimental measurements for all numerical simulations. The demonstrated validity of the SDOF method gives confidence that this approach is suitable for initial analyses of loading events for geometrically simple scenarios. Furthermore, the low computational expense of the SDOF method coupled with the dimensionless formulation of the Hudson clearing predictions permits a wider investigation of the influence of blast wave clearing on the dynamic response of finite, flexible targets subjected to blast loads.

Chapter 6

The Influence of Clearing on Dynamic Response

6.1 Introduction

In the previous chapters it has been demonstrated that the Hudson (1955) clearing corrections provide a fast and accurate means for determining the cleared blast load acting on a target. When combined with the single-degree-of-freedom method for predicting target response, we are equipped with a simple and powerful way to determine the response of a target to cleared blast loading which has been shown to be in good agreement with a series of well controlled experimental trials.

Arguably, the main benefit of a scheme of such low computational cost is the ability to study a wide range of parameters in a short space of time. Many configurations of blast event and target properties can be analysed to enable a more complete description of the influence of blast wave clearing to be formulated. Due to the nature of the malicious use of high explosives, blast engineers are not given the luxury of being able to definitively say when or where a load will be acting, and can at best only estimate the magnitude of the load. This makes such a parametric study all the more important as it gives an idea of the likely target response over a broad range of scenarios, and should certainly be favoured over more computationally expensive 'higher order' schemes.

The US Department of Defence (2008) Design Manual UFC-3-340-02, *Structures to Resist the Effects of Accidental Explosions*, recommends the use of SDOF design charts first formulated by Biggs (1964). These charts present values of peak dynamic displacement, found from solution of the equivalent SDOF equation of motion under a number of load shapes and different target properties. Whilst this method is widely accepted in the literature (US Army Materiel Command 1974, US Department of Defence 2008, Cormie et al. 2009), one limitation is the fact that the blast load must be simplified, typically as an equivalent triangular pulse, in order for the peak displacement to be obtained.

Gantes & Pnevmatikos (2004) present improved design charts based on a more realistic exponential Friedlander (1946) load, which also takes into account a form of the negative phase (see Section 2.2.5), however this is under the assumption that the target forms part of a semi-infinite reflecting surface.

In the current literature, research into the effect of blast wave clearing on finite, flexible targets (Van Netten & Dewey 1997, Shi et al. 2007) has been limited to situations where the reflecting surface is so small and the 'length' of the blast wave is so large such that the deformable target is effectively loaded by the incident pressure (see Section 4.3). To date, there remains no published work detailing the influence of clearing on the response of flexible targets and no means to quantify this effect.

This chapter has two connected aims: the response of finite targets subjected to cleared blast loads will be evaluated for a range of parameters in an attempt to both understand and quantify the influence of blast wave clearing; and also to develop and provide detailed guidance on the likely response and damage a given target will sustain for a given cleared blast load. This will be achieved through a parametric study using the KB (Kingery & Bulmash 1984) semi-empirical load predictions with Hudson (1955) clearing corrections to determine the blast load, and the equivalent SDOF method to calculate the target response to this load.

6.1.1 Underlying Assumptions and Implementation

To facilitate the parametric study of this chapter, the following assumptions have been made relating to both prediction of the load and the application of this load to dynamic response calculations. These assumptions will be justified and their impact discussed with reference to the current literature as appropriate.

Loading Assumptions

The Hudson method assumes the following conditions:

- The blast wave is plane and parallel to the target surface, with the direction of travel perpendicular to the target face. This implies that the target dimensions are small relative to the charge stand-off, or that the stand-off is large.

- The depth of the target is sufficiently large so that no diffraction waves arrive from the rear of the target. Rose & Smith (2000) have shown these waves have negligible effect on the front-face load.

- The clearing wave propagates into stagnant air across the target face, i.e. no flow conditions exist in the direction of travel of the rarefaction wave.

- The velocity of the rarefaction wave is equal to the ambient sonic speed in air. This requires the incident pressure to be relatively low - Hudson judged that the

assumption was reasonable for peak incident pressures of less than 300 kPa, i.e. $Z > 2.0$ m/kg$^{1/3}$.

The following assumptions have been made when applying the load to the model:

- The clearing waves can be split into principal directions from vertical and horizontal target edges and can be superimposed to give the cleared pressure at any point on the target (Tyas et al. 2011a).

- Only one clearing wave propagates per free edge. The numerical study in Section 4.3.3 has shown that the Hudson predictions are adequate to describe this wave for the entire duration of the positive phase.

- Any clearing waves are neglected for $\eta > 1$ and the full reflected negative phase is modelled. Whilst in practice the clearing waves may arrive at some nodes during the negative phase, neglecting this will result in a conservative approximation of the negative phase. It is estimated that this will have little effect as it will only feature for large targets where the blast pressure is close to the full reflected pressure. The peak magnitude of a clearing wave for $\eta = 1$ is around 15% of the peak incident pressure and rapidly decreases for larger values of η.

- The Hudson formulation is based on a decay parameter, b, of 1. Within the report, however, Hudson (1955, page 16) states that *'the errors introduced by a variation $0.5 < b < 2.0$ are minor... the effect of variation in b for values near unity is very small, becoming noticeable only as $b \to 0$ or as b exceeds 5'.*[i] The waveform parameter varies between 2.0 and 0.5 for $4 < Z < 20$ (see Figure 2.4) and only exceeds 5 when $Z < 1.5$. The Hudson clearing corrections can be used throughout this range without any noticeable error.

Modelling Assumptions

Further to the above, a number of modelling assumptions are made throughout this chapter which are detailed here:

- The target forms the entire front face of the reflecting surface.

- When the target is deforming elastically, the normalised elastic deformed shape, ϕ (Section 5.5.2), is assumed to remain constant. When the target is deforming plastically, the normalised plastic deformed shape is assumed to remain constant.

- The transition between elastic and plastic and hence the change in deformed shape is assumed to occur instantaneously. This is a limit of the SDOF method in general

---

[i]In the original report, Hudson uses the symbol C to represent the decay coefficient. Here it has been changed to b to be consistent with the notation used in this thesis.

– whilst this could be addressed during this thesis, the effect is likely to be small in magnitude in comparison to the influence of blast wave clearing.

- The spatial load factor, K_S (Section 5.5.6), is calculated based on the assumed elastic or plastic deformed shape under a uniform load, hence the displacement of the target is assumed to be unaffected by the non-uniformity of the load. This can be justified by the fact that when blast wave clearing occurs, the load is changing significantly quickly and the magnitude of non-uniformity (i.e. the magnitude of K_S compared to unity) is relatively small.[ii] The results in Section 5.6 give confidence in the ability of the SDOF method to model plate deformation under cleared blast loads.

- Fluid-structure interaction (FSI) effects are neglected and the reflected pressure is assumed to be unaffected by target compliance. Further to this, the clearing waves are assumed to propagate along a flat, regular surface and the cleared pressure is also assumed to be unaffected by target compliance. FSI has shown to be important only for very low mass or very low stiffness systems, where the initial velocity of the target is comparable to the peak particle velocity (Kambouchev et al. 2006, 2007, Subramaniam et al. 2009, Teich & Gebbeken 2012). FSI was ignored in the uncoupled FE and SDOF analyses in Chapter 5 and the numerical results still showed good agreement with the measured experimental displacements, suggesting that the FSI effect is negligible for the situations considered in this thesis.

6.2   Elastic Response to Cleared and Non-Cleared Blast Loads

6.2.1   Numerical Example

Whilst a difference between cleared and non-cleared loading has already been shown in Chapter 5, this chapter takes a more general approach to quantifying this effect. In order to demonstrate how the consideration of clearing effects may influence the dynamic response of a target, the SDOF equivalent equation of motion was solved for two undamped elastic systems subjected to the same blast load – a 1 kg TNT hemispherical surface burst detonated 10 m from the target. Three load cases were considered: an idealised linear decay; a full positive and negative phase acting on an infinite surface; and the pressure acting on a 2×2 m target with Hudson clearing corrections. The relevant blast load parameters are given in Table 6.1.

The linear approximation was taken to have the same peak overpressure as the non-cleared load case, with a reduced loading duration to preserve positive phase impulse. The clearing pressure was calculated by discretising the target face into a grid of 100×100 elements and determining the Hudson clearing function at each node. Diffraction was allowed around the top edge and side edges only with the bottom edge of the plates situated on a rigid

---

[ii]Remembering that the spatial load factor effectively serves as a measure of the non-uniformity of the load and $K_S = 1$ when the load is spatially uniform.

Loading	Parameter						
	t_a (ms)	$p_{r,max}$ (kPa)	$p_{r,min}$ (kPa)	t_d (ms)	t_d^- (ms)	i_r (kPa.ms)	i_r^- (kPa.ms)
Cleared	21.64	31.54	6.43	3.39	15.27	49.74	38.71
Non-Cleared	21.64	31.54	7.68	4.79	14.45	59.33	62.39
Linear	21.64	31.54	-	3.76	-	59.33	-

Table 6.1: Loading parameters applied to the numerical model

reflecting surface. The spatially varying pressure was then transformed into an equivalent SDOF force at each time step by multiplying the pressure by the product of the load transformation factor, $K_L = 0.308$, the target area, $A = 4$ m^2, and the spatial load transformation factor, K_S, given by the methodology outlined in Section 5.5.6. The three load cases are shown in Figure 6.1.
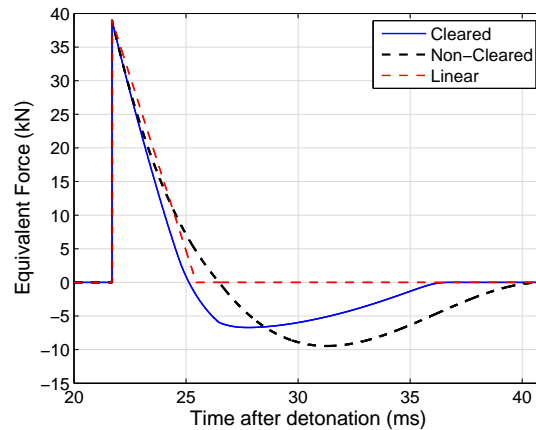
Figure 6.1: Three load cases applied to the numerical model

The 2×2 m targets were modelled as linear elastic, two-way spanning aluminium panels, fixed on all sides. Plate A was modelled with a thickness of 7 mm and plate B was modelled with a thickness of 27.5 mm. The shape functions for $\phi(x)$ and $\phi(y)$ are given as the normalised deformed shape of a one-way spanning, elastic clamped beam (Blevins 1979), shown in Equation 5.23, and the two-dimensional shape function is given as the product of these two variables, i.e. $\phi(x,y) = \phi(x)\phi(y)$. The relevant dynamic model parameters are shown in Table 6.2, where the dynamic coefficients are given using the revised values from Morison (2006).

Figure 6.2 shows the dynamic displacement-time histories of the two plates, annotated with values of peak displacement under the three different load cases – $z_{max,clear}$, $z_{max,inf}$ and $z_{max,lin}$ corresponding to the peak displacement under the cleared, non-cleared (infinite surface) and linear (triangular decay) loads respectively.

Parameter	Symbol	Plate A	Plate B
Young's modulus	E	69 GPa	69 GPa
Density	ρ	2700 kg/m^3	2700 kg/m^3
Poisson's ratio	ν	0.35	0.35
Load factor	K_L	0.308	0.308
Mass factor	K_M	0.182	0.182
Elastic stiffness coefficient	$k/(EI/L^3)$	808.5	808.5
Span	L	2 m	2 m
Thickness	d	7 mm	27.5 mm
Equivalent stiffness	k_e	140 kN/m	8484 kN/m
Equivalent mass	m_e	13.76 kg	54.05 kg
Natural frequency	f	16.05 Hz	63.05 Hz
Natural period	T	62.31 ms	15.86 ms
Time ratio	t_d/T	0.077	0.302

Table 6.2: Dynamic properties for 2×2m linear elastic, two-way spanning aluminium panels, fixed on all sides

(a) Plate A   (b) Plate B
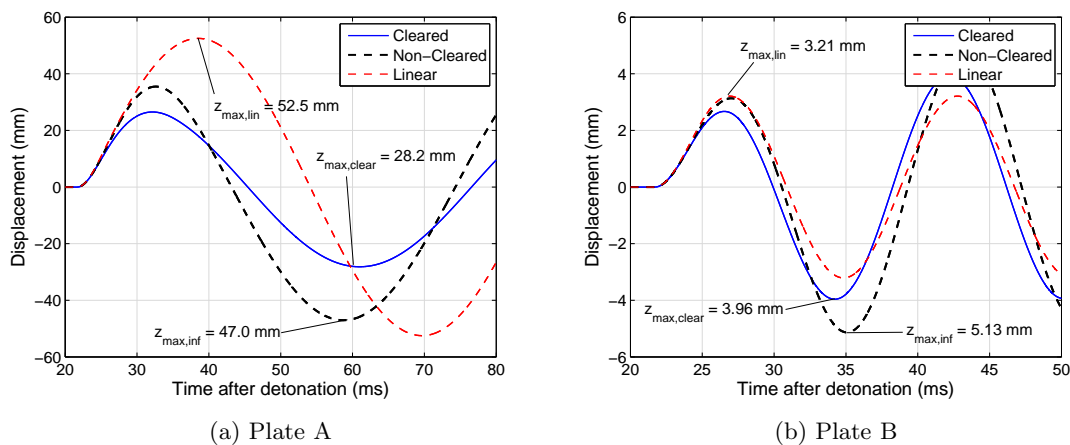
Figure 6.2: Displacement-time histories for plate A and plate B under the three different load cases shown in Figure 6.1

For plate A, with the displacement-time history shown in Figure 6.2(a), it can be seen that the cleared SDOF response begins to diverge from the non-cleared and linear load target response at around 26 ms, which roughly corresponds to the beginning of the cleared negative phase (the shortening of the positive phase caused by the reduction in pressure attributed to clearing). The system reaches a peak outward displacement of around 26 mm at 32 ms after detonation, after which the plate begins to rebound with velocities acting towards the origin of the blast. There is still ~4 ms of negative pressure acting on the target during this rebound phase, hence there is a small magnification in dynamic displacement and the peak elastic response of 28.2 mm is reached during rebound. This effect is also seen for the model under the non-cleared load, where the negative phase causes greater displacement (47.0 mm) in rebound. The model under the linear load is not subjected to negative overpressures and therefore reaches a peak displacement of 52.5 mm much later on in the analysis, at 39 ms after detonation. In this case, neglecting

blast wave clearing and designing for a simplified triangular load function would lead to an over-prediction of peak displacement.

For plate B, displacement-time history shown in Figure 6.2(b), the system under the cleared load reaches peak outward displacement of 2.7 mm relatively early during the load application, at around 26 ms after detonation. After this, there is still a large duration of the cleared negative phase remaining, hence the rebound effect again causes greater inward displacement, reaching a peak value of 3.96 mm. For this system, the rebound effect is large enough such that the peak displacement under the cleared load is greater than the peak displacement of 3.21 mm caused by the linear load. In this case, modelling the plate under a linear load approximation would be under-conservative and the peak displacement would be under-predicted. As with plate A, the rebound effect is even more pronounced for the non-cleared load model.

A representative parameter used in structural dynamics is the ratio of the load duration to the natural period of the structure, t_d/T, known as the time ratio. Larger values of t_d/T indicate that the target response is quick in relation to the loading duration and the loading can be considered as quasi-static, whereas smaller values of t_d/T indicate that the loading is tending towards impulsive. Plate A and plate B have time ratios of 0.077 and 0.302 respectively, i.e. the two plates lie within the dynamic region of loading, and hence are sensitive to the time-varying effects of clearing relief.

The displacement ratio, is a useful parameter for determining the influence of clearing relief on the dynamic response of SDOF systems, and is given as the ratio of the peak displacement (under either the cleared or non-cleared load) to the peak displacement under the linear load,

$$\text{displacement ratio} = z_{max}/z_{max,lin}. \tag{6.1}$$

The displacement ratio is effectively a measure of the level at which the traditional approach (linear load) may under or over-predict the peak elastic deformation. For plate A and plate B, the cleared displacement ratios are 0.54 and 1.23 respectively, showing that clearing cannot simply be neglected on the assumption that it will always reduce target response. Table 6.3 summarises the results of the numerical example.

Plate	t_d/T	$z_{max,lin}$ (mm)	Loading			
			Cleared		Non-Cleared	
			$z_{max,clear}$ (mm)	disp. ratio	$z_{max,inf}$ (mm)	disp. ratio
Plate A	0.077	52.49	28.16	0.54	47.04	0.90
Plate B	0.302	3.21	3.96	1.23	5.13	1.60

Table 6.3: Summary of results from the numerical example

6.2.2 Elastic Response Spectra

In order to be able to determine the influence of clearing relief on a given target, a parametric study was conducted. It has been demonstrated in Section 4.2.1 that for two given targets, providing they are subjected to the same scaled blast load and are geometrically similar, they will both be subjected to the same scaled cleared blast load. Therefore, by varying the scaled distance, Z, scaled target height, H, and t_d/T (target dynamic properties), the influence of clearing relief on the peak elastic deformation of finite targets (i.e. the displacement ratio, $z_{max,clear}/z_{max,lin}$) can be determined over a range of target properties and blast scenarios that may be of interest to the engineer.

Figures 6.3, 6.4, 6.5 and 6.6 show the response spectra for linear elastic, clamped square targets subjected to blast loads at scaled distances of 2, 4, 8 and 16 m/kg$^{1/3}$. Target size parameters are given as ratios of the scaled distance to scaled target height, Z/H, where $Z/H = 0$ indicates a target which forms part of a reflecting surface that is infinite in lateral extent and is therefore subjected to the full reflected pressure. $Z/H = \infty$ indicates a small target which can be assumed to be loaded by the incident pressure only. For far-field loading ($Z \geq 4$m/kg$^{1/3}$), the limit of $Z/H = 100$ exists whereby targets smaller than this size (larger values of Z/H) will effectively experience the incident pressure only. This value is based on findings from the study of blast wave clearing on small targets detailed in Section 4.3.

The target size and dynamic properties are independent of scale and can be used to determine the effect of clearing for any blast event, offering a quick and simple first approximation to the influence of clearing relief.
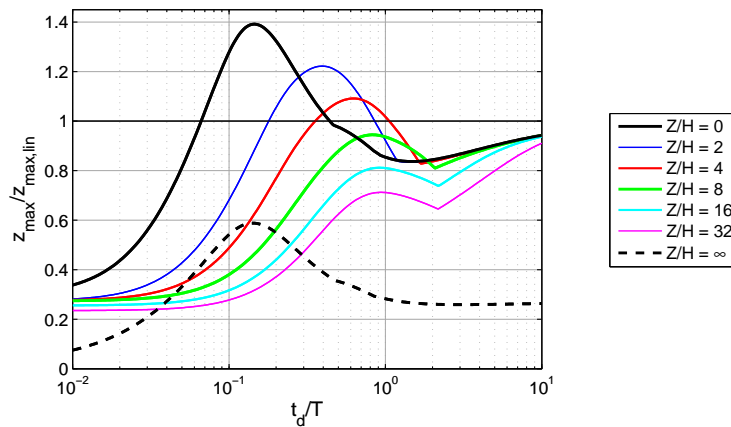
Figure 6.3: Elastic response spectra for $Z = 2$ m/kg$^{1/3}$
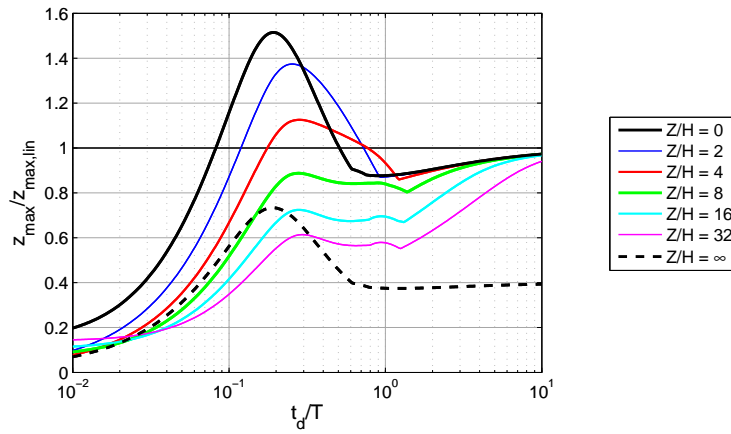
Figure 6.4: Elastic response spectra for $Z = 4$ m/kg$^{1/3}$
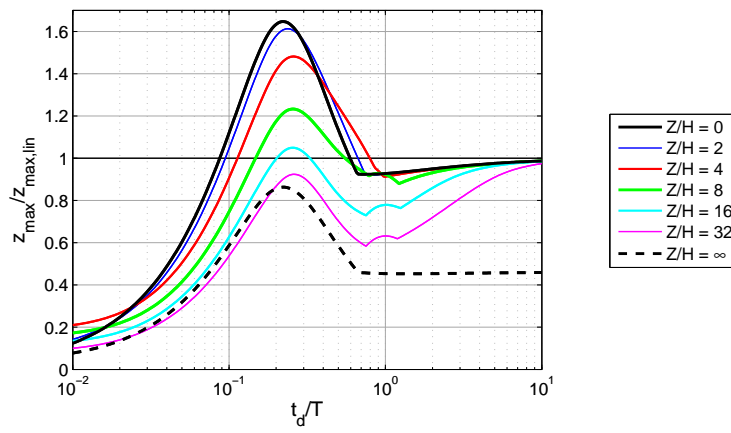
Figure 6.5: Elastic response spectra for $Z = 8$ m/kg$^{1/3}$
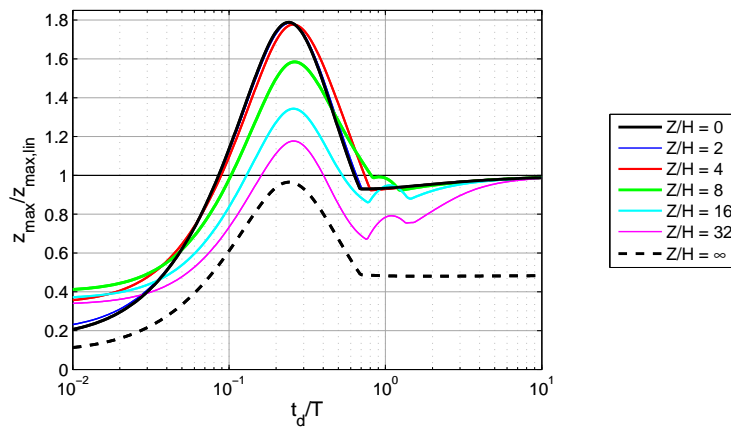
Figure 6.6: Elastic response spectra for $Z = 16$ m/kg$^{1/3}$

6.2.3 Discussion

The Influence of Clearing

The response spectra can be used to make a number of general observations on the scenarios where clearing relief is likely to be a significant factor.

When t_d/T is large, the natural frequency of the system is sufficiently high to ensure that the target reaches its peak displacement before the onset of clearing. For all scaled distances, as the natural period of the structure decreases the displacement ratio tends towards 1, so it can be said that clearing relief has negligible effect at larger time ratios.

When t_d/T is small, the key loading parameter is the net impulse imparted to the target. Clearly the consideration of the negative phase alone significantly reduces the total impulse – the displacement ratio for $Z/H = 0$ ranges between 0.15–0.35 for the scaled distances studied. For small scaled distances, the influence of clearing is to reduce the total impulse, further reducing the displacement of the SDOF system. This finding is in agreement with the observations of Ballantyne et al. (2010), whereby a series of numerical analyses demonstrated that clearing relief reduces the impulse acting on a finite target by around 50% of the reflected value. In Figures 6.3 and 6.4, the displacement ratios for finite targets at the impulsive extreme are roughly 0.5 of the displacement ratio for $Z/H = 0$. For larger scaled distances, as the negative phase begins to play a more important role (Teich & Gebbeken 2010), reduction of positive phase impulse caused by clearing can, for some target sizes, actually increase the net impulse acting on the target, increasing the peak displacement.

There exists a region in the dynamic realm of loading, broadly $0.1 < t_d/T < 1.0$, where negative pressures coincide with negative velocities of the target and the result is a greater peak displacement in rebound – an effect that has already been observed for targets situated in an infinite sized reflecting surface (Teich & Gebbeken 2010). This rebound effect is at its peak when the onset of the negative phase coincides with the peak positive displacement, which occurs at the end of the first quarter cycle of displacement, i.e. when $t_d/T = 0.25$. The influence of clearing is to reduce the value of peak displacement, but a reduced positive duration means that this rebound effect is amplified at different values of t_d/T than would be the case with no clearing. This results in a region where the displacement ratio of the target is *greater* than would be predicted even if negative phase effects were taken into account. In this case, the reduction of pressure initiates 'clearing resonance' and neglecting clearing could be significantly under conservative.

These observations are consistent throughout the range of scaled distances studied, with a general trend of increasing displacement ratio with increasing scaled distance. The response spectra can be used to dispel the notion that clearing relief simply acts to reduce the pressure and provides evidence for the argument that neglecting clearing is not always conservative.

Target Size Limits

The influence of target size can also be observed – a reduction in target size (increase in Z/H) results in more complete clearing relief and, by reducing the pressure acting on the target, reduces the peak dynamic displacement. In the clearing resonance region ($0.3 < t_d/T < 1.8$ for $Z = 2$ m/kg$^{1/3}$), the relationship between target size and displacement ratio is less simple, due to each target size having a different reduced positive phase. It is acknowledged that clearing resonance requires very specific target properties, however it is important to be aware of the phenomenon and the conditions in which it exists.

Interestingly, the curves for $Z/H = 2$ and $Z/H = 4$ are almost coincident with the curve for $Z/H = 0$ at $Z = 8$ and 16 m/kg$^{1/3}$ respectively (Figures 6.5 and 6.6), suggesting that for far-field loading, any target with $H > 4$ m/kg$^{1/3}$ can effectively be designed assuming a full reflected pressure load.

It can also be seen that the target response spectrum approaches the incident spectrum as the target size decreases – as would be expected – and that the convergence is achieved more quickly for far-field conditions. This is in agreement with the numerical study on the mechanism of blast wave clearing undertaken in Chapter 4. Also, neither the largest nor the smallest target spectra appear to be close to the reflected or incident spectra respectively for $Z = 2$ m/kg$^{1/3}$. The fact that clearing has a quantifiable effect on the dynamic response for all target sizes at small scaled distances confirms the findings from Chapter 4 that blast wave clearing should still be considered in the near-field.

6.3 Elastic-Plastic Response to Cleared and Non-Cleared Blast Loads

Consideration of elastic response only is useful for broadly characterising the influence of clearing and typical loading and target parameters which may result in unsafe design if clearing is neglected. Often during blast events, a target will experience some form of permanent plastic deformation or material failure. In this case, an elastic-plastic material model should be used.

6.3.1 Linear Load Response Spectra

In the analysis performed by Biggs (1964), elastic-plastic SDOF systems are subjected to a linearly decaying uniform load

$$F_e(t) = \begin{cases} F_{e,max} \left(1 - \frac{t}{t_{d,lin}}\right), & t \leq t_{d,lin} \\ 0, & t > t_{d,lin} \end{cases} \tag{6.2}$$

where $F_{e,max}$ is the peak force and $t_{d,lin}$ is the duration of the triangular load.

The SDOF system has a bilinear elastic-perfectly plastic resistance function as shown in Figure 6.7. This comprises linear elastic behaviour with spring resistance $k_e z$ until the elastic limit, z_E, is reached, followed by plastic behaviour with constant spring resistance, R_u, thereafter. After the peak displacement, z_{max}, is reached, the displacement decreases and the system begins to rebound. When rebounding, the system again behaves elastically until a spring force of $-R_u$ is attained, whereby the system returns to plasticity.
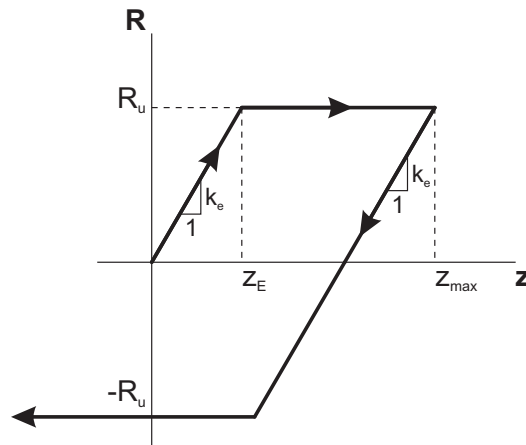
Figure 6.7: Resistance-deflection function of an elastic-plastic SDOF system

The SDOF equation of motion (5.6) is solved using the linear acceleration method (see Biggs (1964) and Section 5.5.4). The response spectra of elastic-plastic SDOF systems subjected to triangular loads are be presented in Figure 6.8, where the peak response is normalised against the elastic limit, i.e. z_{max}/z_E.
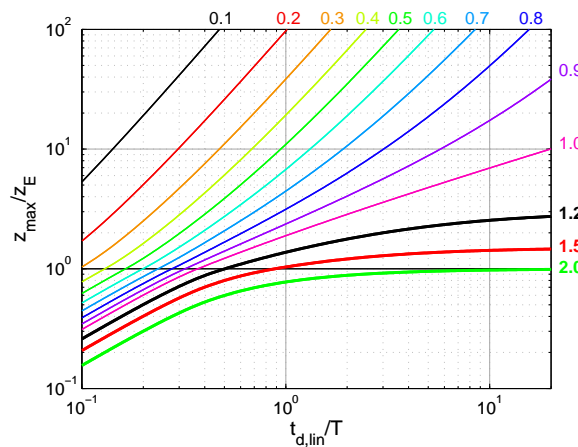
Figure 6.8: Maximum deflection of an elastic-plastic SDOF System under a triangular load (Biggs 1964). Numbers next to curves are resistance ratio, $R_u/F_{e,max}$

The time ratio, t_d/T, as defined previously, gives an indication of the response time of the target with respect to the load duration – low values of time ratio indicate impulsive conditions where the loading is completed during the early stages of displacement, whereas high values of time ratio indicate quasi-static conditions where the target can be expected

to reach peak displacement long before the loading is complete. The resistance ratio, $R_u/F_{e,max}$, gives an indication of the resistance of the target in relation to the magnitude of the peak applied force. Providing the mass, stiffness, resistance and load-time history are known, the peak displacement can be read from the response spectra.

6.3.2 Target Response to Exponential Blast Loads

The triangular load model, from which the response spectra of Biggs (1964) are based, has two main limitations: firstly, it neglects the negative phase, which Teich & Gebbeken (2010) and Krauthammer & Altenberg (2000) have shown to be under-conservative if the scaled distance is large; secondly, the linear load model does not capture the correct decay of the positive phase pressure-time curve. Gantes & Pnevmatikos (2004) addressed this limitation by providing response spectra for exponential loading, where the Friedlander equation (2.9) was simply extended to $t \rightarrow \infty$ to capture the negative phase. This was then compared to the triangular response spectra of Biggs, but as discussed in the literature review of this thesis (Chapter 2), the fact that the positive phase impulse was not kept constant with changing decay coefficient makes it difficult to draw a distinction between the effects of the negative phase and the reduction in positive phase impulse from increasing the rate of decay of the pressure-time curve.

In this thesis, based on the experimental validation in Section 2.2.5, the reflected negative phase is modelled using the cubic expression given by Granström (1956). The piecewise force-time function applied to the SDOF model is given in Equation 6.3

$$
F_e(t) = \begin{cases} F_{e,max} \left(1 - \dfrac{t}{t_d}\right) e^{-bt/t_d}, & t \leq t_d \\[2ex] F_{e,min} \left(\dfrac{6.75(t - t_d)}{t_d^-}\right) \left(1 - \dfrac{(t - t_d)}{t_d^-}\right)^2, & t_d < t \leq t_d + t_d^- \\[2ex] 0, & t > t_d + t_d^- \end{cases} \tag{6.3}
$$

where $F_{e,max}$ and $F_{e,min}$ are given by the peak overpressure and peak negative pressure multiplied by the target area and load transformation factor. These parameters, along with the positive phase duration, t_d, negative phase duration, $\bar{t_d}$, and waveform parameter, b, are found using the KB semi-empirical predictive method.

Figure 6.9 shows as an example the response spectrum for an elastic-plastic SDOF system under an exponential blast load at $Z = 8$ m/kg$^{1/3}$ and resistance ratio, $R_u/F_{e,max} = 0.5$. The triangular response spectrum is also shown, with $t_{d,lin} = 2i_r/p_{r,max}$ to preserve positive phase impulse. Dashed regions of the exponential response spectrum indicate regions where the peak displacement is in rebound.

With reference to Figure 6.9, the exponential load response spectrum for $R_u/F_{e,max} = 0.5$ is defined by four distinct regions:
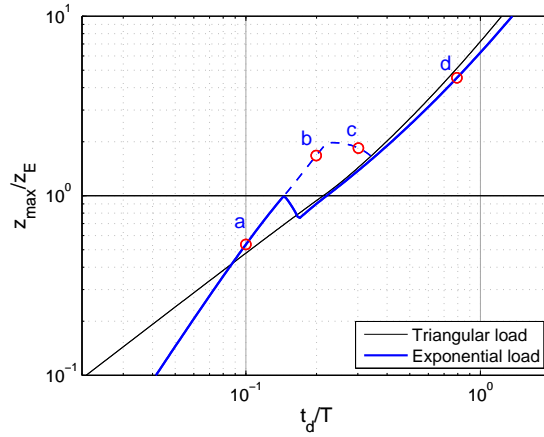
Figure 6.9: Response spectra for $Z = 8$ m/kg$^{1/3}$ and $R_u/F_{e,max} = 0.5$ under triangular and exponential loads. Dashed lines indicate regions of the exponential response spectrum where the peak displacement is in rebound. Peak displacements from the examples in Figure 6.10(a-d) are shown with corresponding values of t_d/T

a. Elastic deformation only, $t_d/T < 0.15$
   Figure 6.10(a) shows the SDOF response at $t_d/T = 0.1$ (force-time history shown on the minor y axis). In this region of the response spectrum, $z_{max} < z_E$ and no plastic deformation occurs. As the system reaches peak displacement on the first cycle, the velocity of the system becomes negative whilst the negative phase load is still applied, increasing deflection in the negative ('rebound') direction and causing peak displacement to occur during rebound. This behaviour continues as t_d/T increases, until the rebound is sufficient to cause plasticity in the negative direction.

b. Plastic deformation in rebound only, $0.15 \leq t_d/T < 0.22$
   Figure 6.10(b) shows the SDOF response at $t_d/T = 0.2$. It can be seen that the only permanent plastic deformation is in the negative direction, i.e. towards the blast. As the ratio of t_d/T increases the magnitude of positive displacement on the first cycle increases until the elastic limit is reached.

c. Plastic deformation in both directions, $0.22 \leq t_d/T < 0.35$
   Figure 6.10(c) shows the SDOF response at $t_d/T = 0.3$. The system undergoes plastic deformation on the first positive cycle of displacement and undergoes further plastic deformation in rebound. The system still reaches peak displacement in rebound in this region of the response spectrum, with the positive plastic deformation increasing relative to the negative deformation with increasing t_d/T.

d. Peak plastic deformation during the first half cycle of displacement, $t_d/T \geq 0.35$
   Figure 6.10(d) shows the SDOF response at $t_d/T = 0.8$. The positive phase of the load is sufficient to cause gross plastic deformation ($z_{max} >> z_E$). Little or no rebound plasticity occurs.

(a) Region a. response, $t_d/T = 0.1$

(b) Region b. response, $t_d/T = 0.2$

(c) Region c. response, $t_d/T = 0.3$

(d) Region d. response, $t_d/T = 0.8$
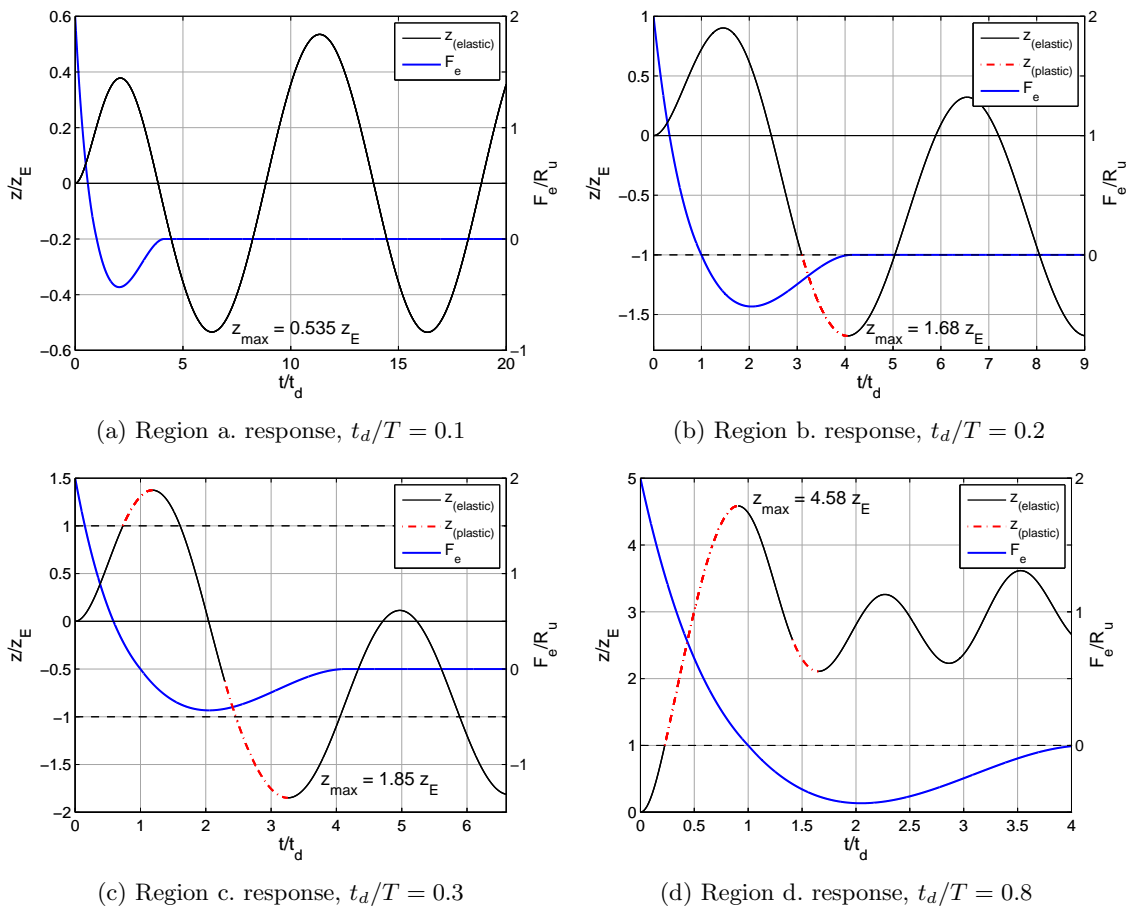
Figure 6.10: Normalised displacement-time history of elastic-plastic SDOF systems under an exponential blast load at $Z = 8$ m/kg$^{1/3}$

The discontinuities in the response spectrum are caused by the transitions between these regions. Whilst the bounds of each region will change with different values of resistance ratio, $R_u/F_{e,max}$, the behaviour within each region will be similar.

From comparison of the triangular and exponential response spectra, it is apparent that the loading assumption has a significant impact on the response of the SDOF system. The triangular load model is over-conservative for impulsive scenarios (low values of t_d/T), yet non-conservative for particular ranges of t_d/T where the exponential load response spectrum is in regions b. and c. and peak displacement occurs during rebound.

6.3.3 Target Response to Cleared Blast Loads

Elastic-plastic response spectra were evaluated for $Z = 2$, 4, 8 and 16 m/kg$^{1/3}$, for target sizes of $Z/H = 0$, 4, 8 and 16 and are shown in Figures 6.11, 6.12, 6.13 and 6.14 respectively. The cleared load was evaluated for each scaled distance and target size by applying the Hudson (1955) clearing corrections to ConWep (Hyde 1991) predictions of reflected pressure on a grid of 100×100 nodes. This was converted into an energy equivalent uniform load using the spatial load transformation factor, K_S, derived in Section 5.5.6.

The beams were modelled as one way-spanning square panels, with the normalised deflected shape, ϕ, given as

$$\phi(x) = \frac{16x}{5L^4} \left(L^3 - 2Lx^2 + x^3 \right), \tag{6.4}$$

where x is the length along the beam and L is the total length. For a one-way spanning member, $\phi(x, y) = \phi(x)$.

6.4 Discussion

6.4.1 The Influence of Scaled Distance and Target Size

The target response spectra for $Z = 2$ m/kg$^{1/3}$ in Figure 6.11 mainly shows region a. and d. response, with a very narrow range of values of t_d/T where peak displacement occurs during rebound (region b. and c. response). For small scaled distances, the magnitude of the reflected pressure is large relative to the incident pressure, hence the clearing waves are small in magnitude relative to the reflected pressure. The influence of clearing, therefore, is fairly minimal and the response of the target is dominated by the reflected pressure profile. Some small reductions in peak displacement can be seen as the target size decreases, although it is known that the cleared pressure does not converge with the incident pressure at small scaled distances. Broadly speaking, the response spectra for $Z = 4$ m/kg$^{1/3}$ in Figure 6.12 exhibit similar characteristics to the response spectra for $Z = 2$, albeit with more pronounced rebound regions.

(a) $Z/H = 0$

(b) $Z/H = 4$

(c) $Z/H = 8$

(d) $Z/H = 16$
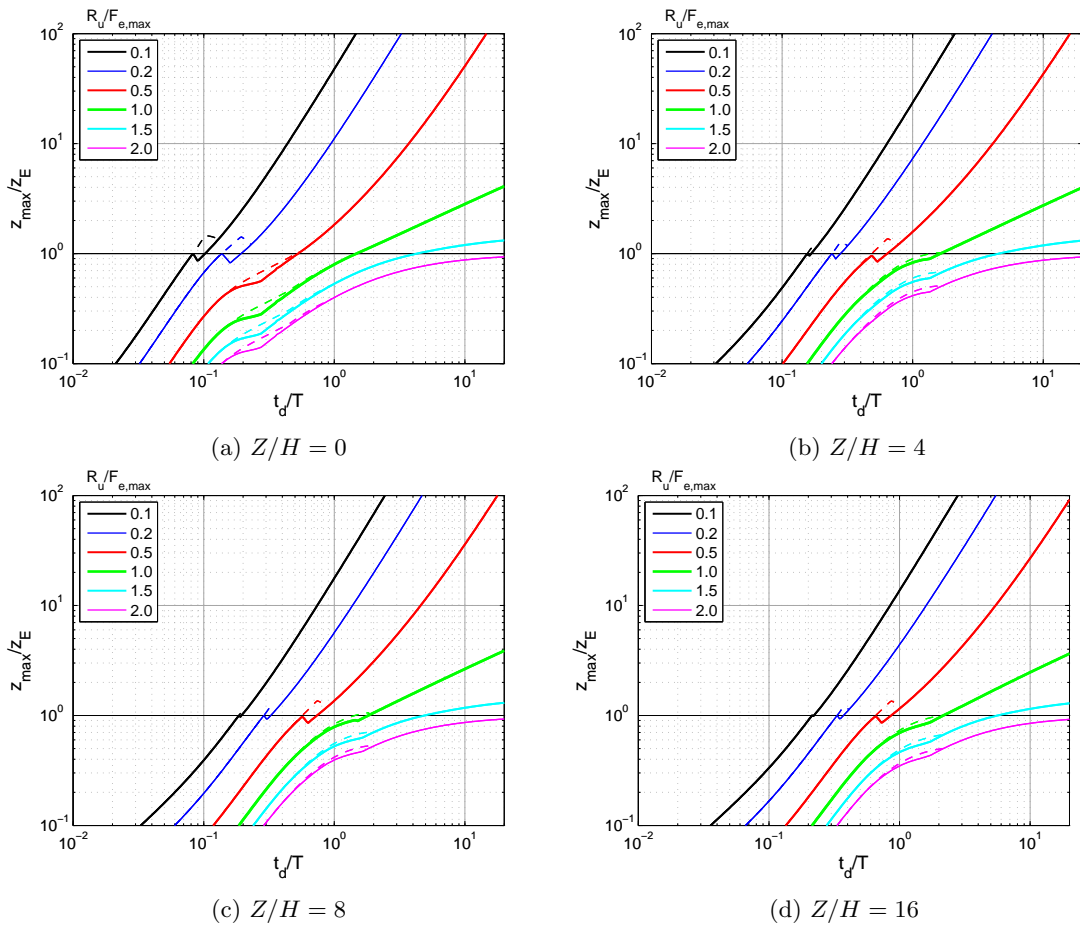
Figure 6.11: Elastic-plastic response spectra for $Z = 2$ m/kg$^{1/3}$. Dashed lines indicate regions where the peak displacement is in rebound
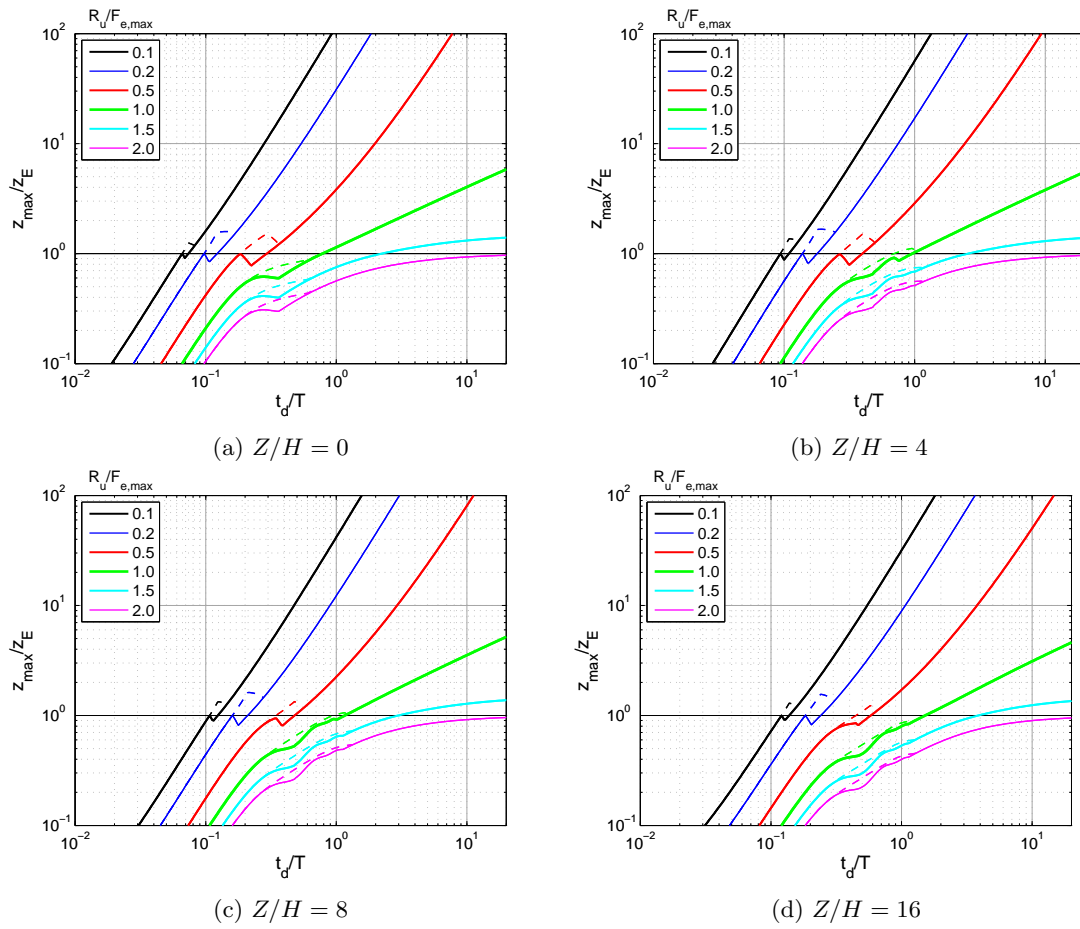
Figure 6.12: Elastic-plastic response spectra for $Z = 4$ m/kg$^{1/3}$. Dashed lines indicate regions where the peak displacement is in rebound
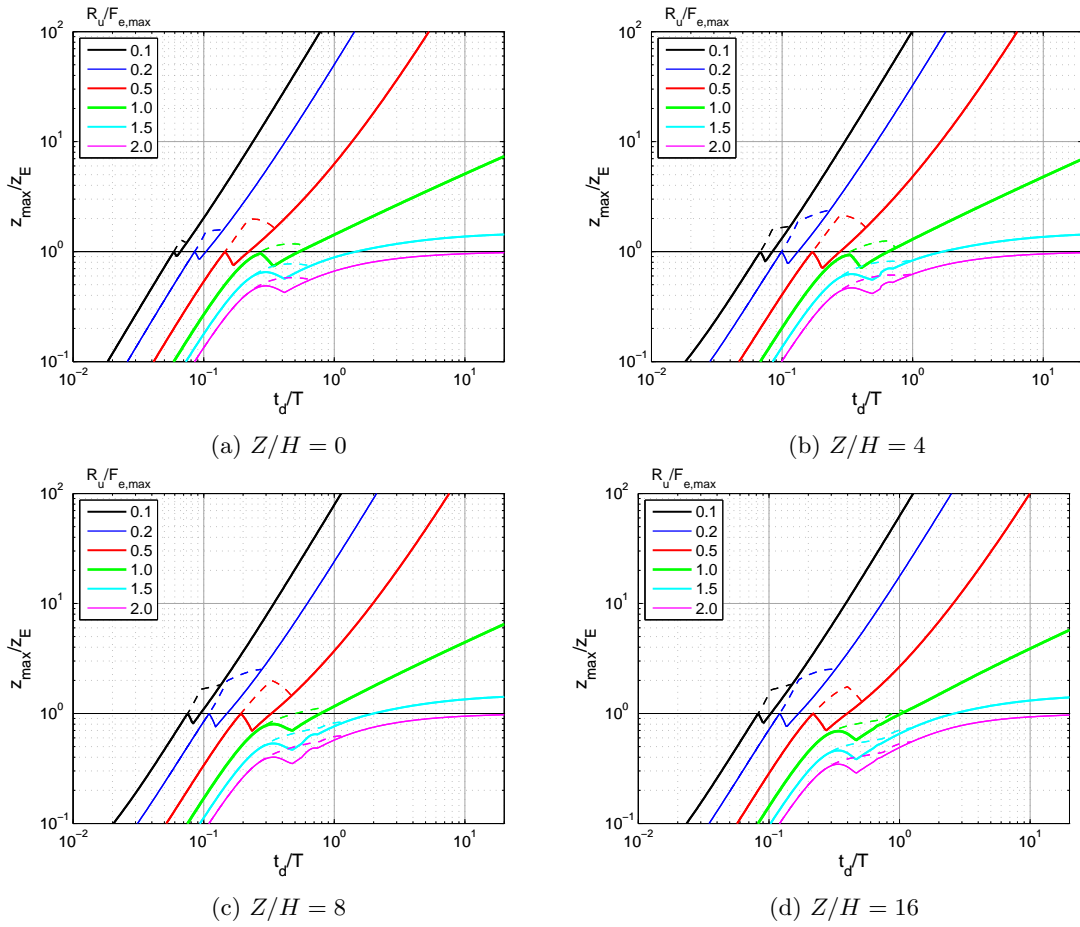
Figure 6.13: Elastic-plastic response spectra for $Z = 8$ m/kg$^{1/3}$. Dashed lines indicate regions where the peak displacement is in rebound
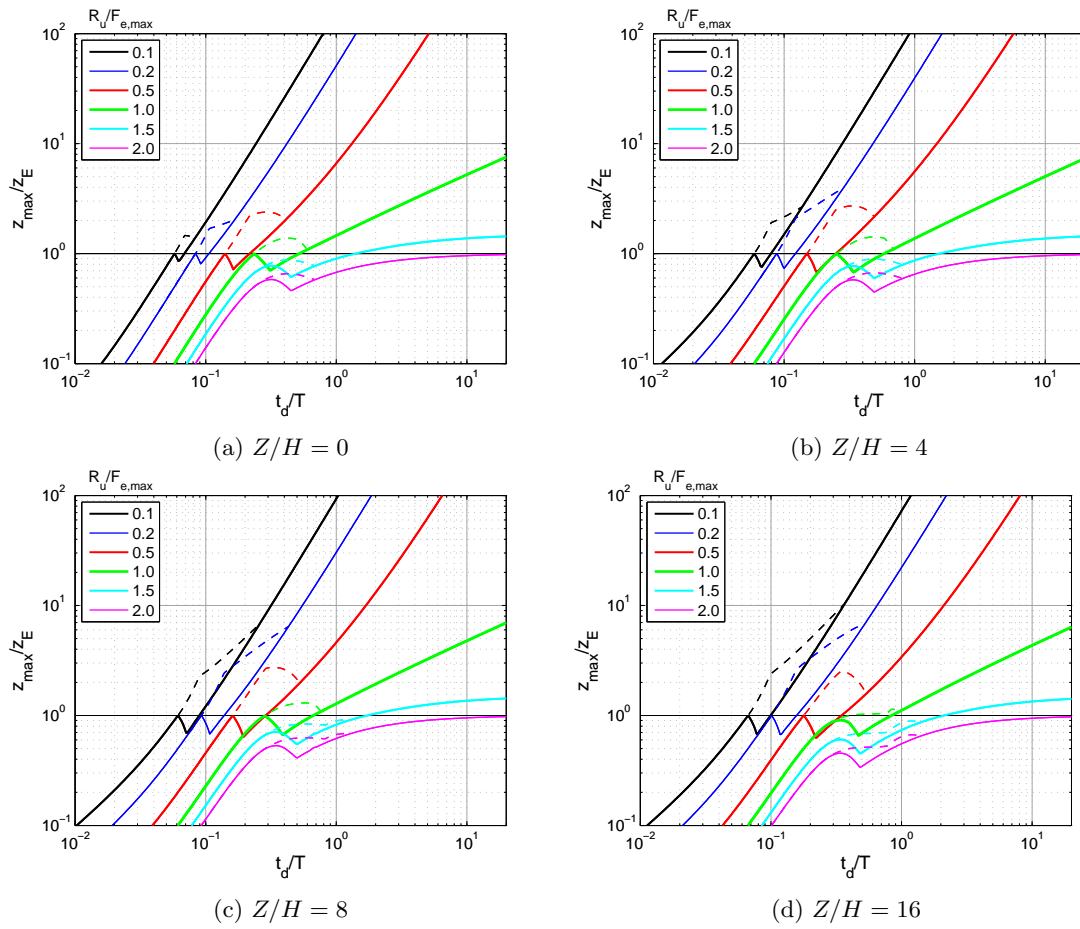
Figure 6.14: Elastic-plastic response spectra for $Z = 16$ m/kg$^{1/3}$. Dashed lines indicate regions where the peak displacement is in rebound

The influence of target size can be more clearly seen in the response spectra for $Z = 8$ and $Z = 16$ m/kg$^{1/3}$ in Figures 6.13 and 6.14. For larger scaled distances, the response of the target is influenced by the positive phase, negative phase and the contribution of clearing, rather than being dominated by the reflected pressure as is the case for near-field loading. It is apparent that for far-field loading, the regions of the response spectra where the peak displacement occurs during rebound (regions b. and c., as indicated by the dashed lines) happen over a wider range of t_d/T. This can be justified by the fact that as the expansion wave propagates over the target face, the magnitude of the relief pressure decreases and the pressure pulse becomes more rounded and longer in duration (Hudson 1955). With smaller targets, therefore, a sharper drop-off in pressure occurs more uniformly across the loaded face, making smaller targets more susceptible to the dynamic effects that cause increased displacement in rebound.

Table 6.4 shows the comparison of peak displacements under the non-cleared blast load for $H = \infty$ and the cleared blast load for $H = 1$, over a range of resistance ratios, $R_u/F_{e,max}$, and time ratios, t_d/T. The results are in agreement with the observation of more complete clearing occurring at increased distance from the blast source (Rose & Smith 2000, Tyas et al. 2011a) – the difference in response due to the non-cleared and cleared blast load is greater in almost every case at $Z = 16$ when compared to $Z = 4$.

$R_u/F_{e,max}$	t_d/T	z_{max}/z_E					
		Z = 4			Z = 16		
		$H = \infty$	$H = 1$	% diff.	$H = \infty$	$H = 1$	% diff.
0.2	0.2	1.96	1.66	15	2.75	3.32	-21
	0.5	8.78	4.91	44	13.86	6.69	52
	1.0	31.06	17.03	45	51.18	22.17	57
0.5	0.2	1.09	0.71	34	1.90	1.19	37
	0.5	1.68	1.27	25	2.59	1.82	30
	1.0	3.83	2.87	25	6.62	3.40	49
1.0	0.2	0.54	0.36	34	0.84	0.59	30
	0.5	0.84	0.83	1	1.35	1.03	24
	1.0	1.14	1.07	6	1.46	1.11	24

Table 6.4: Comparison of peak displacement for $H = \infty$ and $H = 1$ at $Z = 4$ and $Z = 16$

6.4.2   Comparison Against Triangular Load Response Spectra

Knowing that clearing has a more pronounced effect at larger scaled distances, the following sections are concerned with discussing the influence of clearing in the far-field. A number of observations on the influence of clearing can be made when the cleared response spectra are compared with the triangular load response spectra. Figure 6.15 shows the spectra for $R_u/F_{e,max} = 0.5$ and $Z = 8$ m/kg$^{1/3}$ from Figures 6.13(a-d), as well as the linear load response spectrum from Figure 6.8. Towards the impulsive end of the response

spectra (low values of t_d/T) the reduction in net impulse associated with clearing and the negative phase can be seen to significantly reduce the peak displacement of the SDOF system under the cleared load relative to the triangular load. The influence of target size can be seen to further reduce peak displacement. For example, at $t_d/T = 0.2$, the displacement of the cleared plate with $Z/H = 16$ is $0.9z_E$, whereas the displacement under the exponential load ($Z/H = 0$) is $1.7z_E$. Furthermore, the peak displacement under the cleared load at $Z/H = 16$ is around 33% of the peak displacement under the exponential load at large values of t_d/T. Clearing is therefore an important consideration for elastic-plastic systems, even at large values of t_d/T where it is unimportant for elastic systems.
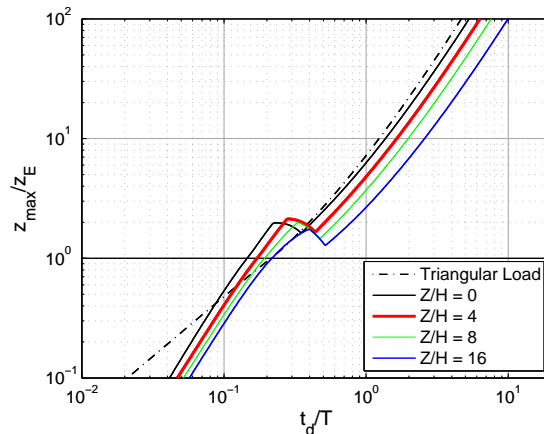
Figure 6.15: Response spectra for $Z = 8$ m/kg$^{1/3}$ and $R_u/F_{e,max} = 0.5$ for different scaled target sizes, normalised against elastic limit

Figures 6.16(a), (c) and (e) show contours of peak displacement, z_{max}, normalised against the peak displacement of the SDOF under the triangular load, $z_{max,lin}$. The dashed line indicates the time ratio at which the system begins to deform plastically (i.e. when $z_{max}/z_E > 1$ in Figure 6.13), with elastic behaviour to the left and plastic behaviour to the right of the curve. The response spectra for $R_u/F_{e,max} = 2.0$ are identical to the elastic response spectra of Section 6.2.2, hence contour lines in the elastic regime are parallel.[iii] The response spectra for $R_u/F_{e,max} = 2.0$ lies entirely in the elastic region.

Figures 6.16(b), (d) and (f) show the normalised response spectra at select values of $R_u/F_{e,max}$. It can be seen from both the normalised response spectra and the displacement contours that peak values of displacement typically occur between $0.3 < R_u/F_{e,max} < 0.7$, when the system undergoes plastic deformation in rebound only. If the temporal characteristics of the loading relative to the response of the target are such that greater displacement is caused in rebound ($t_d/T \approx 0.25$), and the resistance of the target is such that it enters plasticity in rebound (as, for example $R_u/F_{e,max} = 0.5$), then an amplification in displacement will occur.

It is apparent that blast wave clearing can serve to adversely affect target response when

---

[iii]Contour lines that are not parallel in the elastic region *near* to the dashed transition line (between elastic and plastic behaviour) show situations where the non-cleared load causes plasticity and the cleared load does not

Figure 6.16: (a), (c), (e) Contours of peak displacement normalised against peak displacement under the triangular load for $Z = 8$ m/kg$^{1/3}$. The dashed line indicates the time ratio at which the system begins to deform plastically. (b), (d), (f) Response spectra for select values of $R_u/F_{e,max}$

the magnitude of load is comparable to the resistance of the target, and can serve to severely lessen the peak displacement when the magnitude of load far exceeds the elastic resistance. For elastic SDOF systems subjected to cleared blast loads, $R_u/F_{e,max} \geq 2.0$, the normalised response spectra approach 1.0 as t_d/T increases, as the natural frequency of the system is sufficiently high to ensure that the target reaches its peak displacement before the onset of clearing – i.e. there is no difference between the triangular, full reflected and cleared blast load, hence clearing has no effect. Elastic-plastic systems, however, experience gross plastic deformation at higher time ratios (region d. of the response spectra) and hence the time taken to reach peak displacement increases, allowing time for the effects of clearing to decelerate the SDOF system. The peak displacement for $R_u/F_{e,max} = 0.1$ remains constant at between 0.25 and 0.40 for all scaled target sizes at higher time ratios.

6.4.3   Comparison Against Exponential Load Response Spectra

Normalising the peak SDOF displacement under the cleared load, z_{max}, against the peak SDOF displacement under the exponential load, $z_{max,inf}$, allows the influence of clearing to be isolated and further quantified. Figures 6.17(a), (c) and (e) show contours of the normalised peak displacement. As with Figure 6.16 the dashed line indicates the time ratio at which the system begins deform plastically. Figures 6.17(b), (d) and (f) show the normalised response spectra at select values of $R_u/F_{e,max}$.

When comparing the cleared elastic response to the non-cleared elastic response, there is a small region between $0.47 < t_d/T < 0.80$ where 'clearing resonance' occurs and peak displacement is in the order of 10% greater than the SDOF under the full reflected pressure, for $Z/H = 4$ only. For the smaller targets, the elastic peak displacement is always less than the non-cleared response. When plasticity is included in the model, however, there are certain combinations of t_d/T and $R_u/F_{e,max}$ that will result in a greater peak displacement for the cleared blast load. For $Z/H = 4$, this clearing resonance can cause displacements over 30% greater than if clearing were neglected. This value decreases to 21% for $Z/H = 8$ and 10% for $Z/H = 16$.

Whilst it requires specific conditions for this adverse response to occur, it is worth noting that the phenomenon exists and blast wave clearing should not be neglected on the assumption that it is conservative. In practice, it is unlikely that the engineer will have knowledge of the exact properties of the target and exact parameters of the blast event, and instead of designing for a single event, a sensitivity-based study may be undertaken; in which case, it is all the more important to be able to quickly determine if clearing will have a significant effect on target response – whether it acts to reduce displacement or cause further damage – in order to allow for clearing in the early stages of design.

The influence of blast wave clearing on target response is complex and dependant on many parameters, however the response spectra presented in this section provide an effective method for quantifying its effect.

(a) $Z/H = 4$

(b) $Z/H = 4$
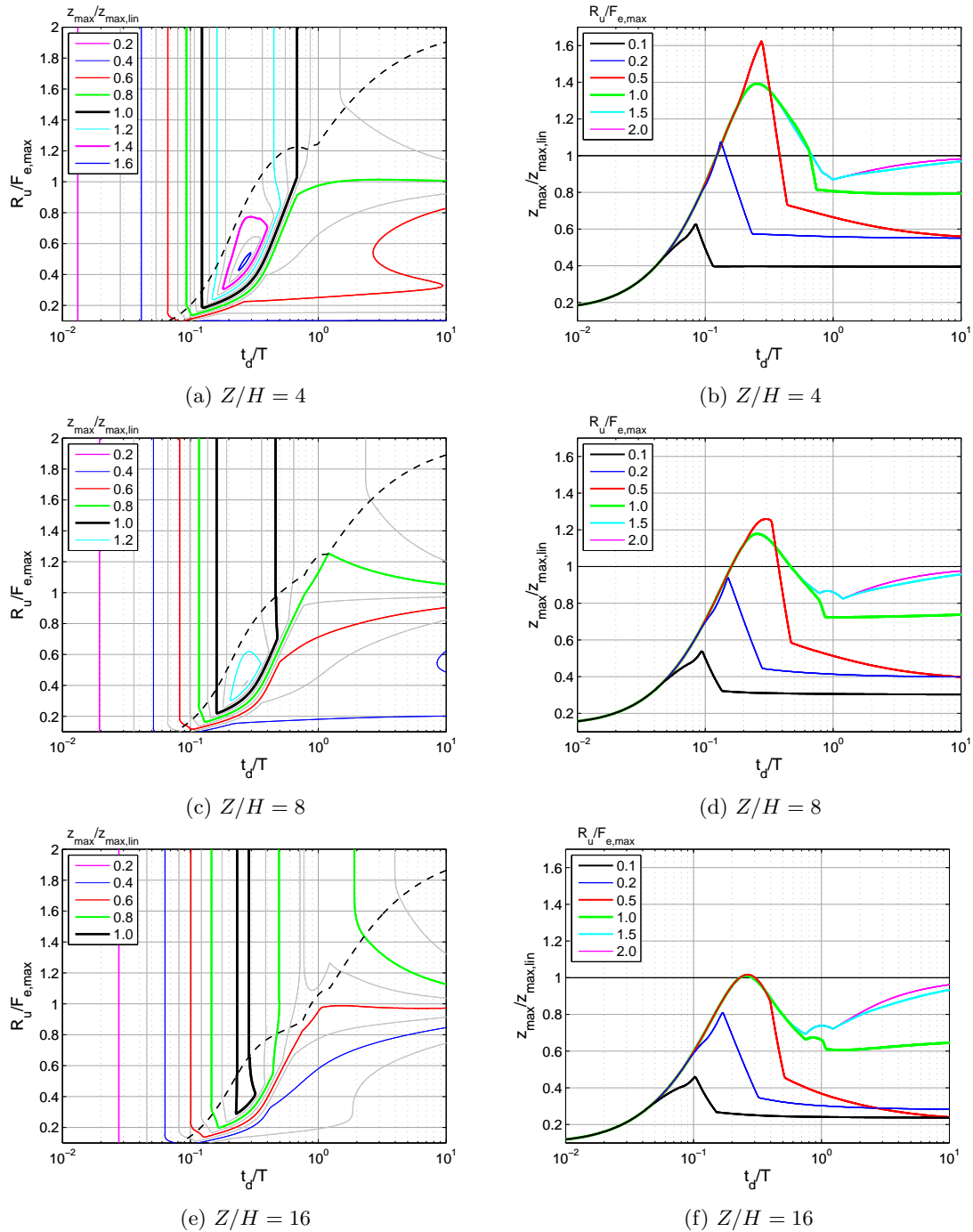
(c) $Z/H = 8$

(d) $Z/H = 8$

(e) $Z/H = 16$

(f) $Z/H = 16$
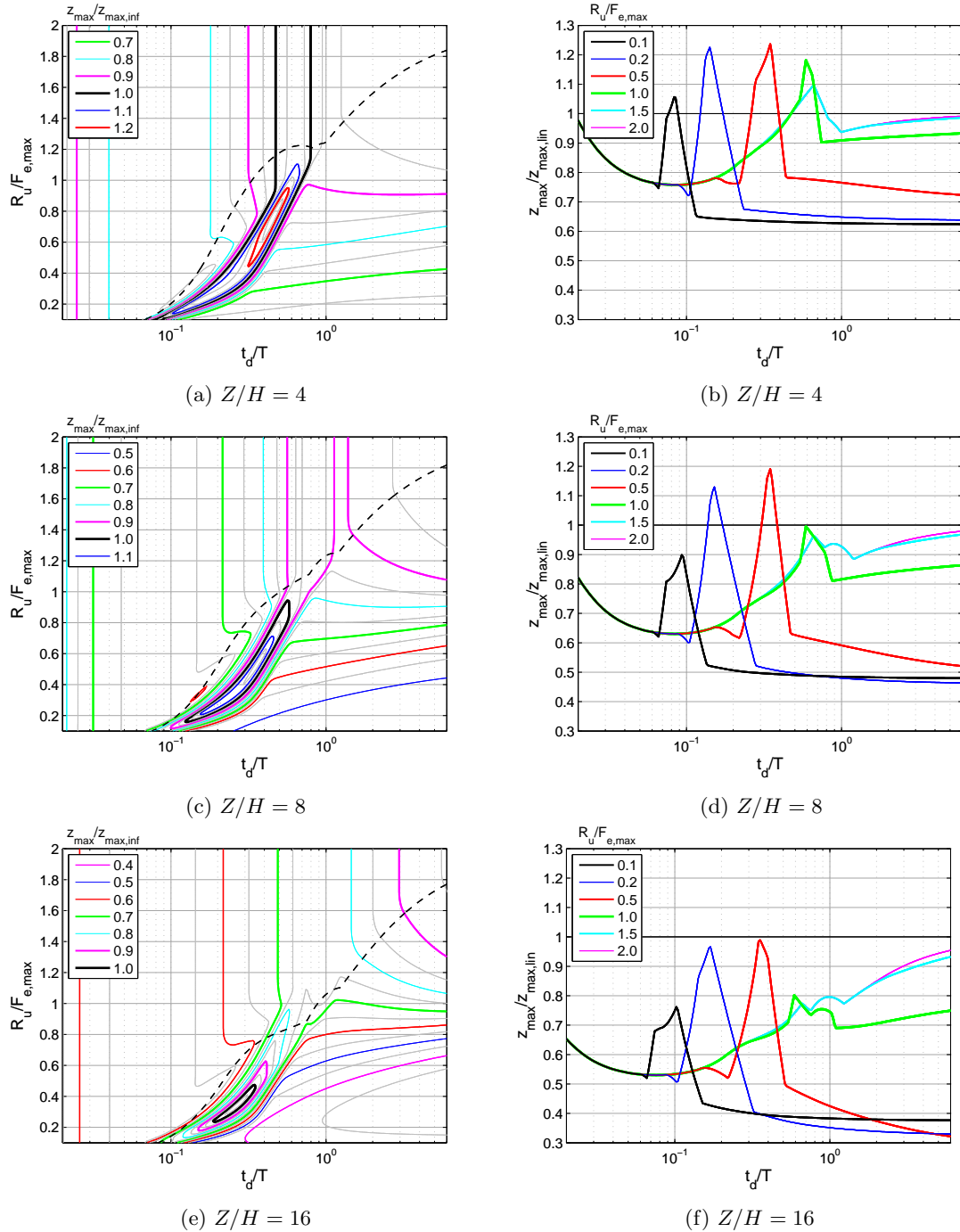
Figure 6.17: (a), (c), (e) Contours of peak displacement normalised against peak displacement under the exponential load for $Z = 8$ m/kg$^{1/3}$. The dashed line indicates the time ratio at which the system begins to deform plastically. (b), (d), (f) Response spectra for select values of $R_u/F_{e,max}$

6.5   The Design Charts in Use

The following section details the practical application of the response spectra using numerical and graphical examples. The results are compared to both an explicit FE model and current design methods to highlight the error that may be encountered when neglecting clearing.
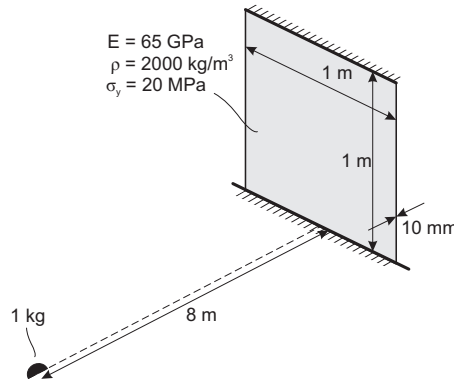
Figure 6.18: Dimensions and properties of the light cladding panel

A square, simply supported, one-way spanning light cladding panel, shown schematically in Figure 6.18 – with Young's Modulus, $E = 65$ GPa, Density, $\rho = 2000$ kg/m^3 and Yield strength, $\sigma_y = 20$ MPa – was subjected to a 1 kg hemispherical TNT burst at a distance of 8 m. The panel has a span, L, of 1 m and thickness, d, of 10 mm. The dynamic SDOF properties of the panel, i.e. the equivalent mass, equivalent stiffness, elastic resistance, elastic limit and natural period, were determined using the following equations, after Biggs (1964)

$$m_e = K_M \rho L^2 d \tag{6.5}$$

$$k_e = K_L 384EI/5L^3 \tag{6.6}$$

$$R_u = 8M_m/L \tag{6.7}$$

$$z_E = R_u/k_e \tag{6.8}$$

$$T = 2\pi\sqrt{m_e/k_e} \tag{6.9}$$

where I is the second moment of area and M_m is the moment capacity at midspan. The relevant loading parameters and dynamic properties are summarised in Table 6.5. Stiffness, mass and resistance parameters are shown for elastic response only, using elastic load and mass factors, $K_L = 0.64$, and $K_M = 0.50$ respectively.

In numerical SDOF analyses, the material properties can simply be switched between elastic and plastic properties when the displacement goes from one type to the other. In order to use the graphical methods (i.e. the response spectra), however, one value must be assumed. When the response is expected to extend beyond the elastic range, Biggs (1964)

recommends using an approximate weighted average of the elastic, elastic-plastic (for two-way spanning elements, if appropriate) and plastic factors. In this example, elastic factors are only used as the response is assumed to be predominantly elastic.

Parameter	Symbol	Value	Unit
Peak reflected pressure	$p_{r,max}$	44.11	kPa
Positive phase duration	t_d	4.454	ms
Young's modulus	E	65	GPa
Density	ρ	2000	kg/m^3
Yield strength	σ_y	20	MPa
Load factor	K_L	0.64	-
Mass factor	K_M	0.50	-
Span	L	1	m
Thickness	d	10	mm
Equivalent stiffness	k_e	266.2	kN/m
Equivalent mass	m_e	10	kg
Elastic resistance	R_u	2.67	kN
Elastic limit	z_E	10.01	mm
Natural period	T	38.5	ms
Time ratio	t_d/T	0.116	-
Resistance ratio	$R_u/F_{e,max}$	0.094	-

Table 6.5: Loading parameters and dynamic properties for a 1×1 m elastic-plastic, one way spanning, simply supported panel.

For the FE analysis, the panel was discretised using 100×100 shell elements using the *MAT_PLASTIC_KINEMATIC material model in LS-DYNA (Hallquist 2006), with the cleared loading applied as force-time curves at every node using the method detailed in Section 5.4.1. The Hudson method has been shown to accurately capture the spatial variation of cleared blast pressure loading (Tyas et al. 2011a,b) and can, when combined with an FE model, predict the dynamic deflection of finite plates to a good level of agreement with experimental results (see Section 5.4.2). The FE model can therefore be considered as an accurate representation of how the panel would perform in real life.

Figure 6.19 shows the transient displacement of the SDOF models and FE simulation, with the bottom/left axes showing the real displacement-time history and the top/right axes showing the normalised history. The values of peak displacement are summarised in Table 6.6, where it can be seen that the peak SDOF displacement under the cleared load is within 13% of the FE model on the first rebound.

$R_u/F_{e,max}$	t_d/T	z_{max} (mm)			
		LS-DYNA	Clearing	Exponential	Triangular
0.094	0.116	15.3	17.3	28.1	47.7
		% diff.	13	83	211

Table 6.6: Maximum response for FE and SDOF model from numerical analysis and percentage difference between FE and SDOF displacements
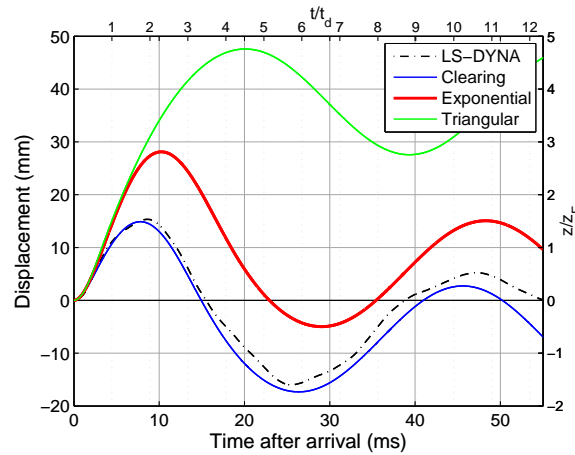
Figure 6.19: FE and SDOF response under different loading conditions for a 1 m square cladding panel

It is possible to determine the peak displacement without the need for numerical analysis, simply by using the response spectra provided in Figure 6.13. Taking $R_u/F_{e,max}$ and t_d/T as 0.10 and 0.12 respectively, the peak displacement for $Z/H = 8$ can be read off Figure 6.13(c) to give $z_{max} = 1.7z_E$, which compares well with $1.53z_E$ determined from the FE analysis.

If clearing is neglected and the peak displacement under the exponential load is read from Figure 6.13(a), the peak displacement would be estimated at $2.6z_E$. If the loading is further simplified as a triangular load with no provision for clearing or the negative phase, the peak displacement would be estimated from Figure 6.8 as $5.0z_E$. These correspond to over-predictions of 70% and 230% respectively, demonstrating the need to take blast wave clearing into account, especially during the early stages of design.

Peak displacements obtained using the graphical response spectra method are summarised in Table 6.7.

$R_u/F_{e,max}$	t_d/T	z_{max}/z_E			
		LS-DYNA	Clearing Fig. 6.13(c)	Exponential Fig. 6.13(a)	Triangular Fig. 6.8
0.1	0.12	1.53	1.7	2.6	5.0
		% diff.	11	70	230

Table 6.7: Normalised maximum response for FE and SDOF model using graphical method and percentage difference between FE and SDOF displacements

6.6   Summary

The objective of this chapter has been to quantify the effect of blast wave clearing on elastic and elastic-plastic targets via rigorous analysis of one degree systems.

For a given target size and scaled distance, the cleared blast pressure was given as a superposition of the ConWep (Hyde 1991) reflected pressure and Hudson (1955) clearing corrections at a grid of 100×100 points on the loaded face. The spatially and temporally varying pressure was converted into an energy equivalent uniform pressure at each timestep using the temporally varying spatial load transformation factor, $K_S(t)$, derived in Section 5.5.6.

First, linear elastic single-degree-of-freedom systems were analysed using this modified load model to take into account the pressure relief caused by clearing, with the values of peak displacement compared against a traditional SDOF model; a linear system subjected to an equivalent triangular blast load under the assumption that the target is sufficiently large so that edge effects can be neglected. For two sample targets, it was shown that, depending on the dynamic properties of the system, clearing relief may be either beneficial or adverse.

This study was extended to produce full elastic response spectra, where the peak SDOF displacement – normalised against the peak SDOF displacement under the linear load – was given as a function of scaled target size, Z, the time ratio of the load duration to natural period of the target, t_d/T, and the scaled distance, Z. It was found that, for elastic systems, clearing has little effect when $t_d/T \to \infty$ and for systems where $t_d/T \to 0$, clearing acts favourably; reducing the net impulse and hence the peak displacement of the target.

If the loading lies within the dynamic realm, i.e. the period of the system is similar in magnitude to the duration of the loading event $(0.1 < t_d/T < 1.0)$, negative pressures may coincide with the rebound of the target and result in a greater peak displacement. It is known that clearing may result in early negative pressures, and this effect may initiate 'clearing resonance', causing greater peak displacements than would have been predicted had clearing not been considered.

In the second part of this chapter, elastic-plastic SDOF systems were studied. A simple example using a non-cleared exponential load was used to characterise the regions of the elastic-plastic response spectrum, with regions a., b., c. and d. representing: elastic deformation; plastic deformation in rebound; plastic deformation in both directions; and peak plastic deformation during the first half cycle of displacement – the system changes between different regions of the response spectrum with increasing values of t_d/T.

Response spectra were generated for elastic-plastic systems under cleared and non-cleared blast loads for a variety of scaled distances and scaled target sizes. Comparing these spectra to the linear load response spectra of Biggs (1964) indicated that certain configurations

of target size, mass, stiffness and elastic resistance will cause a greater increase in peak displacement for elastic-plastic systems than for elastic systems. The results tend towards the elastic response spectra as the ratio of the strength of the target to the peak applied force, $R_u/F_{e,max}$, increases.

Comparing the cleared response spectra to the non-cleared spectra enabled a further quantification of the effects of blast wave clearing. It was found that if the early negative cleared pressure causes plasticity in rebound when the non-cleared load does not, then displacements can be as high as 30% greater under the cleared blast load. Generally, blast wave clearing serves to reduce the peak displacement of the target, particularly when the magnitude of the load is large relative to the resistance of the target, and the load duration is large relative to the response time of the target. Because neglecting blast wave clearing can either lead to an over-designed target or, occasionally, an un-safe design, it is argued that blast wave clearing should be considered at all stages of blast resistant design – particularly when a quick and physically valid method for predicting target response, such as the one in this thesis, exists.

Finally, numerical and graphical examples have been used to demonstrate how this method would work in practice. It was shown that the response spectra can be used to predict the peak response of a finite target to within 11% of an explicit finite element model, compared to a 230% over-prediction when simplifying the load as a triangular pulse and reading off the response spectra provided in current design guidance.

Chapter 7

Summary and Conclusions

7.1 Summary

This thesis has aimed to investigate the effect of blast wave clearing on the dynamic response of finite targets subjected to blast loads.

A high explosive detonation is characterised by the rapid release of energy as a mass of explosive material is converted into a high pressure, high temperature gas. As this gas expands it displaces the surrounding air, causing a high pressure shock wave to travel through the air away from the explosive at supersonic speed. This shock wave can potentially cause significant damage as it impacts a structure – it is the challenge of the engineer to ensure that our infrastructure is robust enough to be able to withstand such extreme loading.

The first aspect of blast engineering is to be able to predict and quantify the spatial and temporal variation of the load acting on the target to a sufficient level of accuracy. In Chapter 2 a review of the current literature is provided, as well as background information relating to blast wave phenomology, methods for predicting the blast load acting on a finite target and the state-of-the-art for predicting target response. A full review of the theory of blast wave clearing is also given, along with a review of the available methods for predicting it. In Chapter 3, the Arbitrary Lagrangian Eulerian method is introduced. The explicit finite element solver LS-DYNA can be used to simulate explosive events and is validated for three conditions: incident blast waves; reflected pressure on a semi-infinite surface and reflected pressure on a finite surface. This validated model is then used in Chapter 4 to study the mechanism of clearing for small targets and to investigate the current theory.

Secondly, the target response to this load must be predicted. An experimental trial, conducted to validate different response-predictive methods, is detailed in Chapter 5. Target response is simulated using three modelling techniques which are then compared against the experimental results to determine which method is most appropriate. The single-degree-of-freedom (SDOF) method approximates the distributed properties of the real life

153

system into single point equivalent values – this procedure is already well established for transformation of the target properties. In this thesis, the spatial variation of cleared blast pressure is transformed in a similar manner by conserving energy between the real life distributed load and an equivalent uniform load which is applied to the SDOF system. By transforming the load in this way, non-uniform clearing blast pressure loads can now be modelled in SDOF analyses.

The combined improvements to both load prediction and response modelling has allowed a full parametric study to be conducted on finite-sized targets subjected to blast loads. Linear elastic and elastic-plastic SDOF systems are analysed in Chapter 6, using a modified load model to take into account the pressure relief caused by clearing. Various combinations of scaled distance, target size, dynamic target properties and target strength are analysed and the values of peak displacement are compared against a traditional SDOF model: a linear system subjected to an equivalent triangular blast load under the assumption that the target is sufficiently large so that edge effects can be neglected.

Findings in this PhD thesis should be used to highlight the complex nature of blast-target interaction, particularly when blast wave clearing is concerned, and should dispel the myth that a design will be safe if clearing is neglected. Results presented in the study can also be used by practicing engineers to determine the likely effect that blast wave clearing will have on any configuration of explosive mass, stand-off, target size and dynamic properties, and the numerical models developed within have the potential for widespread use in existing commercial software.

7.2 Conclusions

The output of this thesis can be summarised in the following conclusions, which are listed in the order that they appear in the current work:

- ConWep predictions for arrival time, peak reflected overpressure, positive phase duration and positive phase reflected impulse have shown to be in excellent agreement with a series of well controlled experimental trials.

- The cubic negative phase expression of Granström (1956) gives the best approximation for the negative phase both qualitatively and quantitatively. By simply extending the Friedlander (1946) equation to model the negative phase, the negative impulse can be grossly overestimated.

- The ALE method in LS-DYNA can be used to simulate blast events to a good level of agreement with semi-empirical predictions and experimental results, and can capture features such as shock reflection and blast wave clearing accurately.

- Modelling the explosive using the *initial_volume_fraction keyword should be avoided when modelling a curved charge in a rectangular mesh. A radially symmetric

mesh should be used to correctly model spherical blast wave propagation as transport of material diagonally through elements introduces a second order advection error (Hallquist 2006). The spherical blast wave can then be re-mapped onto a rectangular grid to model blast-target interaction using the *INITIAL_ALE_MAPPING keyword.

- Current literature guidance on predicting clearing (Kinney & Graham 1985, US Department of Defence 2008, Cormie et al. 2009) is based on the assumption that a series of expansion waves interact as they travel back and forth across the target face (Taylor 1972). The work in this thesis has shown this to be an invalid assumption and a new model is proposed, which describes the clearing effect as an over-expanded region of air propagating outwards from the front-centre of the target. This over-expansion effect is reduced with decreasing target size and the load therefore approaches the incident pressure.

- The Hudson (1955) clearing corrections have been shown to be able to predict the blast load acting on targets subjected to mainly diffraction-type loading (Tyas et al. 2011a,b). In this thesis, it is also demonstrated that these predictions can accurately capture the features of blast wave clearing for small target sizes, based on the fact that the load is comprised of only one clearing wave propagating across the target face from each free edge.

- When modelling structural response to a blast wave, one technique is to model both the target and the surrounding air using finite elements and to transfer the blast pressure from the air to the target using fluid-structure interaction. Whilst higher order schemes such as these allow for more rigorous treatment of real-life physical effects, their use may be limited by the need for reasonably sized computer models.

- Modelling the plate using finite elements and applying the blast force using simple nodal-point load curves showed excellent correlation with experimental deflection-time and peak deflection data. Applying Hudson (1955) corrections to nodal-point forces allows cleared blast pressure to be applied to a finite target, and again has been shown to be in excellent agreement with experimental results.

- Transforming the spatially varying pressure acting on a plate into an energy equivalent uniform load using the spatial load transformation factor, K_S, enables cleared loading to be modelled in SDOF analyses, with the values of peak displacement for an elastic one-way spanning target subjected to a cleared blast load predicted typically to within 10% of experimentally measured values. The demonstrated validity of the SDOF method gives confidence that this approach is suitable for initial analysis of loading events for geometrically simple scenarios.

- If the duration of load application is large relative to the natural period of the target and the strength of the target exceeds the peak applied force by a factor of 2.0 or more, the peak response is only affected by the peak reflected pressure and clearing has little or no effect. If the strength of the target is less than twice the peak applied

force, however, then a quasi-statically loaded target will experience gross plastic deformation and the time taken to reach peak displacement will increase. In this case, blast wave clearing will have time reduce the velocity of the target and will act to lessen peak displacement.

• If the duration of load application is small relative to the natural period of the target the peak response is only affected by the applied impulse. In this case, inclusion of clearing in the model will result in a significant reduction in displacement when compared to designing against a linear load with no negative phase, and a small reduction in displacement when compared to designing against an exponential non-cleared load.

• For targets whose response time is comparable to the duration of the load, the influence of clearing is more complex. Neglecting clearing can be largely over-conservative for small targets, however neglecting clearing can also be non-conservative through a combination of target rebound, plasticity and early negative pressures caused by the clearing waves. This increase in displacement can be up to 30% greater than the peak displacement caused by a load model that neglects clearing, and up to 60% greater than the peak displacement caused by a load model that neglects clearing and the negative phase.

• For far-field loading, clearing can be neglected for situations where the ratio of the scaled distance to scaled target height, Z/H, is less than 100, on account of the form of the load converging towards incident blast pressure for targets smaller than this value.

• Clearing can also be neglected for situations where the ratio of the scaled distance to scaled target height, Z/H, is greater than 4, on account of the dynamic response of the target tending towards the response under the full reflected pressure for targets larger than this value.

• For any other situation, clearing should not be neglected at any stage until the engineer is confident that its effects are understood.

• The graphical methods for predicting target response in this thesis have been shown to be able to predict the peak response of a finite target to within 11% of an explicit finite element model and can be used with confidence as a first means for predicting the likely damage a target will sustain when subjected to an explosive load.

7.3   Evaluation and Future Work

In Chapter 2, a series of small scale experimental trials were conducted in order to validate the Kingery & Bulmash (1984) semi-empirical blast pressure predictions. Whilst the series comprised only 4 experimental tests, this was considered an adequate number of tests to demonstrate that the semi-empirical method can be used to predict blast loading to a good degree of accuracy. Bogosian et al. (2002) showed that there was generally good correlation between the Kingery and Bulmash predictions and experimental data from blast trials, but with some considerable spread. It is possible that this was due to the fact that the empirical data was generally from field trials involving very large explosions, with the consequent difficulties in carefully controlling the test parameters. Whilst no repeat tests were conducted for the pressure measurements on semi-infinite targets featured in this thesis, the level of agreement shown – as well as both the demonstrated repeatability and accuracy of the related experimental work on finite targets (Tyas et al. 2011a,b) and the work of Rickman & Murrell (2007) – indicates that in small scale, carefully controlled experimental trials, the correlation between experimental data and the KB predictions for the positive phase parameters in the far-field is remarkably good.

In the near-field, however, the KB method appears to be less accurate, with the semi-empirical predictions regularly over-estimating the incident specific impulse. This observation is confirmed in the numerical study of Cormie et al. (2013), where revised scaled-distance relationships are provided for close-in detonations. Traditionally, a lack of adequately robust instrumentation has prevented the accurate experimental recording of near-field pressure, and instead numerical analysis is used to inform researchers of the form of blast pressure loading in the near-field. The University of Sheffield Blast & Impact research group has recently developed an experimental procedure for capturing the spatial and temporal variation of pressure from extreme loading events (Fay et al. 2013). This experimental setup could be used to research near-field loading in an attempt to provide more accurate guidance for blast parameter prediction.

The negative phase parameters are less well validated than the positive phase. The obvious extension of this work, therefore, is to conduct a further series of blast tests where negative phase parameters are recorded. The results of this study can be used to either provide validation for existing negative phase parameters (e.g. those in UFC-3-340-02), or to generate a new database from which empirical predictions can be drawn. The US Army Blast Effects Design Spreadsheet, SBEDS, (US Army Corps of Engineers 2005, page 3-9) states that *'so little is known about the negative phase blast load, including the effect of angle of incidence...the lack of a well-validated method for predicting the negative phase blast load is a legitimate reason for using the traditional approach of ignoring the negative phase blast load when calculating component response.'* By including various angles of incidence in this study, a more complete picture of reflected negative phase parameters can be developed, enabling for better modelling of the blast load acting on a deformable target.

It was originally intended to conduct this study using LS-DYNA, however the validation in Chapter 3 indicated that, whilst the negative phase impulse was generally well captured by the numerical model, there was a slight difference between the form of the experimental and numerical negative phase. The primary use of ALE analysis in this thesis was to determine the dynamic displacement of a target where the peak displacement was reached a short time after the positive phase. The limitation of the numerical model, therefore, was unimportant in the analyses in this thesis, but will need to be further studied if LS-DYNA is to be used to investigate the negative phase.

The study on blast wave clearing on small targets in Chapter 4 was evaluated for 2D targets only. Whilst qualitatively the mechanism will be similar for 3D targets, an equivalent study conducted on 3D targets would allow for both quantification of this effect, and for those target sizes where clearing becomes unimportant to be highlighted. In this thesis, a study of the mechanism itself was only considered important, hence 3D effects were neglected.

The ALE-FSI analyses in Chapter 5 were shown to be in good agreement for the early stages of target response, but not as much for the later stages when clearing was acting. This is likely due to mesh effects and is not explored further in this thesis – with a run time of 168 hours and initial results to within 15% agreement of the experimental results, any further improvement through mesh refinement (whether this is done locally around the target or is made adaptive to areas of high pressure gradient using the *ALE_REFINE keyword) was considered both unnecessary and time consuming. It is worthwhile, however, highlighting the limitations of a computer model, and this appears to be one of them.

The spatial load transformation factor, K_S, developed in Chapter 5, enables an arbitrary spatially varying load to be represented as a uniform load for use in an SDOF model. This is achieved through balancing the work done between the applied load and an energy equivalent spatially uniform load. Whilst it is first validated for a case where the applied load is spatially non-uniform but the non-uniformity remains constant with time, the main application of the spatial load factor is for loads whose *non-uniformity does not remain constant with time*. In this thesis, it has been shown that K_S can accurately transform the non-uniform cleared blast pressures under the assumption that the non-uniformity is neither great enough nor is it maintained for sufficient duration to cause deviation from the assumed deformed shape under a uniform load. It would be worthwhile to study this assumption, and to develop limits where it begins to have an effect in order for K_S to be used in wider applications, for example near field free air loading or when evaluating the response of a target subjected to a buried explosive – both of which have a spatially non-uniform load for which the non-uniformity changes with respect to time and could in theory be suited for SDOF analyses using the spatial load transformation factor.

Fluid-structure interaction is ignored in the parametric study of this thesis. It has been shown in the literature that FSI can act to decrease the pressure acting on the plate and hence decrease dynamic displacement (Subramaniam et al. 2009, Teich & Gebbeken 2012). It is known that FSI only becomes important for systems whose initial response velocity

is similar to the peak particle velocity of the blast wave. Indeed, the coupled ALE-Lagrangian numerical results in Chapter 5, where FSI was modelled, showed no better agreement than the numerical results where FSI was neglected. This strongly suggests that, for the typical target properties and blast events studied in this thesis, FSI effects can be ignored. It would be of interest, however, to study the mutual effect of clearing and target compliance – to what extent does a flexible target influence the form of the clearing wave? How does this then influence the response of the target? The clearing waves in this study were assumed to travel along a rigid, flat reflecting surface – it is hypothesised that a moving target will increase the available volume for the rarefaction wave to expand into, hence the effects of clearing may be amplified and target response may be further reduced through FSI. Again, it is unlikely that this will have any noticeable effect for the compliant targets studied in this thesis (as evidenced by the level of agreement between the experimental and numerical results of the models ignoring FSI, shown in Chapter 5), but it will be useful to determine the situations in which it will have an effect and to have an idea of the likely magnitude of that effect.

Finally, the influence of clearing was researched for simple geometries and for blast events where the blast wave was unobstructed between source and target and arrived planar and orthogonal to the reflecting surface. To extend the use of the Hudson clearing predictions, it would be valuable to consider clearing effects in more complex scenarios representing blast in an urban environment. Whilst some effort has been undertaken to gain an appreciation of the effect of nearby structures on the form of the blast load using numerical analysis (Rose & Smith 2002, Rose et al. 2004, 2006), modification of semi-empirical procedures and inclusion of Hudson (or modified Hudson) predictions would be of more immediate use to practising civilian engineers. Effects such as shadowing, multiple reflections and non-orthogonal, non-planar blast wave arrival, whilst their effects have already been highlighted to some extent in the literature, should be implemented into simple numerical procedures with corresponding simplified clearing methodologies to allow for the modelling of diffraction effects around the loaded target face. It has been shown in principle that the superposition of multiple relief waves can still be used for the Hudson clearing corrections (Tyas et al. 2011a,b) – it would be of interest to see if a similar procedure could be adopted for clearing predictions in more complex scenarios.

The conclusions drawn in this thesis should be used as evidence for the importance of considering blast wave clearing, and the methodologies outlined could be adapted for future research topics.

Bibliography

Ackland, K., Bornstein, H. & Lamos, D. (2012), An analysis of TNT equivalencies using AUTODYN, *in* 'Australasian Structural Engineering Conference', Perth, Australia.

Alia, A. & Souli, M. (2006), 'High explosive simulation using multi-material formulations', *Applied Thermal Engineering* **26**(10), 1032–1042.

Anderson, J. D. (2001), *Fundamentals of aerodynamics*, Mc-Graw Hill, New York, NY, USA.

Aquelet, N. (2012), ALE adaptive mesh refinement in LS-DYNA, *in* '12th International LS-DYNA Users Conference', Dearborn, MI, USA, pp. 1–20.

Aquelet, N. & Souli, M. (2008), 2D to 3D ALE mapping, *in* '10th International LS-DYNA Users Conference', Dearborn, MI, USA, pp. 23–34.

Baker, W. E. (1973), *Explosions in air*, University of Texas Press, Austin, TX, USA.

Ballantyne, G. J., Whittaker, A. S., Dargush, G. F. & Aref, A. J. (2010), 'Air-blast effects on structural shapes of finite width', *Journal of Structural Engineering* **136**(2), 152 – 159.

Biggs, J. M. (1964), *Introduction to Structural Dynamics*, McGraw-Hill, New York, NY, USA.

Blevins, R. D. (1979), *Formulas for natural frequency and mode shape*, Van Nostrand Reinhold, New York, NY, USA.

Bogosian, D., Ferritto, J. & Shi, Y. (2002), Measuring uncertainty and conservatism in simplified blast models, *in* '30th Explosives Safety Seminar', Atlanta, GA, USA, pp. 1–26.

Borenstein, E. & Benaroya, H. (2013), 'Loading and structural response models of circular plates subjected to near field explosions', *Journal of Sound and Vibration* **332**(7), 1725–1753.

Børvik, T., Hanssen, A., Langseth, M. & Olovsson, L. (2009), 'Response of structures to planar blast loads – a finite element engineering approach', *Computers & Structures* **87**(9-10), 507–520.

Britt, J. R. & Lumsden, M. G. (1994), Internal blast and thermal environment from internal and external explosions: a user's guide for the BLAST-X code, Version 3.0, Technical Report SAIC 405-94-2, Science Applications International Corporation, St. Joseph, LA, USA.

Brode, H. L. (1955), 'Numerical solutions of spherical blast waves', *Journal of Applied physics* **26**(6), 766–775.

Chafi, M. S., Karami, G. & Ziejewski, M. (2009), 'Numerical analysis of blast-induced wave propagation using FSI and ALE multi-material formulations', *International Journal of Impact Engineering* **36**(10-11), 1269–1275.

Christensen, S. O. & Hjort, Ø. J. S. (2012), Back calculation of the oslo bombing on july 22nd, using window breakage, *in* '22nd Symposium on the Military Aspects of Blast and Shock (MABS22)', Bourges, France.

Cormie, D. & Arkinstall, M. (2012), SDOF isn't dead – The role of single degree of freedom analysis in the design of columns against close-in blast, *in* 'Structures Congress 2012', Chicago, IL, USA, pp. 114–125.

Cormie, D., Mays, G. & Smith, P. (2009), *Blast effects on buildings, 2nd ed.*, Thomas Telford, London, UK.

Cormie, D., Wilkinson, W., Shin, J. & Whittaker, A. (2013), Scaled-distance relationships for close-in detonations, *in* '15th International Symposium on the Interaction of the Effects of Munitions with Structures (ISIEMS)', Potsdam, Germany.

Cranz, C. (1926), *Lehrbuch der Basllistik*, Springer, Berlin, Germany.

Danesi, R. F., Jacinto, A. C. & Ambrosini, R. D. (2002), 'Dynamic response of plates subjected to blast loading', *Proceedings of the ICE - Structures and Buildings* **152**(3), 269–276.

Dennis, S. T., Baylot, J. T. & Woodson, S. C. (2002), 'Response of 1/4-scale concrete masonry unit (CMU) walls to blast', *Journal of engineering mechanics* **128**(2), 134–142.

Dharani, L. R. & Wei, J. (2004), Dynamic response of laminated glass under blast loading: effect of negative phase, *in* 'Structures under shock and impact VIII', Crete, Greece, pp. 181–190.

Dobratz, B. M. & Crawford, P. C. (1985), LLNL explosives handbook - properties of chemical explosives and explosive simulants, Technical Report UCRL 52997, Lawrence Livermore National Laboratory, University of California, CA, USA.

Dusenberry, D. O. (2010), *Handbook for blast-resistant design of buildings*, John Wiley & Sons, Hoboken, NJ, USA.

Esparza, E. (1986), 'Blast measurements and equivalency for spherical charges at small scaled distances', *International Journal of Impact Engineering* **4**(1), 23–40.

Ethridge, N. H. (1977), Blast diffraction loading on the front and rear surfaces of a rectangular parallelepiped, Technical Report ARBRL-MR-2784, U.S Army BRL, Aberdeen Proving Ground, MD, USA.

Fay, S., Clarke, S., Warren, J. A., Tyas, A., Bennett, T., Reay, J., Elgy, I. & Gant, M. (2013), Capturing the spatial and temporal variations in impulse from shallow buried charges, *in* '15th International Symposium on the Interaction of the Effects of Munitions with Structures (ISIEMS)', Potsdam, Germany.

Friedlander, F. G. (1946), 'The diffraction of sound pulses. I. Diffraction by a semi-infinite plane', *Proceedings of the Royal Society A: Mathematical, Physical and Engineering Sciences* **186**(1006), 322–344.

Gantes, C. & Pnevmatikos, N. (2004), 'Elastic-plastic response spectra for exponential blast loading', *International Journal of Impact Engineering* **30**(3), 323–343.

Granström, S. A. (1956), Loading characteristics of air blasts from detonating charges, Technical Report 100, Transactions of the Royal Institute of Technology, Stockholm.

Hallquist, J. O. (2006), *LS-DYNA Theory Manual*, Livermore Software Technology Corporation, CA, USA.

Hirsch, C. (1988), *Numerical computation of internal and external flows. Volume 2: computational methods for inviscid and viscous flows.*, John Wiley & Sons, Chichester, UK.

Hooper, P., Sukhram, R. A. M., Blackman, B. R. K. & Dear, J. P. (2012), 'On the blast resistance of laminated glass', *International Journal of Solids and Structures* **49**(6), 899–918.

Hopkinson, B. (1915), *British Ordnance Board Minutes, 13565*.

Hudson, C. C. (1955), Sound pulse approximations to blast loading (with comments on transient drag), Technical Report SC-TM-191-55-51, Sandia Corporation, MD, USA.

Hunter, J. K. & Keller, J. B. (1984), 'Weak shock diffraction', *Wave motion* **6**(1), 79–89.

Hyde, D. W. (1991), *Conventional Weapons Program (ConWep)*, U.S Army Waterways Experimental Station, Vicksburg, MS, USA.

Jacinto, A. C., Ambrosini, R. D. & Danesi, R. F. (2001), 'Experimental and computational analysis of plates under air blast loading', *International Journal of Impact Engineering* **25**(10), 927–947.

Jones, N. (1971), 'A theoretical study of the dynamic plastic behaviour of beams and plates with finite-deflections', *International Journal of Solids and Structures* **7**(33), 1007–1029.

Kambouchev, N., Noels, L. & Radovitzky, R. (2006), 'Nonlinear compressibility effects in fluid-structure interaction and their implications on the air-blast loading of structures', *Journal of Applied Physics* **100**(063519).

Kambouchev, N., Noels, L. & Radovitzky, R. (2007), 'Numerical simulation of the fluid-structure interaction between air blast waves and free-standing plates', *Computers & Structures* **85**(11 - 14), 923 – 931.

Kaurin, C. M. & Varslot, M. O. (2010), *Blast loading on square steel plates; A comparative study of numerical methods*, Master's Thesis, Norwegian University of Science and Technology, Trondheim, Norway.

Kingery, C. N. & Bulmash, G. (1984), Airblast parameters from TNT spherical air burst and hemispherical surface burst, Technical Report ARBRL-TR-02555, U.S Army BRL, Aberdeen Proving Ground, MD, USA.

Kinney, G. F. & Graham, K. J. (1985), *Explosive Shocks in Air*, Springer, NY, USA.

Krauthammer, T. & Altenberg, A. (2000), 'Negative phase blast effects on glass panels', *International Journal of Impact Engineering* **24**(1), 1–17.

Lapoujade, V., Van Dorsselaer, N., Kevorkian, S. & Cheval, K. (2010), A study of mapping technique for air blast modeling, *in* '11th International LS-DYNA Users Conference', Detroit, MI, USA, pp. 5–23–5–32.

Larcher, M. (2007), Simulation of the effects of an air blast wave, Technical Report JRC 41337, Joint Research Centre, European Communities, Luxembourg.

Larcher, M., Solomos, G., Casadei, F. & Gebbeken, N. (2012), 'Experimental and numerical investigations of laminated glass subjected to blast loadings', *International Journal of Impact Engineering* **39**(1), 42–50.

Lee, E. L., Hornig, H. C. & Kury, J. W. (1968), Adiabatic expansion of high explosive detonation products, Technical Report TID 4500-UCRL 50422, Lawrence Radiation Laboratory, University of California, CA, USA.

Li, Q. M. & Meng, H. (2002), 'Pressure-impulse diagram for blast loads based on dimensional analysis and single-degree-of-freedom model', *Journal of Engineering Mechanics* **128**(1), 87–92.

Lottero, R. E. (1981), A detailed comparison of 3-D hydrocode computations for shock diffraction loading on an S-280 electrical equipment shelter, Technical Report ARBRL-TR-02334, U.S Army BRL, Aberdeen Proving Ground, MD, USA.

Luo, H., Baum, J. D. & Löhner, R. (2004), 'On the computation of multi-material flows using ALE formulation', *Journal of Computational Physics* **194**(1), 304–328.

Morison, C. M. (2006), 'Dynamic response of walls and slabs by single-degree-of-freedom analysis – a critical review and revision', *International Journal of Impact Engineering* **32**(8), 1214 – 1247.

Morris, W. E. (1959), Shock diffraction in the vicinity of a structure, Technical Report Operation Upshot-Knothole, WT-786, Sandia Corporation, MD, USA.

Murtha, J. P. (1955), Blast loading of structures in the regular reflection and low mach-stem regions, Technical Report SC-TM-5112, Sandia Corporation, MD, USA.

Nassr, A. A., Razaqpur, A. G., Tait, M. J., Campidelli, M. & Foo, S. (2012), 'Single and multi degree of freedom analysis of steel beams under blast loading', *Nuclear Engineering and Design* **242**, 63–77.

Naval Facilities Engineering Command (1986), *Blast Resistant Structures*, Alexandria, VA, DM 2.08.

Needham, C. E. (2010), *Blast Waves*, Springer, Berlin, Germany.

Ngo, T., Mendis, P., Gupta, A. & Ramsay, J. (2007), 'Blast loading and blast effects on structures – an overview', *Electronic Journal of Structural Engineering* **7**, 76–91.

Norris, C., Hansen, R. J., Myle, J. H., Biggs, J. M., Namyet, S. & Minami, J. K. (1959), *Structural Design for Dynamic Loads*, McGraw-Hill, New York, NY, USA.

Norville, H. S., Harvill, N., Conrath, E. J., Shariat, S. & Mallonee, S. (1999), 'Glass-related injuries in Oklahoma City bombing', *Journal of Performance of Constructed Facilities* **13**(2), 50–56.

Rajendran, R. & Lee, J. (2009), 'Blast loaded plates', *Marine Structures* **22**(2), 99–127.

Randers-Pehrson, G. & Bannister, K. (1997), Airblast loading model for DYNA2D and DYNA3D, Technical Report ARL-TR-1310, U.S Army Research Laboratory, Aberdeen Proving Ground, MD, USA.

Remennikov, A. M. (2003), 'Review of methods for predicting bomb blast effects on buildings', *Journal of Battlefield Technology* **6**(3), 5–10.

Rickman, D. D. & Murrell, D. W. (2007), 'Development of an improved methodology for predicting airblast pressure relief on a directly loaded wall', *Journal of Pressure Vessel Technology* **129**(1), 195–204.

Rigby, S. E., Tyas, A. & Bennett, T. (2012), 'Single-degree-of-freedom response of finite targets subjected to blast loading - the influence of clearing', *Engineering Structures* **45**, 396–404.

Rigby, S. E., Tyas, A. & Bennett, T. (2014), 'Elastic-plastic response of plates subjected to cleared blast loads', *International Journal of Impact Engineering* **66**, 37–47.

Rigby, S. E., Tyas, A., Bennett, T., Clarke, S. D. & Fay, S. D. (2014), 'The negative phase of the blast load', *International Journal of Protective Structures* **5**(1), 1–20.

Rigby, S. E., Tyas, A., Bennett, T., Fay, S. D., Clarke, S. D. & Warren, J. A. (2014), 'A numerical investigation of blast loading and clearing on small targets', *International Journal of Protective Structures* **5**(3), 523–574.

Rigby, S. E., Tyas, A., Bennett, T., Warren, J. A. & Fay, S. (2013), 'Clearing effects on plates subjected to blast loads', *Engineering and Computational Mechanics* **166**(3), 140–148.

Rose, T. A. (2002), *Air3d User's guide*, Shrivenham, Cranfield University, Royal Military College of Science, UK.

Rose, T. A. & Smith, P. D. (2000), An approach to the problem of blast wave clearing on finite structures using empirical procedures based on numerical calculations, *in* '16th Symposium on the Military Aspects of Blast and Shock (MABS16)', Oxford, UK, pp. 113–120.

Rose, T. A. & Smith, P. D. (2002), 'Influence of the principal geometrical parameters of straight city streets on positive and negative phase blast wave impulses', *International Journal of Impact Engineering* **27**(4), 359–376.

Rose, T. A., Smith, P. D. & May, J. H. (2006), 'The interaction of oblique blast waves with buildings', *Shock Waves* **16**, 35–44.

Rose, T. A., Smith, P. D. & McLennan, C. P. (2004), 'Blast loading and clearing on tall buildings', *Journal of Battlefield Technology* **7**(3), 1–8.

Safari, K. H., Zamani, J., Khalili, S. M. R. & Jalili, S. (2011), 'Experimental, theoretical, and numerical studies on the response of square plates subjected to blast loading', *The Journal of Strain Analysis for Engineering Design* **46**(8), 805–816.

Sauvé, R. G. & Morandin, G. D. (2004), 'Simulation of contact in finite deformation problems - algorithm and modelling issues', *International Journal of Mechanics and Materials in Design* **1**, 287–316.

Schwer, L. (2010), A brief introduction to coupling Load Blast Enhanced with Multi-Material ALE: The best of both worlds for air blast simulation, *in* '9th LS-DYNA Forum', Bamberg, Germany, pp. 1–12.

Shi, Y., Hao, H. & Li, Z. X. (2007), 'Numerical simulation of blast wave interaction with structure columns', *Shock Waves* **17**, 113–133.

Slavik, T. P. (2009), A coupling of empirical explosive blast loads to ALE air domains in LS-DYNA, *in* '7th European LS-DYNA users conference', Salzburg, Austria.

Smith, P. D., Rose, T. A. & Saotonglang, E. (1999), 'Clearing of blast waves from building façades', *Proceedings of the Institution of Civil Engineers - Structures and Buildings* **134**(2), 193–199.

Souli, M., Ouahsine, A. & Lewin, L. (2000), 'ALE formulation for fluid-structure interaction problems', *Computer methods in applied mechanics and engineering* **190**, 659–675.

Spranghers, K., Vasilakos, I., Lecompte, D., Sol, H. & Vantomme, J. (2012), 'Full-field deformation measurements of aluminum plates under free air blast loading', *Experimental Mechanics* **52**(9), 1371–1384.

Spranghers, K., Vasilakos, I., Lecompte, D., Sol, H. & Vantomme, J. (2013), 'Numerical simulation and experimental validation of the dynamic response of aluminum plates under free air explosions', *International Journal of Impact Engineering* **54**, 83–95.

Subramaniam, K. V., Nian, W. & Andreopoulos, Y. (2009), 'Blast response simulation of an elastic structure: Evaluation of the fluid-structure interaction effect', *International Journal of Impact Engineering* **36**(7), 965–974.

Swisdak, M. M. (1994), Simplified Kingery airblast calculations, *in* '26th Department of Defense Explosives Safety seminar', Miami, FL, USA.

Tabatabaei, Z. S., Volz, J. S., Baird, J., Gliha, B. P. & Keener, D. I. (2013), 'Experimental and numerical analyses of long carbon fiber reinforced concrete panels exposed to blast loading', *International Journal of Impact Engineering* **57**, 70–80.

Taylor, G. I. (1950), 'The formation of a blast wave by a very intense explosion', *Proceedings of the Royal Society A: Mathematical, Physical and Engineering Sciences* **201**(1065), 159–174.

Taylor, W. J. (1972), 'A method for predicting blast loads during the diffraction phase', *The Shock and Vibration Bulletin* **42**(4), 135.

Teich, M. & Gebbeken, N. (2010), 'The influence of the underpressure phase on the dynamic response of structures subjected to blast loads', *International Journal of Protective Structures* **1**(2), 219–234.

Teich, M. & Gebbeken, N. (2012), 'Structures subjected to low-level blast loads: Analysis of aerodynamic damping and fluid-structure interaction ', *Journal of Structural Engineering* **138**(5), 625 – 635.

Tyas, A., Bennett, T., Warren, J. A., Fay, S. D. & Rigby, S. E. (2011b), 'Clearing of blast waves on finite-sized targets – an overlooked approach', *Applied Mechanics and Materials* **82**, 669–674.

Tyas, A. & Pope, D. J. (2003), The energy take-up of panels subjected to near-field blast loading, *in* 'International Conference on the Response of Structures to Extreme Loading', Toronto, Canada.

Tyas, A. & Pope, D. J. (2004), Response number analysis of the response of steel plate panels to near-field blast loading, *in* '2nd Asia-Pacific Conference on Protection of Structures Against Hazards', Singapore, pp. 311–316.

Tyas, A., Warren, J., Bennett, T. & Fay, S. (2011a), 'Prediction of clearing effects in far-field blast loading of finite targets', *Shock Waves* **21**(2), 111–119.

US Army Corps of Engineers (2005), *Methodology manual for the Single-Degree-of-Freedom Blast Effects Design Spreadsheets (SBEDS)*, ACE Protective Design Center, Omaha, NE, USA, PDC-TR-06-01.

US Army Materiel Command (1974), *Explosions in air part one*, Department of the Army, Alexandria, VA, USA, AMCP-706-181.

US Department of Defence (2008), *Structures to resist the effects of accidental explosions*, US DoD, Washington DC, USA, UFC-3-340-02.

Van Leer, B. (1977), 'Towards the ultimate conservative difference scheme. IV. A new approach to numerical convection', *Journal of Computational Physics* **23**, 276–299.

Van Netten, A. A. & Dewey, J. M. (1997), 'A study of blast wave loading on cantilevers', *Shock Waves* **7**(3), 175–190.

Wang, J. (2001), Simulation of landmine explosion using LS-DYNA, Technical Report DSTO-TR 1168, Aeronautical and Maritime Research Laboratory, Melbourne, Australia.

Wei, J. & Dharani, L. R. (2006), 'Response of laminated architectural glazing subjected to blast loading', *International Journal of Impact Engineering* **32**(12), 2032–2047.

Xu, S., Tiwari, V., Deng, X., Sutton, M. A. & Fourney, W. L. (2010), 'Identification of interaction pressure between structure and explosive with inverse approach', *Experimental Mechanics* **51**(6), 815–830.

Zakrisson, B., Wikman, B. & Häggblad, H. (2011), 'Numerical simulations of blast loads and structural deformation from near-field explosions in air', *International Journal of Impact Engineering* **38**(7), 597–612.